UNIVERSIDAD COMPLUTENSE DE MADRID

FACULTAD DE CIENCIAS GEOLÓGICAS
Departamento de Cristalografía y Mineralogía

TESIS DOCTORAL

Petrologic-metallogenic characterization of a specialized granite: the Logrosán stock (Cáceres)

Caracterización petrológico-metalogénica de un granito especializado : el stock de Logrosán (Cáceres)

MEMORIA PARA OPTAR AL GRADO DE DOCTOR

PRESENTADA POR

Eva Chicharro Álvarez

Directores

Carlos Villaseca González
José Ángel López García

Madrid, 2016

PhD Thesis - Tesis doctoral

Petrologic-metallogenic characterization of a specialized granite: the Logrosán stock (Cáceres)

Caracterización petrológico-metalogénica de un granito especializado: el stock de Logrosán (Cáceres)

Eva Chicharro Álvarez

Madrid, 2015

PhD THESIS / TESIS DOCTORAL

Petrologic-metallogenic characterization of a specialized granite: the Logrosán stock (Cáceres)

Caracterización petrológico-metalogénica de un granito especializado: el stock de Logrosán (Cáceres)

Eva Chicharro Álvarez

Departamento de Cristalografía y Mineralogía, Facultad de Ciencias Geológicas
Departamento de Petrología y Geoquímica, Facultad de Ciencias Geológicas

Universidad Complutense de Madrid
Madrid, 2015

PhD THESIS / TESIS DOCTORAL

Eva Chicharro Álvarez

To obtain the degree of DOCTOR IN GEOLOGY AND GEOLOGICAL ENGINEERING (RD 1393) with EUROPEAN MENTION by the COMPLUTENSE UNIVERSITY OF MADRID

Para obtener el grado de DOCTOR EN GEOLOGÍA E INGENIERÍA GEOLÓGICA (RD 1393) con MENCIÓN EUROPEA por la UNIVERSIDAD COMPLUTENSE DE MADRID

Petrologic-metallogenic characterization of a specialized granite: the Logrosán stock (Cáceres)

Caracterización petrológico-metalogénica de un granito especializado: el stock de Logrosán (Cáceres)

Carlos Villaseca González

José Ángel López García

CARLOS VILLASECA GONZÁLEZ (Director), Catedrático
Dpto. de Petrología y Geoquímica, Facultad de CC. Geológicas, UCM
JOSÉ ÁNGEL LÓPEZ GARCÍA (Codirector), Profesor Titular
Dpto. de Cristalografía y Mineralogía, Facultad de CC. Geológicas, UCM

This PhD Thesis has been performed at the Crystallography and Mineralogy Department and at the Petrology and Geochemistry Department of the Geological Sciences Faculty, Complutense University of Madrid. This work was financially supported by the national FPU grant from the Education and Science Ministry of Spain, the projects DGICYT nº CGL2008-05952 (U–Pb geochronology of the Variscan magmatism of central Spain), CGL2011-23560 (The peraluminous Montes de Toledo batholith and the rare-metal mineralisations linked to felsic granitic domes), CGL2012-32822 (P-rich peraluminous granitoids from central Spain and mineralisations linked to felsic granitic domes) of the MICINN-MINECO (Spain), and the Project 910492 (Magmatism and mineralization from the Variscan Central Iberian Zone) of the Complutense University of Madrid. This PhD Thesis is a compendium of a research of more than four years and most results have been published in relevant SCI journals. Nevertheless, this PhD dissertation includes new unpublished data and could be considered as an extended version of the published articles. All authors have given their consent and their approval for the presentation of the data shown in this manuscript.

Esta Tesis Doctoral se ha realizado en el Departamento de Cristalografía y Mineralogía y en el Departamento de Petrología y Geoquímica de la Facultad de CC. Geológicas de la Universidad, Complutense de Madrid. Este trabajo ha sido financiado por una beca FPU del Ministerio de Eduación y Ciencia (España), los proyectos DGICYT nº CGL2008-05952 (Geocronología U-Pb del magmatismo Varisco en el centro de España), CGL2011-23560 (El batolito peralumínico de los Montes de Toledo y las mineralizaciones de metales raros ligadas a cúpulas graníticas félsicas), CGL2012-32822 (Granitoides peralumínicos ricos en P del centro de España y mineralizaciones ligadas a las cúpulas graníticas félsicas) del MICINN-MINECO (España), y el Proyecto 910492 (Magmatismo y mineralizaciones en la zona Centro-Ibérica Hercínica) de la Universidad Complutense de Madrid. Esta Tesis Doctoral es un compendio de una investigación de más de cuatro años de duración y la mayoría de los resultados han sido publicados en revistas de tipo SCI. Sin embargo, este trabajo incluye nuevos datos inéditos y podría considerarse como una versión extendida de los artículos publicados. Todos los autores han dado su consentimiento y su aprobación para la presentación de los datos mostrados en el presente manuscrito.

Los niños habían de recordar por el resto de su vida la augusta solemnidad con que su padre se sentó a la cabecera de la mesa, temblando de fiebre, devastado por la prolongada vigilia y por el encono de su imaginación, y les reveló su descubrimiento:

- La Tierra es redonda como una naranja.

Úrsula perdió la paciencia. "Si has de volverte loco, vuélvete tú solo", gritó. "Pero no trates de inculcar a los niños tus ideas de gitano."

(Gabriel García Márquez – Cien años de soledad)

Agradecimientos / Acknowledgments / Remerciements

No podría agradecer con más sinceridad a mis directores de tesis, Dr. Carlos Villaseca y Dr. José Ángel López, por el apoyo, el cariño y los conocimientos que me han transmitido a lo largo de estos años. Han sido pilares fundamentales para que esta tesis haya salido adelante y se han convertido en mis padres científicos, con la consiguiente mezcla de respeto y afecto que merecen. Al Dr. Roberto Oyarzun, mi director no oficial, de quien he adquirido consejos, ideas y muchas conversaciones y reflexiones interesantes.

Gracias a los miembros del departamento de Cristalografía y Mineralogía, y del departamento de Petrología y Geoquímica. No me han faltado las palabras de ánimo. Muy especialmente agradezco la confianza que en mí han depositado las Dras. Elena Vindel, Victoria López-Acevedo y Sol López de Andrés. Igualmente quiero agradecer su apoyo a la Dra. Cecilia Pérez-Soba y al Dr. David Orejana. Un agradecimiento obligado por incontables razones es el dedicado a Conchi.

Las estancias y participaciones en laboratorios han sido para mí un aprendizaje que considero esencial. Merci beaucoup à la Dr. Marie-Christine Boiron, au Dr. Michel Cathelineau, et au Dr. Jean Dubessy pour leur accueil à Nancy et pour toute leur aide du côté des inclusions fluides. Very special thanks to Dr. Fin Stuart and Dr. Dan Barfod for helping me with the Ar-Ar measurements and making my visit to Glasgow nice and productive. I also want to thank Dr. Teresa Jeffries for her help with the LA-ICP-MS technique. Gracias al Dr. Pablo Valverde, del IGME, por sus enseñanzas sobre la técnica ID-TIMS; al Dr. Clemente Recio, de la Universidad de Salamanca, que me permitió asistir en las mediciones de isótopos de azufre, oxígeno e hidrógeno; al Dr. José Ignacio Gil-Ibarguchi, de la Universidad del País Vasco y a Sonia García de Madinabeitia, por ayudarnos con las mediciones en apatito de LA-ICP-MS. Muchas gracias a Alfredo Fdez. Larios del Centro Nacional de Microscopía Electrónica, por hacer mucho más amenas las innumerables horas de microsonda. Gracias a los técnicos de los laboratorios UCM e IGEO: a José Luis, del Dpto. de Cristalografía y Mineralogía, por sus láminas delgadas; a Marian, Carmen y Pedro, del Dpto. de Petrología y Geoquímica, por su ayuda en la preparación de muestras y separado mineral; y a David M. Freire e Inmaculada Ruiz, del laboratorio de petrofísica.

Son muchos los compañeros geólogos de diversas instituciones que en algún momento me han echado una mano y a los que estoy enormemente agradecida. Entre ellos, cabe destacar a Ester Boixereu, del IGME; a los Dres. Tomás Martín-Crespo y David Gómez, de la Universidad Rey Juan Carlos; al Dr. Miguel Ángel Caja, de Repsol; a Eduardo Rebollada y Alfonso de las

Llanderas, de la Junta de Extremadura; a la Dra. Fátima Martín Hernández, de la Facultad de CC. Físicas, UCM; y al Dr. Luis Barbero, de la Universidad de Cádiz.

El pueblo de Logrosán me ha acogido siempre de manera impecable. No sólo me han permitido realizar el trabajo de campo sin ningún impedimento, sino que me han ofrecido su ayuda en cuanto les ha sido posible. Mi reconocimiento especial a Paqui Peñas y Mari Paz Casado, de las Minas de Logrosán, a Juan Gil, de la AGEX y a Carlos Carmona.

Gracias a todos los compañeros que han pasado por el despacho de doctorandos y con los que he compartido vivencias durante mi estancia en él (Juncal, Helena, Carlos, Williams…). Principalmente a Juan, Darío y Pimen, gracias por todo lo que nos hemos reído y apoyado. No querría que faltase mi gratitud por empatía a los doctorandos de otros departamentos, en especial a Kike.

Agradezco el apoyo económico de los ciudadanos que con sus impuestos han contribuido a la partida presupuestaria de las becas FPU y Proyectos de Investigación del Ministerio de Educación y Ciencia, y del Ministerio de Economía y Competitividad.

Mi llano agradecimiento a Sara y Miriam, por habernos sostenido las unas a las otras en los malos momentos, y por haber vivido los buenos como únicos. A los "euitas y asociados" que han aguantado entre cervezas, o gracias a ellas, mis desencuentros con esta tesis doctoral.

Gracias a mi familia en general, sobre todo a mis padres. Por intentar entender, aunque sin demasiado éxito. Por educarme en los valores que les representan: trabajo, perseverancia, honradez, alegría y una pizca de resignación.

A Gustavo Bulla, mi compañero de vida.

TABLE OF CONTENTS

Petrologic-metallogenic characterization of a specialized granite: the Logrosán stock (Cáceres)

ABSTRACT

The Variscan Orogeny produced widespread granites along the European Variscan belt. In relation to crustal thickening, post-collisional multiple Sn-bearing highly fractionated S-type leucogranites were emplaced. The Logrosán granite represents one of those granitic bodies and is the focus of this study.

The Logrosán granite is located in the Central Extremadura Batholith, within the Central Iberian Zone (CIZ) and was emplaced during post kinematic stages of the Variscan Orogeny at *ca*. 308 Ma, as determined by combined U-Pb ID-TIMS and LA-ICPMS geochronology. The granitic body intruded the metasedimentary Schist Greywacke Complex (SGC) of Neoproterozoic age, which is characterized by a monotonous centimetric to decametric alternation of metagreywackes and slates with a minor presence of coarser-grained metasedimentary facies. The emplacement triggered thermal metamorphism; the contact metamorphic aureole consists of three zones ranging from a proximal narrow hornfels zone, an intermediate spotted slate zone, to an external recrystallized slate zone. The granite emplacement took place at shallow depths and low confining pressures (P: about 2 kbar), thanks to the presence of some elements in the melt (B, Li, F) which allow lowering the solidus and, consequently, increasing the fractionation time. Eventually, this resulted in a major concentration of HFSE elements in the residual melt, notably tin (Sn).

The Logrosán granite is a tin-rich, highly evolved, S-type pluton with a felsic, phosphorous-rich and strongly peraluminous character that forms a 4 km^2 cupola displaying a sub-elliptical shape elongated in the NE-SW axis. A moderately evolved medium- to coarse-grained two mica leucogranite (Main Unit) and several highly evolved aplitic or microporphyritic units (Evolved Units) have been distinguished based on their petrography and whole rock geochemistry. Initial $^{87}Sr/^{86}Sr$ ratios vary from 0.7125 to 0.7286, whereas initial εNd shows a restricted range from -4.3 to -4.0, and $\varepsilon Hf_{(t)}$ ranges from +5.7 to -10.5 for Variscan-age zircons. Inherited zircons exhibit mostly Neoproterozoic ages and juvenile Hf-isotope composition (εHf up to +14.7) analogous to

zircons from the SGC metasediments. The available geological, geochronological, geochemical and isotopic data allow considering the formation of the Logrosán granite by partial melting of heterogeneous Neoproterozoic metasediments, similar to the outcropping SGC materials.

The Logrosán Sn-(W) ore deposit belongs to the metallogenic Sn-W province of the European Variscan Belt. This ore deposit is characterized by the occurrence of quartz-cassiterite veins and greisen-like ores within the granitic cupola (Cerro de San Cristóbal ore deposit) and its surrounding host-rocks (El Serranillo ore deposit). An early stage of boron metasomatism is widely represented in the host-rocks, both the granite, and the metasediments. This metasomatism consists of a well-represented network of quartz-tourmaline veins and veinlets with different strikes. Besides tourmalinization, the granite and the SGC rocks underwent muscovitization/greisenization, silicification and kaolinization. The paragenetic sequence of the Logrosán ore deposits allows distinguishing three stages: (i) Oxide stage, characterized by the precipitation of cassiterite, Nb-Ta phases, and minor wolframite; (ii) Sulfide stage, consisting of a suite of sulfide minerals, principally arsenopyrite, stannite and sphalerite; and (iii) Supergene stage, mostly represented by the alteration of primary minerals.

The endogranitic (Cerro de San Cristóbal) and exogranitic ore deposits (El Serranillo) are supposed to belong to the same process, although more of one mineralization pulse may be considered on the basis of the Ar-Ar geochronology results and the ore textural evidences. Therefore, a relatively long-lived hydrothermal system is suggested with, at least, two pulses (~ 308-306 and 303 Ma), during or soon after the emplacement of the Logrosán related-granite (at *ca*. 308 Ma). Mineral characterization, fluid inclusion study, isotope geochemistry and Ar-Ar geochronology have been combined in order to reconstruct the conditions for the Sn-(W) ore precipitation. The metal-bearing fluids are characterized by the presence of complex mixtures of aqueous and volatile phase fluid inclusions (H_2O-N_2-CO_2-CH_4-NaCl). Microthermometry and Raman analyses indicate that volatile-phase fluid composition evolved from 50 per cent N_2-CH_4 mixtures, to N_2 dominant fluids, followed by CO_2-rich fluids. All these mixtures show varying amounts of H_2O, evolving through pure vapor phases in the late stages of the mineralizing process. The presence of N_2 and CH_4 strongly suggests a metamorphic component, derived from the nearby metasedimentary host rocks. Isotope data for silicate minerals from the quartz-tourmaline, quartz-cassiterite veins, and the muscovitized altered host-rocks also denote a metamorphic signature. The isotopic composition of water calculated from $\delta^{18}O$ of cassiterite, muscovite, tourmaline and quartz, and from δD of muscovite and tourmaline range from 10.9 to 14.6 ‰, and from -53.4 to -80.1 ‰, respectively; which is consistent with a metamorphic fluid origin and a possible magmatic mixing. A model of host-rock interaction, assimilation, and mixing of metamorphic and magmatic fluids, resulting in changes of the redox conditions, is proposed for

the tin deposition. Tin (Sn^{2+}) was remobilized by metamorphic fluids under highly reduced conditions and precipitated as cassiterite (in the form of Sn^{4+}) in association with muscovitization and greisen alteration, owing to a decrease of pressure and an increase of the oxygen fugacity. A mixing of metamorphic fluids with late-magmatic fluids may well have contributed to these redox changes. The temperature and pressure conditions of cassiterite precipitation in the Logrosán ore deposits are estimated between 460 and 540 ºC and 120-270 MPa. These values overlap the P-T conditions estimated for the emplacement of the Logrosán granite, which are in agreement with the penecontemporaneous formation of the Sn-(W) ores and the granite emplacement. Later sulfide minerals precipitated as the result of a probably fluctuant release of pressure and temperature, successive openings and closures of the veins are represented by the late vapor-rich fluid inclusions.

A gravity survey was carried out to determine the shape and subsurface extension of what appeared to be a shallow, flat shaped granitic intrusion in the area. Field gravity and geologic data allow the modeling of hidden granite bodies. However, gravity as a tool for "brownfield type" exploration in a mature granite-related ore setting has not been widely used. The Logrosán area provides a perfect case scenario with Sn-(W) endo- and exogranitic ore deposits within a relatively small-scale realm. The understanding of the subsurface of the Logrosán area provides a key tool to develop a more comprehensive geological and metallogenic model for the ore deposits. In addition, a better explanation for the mineral evolution and the Sn-W ore precipitation can be achieved, by comparing the chemical and textural features of ores from several of the Logrosán deposits. Combining the gravity information with detailed mineralogical, geochemical data and ore deposit modeling has allowed a definition of targets for probable new Sn-(W) deposits, all within a few kilometers of the main intrusion center.

The phosphate ore deposit of La Costanaza is found nearby the Logrosán granite, and represented in the XIX century the most important phosphate mine in Europe. It consists of high grade hydrothermal quartz veins hosted by the Neoproterozoic metasediments of the SGC complex. Some other hydrothermal phosphate veins also occurred around the Logrosán granite (e.g., Mingote, Barrero, etc.). Hydrothermal quartz-apatite veins, called "Iberian Type", occur exclusively in the southern Central Iberian Zone. The mineral assemblage of these veins comprises quartz, apatite, minor sulfides, dolomite, Fe-Mg-carbonates and Fe-Mn-oxides. Apatite occurs mainly as fibrous-radial aggregates (the so-called 'dahllite') with beautiful colloform textures, which in the past caused that these ores were misinterpreted as fossils. Apatite displays other different textures, such as needle-like, tabular, prismatic, or pseudohexagonal crystals. Alternating and/or concentric bands of quartz and apatite dominate the veins.

A comparison between the hydrothermal apatite from the veins (H-apatite), the magmatic apatite from the associated granites (M-apatite) and the apatite occurring in phosphate-nodules from the SGC (S-apatite) allows inquiring into the possible origin of the hydrothermal phosphate ores. Hydrothermal apatite from veins (H-apatite) is enriched in Sr and depleted in Mn-Y-REE-Th-U-Pb compared to magmatic apatite (M-apatite) from the granitic plutons. However, trace element composition of apatite from metasedimentary phosphorous-rich levels (phosphorite) or nodules from the Schist Greywacke Complex (S-apatite) shows similar characteristics to the H-apatite composition, although the H-apatite stands out for its relatively high Sr-contents. The relative Sr enrichment in H-apatite is interpreted as inherited from both, the phosphate from the Neoproterozoic metasediments (S-apatite) and the carbonate levels within it. Fluid inclusion studies undertaken on quartz reveal the involvement of aqueous low salinity fluids (0.2 – 0.4 %wt. NaCl equiv.) at moderate to low Th (140-360ºC). Similar fluid inclusion results and chemical features are found in the analogous northern quartz-apatite veins of Belvís de Monroy and Navalmoral de la Mata (Montes de Toledo Batholith).

REE, fluid inclusion and stable isotope data are consistent with a long episode of hydrothermal activity implying cooling and dilution processes while interacting with phosphate-rich shale and carbonate beds in the SGC. All available data suggest a recycling event of the southern CIZ metasediments (the SGC) during post-Variscan hydrothermal fluid circulation as the more plausible origin of the phosphate vein-type ores.

Caracterización petrológico-metalogénica de un granito especializado: el stock de Logrosán (Cáceres)

RESUMEN

La orogenia Varisca produjo un magmatismo félsico generalizado en el Cinturón Varisco Europeo. Numerosos leucogranitos post-tectónicos altamente fraccionados, ricos en estaño, y de tipo S se emplazaron como consecuencia del engrosamiento cortical. El granito de Logrosán es uno de estos cuerpos graníticos y constituye el eje principal de este estudio.

El granito de Logrosán forma parte del Batolito de Extremadura Central, en la Zona Centro Ibérica (ZCI) y se emplazó durante los estadios post-cinemáticos de la orogenia Varisca, hace aproximadamente 308 Ma, tal como ha sido determinado por combinación de geocronología U-Pb ID-TIMS y LA-ICPMS. El cuerpo granítico intruyó a los metasedimentos del Complejo Esquisto Grauváquico (CEG) de edad neoproterozoica. El CEG está caracterizado por una monótona alternancia, de centimétrica a decamétrica, de metagrauvacas y pizarras con menor presencia de facies metasedimentarias de grano grueso. El emplazamiento granítico dio lugar a un metamorfismo de tipo térmico; la aureola de metamorfismo de contacto está constituida por tres zonas que gradan desde una estrecha zona proximal de corneanas, a una zona intermedia de pizarras mosqueadas, hasta una zona externa de pizarras recristalizadas. El emplazamiento del granito tuvo lugar a profundidades someras y bajas presiones confinantes (P: alrededor de 2 kbar) gracias a la presencia de ciertos elementos en el fundido (B, Li, F) que permitieron una disminución de la temperatura del sólidus y, por consiguiente, incrementaron el tiempo de fraccionamiento cristalino. Como consecuencia, se produjo una mayor concentración de elementos HFSE en el fundido residual, especialmente de estaño (Sn).

El granito de Logrosán es un plutón muy evolucionado, rico en estaño, de tipo S y con un carácter perfosfórico y fuertemente peralumínico. Se trata de una cúpula granítica de unos 4 km^2 de área, de forma sub-elipsoidal y con el eje mayor dispuesto en dirección NE-SW. En cuanto a su petrología y geoquímica de roca total se han distinguido dos unidades: (i) un leucogranito de dos micas de grano medio-grueso moderadamente fraccionado (Unidad Principal – Main Unit), y (ii)

otras variedades graníticas más evolucionadas de tipo aplítico o microporfídico (Unidades Evolucionadas – Evolved Units). Las relaciones iniciales $^{87}Sr/^{86}Sr$ varían desde 0.7125 a 0.7286, mientras que los valores iniciales de εNd muestran un rango muy restringido entre -4.3 y -4.0; por último, el $\varepsilon Hf_{(t)}$ de los circones de edades variscas varía entre +5.7 y -10.5. Los circones heredados presentan principalmente edades neoproterozoicas y composiciones isotópicas de Hf juveniles (εHf hasta +14.7) análogas a las composiciones isotópicas de los metasedimentos del CEG. Los datos geológicos, geocronológicos, geoquímicos e isotópicos disponibles permiten considerar que la formación del granito de Logrosán se produjo por fusión parcial de metasedimentos neoproterozoicos similares a los materiales del CEG.

Los yacimientos de Sn-(W) de Logrosán están localizados dentro de la provincia metalogénica de Sn-W del Cinturón Varisco Europeo. Este yacimiento está caracterizado por la presencia de filones de cuarzo-casiterita y depósitos tipo greisen localizados tanto en la cúpula granítica (yacimiento del Cerro de San Cristóbal), como en los metasedimentos encajantes (yacimiento de El Serranillo). En las rocas encajantes, tanto en el granito como en los metasedimentos, se reconoce un estadio inicial de metasomatismo de boro bastante desarrollado y representado. El metasomatismo de boro consiste en concentraciones turmaliníferas, así como en el desarrollo de una importante red de filones y filoncillos de cuarzo-turmalina con direcciones variables. Además de turmalinización, el granito y las rocas del CEG presentan otras alteraciones, tales como moscovitización/greisenización, silicificación y caolinización. La secuencia paragenética de los yacimientos de Logrosán permite distinguir tres episodios: (i) estadio Oxidado, caracterizado por la precipitación de casiterita, fases de Nb-Ta, y en menor medida, wolframita; (ii) estadio Sulfurado, representado por la asociación de sulfuros, principalmente arsenopirita, estannita y esfalerita; y (iii) estadio Supergénico, que consiste fundamentalmente en la alteración de los minerales primarios.

Los depósitos endogranítico (Cerro de San Cristóbal) y exogranítico (El Serranillo) son el resultado de un mismo proceso, aunque se considera que pudo haber más de un pulso mineralizante en base a los resultados de geocronología de Ar-Ar y a datos texturales de algunas de las fases minerales. Por lo tanto, se deduce que durante o poco después al emplazamiento del granito (*ca*. 308 Ma) se desarrolló un sistema hidrotermal relativamente prolongado en el tiempo con, al menos, dos pulsos mineralizadores (~ 308–306 Ma y 303 Ma). La caracterización mineral, el estudio de inclusiones fluidas, la geoquímica isotópica y la geocronología de Ar-Ar se han analizado de manera integrada con el objetivo de reconstruir las condiciones de la precipitación de la mena del yacimiento. Las inclusiones fluidas de los fluidos portadores de metales en solución están caracterizados por la presencia de mezclas complejas de fases acuosas y volátiles (H_2O-N_2-CO_2-CH_4-NaCl). Los análisis de microtermometría y Raman indican que la

composición volátil del fluido evolucionó desde mezclas al 50 por ciento de N_2-CH_4, a composiciones con N_2 dominante, seguidas de fluidos ricos en CO_2. Estas mezclas de fases volátiles se presentan con cantidades variables de H_2O, que evolucionan hacia fases gaseosas puras en los estadios más tardíos de la mineralización. La presencia de N_2 and CH_4 claramente apunta a un componente de origen metamórfico derivado de las rocas metasedimentarias encajantes. Los datos isotópicos de los minerales silicatados de los filones de cuarzo-turmalina, cuarzo-casiterita y de los granitos y metasedimentos alterados por turmalinización, greisenización y/o moscovitización también denotan una signatura metamórfica. La composición isotópica de las aguas calculada a partir del $\delta^{18}O$ de la casiterita, moscovita, turmalina y cuarzo, y de δD de la moscovita y turmalina varían desde 10.9 a 14.6 ‰, y de -53.4 a -80.1 ‰, respectivamente; estos valores son consistentes con un origen metamórfico del fluido y una posible mezcla del mismo con un fluido magmático. Para la precipitación de la casiterita se propone un modelo de interacción con la roca encajante, asimilación y mezcla de fluidos metamórficos y magmáticos que tendría como resultado el cambio en las condiciones redox. Los fluidos metamórficos permitieron la movilización del estaño (Sn^{2+}) bajo condiciones muy reducidas; posteriormente, el estaño (en forma Sn^{4+}) precipitó como casiterita en asociación con moscovitización y alteración tipo greisen, debido a una disminución de presión y a un incremento de fugacidad del oxígeno. Una mezcla entre fluidos metamórficos con fluidos tardi-magmáticos muy probablemente contribuyó a estos cambios en las condiciones redox. Las condiciones de precipitación de la casiterita en el yacimiento de Logrosán se estiman entre 460 y 540 ºC de temperatura, y 120-270 MPa de presión. Estas estimaciones se superponen a las condiciones P-T consideradas para el emplazamiento del granito de Logrosán, lo cual está de acuerdo con una situación de penecontemporaneidad en la formación del yacimiento de Sn-(W) y del granito. Los minerales sulfurados, más tardíos, precipitaron como consecuencia de una caída de presión y de temperatura. Estos cambios P-T se produjeron probablemente de manera fluctuante, dado que las inclusiones fluidas más tardías y ricas en vapor reflejan posibles aperturas y cierres sucesivos en estos filones.

Con el objetivo de determinar la forma y extensión bajo la superficie del granito de Logrosán se llevó a cabo una campaña gravimétrica de lo que parecía ser una intrusión granítica somera, con forma achatada (‘flat shaped’). La gravimetría de campo y los datos geológicos permiten el modelado de granitos no aflorantes. Sin embargo, la gravimetría como técnica de exploración en granitos asociados a mineralizaciones dentro de contextos geológicos clásicos no se utiliza habitualmente. La zona de Logrosán representa un escenario excepcional para estudios de este tipo ya que presenta mineralizaciones de Sn-(W) endo- y exograníticas en un área relativamente reducida. El conocimiento del subsuelo en la zona de Logrosán aporta herramientas esenciales para desarrollar un modelo metalogénico más fundado del yacimiento. Además, se puede

conseguir una interpretación más robusta de la evolución mineral y de la precipitación de las menas de Sn-(W) comparando las características texturales y químicas de los depósitos endo- y exograníticos de Logrosán. La combinación de la información gravimétrica, de los datos geoquímicos y mineralógicos y del modelado del yacimiento permite la definición de nuevos indicios de Sn-(W) en una distancia radial de unos pocos kilómetros en torno a la intrusión.

El yacimiento de fosfato de La Costanaza se localiza en las inmediaciones del granito de Logrosán, y fue durante el siglo XIX la mina de fosfatos más importante de Europa. Consiste en filones de cuarzo-apatito altamente mineralizados, encajados en los metasedimentos neoproterozoicos del Complejo Esquisto Grauváquico. Otros filones hidrotermales de fosfato también localizados en las inmediaciones del granito de Logrosán son, por ejemplo, el filón Barrero o el filón Mingote. Los filones hidrotermales de cuarzo-apatito, denominados "de tipo Ibérico", están localizados exclusivamente en el sur de la Zona Centro Ibérica. La asociación mineral de estos filones incluye cuarzo, apatito, y en menor medida, sulfuros, dolomita, carbonatos de Fe-Mg y óxidos de Fe-Mn. El apatito se presenta principalmente en forma de agregados fibroso-radiados (conocidos como 'dahllita') con texturas coloformes espectaculares, lo cual en el pasado llevó a la confusión de ser malinterpretados como fósiles. El apatito presenta otras texturas diversas, como texturas aciculares, tabulares, prismáticas o cristales pseudohexagonales. Los filones suelen estar constituidos de bandas alternantes y/o concéntricas de apatito y cuarzo.

La comparación del apatito hidrotermal de los filones (H-apatito), el apatito magmático de los granitos asociados (M-apatito) y el apatito presente en nódulos fosfatados del CEG (S-apatito) permite indagar sobre el posible origen de las mineralizaciones hidrotermales fosfatadas. El apatito hidrotermal de los filones (H-apatito) está enriquecido en Sr y empobrecido en Mn-Y-REE-Th-U-Pb en comparación con el apatito magmático (M-apatito) de los plutones graníticos. Sin embargo, las composiciones de elementos traza del apatito de los niveles fosfatados (fosforita) o nódulos del Complejo Esquisto Grauváquico (S-apatito) muestran características similares al H-apatito, aunque el H-apatito destaca por sus relativamente altos contenidos en Sr. El enriquecimiento relativo en Sr del H-apatito se interpreta como heredado, tanto de los fosfatos presentes en los metasedimentos del CEG (S-apatito) como de los niveles carbonatados en el mismo. El estudio de inclusiones fluidas llevado a cabo en cuarzo revela la participación de fluidos de baja salinidad (0.2 – 0.4 %wt. NaCl equiv.) y moderadas o bajas temperaturas (Th: 140-360ºC). En los filones equivalentes de cuarzo-apatito de Belvís de Monroy y Navalmoral de la Mata (Batolito de los Montes de Toledo) se han observado similares características químicas y se han obtenido análogos resultados de inclusiones fluidas.

Los contenidos en elementos de tierras raras (REE), las inclusiones fluidas y los datos de isótopos del apatito hidrotermal son consistentes con una actividad de fluidos de larga duración. Un proceso hidrotermal prolongado permitiría que se produjese un enfriamiento y dilución progresiva de los fluidos hidrotermales, al tiempo que interaccionaban con las unidades ricas en fosfato y niveles carbonatados del CEG. Los datos disponibles sugieren que el origen de los yacimientos de fosfato hidrotermales (de tipo Ibérico) obedece a un evento de reciclaje de los metasedimentos de la parte sur de la Zona Centro Ibérica (el CEG) debido a procesos de actividad hidrotermal post-varisca.

Chapter 1: INTRODUCTION

SUMMARY:

The aim of this chapter is to introduce the objectives and contributions of the present PhD dissertation. The global geological, metallogenic and historical framework of the Logrosán ore deposits is also presented.

INTRODUCTION

1.1. Principles

The Iberian Belt shows the largest concentration of felsic magmatism within western Europe, mainly in its inner parts. The Central Iberian Zone (CIZ) is composed by vast granite batholiths drawing sub-concordant major linear arrays (e.g., López Plaza and Martínez Catalán, 1987). Numerous quartz-cassiterite and quartz-wolframite ores are associated with highly evolved tin-rich Variscan S-type granites from the Iberian Belt. They constitute the southwestern part of the Sn-W metallogenic province of the European Variscan Belt. These Sn-W ore deposits are represented by granite-hosted or metasedimentary-hosted mineralization close to granite cupolas. Breccia pipes (Breiter et al., 1999), and sulfide replacement or skarn types (Cheilletz et al., 2005) are less often developed. On the whole, greisen alteration and mineralized veins may be found within the granite, in endo- or exogranitic zones, and less frequently beyond the contact metamorphic aureoles. They may also be found within granite pegmatite fields surrounding the plutons (e.g., Roda-Robles, 2010; Martins et al., 2011; Llorens, 2011). Nonetheless, tin-tungsten ore deposits of economic importance, such as Panasqueira in Portugal (Kelly and Rye, 1979) or Dadoshua in China (Cheng et al., 2012), are hosted by metasedimentary and carbonate country rocks and known to be related to hidden granites. Other important Sn-W metallogenic provinces in the world are the SE Asian tin belt (Burma, Thailand, Malaysia, Indonesia), the South China tin province, the Bolivian tin belt, the Central African tin province, the Jos Plateau tin fields (Nigeria) or the West Australian tin fields.

The granites of the Iberian Zone have been largely studied during the last few decades, existing precise dating of granites and theories of their petrogenesis (e.g., Dias et al., 1998; Castro et al., 2000; Fernández-Suárez et al., 2000; Bea et al., 2003; Villaseca et al, 2008; Carracedo et al., 2009; Martins et al., 2009; Solá et al., 2009; Antunes et al., 2010; Gutiérrez-Alonso et al., 2011; Teixeira et al., 2011; Orejana et al., 2012; Merino et al., 2014). Most of the outcropping Variscan granites in the CIZ have a peraluminous character, as expected in an intracontinental orogenic setting (Sylvester, 1998; Villaseca et al., 1998a; Bea et al., 2003). Despite the vast quantity of research about these granites, the nature of the protoliths and some aspects regarding the origin and composition of granites (contamination during magma ascent or emplacement, incorporation of restites, presence of inherited components, etc.) are still a matter of debate (e.g., Villaseca et al., 2008; Merino, 2014). The petrogenetic theories include granite formation from crustal-recycling by lower crustal derivation (e.g., Villaseca et al., 1999) or by melting at mid-crustal levels (e.g., Bea et al., 2003); to mantle-derived processes, either by mixing (e.g.,

Dias and Leterrier, 1994; Moreno Ventas et al., 1995) or by assimilation (e.g., Castro et al., 1999). The relationship of Sn-W mineralization with magmatism is widely recognized (e.g., Roedder, 1984; Lehman, 1990; Pirajno, 1992; Burnham, 1997). Some Variscan granites are tin-rich and/or are cut by tin-bearing pegmatites and veins (Neiva, 2008). These granites, which are supposed to be the parent rocks of the Sn-W deposits, are peraluminous S-type two-mica leucogranites. They usually display negative Eu anomalies, crustal-like isotopic values ($^{87}Sr/^{86}Sr)\geq0.708$, εNd_t between −4.5 and −16.4, and $\delta^{18}O$ values between 11.0 and 12.8‰ (e.g., Neiva et al., 2011). In general, these granites were formed after partial melting of heterogenous metasediments (Neiva et al., 2009; Teixeira et al., 2012). Tin enrichment in residual melts is mainly due to fractional crystallization processes and favored by low fO_2 in reduced ilmenite-serie granites (Ishihara et al., 1989; Lehman, 1990). Hydrothermal alteration (e.g., greisenization) is also considered as responsible of the tin enrichment (e.g., Gomes and Neiva, 2002).

Different interpretations of fluid inclusion and stable isotope data have led to competing hypotheses on the source of mineralizing fluids and the mechanisms of Sn-W concentration and precipitation. Magmatic, metamorphic, and meteoric waters have been proposed as sources of the metal-bearing fluids (e.g., Kelly and Rye, 1979; Wilkinson, 1990; Alderton and Harmon, 1991). Fluid mixing, interaction with the country rocks, and fluid immiscibility are some of the proposed mechanisms for ore deposition. An interval of several million years between the solidification of the related granite and the ore formation has been recorded for tin ore deposits (Lehman, 1990). Nevertheless, geochronological data on Variscan tin-tungsten ore deposits in West and Central Europe have shown good agreement between granite and mineralization timing (Darbyshire and Sheperd, 1985; Snee et al., 1988; Chesley et al., 1993; Romer et al., 2007; Moura et al., 2014). For instance, in the Sn-W Carris granite from Portugal, Moura et al. (2014) obtained a Re-Os age of molybdenite of 279.4±1.2 Ma (2σ), while the ID-TIMS U-Pb dating of zircon from the granite was 280±5 Ma (2σ). Similar ages were obtained for several plutons with Sn-W mineralization in the Cornubian batholith, UK (Chesley et al., 1993); e.g., the St. Austell pluton displays a weighted average $^{207}Pb/^{235}U$ age of 281.8±0.4 Ma (2σ), and Ar-Ar data for muscovite ranging from 270.3±0.8 Ma (2σ) to 278.3±0.8 Ma (2σ). Ar-Ar dating of muscovite combined with recent U-Pb direct dating on cassiterite shows a coeval relationship of the ore with nearby cupolas of highly fractionated granites in Chinese deposits (Yuan et al., 2011; Cheng et al., 2012; Cheng et al., 2013; Chen et al., 2014; Zhang et al., 2014).

Hydrothermal phosphate veins occur exclusively in the southern Central Iberian Zone (CIZ), which is the innermost part of the Iberian Variscan Massif. These ore deposits are spatially related to peraluminous and phosphorous-rich granitic intrusions as intra or extra-batholitic

veins. The phosphate veins, so-called "Iberian Type" by Aizpurúa et al. (1982), are of relevant importance since they have been recognized only in this part of the Variscan Belt of Western Europe. These veins are of hydrothermal origin and their relationship with the associated granites remains unclear. Two types of mineralization were exploited: (1) quartz-apatite veins of hydrothermal origin and (2) stratabound deposits related to Lower Carboniferous carbonate rocks filling karstic cavities. There are only old and incomplete studies in the literature about the hydrothermal quartz-apatite veins (Aizpurúa et al., 1982, Rambaud et al., 1983). Among the main mining districts of this type, the most productive during the first part of the 20th century was Logrosán (Boixereu, 2003). There are other small occurrences in the Central Iberian Zone, such as Belvís de Monroy, Millanes, and Navalmoral de la Mata.

1.2. Scope of research

This PhD dissertation focuses on a small granitic cupola and its associated Sn-(W) and P mineralization at Logrosán (Cáceres, Spain). The Logrosán granite is located in the Central Iberian Zone, within the southern part of the Sn-W metallogenic province of the Variscan European Belt. It is related to two types of mineralization: i) an endo- and exogranitic Sn-(W) cassiterite-bearing vein-complex, related to greisen-like, muscovitization and tourmalinization alterations, ii) an exogranitic P-rich ore of hydrothermal apatite (dahlite)-quartz veins. The purpose is to determine the origin of the Sn-(W) and P ore deposits spatially associated with the highly fractionated, S-type, and phosphorous-rich Logrosán granite. The choice of the Logrosán granite as the matter of study of this Thesis responded to the variety of mineralization set in a relatively small area (a few km^2). Therefore, the Logrosán area became an excellent field laboratory for a Sn-W granite related case-study.

The main interests of this work are the Sn-(W) ore formation, and the petrogenesis and nature of the granitic source rocks; additionally, the P ore characterization and genetic conditions have been also considered. The key objectives accomplished in this PhD research are:

- Plutonic rocks:
    - Cartography and petrographic characterization of the intrusive body.
    - Major and minor whole-rock geochemistry, as well as isotopic characterization of the different granitic units.
    - Mineral chemistry characterization (major analyses by EMPA, and trace analyses by LA-ICP-MS).

  - U-Pb zircon geochronology and study of the inheritances (TIMS and LA-ICP-MS).
  - Nature and sources of the granitic melts (Sm-Nd, Rb-Sr, Lu-Hf in zircons).
  - Synthesis and comparison with similar granites of the region.

- Mineralization:
  - Study and characterization of the mineralization styles.
  - Textural and chemical characterization of the Sn-(W) and P ores.
  - Study of the associated alteration processes (greisinization, muscovitization, tourmalinization, kaolinitation).
  - Spatial and temporal relationships between host rocks and ore bodies (field observations, Ar-Ar geochronology).
  - Fluid inclusion studies.
  - Nature and source of the hydrothermal metal-bearing fluids (O/H, S, and C isotopes)
  - Identification of the conditions responsible of the ore accumulation and precipitation.

These objectives allowed picturing an integrate outlook where different questions needed to be asked. The essential issues discussed in this PhD dissertation are: (i) the degree of fractionation, composition, and nature of granite magmas; (ii) the P-T granite emplacement conditions; (iii) the nature and chemistry of fluids involved in the Sn-(W) and P mineralization; (iv) the oxidation state conditions, and other aspects regarding the mobility of metals; (v) the gap timing and relationship of the granite emplacement and the precipitation of Sn-(W) and P ores.

1.3. Previous works

Owing to its historic mining relevance, there are numerous previous works and reports from this region. The scientific works about the granite petrology and the Sn-W ore deposits date from the last decades of the XX century and contain valuable information. On the contrary, the phosphate ore deposits were largely studied since the XVIII century; unfortunately, most of the works are very old and lack of scientific accuracy, although they provide very interesting ideas and worthy descriptions.

The first document regarding the Logrosán granite is a geologic profile attached to the map included in the report “Memoria sobre la fosforita de Logrosán” by Naranjo y Peñuelas (1860). The Logrosán granite is described for the first time in the “Memoria Geológica de la Provincia

de Cáceres" by Egozcué and Mallada (1876). Nevertheless, it is remarkable that no indications about the Sn-W ore deposits or the metal-bearing potential are included in these previous works. Roso de Luna (1898) in his work "Descripción del horizonte geológico de Logrosán" is, to my knowledge, the first person who mentions the presence of tin, tungsten, and other metals in the Logrosán granite and in the El Serranillo hill (extragranitic mineralization). But it is not until more recent works that the Sn-W ores became relevant. This works correspond to Sos Baynat (1967) and provide the first complete report describing the petrology, mineralogy, structural geology and mineralization of the Logrosán granite. The works of Rossi (1975) include the first modal composition and classification of the Logrosán granite, microscopic characterization of magmatic minerals and ores, description of the alteration, and the first dating of the granite using the K-Ar method, obtaining an age of 335 ± 10 Ma. Nonetheless, Sos Baynat (1981) suggests that both, the granite and the mineralization, are of Precambrian age, related to the Sardic deformation phase (Caledonide orogeny). More recently, the works of Guijarro (1982a) and Guijarro et al. (1985b) dealing with the Sn-W ores from Logrosán, provide a study about the structural control of the mineralization, and propose a pneumatolytic-hydrothermal origin for the Logrosán Sn-W ore deposits. The first fluid inclusion microthermometric study of the Logrosán ores is performed by Guijarro et al. (1983). Guijarro et al. (1986) focus on the petrographic characterization, and include the first whole rock analyses of the Logrosán granite. The alteration of cassiterite is also revised using X-ray techniques by Guijarro et al. (1982b). Finally, Guijarro et al. (1985a) study the distribution of Th and U, and suggest that the greisenization process may have produced the leaching of these elements and contributed to uranium mineralization sources outside the granite. It is also worth to note the geological studies of ENADMISA (1982), Billinton Española S.A. (1982), and the geological maps 1: 50.000 and memories of the area published by the Instituto Geológico y Minero de España (IGME, 1981a; 1981b; 1990; 1995). There are also several publications produced by the Junta de Extremadura (1993a; 1993b; 2007; 2010) with short mentions to the Logrosán granite and associated Sn-W and P mineralization. Finally, my Master Thesis (Chicharro, 2009) focuses on the cartography, a short structural study of metal-bearing veins, the characterization by EMPA of minerals from the granite and the Sn-W ores, and a preliminary P-T estimation for the granite and ore formation.

The oldest scientific notes about the geology of Logrosán deal with the phosphorite deposits and are included in the work "Introducción a la historia natural y a la geografía de España" (Bowles, 1789). Since then, some scientists were very interested in the chemistry of this new mineral. Among them, Proust (1799) characterizes the chemistry and properties of the Logrosán apatites in his work "La piedra fosfórica de Extremadura", making the site of Logrosán the phosphorite type-locality. Herrger (1800) refines the first descriptions of the physical properties of the

Logrosán apatite in the work "Descripción orictognóstica del apatito térreo de Logrosán", where he misidentifies the apatite as a fossil. Naranjo y Peñuelas presented in 1849 a report on behalf of the Spanish Government entitled "Memoria sobre la fosforita de Logrosán, which was not published until 1860 (Naranjo y Peñuelas, 1860). This review contains new chemical analyses, and a topographic and geologic map. One of the most significant work is the "Memoria Geológica de la Provincia de Caceres" by Egozcué and Mallada (1876). It contains petrologic, mineralogical, paleontological, and stratigraphic descriptions, but also a tectonic summary and detailed maps of the region. Some other works focused on describing the phosphate ores and calculating reserve estimations during these years (see Sos Baynat, 1967). The works of Vilanova (1890) should be noted, this author attributed the apatite to an orthoceras fossil. This initiated a scientific debate about the origin of the Logrosán phosphorite. Nonetheless, the last works of Vilanova are in agreement with the genesis theories sustained by Egozcué y Mallada. This hypothesis suggested a geyser scenario for the phosphorite formation. The reports of Roso de Luna (1898) include a vast revision of the geography, geology and history of the town of Logrosán. Roso de Luna (1898) also proposes a theory for the origin of the concentric textures of the phosphorite, which, according to his ideas, would have been affected by metamorphism and folding. Later works deal with the description of the main mining vein (La Costanaza), such as the works of Choffat (1909). The mining report of Gutzwiller (1919) focuses on the deposit evaluation from a technical and economic point of view, including detailed mine maps. A most modern work is that by Aizpurúa et al. (1982), which distinguishes two phosphate occurrences in the Central Iberian Zone: (i) quartz-apatite veins related to granites, and (ii) phosphate ore deposits hosted by carbonates. They denote the former group as Iberian-type owing to its singularity in the southern part of the CIZ, and suggest a hydrothermal origin. Rambaud et al. (1983) describe the paragenesis and textures of different quartz-apatite veins of the region, assuming a high-T hydrothermal origin related to a magmatic episode. Most recently, a cartography of the recent galleries of the La Costanaza mine has been undertaken by Rivas Dorado (2013) in his Master Thesis.

1.4. Historic and economic background

1.4.1. Tin mining history in Logrosán

Archaeometallurgical evidence for early tin mining metallurgical settlement by the Tartessians (Bronze Age; 800-860 B.C.) has been found in the Logrosán granite (Sos Baynat, 1977; Calles et al., 1994; Meredith, 1998; Pavón Soldevila et al., 2010; Rodríguez Díaz, 2013). The first archaeological finds were those of Sos Baynat (1977), and include stone crushers, stone molds,

hammers, escoria, pottery, jewelry, etc. Sos Baynat (1977) remarks the strategic location of the San Cristóbal hill (Logrosán granite) with privileged views of the plain, and the importance of the south of Spain in Bronze Age metallurgy. Meredith (1998) undertook several excavation work surveys in the San Cristóbal hill between 1992 and 1998, and confirms the archaeological surface evidence for ancient mining and settlement activity. The work of Meredith (1998) suggests that the stone ruin remnants from the eastern summit of the San Cristóbal hill may consist of man-made levered areas corresponding to a defense wall, as also proposed by Calles et al. (1994). Nevertheless, the age of this defense wall is still uncertain and may correspond to the foundation of the Logrosán modern-town age (1545 A.D.) (Sos Baynat, 1977; Meredith, 1998; Andrews, 2014). On the other hand, the western summit provides remains of stone wall foundations for round structures, hammer/crushing stone fragments, pottery fragments, and stone loom weight, although most of them have been moved during the modern mining activities. Moreover, a grooved stone mining hammer similar to those used in the Bronze Age in Río Tinto mine was also found, suggesting similar metallurgical techniques (Meredith, 1998). More metalworking evidence (crucibles, molds, copper ingots, bronze weapons) is described by Andrews (2014). Pavón Soldevila et al. (2010) analyze the surface of a grinding mill, finding Sn, Ni and Pb residues, which indicates that it was used for mining purposes instead of the grinding of wheat or other grains. Rodríguez et al. (2013) propose an ancient mining-metallurgical process very similar to the current processes. Andrews (2014) suggests the possibility that crushed cassiterite instead of tin metal was added directly to the molten copper in the crucible. Moreover, Pavón Soldevila et al. (1998; 2010) and Rodríguez et al. (2013) consider that the Logrosán site was a significant location within the Bronze Age culture tin trade networks in the south-western Iberia.

Modern phase of mining dates from 1949, when migrant miners and local residents rediscovered cassiterite veins in the Logrosán granite while looking for gold deposits. The geologist Sos Baynat was the head-of the mining operations. The mining activities were afforded by the businessman José Fernández López, who needed tin for his canned fish company. Mining works were also carried out by mining companies from 1952 to 1962 (Chicharro et al., 2011). Cassiterite veins and eluvial and alluvial deposits were exploited until the end of the 1960s (Fig. 1.1). Unfortunately no proper records of the mineral activities and the volume of cassiterite production remained (Meredith, 1998). The discovery of the Sn-(W) ore deposits of the San Cristóbal hill is related to a production increase in Cáceres of 233%, although the prices of Sn were also very high (IGME, 1950). Chicharro et al. (2011) estimate that Logrosán would represent between the 30-50% of the Cáceres tin production in 1950.

Fig. 1.1.: a) Miners in a small gallery (J.M. Sanchís collection). **b)** Women panning in an alluvial deposit (Fot. Villas, 1954). **c)** Gravimetric concentration table (Fot. Villas, 1954). **d)** Mineral drying process (Fot. Villas, 1954).

According to the Spanish Governmental Bulletin (BOE), most mining licenses in the area expired in the late 1970s, while the last one expired in the early 1990s. Owing to the economic potential of the Logrosán area new prospecting and exploration licenses have been recently granted to a Finnish mining company (Mineral Exploration Network Ltd.).

1.4.2. Phosphate mining history in Logrosán

Western-central Spain was one of the most important phosphate producer regions in Europe from the 1850's to the end of the Second World War (Boixereu, 2004). La Costanaza (Logrosán) was the most important phosphate mining site during the XIX and XX centuries. The development of the fertilizer industry in the XIX century required more and more prime matters, which induced the growth of the phosphate mining. In 1856 there was an official announcement in the Spanish Courts (Cortes Españolas) about the discovering of the phosphate mine of La Costanaza, although the academic world was already aware of its existence (see 1.3 Previous Works section). Even though a characterization of these ore deposits was done, the transportation difficulties avoided the progress of the business. The mining production of La Costanaza mine (Logrosán) was active from 1907 until 1946, providing 200.000 tons of mineral, the half of the national phosphate production (Junta de Extremadura, 1993a). In 1922, the mine reached 162 m underground; in the following years until its closure in 1946, it reached

more than 210 m in 15 levels (Fernández-Amo et al., 2010). The transportation of the required processing products and the final mineral were the main issues during the mining activities. A superphosphate plant was set up near the mine to process ores with a grade below 60%, but the costs of the sulfuric acid transportation from Peñarroya (Córdoba) were very high (Boixereu, 2004). The increase of the production allowed setting up a sulfuric acid plant in 1923 and shutting down the superphosphate plant. Unfortunately, in 1928 a fire forced to close the sulfuric acid plant. The production still continued, in part because the Villanueva-Logrosán-Talavera train project was about to start, which would have allowed a significant expense reduction. However, the Spanish Civil War broke out (1936-1939) and the train project was abandoned. The communications between the Villanueva de la Serena sulfuric plant were also cut, and the production ceased until the end of the war. La Costanaza mine restarted the operations after the war, thanks to the technical innovations that were implemented. However, the mine was forced to close definitively in 1946 (Boixereu, 2003; 2004). At this moment the sedimentary phosphate deposits of Bucraa in Western Sahara were discovered, becoming the main source of supply for phosphate industry. Since the discovery of the Bucraa phosphate deposits, the mines of western Spain have remained inactive, except for small operations.

1.4.3. Economic notes about the tin market

The main tin producers are located outside Europe (e.g., China, Indonesia, Bolivia, the Democratic Republic of Congo). World resources are extensive in western Africa, southeastern Asia, Australia, Bolivia, Brazil, China, Indonesia, and Russia (USGS, 2015). Nonetheless, the European Variscan Belt also hosts numerous Sn-W ore fields (e.g., Panasqueira (Portugal), Cornwall (United Kingdom), the Erzgebirge Zone (Germany and Czech Republic)).

The major uses for tin are cans and containers, 23%; construction, 18%; transportation, 17%; electrical, 12%; and other, 30% (USGS, 2015). It is worth to note that tin is a technology metal, being mostly used in electronic devices. Moreover, tin is commonly associated with niobium and tantalum. These metals have unique properties for high strength alloy steels and superconductor manufacture, among other uses. Since 2007, the tin market has experienced a significant rise, following a long depression that started in the early 1980s (Fig. 1.2).

The world production has remained in a general positive slope since 1905 (Fig. 1.3) with the exception of the Great Depression, the Second World War, the 1953-1954 recession, the world-wide recession in the early 1980s, and the financial crisis of 2007-2008. Tin prices have been oscillating broadly since 2011. During 2015 they have broken the floor, falling about 20 percent

on the London Metal Exchange (LME). This instability has caused a reduction of the refined tin production in the world leader tin producer country, Indonesia. Other main producers, such as Peru, have lowered their production. For instance, the San Rafael tin mine (Perú) is expected to close in 2017 (Roskill Market Outlook Report, 2015). On the contrary, China has climbed up to 22% its refined tin production since 2014, thanks to the importation of low-grade tin ores from the emerging Myanmar (Adams, 2015). To conclude, as the estimations are that tin world consumption will increase, especially in the newly industrialized Asian countries and Europe, the study of Sn-W ore deposits seems to be not only an academic matter.

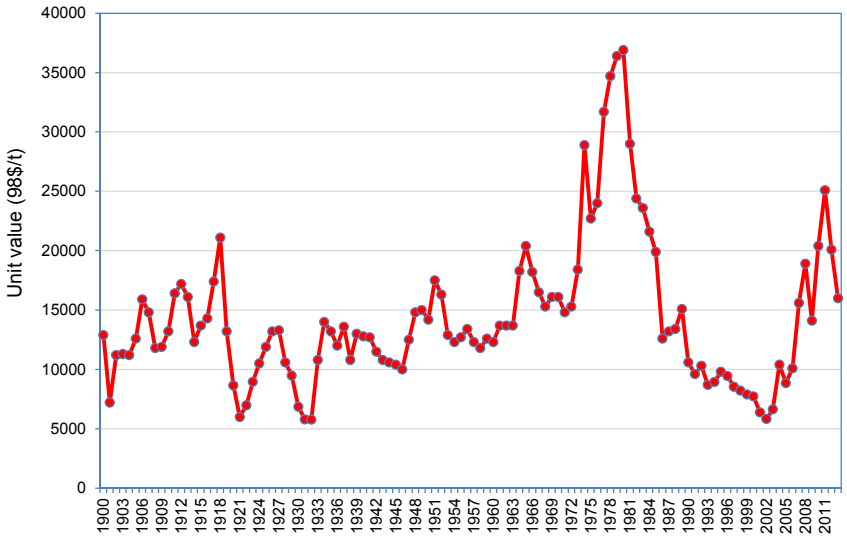

Fig. 1.2: Historical tin prices. Unit value is the value in dollars of 1 metric ton (t) of apparent consumption. Unit value ($/t) was estimated in actual dollars for 1900–98 from a price series for domestic refined tin from MP98, and from the MYB for 1999–2003. Unit values for 2004 to the most recent year are based on the Platts Metals Week composite price reported in the MCS (USGS, 2013).

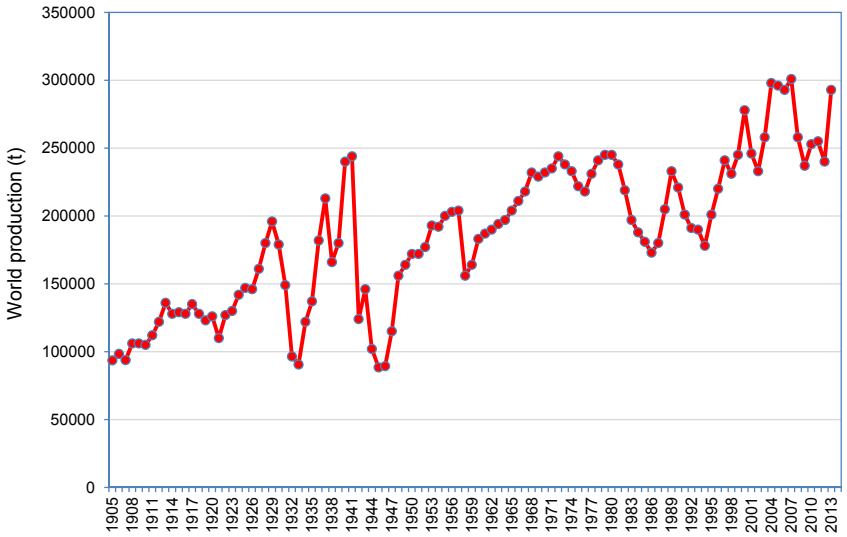

Fig. 1.3: World production data for tin content of mine and mill production. Data from the MYB (Mineral Yearbook) and MR (Mineral Resources of the United States) (USGS, 2013).

1.5. Geological and metallogenic setting

1.5.1. The Variscan Orogeny

The Variscan belt forms part of a large intra-Paleozoic belt extending on both sides of the Atlantic, from the Ouachitas in the US and the Mauritanides in West Africa, to the Bohemian Massif in Czechoslovakia and Poland. This belt resulted from the convergence and collision of two main continents, Gondwana to the South and Baltica-Laurentia (or Laurussia) to the North (Matte, 1986, 1991; Ziegler, 1989; Kroner and Romer, 2013), which caused ultimately the formation of Pangaea. Gondwana corresponds roughly with the currently Europe, Africa, South America, Antarctica, India, and Australia; Baltica, with Scandinavia, northern belt of Europe, and Russia; and Laurentia, with North America. The collision took place after the closure of several oceanic basins, such us Iapetus and Rheic, between 450 and 250 Ma (Matte, 2001) (Fig. 1.4).

The closure of the Iapetus Ocean at Late Cambrian was responsible for the convergence of Baltica and Laurentia, which eventually formed Laurussia (Murphy et al., 2010, and references therein). The Rheic Ocean developed in the Late Cambrian–Early Ordovician when several peri-Gondwanan terranes (e.g., Avalonia) drifted northwards away from the northern Gondwanan margin (e.g., Murphy et al., 2006; Nance and Linnemann, 2008; Nance et al., 2010). The Rheic Ocean expanded partly because of the closure of the Iapetus Ocean and the accretion of peri-Gondwanan terranes to Baltica and Laurentia. The accretion of Avalonia to Baltica and the collision with Laurentia resulted in the Caledonide orogeny of western Europe (Nance et al., 2010, and references therein). At the east, the accretion of other peri-Gondwana terranes formed the Appalachian orogeny (e.g., van Staal et al., 1998). The convergence between Gondwana and Laurussia in Silurian to Carboniferous times culminated in the final closure of the Rheic Ocean to create Pangaea. This closure took place diachronously. In Europe, it was essentially complete by the Early Carboniferous as Gondwana collided with southern Baltica to form the Variscan orogeny (e.g., Kroner et al., 2007). In the Early Permian, Gondwana's irregular west African margin collided with southern Baltica and eastern Laurentia, while the Amazonian margin converged with southern Laurentia, forming the Alleghanian and Ouachita orogens, respectively (Nance et al., 2009).

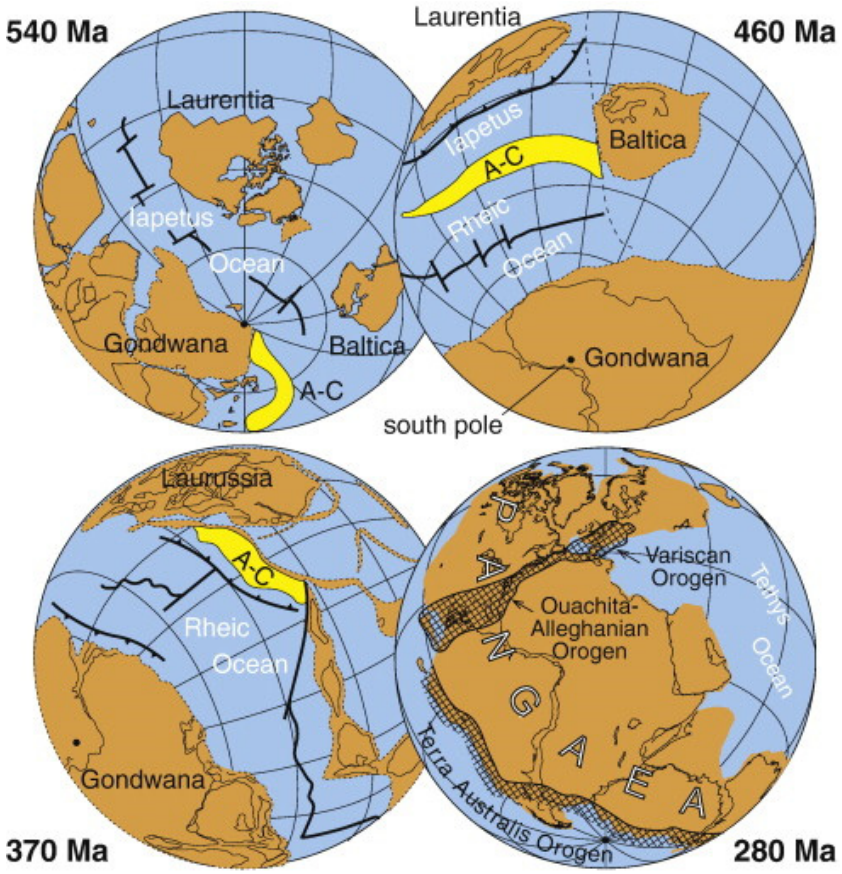

Fig. 1.4: Palaeozoic reconstructions (modified from Scotese, 1997, Cocks and Torsvik, 2002, Stampfli and Borel, 2002, Murphy et al., 2006a and Cawood and Buchan, 2007). By 540 Ma, the Iapetus Ocean had formed between Laurentia and Gondwana. By 460 Ma, Avalonia–Carolinia (A–C) had separated from Gondwana, creating the Rheic Ocean. By 370 Ma, Laurentia, Baltica and Avalonia–Carolinia had collided to form Laurussia, and the Rheic Ocean began to contract, closing by 280 Ma, to form Pangaea. (after Murphy and Nance, 2008).

1.5.2. The Variscan Belt of Western Europe

The configuration of the Variscan Belt of Western Europe is the result of the continental convergence and collision of large continental masses, such as Laurussia and Gondwana, and several Gondwana-derived microplates during the late Paleozoic. The detailed paleogeographic and geodynamic reconstructions of the Variscan Belt remain controversial. The peri-Gondwanan terranes are considered the origin of the European Variscan Belt. The two largest microplates known are Avalonia and Armorica, which drifted from the northern margin of Gondwana. In Europe, Avalonia roughly comprises the northern foreland of the Variscan belt from Ireland to northern Germany and Poland (Unrug et al., 1999). Armorica was composed of several smaller terranes (Tait et al. 1997), such as the Armorican Massif in France, the Iberian Peninsula (except the South Portuguese Zone) and the Saxo-Thuringian and Moldanuvian zones of Central Europe. These units were separated by the Rheic Ocean (Fig. 1.5).

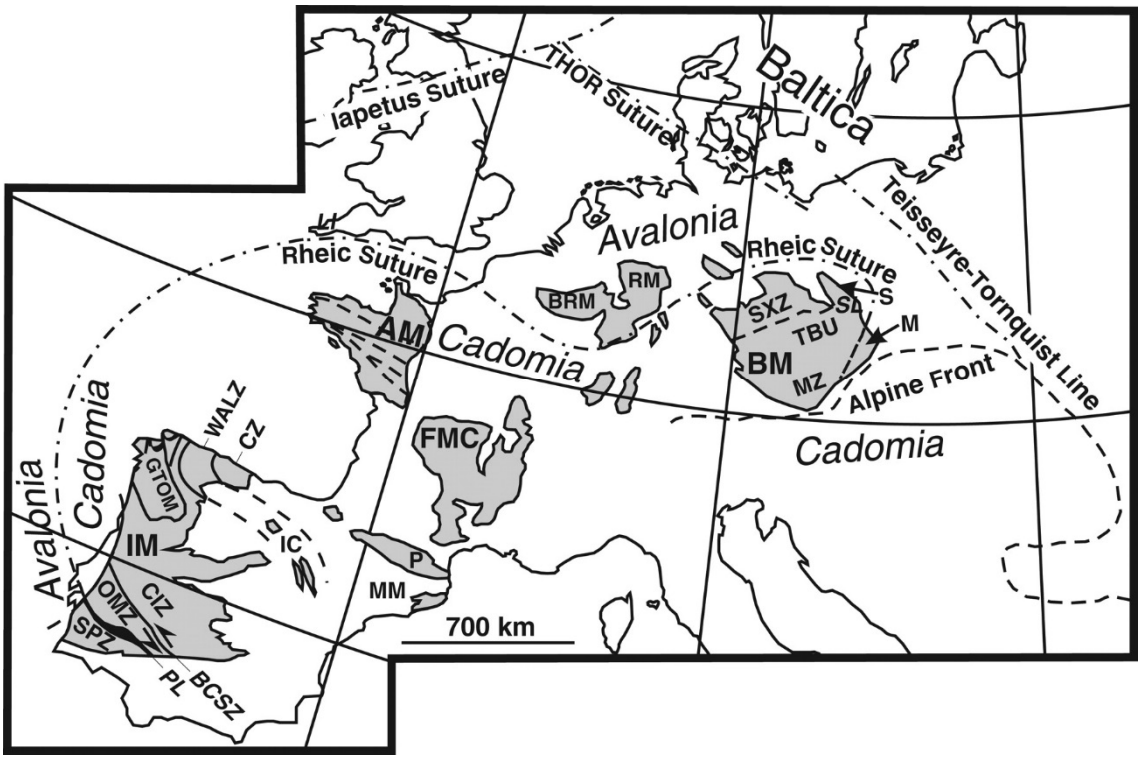

Fig. 1.5: Cadomian and Variscan Massifs in southwestern and central Europe with proposed Variscan oceanic suture of the Rheic Ocean (after Linnemann et al., 2007).
Abbreviations:
(1) Iberia: BCSZ=Badajoz-Córdoba Shear zone, CIZ=Central Iberian zone, CZ=Cantabrian zone, IC=Iberian Chains, IM=Iberian Massif, GTOM=Galicia Trás-os-Montes zone,MM=Maures Massif, OMZ=Ossa-Morena zone, P=Pyrénées, PL=Pulo de Lobo oceanic units, SPZ=South Portuguese zone, WALZ=West Asturian Leonese zone
(2) Western Europe: AM=Armorican Massif, FMC=French Massif Central, Li=Lizard Ophiolite
(3) Central and Eastern Europe: BM=Bohemian Massif, BRM = Brabant Massif, M=Moravo-Silesian zone, MP=Midland Platform, MZ=Moldanubian zone, RM=Rhenish Massif, S=Sudetes, Sl=Sleza ophiolite, SXZ=Saxo-Thuringian zone, TBU=Teplá-Barrandian Unit
In black: oceanic rocks of the Pulo de Lobo suture (Beja-Acebuches ophiolite) in southern Iberia and ophiolitic units of allochthonous complexes in NW Spain (Galicia); IAA: Ibero-Armorican Arc (after Nance et al., 2010)

The European Variscan Belt is interpreted as a fan-like orogen divided by sutures, with opposite vergences of nappes and recumbent folds migrating toward external Carboniferous basins (Matte, 1991). North to northwest vergence is observed through southern Great Britain and east into the Bohemian massif, marking the eastern limit of the orogen. Southerly vergence characterizes the southern flank of the Variscan orogen from Morocco through southern Iberia and across the length of the Mediterranean domain. It is generally accepted that opposite vergences in each side of an oceanic suture are related to continental collisional scenarios. In that sense, the predominant subduction of continental crust makes the Variscan orogeny differing significantly from typical oceanic accretionary orogens like the Andes or the Altaids (Kroner and Romer, 2013). The different domains described in the Variscan Belt have a common feature: the overall occurrence of a Proterozoic basement supposed to have evolved along the margin of Gondwana, and deformed at the end of the Neoproteozoic during the Cadomian orogeny (Fig. 1.5).

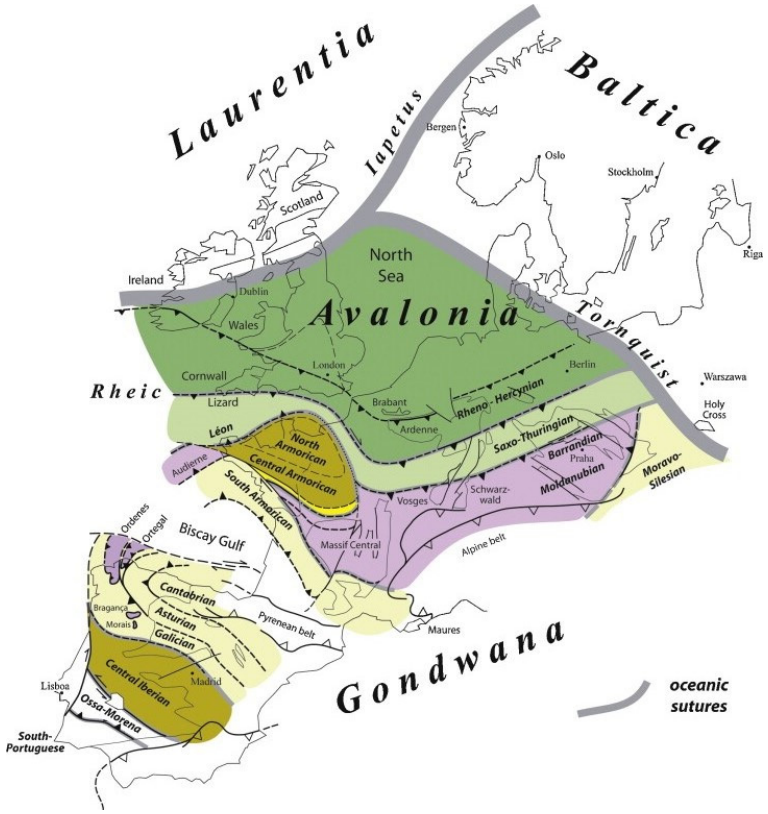

Fig. 1.6: Configuration of the Variscan Belt, inferred positions of the Rheic Ocean suture and other Variscan second-order sutures and potential correlations within the Variscan belt (in color). After Ballèvre et al. (2009).

A correlation between different domains in the Variscan Belt is mainly recognized (Fig. 1.6). The large scale structures have been and continue to be a matter of debate. The main Variscan sutures have been recognized using different paleogeodynamic criteria, such as faunal differentiations, ophiolite sequences, high-pressure metamorphic rocks, major thrusts and nappes, and paleomagnetic discontinuities. There are several disagreements and uncertainties concerning the timing, location, extent and continuity of oceanic domain sutures along the Variscan Orogen (e.g., Ballèvre et al., 1992; Tait et al., 1997; Matte, 2001; Linnemann et al., 2004). For instance, this problematic is noteworthy for the suture locations in the Iberian Massif (Fig. 1.6 and Fig. 1.7). Some authors (e.g., Ribeiro, 1990; Quesada, 1991; Quesada et al., 1994) consider that the Iberian Massif only shows a single suture in the boundary between the SPZ and the OMZ (Fig. 1.6). Alternatively, Matte (2001) considers a Galicia-Southern Brittany suture, running through France and Iberia (through the CCSZ) and separating the Armorica microplate into North Armorica and South Armorica (Fig. 1.6).

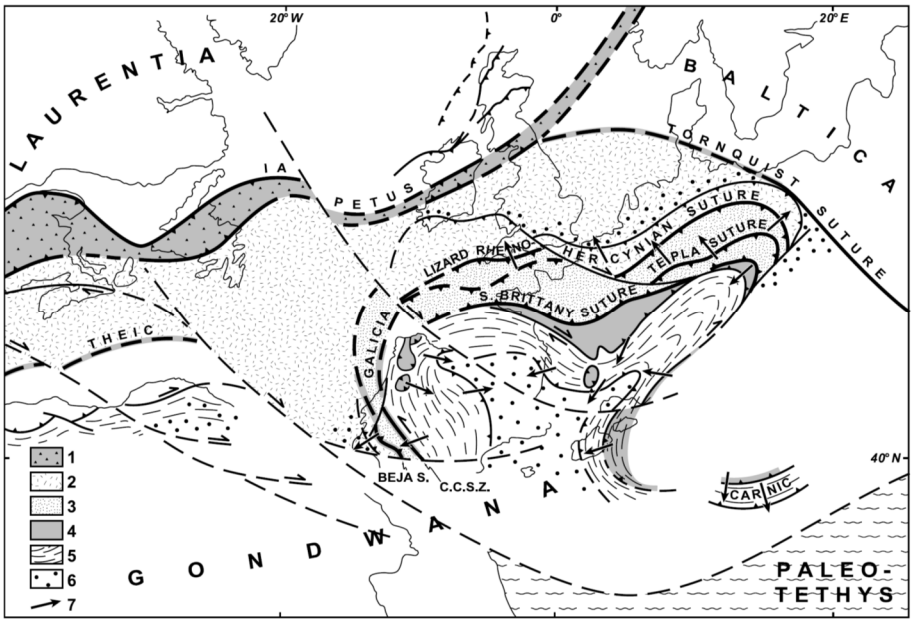

Fig. 1.7: Possible configuration of the Variscan belt of Western Europe and northern Africa in Permian time (at 270 Ma), showing the main sutures and extension of the Avalonia and Armorica continental microplates. 1, Iapetus Caledonian suture and Ordovician island arc; 2, Avalonia; 3, Armorica; 4, ophiolitic nappes rooted in the Galicia-Southern Brittany suture; 5, Schistose nappes in the southern Variscides; 6, Carboniferous (Visean to Westphalian) foredeep basins; 7, main vergence of nappes. CCSZ, Coïmbra-Córdoba Shear Zone; Beja S, Beja suture. After Matte, (2001).

The European Variscides would constitute a jigsaw pattern of high grade domains, showing subduction-exhumation processes, juxtaposed against low grade domains hardly affected by Variscan tectonics (Kroner and Romer, 2013). It is unclear if the peri-Gondwanan terranes separated from Gondwana as a single entity, or as independent crustal units. Similarly, whether the Rheic Ocean was a collage of smaller oceanic tracts or a single ocean is not completely understood. Despite these uncertainties, it is accepted that the peri-Gondwanan terranes separate from the northern margin of Gondwana, favored the rifting of the Rheic Ocean in the Late Cambrian–Early Ordovician. Evidences about the continental rifting which eventually resulted in the opening of the Rheic Ocean can be found in the massive igneous activity from the OMZ and the CIZ (e.g., Sánchez-García et al., 2010), locally evolving towards peralkaline felsic metavolcanic rocks (e.g., Montero et al., 2009; Díez-Fernández et al., 2012, 2015). The northern margin of Gondwana is interpreted as a passive margin during much of the Paleozoic, followed by the diachronous end of arc magmatism during the Late Ediacaran–Early Cambrian (Nance et al., 2008). The closure of the Rheic took place during the Devonian. Nevertheless, numerous Carboniferous ocean domains through the Variscides exist, and have been interpreted as a result of along-strike diachronity in the timing of collision (Matte, 2001). After Ricken et al. (2000) and Gutiérrez-Alonso et al. (2008) these ocean domains are associated to rapid opening and subsequent closure of a number of discontinuous or isolated basins. Subduction was predominantly northward beneath Laurussia (Nance et al., 2010), which constituted the upper plate. The oceanic crust of the Rheic Ocean subducted below Laurussia. Remnants of an island

arc in the Laurussia plate are found in the German Crystalline Zone (Franke and Żelaźniewicz, 2000). Upon ocean closure in the Upper Devonian, the continental crust of Gondwana was too thick to subduct (Kroner and Romer, 2010), causing thickening of the lithosphere and metamorphism. Late Paleozoic closure of the Rheic Ocean is recorded, for instance, in northwest Iberia by deformation associated with the Laurussia–Gondwana collision, and in the oceanic remnants preserved as ophiolites in the allochthonous units of NW Iberia, that are interpreted as a rootless suture between these continents (e.g., Martínez Catalán et al., 2007; Sánchez Martínez et al., 2009). Moreover, the Beja-Acebuches ophiolites in southern Iberia (340-350 Ma; Azor et al., 2008) are also related to the closure of the Rheic Ocean and represent a suture zone between Gondwana (OMZ) and Laurussia (SPZ) terranes. Exhumation of Gondwana high-pressure rocks, strike-slips tectonics and Variscan widespread plutonism are found during Late Devonian-Early Carboniferous as the result of the collision. The Variscan orogeny yielded a large number of granitoid intrusions throughout the Variscan Belt of Western Europe. The granites were intruded syn- or postkinematically; they reflect the recycling of thickened peri-Gondwanan crust with only subordinate contribution of juvenile components (e.g., Kroner and Romer, 2013; and references therein).

1.5.3. The Iberian Massif

The Iberian Massif is the main outcrop of the Variscan belt in the Iberian Peninsula. It is traditionally divided into six major zones according to stratigraphic and petrologic characteristics (Lotze, 1945; Julivert et al., 1972; Farias et al., 1987). These zones are: the Cantabrian Zone, the Astur-Occidental Leonese Zone, the Central Iberian Zone, the Ossa Morena Zone, the Sudportuguese Zone, and the Galicia-Trás-os-Montes Zone. They consist mainly of Paleozoic and Neoproterozoic sequences which lay above the Cadomian basement of the Gondwanan continental crust (e.g., Martínez Catalán et al., 2007). The zones, separated by thrusts and reverse faults, and their Paleozoic sedimentary sequences are interpreted to reflect their proximity to the Gondwanan margin (Fig. 1.8). The Cantabrian and South Portuguese zones are considered external, while the rest are considered internal. The Variscan collision deformed the basement, which is often metamorphosed and intruded by different granitoids.

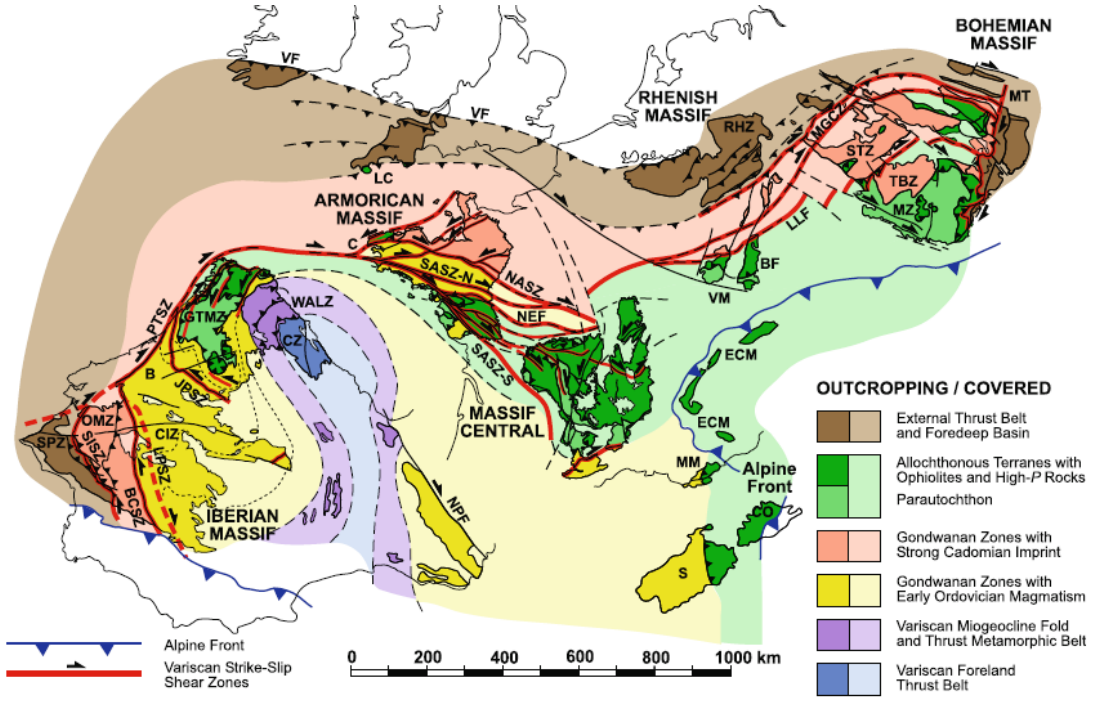

Fig. 1.8: Sketch of the Variscan belt, after Martínez Catalán (2012) with the subdivision of Julivert et al. (1972).
Abbreviations: BCSZ Badajoz-Córdoba shear zone; BF Black Forest; C Crozon; CIZ Central Iberian Zone; CO Corsica; CZ Cantabrian Zone; ECM External crystalline massifs of the Alps; GTMZ Galicia-Trás-os-Montes Zone; JPSZ Juzbado-Penalva shear zone; LC Lizard Complex; LLF Layale-Lubine fault; LPSZ Los Pedroches shear zone; MGCZ Mid-German Crystalline Zone; MM Maures Massif; MT Moldanubian thrust; MZ Moldanubian Zone; NASZ North Armorican shear zone; NEF Nort-sur-Erdre fault; NPF North Pyrenean fault; OMZ Ossa-Morena Zone; PTSZ Porto-Tomar shear zone; RHZ Rheno-Hercynian Zone; S Sardinia; SASZ South Armorican shear zone (N and S: northern and southern branches); SISZ Southern Iberian shear zone; SPZ South Portuguese Zone; STZ Saxo-Thuringian Zone; TBZ Teplá-Barrandian Zone; VF Variscan front; VM Vosges Massif; WALZ West Asturian-Leonese Zone.

1.5.3.1. The Central Iberian Zone

The Central Iberian Zone (CIZ) is defined by massive Variscan granite intrusions into the Neoproterozoic metasedimentary rocks, which corresponds to the autochthonous sequences. The Neoproterozoic mainly consists of a thick (8–11 km) metasedimentary turbidite sequence, comprising mostly pelitic and psammitic beds (e.g., Ribeiro, 1990; Rodríguez Alonso et al., 2004). Two Neoproterozoic domains in the Central Iberian Zone have been distinguished recently on the basis of different geochemical signatures (Villaseca et al., 2014). The South-CIZ domain comprises low grade metasedimentary rocks, which correspond with the common denomination of the Schist Greywacke Complex (SGC); while the North-CIZ domain comprises higher grade metasedimentary rocks with more mature metapelitic protoliths. These domains revisit the classical subdivision of the CIZ by Lotze (1945) (Fig. 1.9). The existence of two micro-terrains within the CIZ and the presence of highly peraluminous Ordovician magmatism in the N-CIZ suggest that the Neoproteorozoic metasediments were deposited in separated basin environments. Thus, Villaseca et al. (2014) propose a geodynamic setting comprising, from S to

N, a magmatic arc, a back-arc basin and a much older foreland from Ediacaran to Early Ordovician. This scenario evolved towards extensional tectonics and subsequent intracontinental rifting during the Early Ordovician, reinforced by the intrusion of tholeitic meta- basic rocks in the N-CIZ at circa 472 Ma (Barbero and Villaseca, 2000; Villaseca et al., 2015).

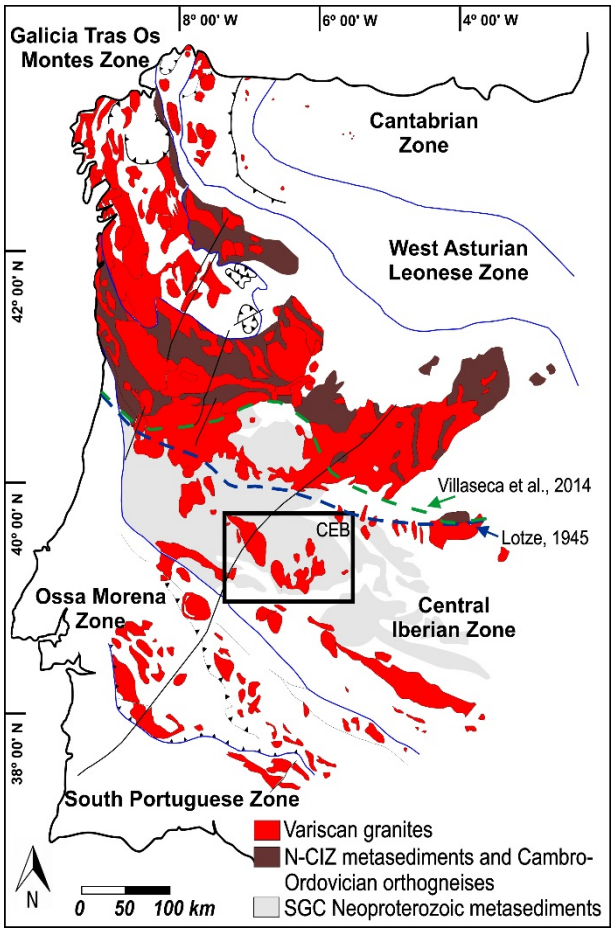

Fig. 1.9: Geological sketch map of the Iberian Variscan Belt showing the Variscan granitoid intrusions, the subdivisions of the CIZ from Villaseca et al. (2014) and Lotze (1945), and the location of the Logrosán granite (black rectangle).

Three main Variscan deformation phases have been described in the CIZ (Dias et al., 1998 and references therein). The Variscan D_1 and D_2 phases are thought to be of Mid-Upper Devonian to Early-Mid-Carboniferous age (Dallmeyer et al., 1997; Ábalos et al., 2002; Martínez Catalán, 2011), which nonetheless may change in intensity and deformation style from one zone to another, within the Iberian Massif. D_1 induced an initial shortening and involved the formation of kilometer-scale folds with subvertical axial planes and a pervasive axial planar cleavage (S_1). Ongoing deformation subsequently led to the D_2 phase that was ultimately characterized by the generation of recumbent folds with a sub-horizontal penetrative foliation (S_2) (Diez Balda et al., 1995). D_1 and D_2 correspond to the collisional stage of the Variscan orogeny, and were accompanied by partial melting and a restricted production of peraluminous granitoids (Dias et al., 1998). However, most of the CIZ granitoids post-date the syn-collisional stage of the Variscan orogeny, and were emplaced under extensional conditions (D_3) from the Mid-Carboniferous to the Permian (Dias et al., 2002; Valle Aguado et al., 2005; López-Moro et al., 2012). A last, brittle deformation tectonic episode, involved the development of large-scale sinistral NE–SW, NNE–SSW and dextral NW–SE fault systems (Pereira et al., 1993).

1.5.4. Variscan Magmatism in the CIZ

Numerous granitic batholiths occupying a NW-SE 600 km-wide band in the Central Iberian Zone were emplaced about 30-50 Ma after the Variscan collision (Ferreira et al., 1987), at 325-300 Ma (Dias et al., 1998; Fernández Suárez et al., 2000; Bea et al., 2003; Orejana et al., 2012) (Fig. 1.10). Most of the felsic magmatism in the CIZ is syn- to postectonic with respect to the last ductile deformation phase (D3) (Dias et al., 1998) with a bulk of data peaks at 320 (mainly syn-D3 leucogranites of Galicia and northern Portugal), 308-306 and 301 Ma (Dias et al., 1998; Fernández-Suárez et al., 2000; Teixeira et al., 2011; Orejana et al., 2012). Capdevila et al. (1973) and Corretgé et al. (1977) classified the granites from the CIZ into three groups: (1) peraluminous, two-mica granites and leucogranites, mostly older; (2) biotite-granodiorite, mostly younger; and (3) cordierite-monzogranite (Table 1.1). These granites are predominantly peraluminous, with low quantities of restitic material and basic varieties (e.g., Villaseca et al., 1998b; Bea et al., 1999). A minor group of metaluminous to peraluminous granites, some of the Bt-rich granodiorites of I-type affinity, also appear dispersedly within the CIZ (e.g, Capdevila et al., 1973; Mendes and Dias, 2004; Villaseca et al., 2009).

A large number of CIZ granite bodies are leucocratic, highly evolved, and can be mineralized (Sn-W-Li-P-U) (e.g., Ramírez et al., 1999; Teixeira et al., 2012). Owing to the high tin contents of some of these granites, they are identified as tin-granites or stanniferous granites having a high mineralizing potential (e.g., Neiva et al., 2012). Most of the Variscan granitic magmas in the CIZ have been ascribed to melting of the continental crust on the basis on their Sr-Nd signatures. This is due to high heat production of highly radiogenic lithotypes after crustal thickening during the Variscan orogeny (e.g., Villaseca et al., 1998b; Bea et al., 1999). Nevertheless, interaction with basic mantle-derived magmas have been observed elsewhere (e.g., Dias et al., 1998; Castro et al., 1999).

Table 1.1: General features of granitoids from the Iberian Massif (after García Moreno et al., 2007)

	Bt –rich granodiorites	**Crd- monzogranites**	**Peraluminous leucogranites and two-mica granites**
Relative age	Mostly younger	Mostly younger	Mostly older
Relative abundance	> 50%	< 50%	< 20%
Occurrence	Allochthonous massifs. Associations with grabbroic rocks	Normally in zoned, epizonal plutons	Normally in para-autochthonous massifs. Transitions to migmatites
Mineral assemblage	Qtz -Pl -Kfs-Bt ±(Crd) or ±(Hb–Px)	Qtz -Kfs -Pl -Crd -Bt ±Ms ±And ±Tur	Qtz –Pl –Kfs ±Bt ±Ms ±Crd
Kfs megacrysts	Abundant	Typical	Rare
Microgranular enclaves	Typical	Scarce	Absent
Ore deposits	Rare (barren granites)	U, W, P	Sn
Sr initial ratios*	0.705 – 0.707	0.706 – 0.712	0.723 – 0.763
K_2O/Na_2O	> 1	> 1	> 1
Al-saturation index A/CNK	(n=212) average 1.09 (st.dev. 0.12)	(n=145) average 1.22 (st.dev. 0.14)	(n=255) average 1.29 (st.dev. 0.17)

* Data from Moreno-Ventas et al. (1995), Castro et al. (1999) and Alonso Olazábal (2001).

The Central Extremadura Batholith (CEB) (Fig. 1.9) consists of an alignment of several plutons and minor granitic bodies within the CIZ. They range compositionally from quartz-diorite to alkali-feldspar granites (Castro, 1985), but mostly composed of peraluminous monzogranite batholiths (some of them cordierite-bearing). Similarly to the CIZ granitoids, the granites from the CEB are classified after Castro (1999) as: (1) biotite-tonalites; (2) cordierite-monzogranites; and (3) two-mica leucogranites. The Logrosán granite belongs to the third group (two-mica leucogranites), together with the Plasenzuela and Montánchez granites (Castro et al., 1999). Recently, some two-mica leucogranites of the southern-CIZ (type-3 of Table 2.1) have been interpreted as evolved granite liquids from monzogranitic magma batches (type-2 of Table 2.1) thus forming part of a common large fractionation trend (Villaseca et al., 2008; Merino et al., 2013, 2014).

1.5.5. Metallogenic Context

The European Variscan Belt hosts numerous Sn-W ore fields (e.g., Spain: Mangas and Arribas, 1988; Llorens and Moro 2012a, 2012b; Portugal: Noronha et al., 1992; Moura et al., 2014; Cornwall (UK): Jackson et al., 1989; France: Marignac and Cuney, 1999; Vallance et al., 2001, or in the Erzgebirge Zone (Germany and Czech Republic): Štemprok and Seltmann, 1994). The Sn-W hydrothermal deposits from Western Europe belong to a metallogenic Variscan province related to post-collision tectonics and magmatism (Štemprok, 1981). Routhier et al., (1980) and Derré (1982) indicated that a spatial distribution for Sn-W ore deposits in the West European Province occurs. Sn<W and Sn>W bands independent of the Variscan orogenic domains are defined by Derré (1982) (Fig. 1.10); in the Iberian Massif these bands define an E-W trend.

The Iberian Massif has been one of the leading tin-tungsten producer zones of Europe. The deposits extend from Galicia through the north of Portugal to the southwest of Spain (Fig 1.10). They are mainly associated with syn- to late- Variscan granites, and located towards the apical regions of the granitic cupolas and their immediate country rocks. The associated granite may be a hidden granitic body (e.g., Panasqueira, Rye et al, 1979). Although most deposits are related to granites or pegmatites, some skarns also appear (e.g., Los Santos skarn; Timón, 2008). Most Sn-W ore deposits from the Iberian Massif are found in the Central Iberian Zone, especially in Extremadura, such as Jálama (Llorens, 2011; Llorens and Moro, 2012a; 2012b); or La Parrilla (Mangas and Arribas, 1988). The associated granites are usually highly fractionated porphyritic two mica granites or leucogranites, usually with pegmatitic and aplitic veins (e.g., Jálama, El Trasquilón, Montánchez, Trujillo, Zorita, Albalá, etc.). The style of mineralization varies from disseminated ores in highly fractionated granites, to pegmatites, veins and stockworks within the granite and the country-rocks. Cassiterite, wolframite and scheelite are

the main ores, but some columbite-tantalite might also occur. On the whole, the oxides correspond to the high-T paragenesis phase, followed by a lower-T sulfide stage. The common alteration is greisenization when the ores are granite-hosted, and tourmalinization for the metamorphic-hosted ores (Tornos and Gumiel, 1992; and references therein). A regional spatial metal zoning pattern from Sn-W-(As-Li-Nb-Ta-Mo) to Cu-(P) and Pb-Zn-Cu-(Ag) is inferred from the disposition of most Sn-W ore deposits in the CIZ, similar to the zonation found in equivalent Sn-W districts (e.g., Cornwall; Guilbert and Park, 1986). Accordingly to a zonation pattern (from P, Cu-P to Cu-Zn, Zn-Cu, and Pb-Zn) and the morphology of the Logrosán granite, Locutura and Alcalde (2007) integrated it into a N60-N70E structural band (Alcollarín-Alía band), through which the granite would have been emplaced. Hydrothermal phosphate vein-type ores associated with peraluminous granites are also frequent in the CIZ, and the most important P-rich mine occurs related to the Logrosán granite. Actually, the CIZ is an exclusive worldwide location for this type of phosphate mineralization, known as "Iberian type". The typology and features of these deposits are expanded in Chapter 5.

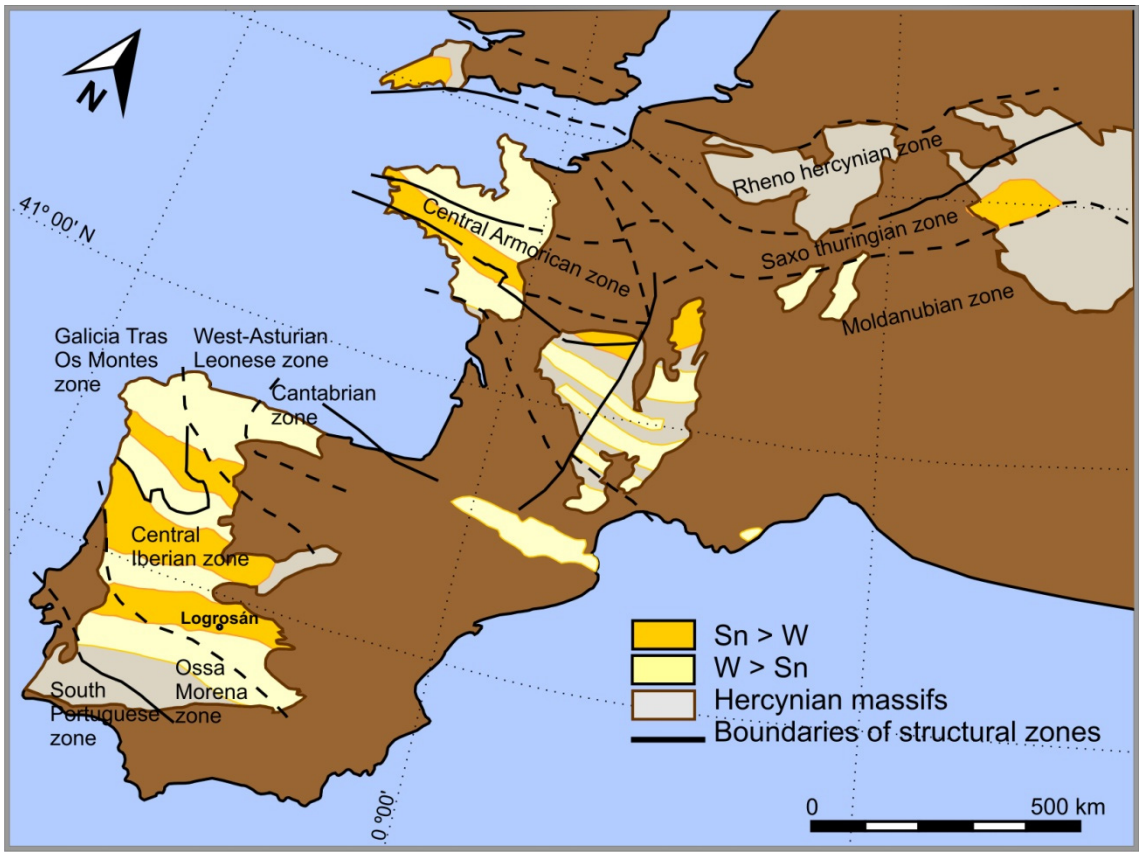

Fig. 1.10: Sn-W metallogenic province of the European Variscan Belt. Sn and W dominant bands. Adapted from Derré (1982).

1.5.6. Geological setting of the Logrosán Sn-W ore deposits

The Logrosán tin mineralization is one of the numerous Sn-W ore deposits associated with granites in the European Variscan Belt. The Logrosán granite is located in the Central Iberian Zone (CIZ) of the Iberian Massif (Fig. 1.9), which constitutes one of the most important Sn-W metallogenic provinces of the European Variscan Belt (Fig. 1.10). The Logrosán cupola belongs to the Central Extremadura Batholith (CEB) (Castro, 1985) (Fig. 1.11), and intrudes into epizonal domains of the southern CIZ.

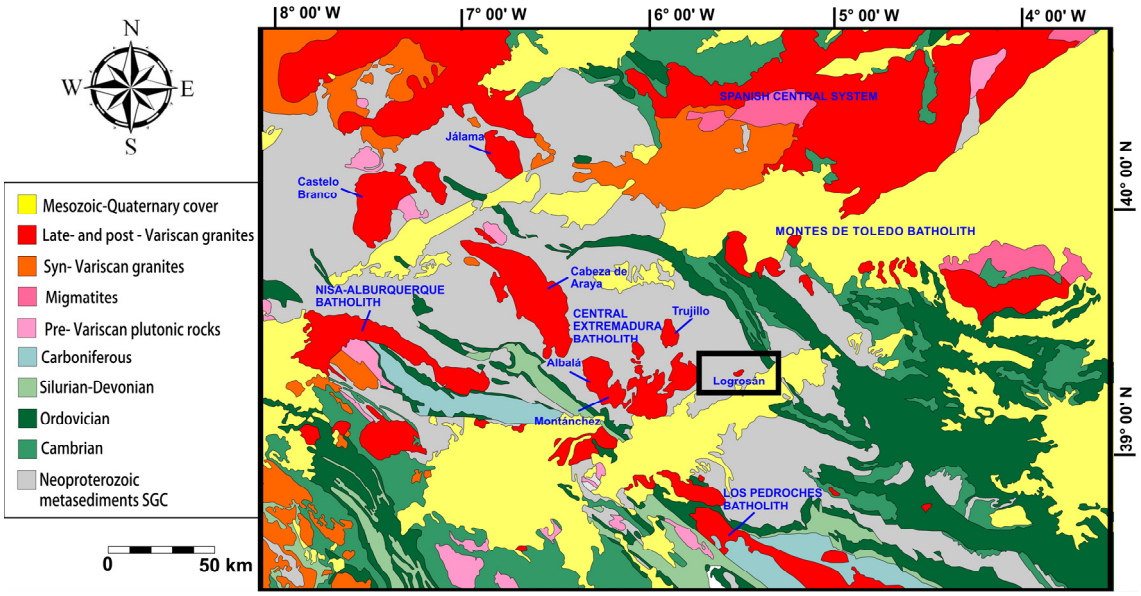

Fig. 1.11: Regional geological sketch displaying the studied area (modified from Rodríguez et al., 2008).

The SGC sequence in the Logrosán area is characterized by a monotonous centimetric to decimetric alternation of metagreywackes and slates with a minor presence of coarser-grained metasedimentary facies (e.g., Moreno et al., 2004). The country rocks show bedding (S_0) as a primary feature and folding and foliation as secondary features. The country rock orientations are parallel or subparallel to the pluton showing a sharp contact. A penetrative foliation corresponding to the first Variscan event (D_1) is widely recognized in this sector. D_1 folds have subvertical axial planes that strike NW-SE and have a steeply SW dipping. The associated S_1 foliation is an axial planar cleavage. Field observations show that S_1 is crenulated by a later foliation (regionally defined as S_3 by Locutura and Alcalde (2007)). The main foliation surrounds the Logrosán granite body, changing its strike from N–S (southeastern and eastern margins of the granite) to N60–N85 (western and northern margins of the granite). The SGC underwent greenschist-facies regional metamorphism (chlorite and biotite zones) of Variscan age and was later affected by thermal metamorphism triggered by the Logrosán granite intrusion. The Logrosán granite intruded the SGC metasediments during the extensional stage of

the Variscan orogeny, whereas subsequent brittle faults provided channels for fluid circulation and ore mineral precipitation. The Logrosán granite is a typical felsic massif related to complex hydrothermal mineralization. The Sn-(W) Logrosán ores occur as quartz veins and greisen zones in two different settings, endo- and exogranitic. On one hand, the Cerro de San Cristóbal deposit consists of quartz-cassiterite veins and greisen-like ores hosted within the Logrosán granite. On the other hand, the El Serranillo deposit comprises a Sn-(W) stockwork hosted by the SGC wall-rocks and is located about 5 km away from the Logrosán granite. Tin mineralization befalls as cassiterite-quartz stockwork and greisen-like styles. Moreover, there is an exogranitic phosphate mineralization consisted of NE-SW strike hydrothermal quartz-apatite veins set around the granite outcrop. The magmatic and hydrothermal evolution, including the nature and source of fluids, as well as the genetic and timing relationships between the Sn-(W) and P ores and the Logrosán granite are the main topics developed through this PhD dissertation.

Chapter 2: MATERIALS AND METHODS

SUMMARY:

A compilation of field works, laboratory procedures, and analytical methods performed in this study is described in the present chapter. Field works include cartography, mapping, sampling and a gravity survey. Mineral chemistry characterization, whole rock analyses, isotope data, and geochronological studies were carried out on a widespread group of carefully selected samples. The analytical techniques have been performed in different national and international laboratories. Numerous first-time data have been obtained, allowing to the interpretation and the understanding of the Logrosán granite emplacement and the genesis of its associated ore deposits.

MATERIALS AND METHODS

The field working, sample preparation, and analytical data were performed mostly by the author, alone or with the attendance of specialized technicians, except when explicit in the text.

2.1. Field works

Firstly, a throughout review of precedent bibliography and cartography were undertaken in order to obtain a broad perspective of the geological background. Following this phase, several field campaigns were accomplished from 2010 to 2014. Every field campaign was monitored by a GPS system and traditional mapping methods. About 200 samples in total were taken. Granite samples were collected from fresh-rock outcrops and altered sectors. Cassiterite and sulfide mineralized samples were gathered from veins and particularly intense altered host-rocks sectors. Quartz-apatite samples were collected from the interior of the La Costanaza mine. Sampling and mapping of the contact metamorphic aureole were performed along four transects, following the main axes of the granitic body.

Additionally, a gravity survey was carried out in the Logrosán area, covering the granite and the surrounded country rocks. Dr. David Gómez, Dr. Tomás Martín-Crespo and Dr. David Orejana collaborated with the author in the gravity data acquisition. A total of 36 gravity stations were obtained. Two transverse gravity profiles along the longer and shorter axes of the outcropping pluton were chosen. The average spacing between gravity stations was c. 250 m on top of the Logrosán granite outcrop, whereas outside this area we chose a spacing of 1 km. Gravity measurements were made with a Lacoste & Romberg gravimeter model G, serial number 665, with a precision of ±0.01 mGal. Elevation data were obtained using a GPS Magellan model MobileMapper CX, with a submetric accuracy equivalent to ±0.1 mGal. Density determinations for the gravity modeling were carried out in the IGEO laboratories (Madrid, Spain). Sixteen samples from the plutonic units and fifteen samples from the contact metamorphic aureole and SGC rocks were collected

2.2. Laboratory procedures and analytical methods

Hand samples were studied macroscopically, and areas of interest were selected for thin section preparation (~30 μm) at the laboratories of the Departments of Crystallography and Mineralogy, and Petrology and Geochemistry of the Complutense University of Madrid. Detailed petrographic and textural studies were carried out by optical microscopy.

2.2.1. Whole rock geochemistry

A total of 14 representative samples weighted between 3-5 kg were collected for whole-rock geochemistry. Fractions of each sample were selected for crushing and powdering. Whole-rock analyses (major and trace elements) were carried out at ACTLABS (Ancaster, Ontario, Canada). Each sample was fused using a lithium metaborate-tetraborate mixture. The melt produced by this process was completely dissolved with 5% HNO_3. Major analyses were carried out using fusion-inductively coupled plasma mass spectrometer (FUS-ICPMS) while trace elements were analyzed by fusion-inductively mass spectrometer (FUS-MS). Uncertainties in major elements are bracketed between 1 and 3% relative, except for MnO (5–10%). The precision for Rb, Sr, Zr, Y, V, Hf and most of the REE range from 1 to 5%, and between 5 and 10% for the rest of trace elements. More information on the procedure, precision and accuracy of ACTLABS ICP-MS analyses can be found at www.actlabs.com.

Fluorine and Li were determined in selected samples by technicians from the laboratory of the Spanish Geological and Mining Institute (IGME), where F was determined by spectrophotometric methods after its extraction by pyrohydrolysis and Li was extracted by digestion with HF-HNO_3-$HClO_4$ and determined by atomic absorption spectrophotometry. An analytical error of ± 10% has been estimated.

2.2.2. Sr-Nd isotopes

Sr-Nd isotopic compositions were measured on 6 representative Logrosán granites. Sr-Nd isotope analyses were performed by technicians from the CAI of the Geochronology and Isotopic Geochemistry Center (Complutense University of Madrid). Whole-rock samples were dissolved in ultra-pure reagents and the isotopes were subsequently isolated by exchange chromatography. Isotopes analyses were carried out using a Sector 54 VG Multicollector Thermal Ionization Mass Spectrometer with data acquired in multidynamic mode. Repeated analyses of the NBS-987 standard gave $^{87}Sr/^{86}Sr = 0.710240 \pm 0.00005$ (2σ, n = 8) and for the La Jolla standard the values

of $^{143}Nd/^{144}Nd = 0.511847 \pm 0.000003$ (2σ, n = 14) were obtained. The 2σ analytical errors are 0.01% for $^{87}Sr/^{86}Sr$ and 0.006% for $^{143}Nd/^{144}Nd$, which yield a 2σ error on $\varepsilon(Nd)$ calculation of ± 0.06.

2.2.3. Separating minerals

Minerals were separated from two representative Logrosán granites, two quartz-tourmaline vein and pegmatite samples, 6 (greisenized) mineralized samples, and two quartz-apatite vein samples for isotopic studies, LA-ICP-MS analyses, and geochronology. About 2-5 kg of each sample was crushed and sieved with a steel jaw-crusher and a disk mill at the Department of Petrology and Geochemistry of the Complutense University of Madrid. The rock sample was crushed and pulverized at the IGME laboratories. Zircon and monazite were previously preconcentrated with a Wifley table using a modified version of the "water-based" separation technique of Söderlund and Johansson (2002). Further separation based on paramagnetic properties was performed using a Franz isodynamic separator. Finally the minerals selected for analyses were hand-picked under a microscope.

2.2.4. Electron microprobe

About 150 thin sections have been analyzed by electron microprobe (EPMA). A total amount of about 2000 spot analyses were performed. Major and minor elements of mineral phases were analyzed by an EMP JEOL Superprobe JXA-8900 M, equipped with four wavelength dispersive spectrometers at the National Center for Electron Microscopy, Complutense University of Madrid (http://www.cnme.es). Silicate and oxide analyses were conducted at an accelerating voltage of 15 kV, an electron beam current of 20 nA, and a beam diameter of 5 μm. An accelerating voltage of 20 kV, an electron beam current of 10 nA, and a beam diameter of 10 μm were used for sulfide minerals. Each element was counted for 15 seconds, except Ta_2O_5 and Nb_2O_5, which were counted for 30 seconds The following minerals were used as standards: sillimanite, albite, almandine, kaersutite, microcline, ilmenite, fluorapatite, scapolite, galena, anglesite, nickeline, AsGa, HR-160 (Co–Ni–Cr), chalcopyrite, Zn, Mo, Ag, Cd, Sb, Bi_2Te_3, cinnabar, hutchinsonite, galena, LiTa, LiNb, and pure W (Lα) and Sn (Lα) metals. Corrections were made using the ZAF (Z: atomic number; A: absorption; F: fluorescence) method.

2.2.5. Micro XRF

Elemental distribution images of veins and altered host rocks were performed on 9 thin sections by a M4 TORNADO Micro X-ray Fluorescence system, with silicon drift detectors (SDD) (Centro Tecnológico de Repsol, Móstoles, Spain). Data processing was performed by Dr. Miguel Ángel Caja.

2.2.6. LA-ICP-MS

A representative selection of zircons were strewn and mounted on epoxy resin for LA-ICPMS microanalytical analysis. The mount was polished to expose the zircon central portions and studied with transmitted and reflected light on a petrographic microscope. The internal structure, inclusions, fractures and physical defects were analyzed using back scattered electron imaging. Similarly, trace element composition on some granite minerals (feldspars, micas, tourmaline, apatite) were performed in thick sections (up to 100 μm). The trace element composition was obtained by laser ablation (LA-ICP-MS) at the Natural History Museum of London (NHM, London, UK) using an Agilent 7500CS ICP-MS coupled to a New Wave UP213 laser source (213 nm frequency-quadrupled Nd-YAG laser). The diameter of the laser beam was 10 μm. A 40 s gas blank was first analyzed to establish the background, followed by 50 s measurements for the remainder of the analysis. Each analysis was normalized to Si using concentrations determined by electron microprobe. Relative element sensitivities were calibrated by a NIST 612 glass standard. See Jeffries (2001) for a detailed discussion of the LA-ICP-MS analytical technique. All the results of REE concentration were normalized to chondrite values after McDonough and Sun (1995).

Trace element analyses of apatite were conducted by LA-ICP-MS at the Geochronology and Isotope Geochemistry facility (Ibercron) of the University of the Basque Country (UPV/EHU Spain) using the method described by Ábalos et al. (2012) and García de Madinabeitia et al. (2013). The analyses involved the ablation of minerals in ca. 90 μm thick petrographic sections with a NewWave UP213 Nd:YAG laser ablation system coupled to a Thermo Fisher Scientific XSeries 2 quadrupole ICP-MS instrument with enhanced sensitivity through a dual pumping system. Spot diameter of ca. 40 μm associated to repetition rates of 10 Hz and laser fluence at the target of ca. 5 J/cm^2 were used for the analysis. The NIST SRM 614 silicate glass and Durango apatite were used for quality control of the results assuming major and trace element concentrations reported by Jochum et al. (2011) and Trotter and Eggins (2006), respectively. Raw data were processed using Glitter 4.4.2 (van Achterbergh et al., 2001; Jackson et al., 2004) and the Ca values obtained by electron microprobe on the same spots.

2.2.7. Stable isotope data

Stable isotope data were obtained at the Stable Isotope Laboratories of the Salamanca University. A total of 36 isotopic compositions were obtained. Whole rock samples and mineral separates of unaltered granite, greisen, quartz-cassiterite veins, quartz-tourmaline veins, quartz-apatite veins, and country host rocks were analyzed for oxygen, hydrogen, and carbon isotope composition. Quartz, muscovite, tourmaline, and cassiterite were separated by handpicking after crushing to 80-120 mesh. $^{18}O/^{16}O$ determinations were carried out by laser fluorination using a conventional vacuum extraction line (Clayton and Mayeda, 1963), but employing ClF_3 as reagent (Borthwick and Harmon 1982). The evolved oxygen gas was converted to CO_2 on a red hot carbon rod. The $^{18}O/^{16}O$ ratios were determined on the CO_2. CO_2 gas liberated from a saddle dolomite sample was also collected after reacting with 103% H_3PO_4 (McCrea, 1950) for the determination of $^{13}C/^{12}C$ isotope composition. H_2 and H_2O extraction for D/H isotopic analyses were carried out by the uranium technique described by Godfrey (1962), with modifications introduced by Jenkin (1988), heating the samples at temperatures up to 1500 ºC. The water was converted to hydrogen gas by reduction over hot depleted uranium. The hydrogen and oxygen isotope ratios were measured in SIRA-II mass spectrometer and data are reported in the normal denotation relative to V-SMOW and VPDB standards.

Sulfur isotopes were determined for two endogranitic polished blocks and one exogranitic polished block. Sulfide samples were analyzed by *in situ* combustion using a Nd:YAG laser (12 W, l =1.060 n) connected to a mass spectrometer and microinlet system (VG SIRA-II). The polished blocks were inserted into a sample chamber which was evacuated, and subsequently filled with an excess of oxygen gas (Fallick et al., 1992; Kelley and Fallick, 1990). Laser calibration data is needed, since an isotopic fractionation between the sulfur in SO_2 gas occurs as the result of a non-complete oxidation of sulfides during laser heating (Crowe et al., 1990). Laser calibration data for arsenopyrite and chalchopyrite were taken from the study of Wagner et al. (2004) and Kelley and Fallick (1990). A series of *in situ* laser combustions is either made of single 100 to 200 μm diameter spots or thin (~50 μm) long channels, so as to avoid heterogeneities. The SO_2 gas produced was subsequently cryogenically purified in order to eliminate the O_2 and CO_2 gases, and then analyzed on a VG SIRA II gas mass spectrometer. The precision and accuracy of the isotopic measurements range from +0.2 ‰ to +0.9 ‰ (1σ).

2.2.8. Fluid inclusion study

Doubly-polished wafers (~ 250 μm in thickness) for the fluid inclusion study were analyzed using an Olympus BX-51 microoscope-mounted Linkam THMSG600 heating-cooling stage at the Department of Crystallography and Mineralogy of the Complutense University of Madrid (Fig. 2.1a). The calibration curve employed was generated from melting points of solid standards at T>25 ºC and melting points of H_2O and H_2O-CO_2 of synthetic inclusions at T<0 ºC. The resulting curve was used to obtain the actual temperatures. The rate of heating was 0.1°C/min when phase transitions were approached, in order to get an accuracy of ±0.2 °C for final melting at T< 0 ºC, and of ±4 °C for homogenization temperatures over 25 ºC. The phase volume-fractions were estimated visually. The salinity of H_2O–NaCl inclusions reported as equivalent weight percent NaCl (wt.% NaCl equiv.) was calculated from microthermometric data (ice melting, $T_m$ice) using the equations from Bodnar (1993). Analyses of the non-aqueous components were determined in individual inclusions by micro-Raman analyses performed on a DILOR X-Y multichannel modular Raman spectrometer at GeoRessources laboratory (Université de Lorraine, Nancy) (Fig. 2.1b).

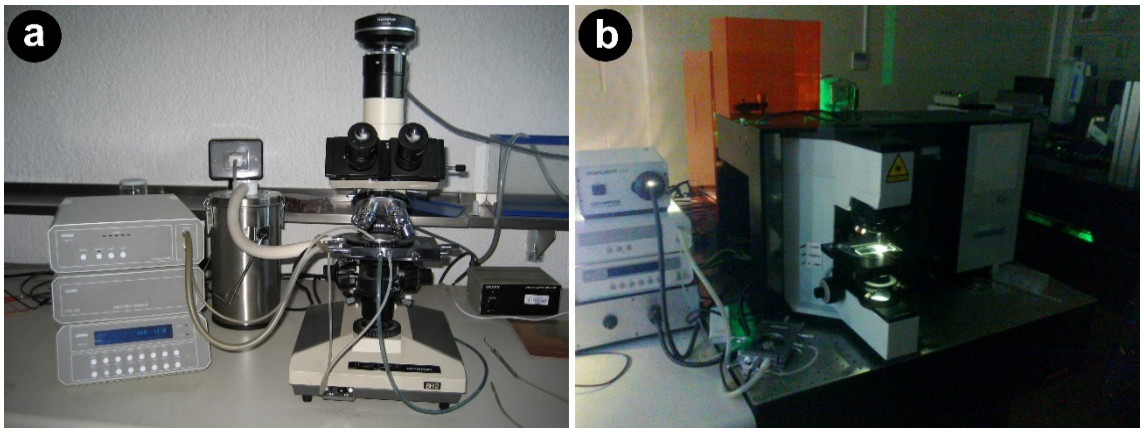

Fig. 2.1: a) Olympus BX-51 microscope-mounted Linkam THMSG600 heating-cooling stage for microthermometric measurements (Dpt. Crystallography and Mineralogy, Complutense University of Madrid). **b)** DILOR X-Y multichannel modular Raman spectrometer (Université de Lorraine, Nancy).

2.2.9. ID-TIMS

Several monazite and zircon crystals were carefully selected by picking the most idiomorphic crystals to avoid all possibility of inheritance for ID-TIMS. The zircon fractions selected for ID-TIMS were pre-treated with the chemical abrasion (CA) method of Mattinson (2005). Zircon annealing was carried at 900ºC for 48 hours and the chemical attack was done in Parrish-type minibombs inside Parr bombs at 180ºC for 12 hours. Final zircon dissolution was achieved after placing the bomb at 240ºC for 72 hours. The procedure for extraction and purification of Pb and

U is a scale-down version of that of Krogh (1973). A ^{208}Pb-^{235}U spike was used to obtain the U/Pb ratios by isotope dilution (ID). Isotopic ratios were measured with a Triton TIMS multi-collector mass spectrometer equipped with an axial secondary electron multiplier (SEM) ion counter. The instrument is set up to do measurements both in static and peak-jumping mode using the SEM. For static measurements the ^{204}Pb was measured with the calibrated SEM (92-93% Yield calibration). The Pb measurements were done in the 1300-1460 ºC range, and U was measured in the 1420-1500 ºC interval (for further analytical details see Rubio-Ordóñez et al. (2012)). Data reduction was done using the PbMacDat spreadsheet (Isacksen et al., 2007; www.earth-time.org). All isotopic ratios are corrected for mass fractionation, blank and initial common Pb after the model of Stacey and Kramers (1975). Ages and uncertainties were calculated with the decay constants of Jaffey et al. (1971), and are reported at the 2σ level. The concordia age was calculated and the data were plotted with Isoplot 3.0 (Ludwig, 2003).

2.2.10. U-Pb in situ

U-Pb *in situ* age determinations were performed by Dr. Carlos Villaseca on 37 polished zircons using a New Wave Research LUV213 laser-ablation microprobe, attached to an Agillent 7500 quadrupole ICP-MS at the ARC GEMOC Centre of the Macquarie University, Sydney (Australia). A laser beam of 30 μm diameter with energies of 60-100 mJ/pulse and 5 Hz repetition rate was shot during 100-120 s resulting in pits of about 30 μm deep. Real-time data were processed using the GLITTER® software package. The correction factors were then checked using the GEMOC-GJ-1 with a TIMS age of 608.5 Ma, the Mud Tank zircon (734 ± 32 Ma, Black and Gulson, (1978) and the 91500 international zircon standard (1064 Ma, Wiedenbeck et al., 1995). Concordia diagrams (2σ error ellipses), concordia ages and upper intercept ages were calculated using the Isoplot/Ex software (Ludwig, 2003).

2.2.11. Ar-Ar geochronology

Five samples were selected for Ar-Ar dating from greisenized wall-rocks. These samples were crushed, sieved, and washed in deionized water. High purity muscovite grains were handpicked under a binocular microscope, and cleaned using ethanol by ultrasonic treatment. Samples were placed in copper or aluminum foil packets, together with neutron flux monitors, and stacked in quartz tubes. The relative positions of packets were precisely measured (±0.5mm) for later reconstruction of neutron flux gradients (Fig. 2.2a). The sample package was irradiated in the Oregon State University reactor, Cd-shielded facility. Fish Canyon sanidine (28.294±0.036 (1σ) Ma, Renne et al., 2011) was used to monitor ^{39}Ar production and establish neutron flux values (J) for the samples. The neutron flux within a given disc is calculated by least-squares fitting of a

surface to the J-monitors. Estimated errors in the neutron flux measurements are calculated from the residual deviation from the fitted surface. Gas was extracted from samples via step-heating using a mid-infrared CO_2 laser, with samples housed in a doubly-pumped ZnS-window laser cell. Individual sample grains were loaded into a copper planchette containing 1x1 cm square wells. Liberated argon was then purified of active gases (e.g., CO_2, H_2O, H_2, N_2, CH_4) using three Zr-Ti-Al getters; one at 25°C and two at 400°C. Data were collected on a GVi instrument ARGUS 5-collector mass spectrometer (Fig. 2.2b) using a variable sensitivity faraday collector array in static collection (non-peak hopping) mode (Sparks et al., 2008; Mark et al., 2009). Time-intensity data are regressed to t_0 with second-order polynomial fits to the data. Mass discrimination was monitored by comparison to running-average values of an air standard. The average total system blank for laser extractions, measured between each sample run, was 1×10^{-15} mol ^{40}Ar, 3×10^{-17} mol ^{39}Ar, 3×10^{-18} mol ^{36}Ar. All data are blank, interference and mass discrimination corrected using the Massspec software package (authored by Al Deino, BGC). Plateau criteria are that the plateau consists of at least three contiguous steps and the scatter between the ages of the steps is low, i.e., MSWD close to 1, and the fraction of ^{39}Ar released for these steps is ≥50%. Isochrons are calculated using only the plateau steps to confirm the composition of the trapped component. A plateau age is accepted if it is concordant at the 2σ level with the isochron age, has a trapped component indistinguishable from air (298.56±0.31, 1σ) at the 2σ level and meets the other criteria listed above. However, we note that the data for muscovites are highly radiogenic, typically >90% 40Ar*) and therefore the uncertainties on the trapped component compositions derived from the inverse isochron regressions are large and highly sensitive to individual data points. It is for this reason that we assume atmospheric trapped components in the micas for purposes of plateau calculation. For plateau ages with MSWD >1, we expand the age uncertainty (SEM) by a factor of (MSWD) 0.5 to account for 'geological' scatter, i.e., non-analytical sources of uncertainty.

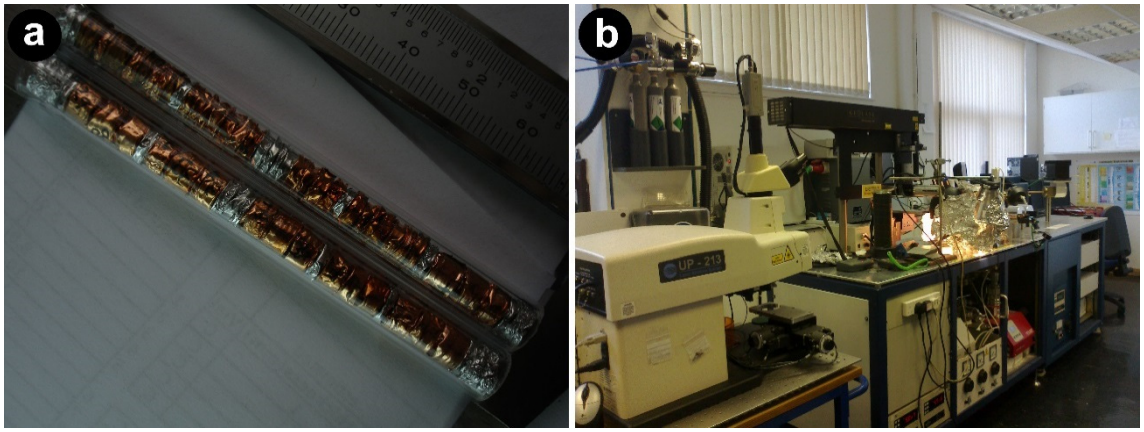

Fig. 2.2: a) Muscovite irradiation packet (picture by Dr. Dan Barfod). **b)** GVi instruments ARGUS 5-collector mass spectrometer (SUERC).

2.2.12. Lu-Hf isotopes

In situ Hf isotopic measurements were analyzed by Dr. Carlos Villaseca on 28 individual previously dated zircon spots at the ARC GEMOC Centre of the Macquarie University (Sydney, Australia). Analyses were carried out using a New Wave Research LUV213 laser-ablation microprobe, attached to a Nu Plasma multi-collector (MC) inductively coupled plasma mass spectrometer (ICPMS). The laser system delivers a beam of 213 nm UV light from a frequency-quintupled Nd:YAG laser. The laser was fired with energy of 5-7 J/cm^2, laser beam diameter was 30 μm and repetition rate was 5 Hz. The laser beam ablated the zircon surface during 100-120 s resulting in pits 30 μm deep. The analytical methods are the same as described in detail by Griffin et al. (2002; 2004). To evaluate the accuracy and precision of the laser-ablation results we have repeatedly analyzed two zircon standards: 91500 and Mud Tank (MT). These reference zircons gave $^{176}Hf/^{177}Hf = 0.282310 \pm 0.000049$ (2σ) and 0.282502 ± 0.000044 (2σ), respectively, which are identical to average published values of 0.282306 ± 0.000008 for 91500 and 0.282507 ± 0.000006 for MT (Woodhead and Hergt, 2005). The 2σ uncertainty on a single analysis of $^{176}Lu/^{177}Hf$ is ± 0.001-0.002% (about 1 epsilon unit), reflecting both analytical uncertainties and the spatial variation of Lu/Hf across many zircons. The ^{176}Lu decay constant value of $1.865x10^{-11}a^{-1}$ was used in all calculations (Scherer et al., 2001). Chondritic $^{176}Hf/^{177}Hf = 0.282772$ and $^{176}Lu/^{177}Hf = 0.0332$ (Bouvier et al., 2008) and the depleted mantle $^{176}Hf/^{177}Hf = 0.28325$ (ƐHf = +16.4) and $^{176}Lu/^{177}Hf = 0.0384$ were applied to calculate ƐHf values and model ages used in this work.

2.3. Presentation of results

Some of the results and conclusions obtained during the development of this PhD Thesis have been exposed as posters or oral presentations in several national and international scientific meetings. Abstracts and papers concerning most aspects of this PhD research have been published in peer-reviewed and SCI journals. The compilation of these results has provided the building up of this PhD dissertation.

The up-to-date contributions related to this PhD Thesis are summarized here and gathered below:

- The works dealing with the detailed petrographic, geochemical and chemical-mineralogical study of the Logrosán granite are Chicharro et al. (2011c; 2013a; 2014d; in press). Accurate granite dating by U-Pb geochronology and Hf- isotopic constraints on the genesis of the Logrosán granite are found in Chicharro et al. (2013a; 2014d). The Sn-

(W) ore deposit characterization is reviewed in Chicharro et al. (2011b; 2014a; in press). Detailed mineral chemistry of the Logrosán cassiterite and Nb-Ta oxides is found in Chicharro et al. (2012b, 2015a). Fluid inclusion microthermometry and Raman studies are revised in Chicharro et al. (2012a; 2015b; in press). Moreover, the first isotopic constraints, ore dating by Ar-Ar geochronology data, and origin and evolution of the mineralization are the main objectives of Chicharro et al. (in press). Chicharro et al. (2015a) provides gravity profile and a model suggesting potential targets. The phosphate ore investigation has been focused on unraveling if the origin of the Iberian-type hydrothermal quartz-apatite veins is linked to the granite emplacement by comparative chemical studies (Vindel et al., 2012; Chicharro et al., 2013b; Vindel et al., 2013; Vindel et al., 2014). Chicharro et al. (2011a; 2014b; 2014c) revise some aspects about the geological patrimony and the historic mining background of the Logrosán area. Finally, Villaseca et al. (2014) review the chemical characteristics of the Neoproterozoic metasedimentary sequences of the Central Iberian Zone, host of the granite intrusions and hydrothermal ores.

Chicharro, E., Boixereu, E., Villaseca, C., López-García, J.Á., 2011a. Contribución a la puesta en valor del patrimonio geológico y minero del geoparque de las Villuercas: el Cerro de San Cristóbal (Logrosán, Cáceres). De Re-Metallica 17: 47-54

Chicharro, E., López-García, J.Á., Villaseca, C., 2011b. Estudio metalogenético de las mineralizaciones de Sn-(Ta)-W del granito de Logrosán (Cáceres) Macla 15: 63-64

Chicharro, E., Villaseca, C., López-García, J.Á., Oyarzun, R., 2011c. Caracterización mineral del granito peralumínico de Logrosán (Cáceres, España). Geogaceta 50-1: 71-74

Chicharro, E., Boiron, M.C., López-García, J.A., Villaseca C., 2012a. Combined microthermometric and Raman spectroscopic techniques to characterize the N_2-CH_4-CO_2-H_2O mixtures in the fluid inclusions of the quartz veins of the Logrosán granitic cupola (Cáceres, Spain). Geo-Raman Xth Meeting, Book of Abstracts

Chicharro, E., López-García, J.Á., V., Villaseca, C., 2012b. Geoquímica de la casiterita de los filones de estaño del granito especializado de Logrosán (Cáceres, España). Geo-Temas 13: 337

Vindel, E., **Chicharro, E.**, Sánchez, V., López-García, J.Á., Villaseca, C., 2012. Estudio Preliminar de las Venas Cuarzo-Apatito de Logrosán y Belvís de Monroy (Cáceres): Datos Geoquímicos y de Inclusiones Fluidas en Apatitos. Macla 16: 74-75

Vindel, E., **Chicharro, E.**, Sánchez, V., López-García, J.Á., Villaseca, C., 2013. Los plutones de Logrosán y Belvís, Cáceres: comparación entre apatitos magmáticos e hidrotermales. Macla 17: 113-114.

Chicharro E., Villaseca C., Valverde-Vaquero P., Belousova E., López-García J.A., 2013a. Zircon U-Pb and Hf isotopic constraints on the genesis of a post-kinematic S-type Variscan tin granite: the Logrosán cupola (Central Iberian Zone). Mineralogical Magazine 77: 874

Chicharro, E., Vindel, E., Sánchez, V., López-García, J.Á., Villaseca, C., 2013b. Estudio geoquímico de los filones de cuarzo-apatito asociados a granitos de Extremadura: Logrosán, Belvís de Monroy y Navalmoral de la Mata. IX Congreso Ibérico - XI Congreso Nacional de Geoquímica, Resúmenes

Chicharro, E., 2014a. Caracterización de las mineralizaciones de Sn-(W) asociadas al stock granítico de Logrosán (Cáceres). Macla 14, 75.

Vindel, E., **Chicharro, E.**, Villaseca, C., López-García, J.A., Sánchez, V., 2014. Hydrothermal phosphate vein-type ores from the southern Central Iberian Zone, Spain: Evidences for their relationship to granites and Neoproterozoic metasedimentary rocks. Ore Geology Reviews 62: 143-155. doi:10.1016/j.oregeorev.2014.03.01

Villaseca, C., Merino, E., Oyarzun, R., Orejana, D., Pérez-Soba, C., **Chicharro, E.,** 2014. Contrasting chemical and isotopic signatures from Neoproterozoic metasedimentary rocks in the Central Iberian Zone (Spain) of pre-Variscan Europe: Implications for terrane analysis and Early Ordovician magmatic belts. Precambrian Research 245: 131-145. doi:10.1016/j.precamres.2014.02.006

Chicharro, E., López-García, J.Á., Villaseca, C., Oyarzun, R., Rivas, S., Boixereu, E., 2014b. Geoguía 5: Ecos de un pasado remoto y otro más cercano: el estaño y el fósforo de Logrosán. Geoguías GEMM. Serie Distritos Mineros, 5.

Chicharro, E., López-García, J.Á., Oyarzun, R., Villaseca C., Boixereu, E., 2014c. Difusión del patrimonio geológico-minero de España a través de la serie Geoguías GEMM (1): Logrosán. XV Congreso Internacional sobre Patrimonio Geológico y Minero – XIX Sesión Científica de la SEDPGYM, Resúmenes.

Chicharro, E., Villaseca, C., Valverde-Vaquero, P., Belousova, E., López-García, J.A., 2014d. Zircon U-Pb and Hf isotopic constraints on the genesis of a post-kinematic S-type Variscan tin granite: the Logrosán cupola (Central Iberian Zone). Journal of Iberian Geology 40: 451-470. doi:10.5209/rev_JIGE.2014.v40.n3.43928

Chicharro, E., Martín-Crespo, T., Gómez-Ortiz, D., López-García, J.A., Oyarzun, R., Villaseca, C., 2015a. Geology and gravity modeling of the Logrosán Sn–(W) ore deposits (Central Iberian Zone, Spain). Ore Geology Reviews 65: 294-307. doi:10.1016/j.oregeorev.2014.10.005

Chicharro, E., Boiron M.C., López-García, J.A., 2015b. Implication of metamorphic fluids on cassiterite precipitation in the Logrosán Sn-(W) ore deposit (Central Iberian Zone, Spain). 13th SGA Biennial Meeting. Proceedings, 2: 433-436.

Chicharro, E., Boiron, M.C., López-García, J.Á., Barfod, D., Villaseca, C. (in press). Origin, ore forming fluid evolution and timing of the Logrosán Sn-(W) ore deposits (Central Iberian Zone, Spain). Ore Geology Reviews. doi:10.1016/j.oregeorev.2015.09.020

2.4. Laboratory stays

During my PhD research I have had the chance of being trained in different national and international laboratories, besides the ones belonging to the Complutense University of Madrid, and to collaborate with other colleagues during short stays:

- NERC Argon Isotope Facility SUERC, University of Glasgow (Glasgow, Scotland, UK)
  Ar-Ar geochronology
  Stay: 17/02/2014 - 03/03/2014
  Advisors: Dr. Fin Stuart and Dr. Dan Barfod

- Natural History Museum of London (London, UK)
  Igneous and hydrothermal mineral analyses by LA-ICP-MS
  Stay: 11/06/2013 - 25/06/2013
  Advisor: Dr. Teresa Jeffries

- Servicio General de Isótopos Estables, Universidad de Salamanca (Salamanca, Spain)
  In-situ sulfur, and O/H isotope determinations
  Stay: 19/03/2013
  Advisor: Dr. Clemente Recio

- Servicio de Geocronología y Geoquímica Isotópica, Universidad del País Vasco UPV/EHU (Bilbao, Spain)
  Trace apatite analyses by LA-ICP-MS
  Stay: 08/11/2012
  Advisor: Dr. José Ignacio Gil Ibarguchi

- GéoRessources Laboratoires, Université Henri Poincaré (Vandoeuvre-lès-Nancy, France)
  Raman spectroscopy training in fluid inclusion
  Stay: 03/02/2012 - 09/04/2012
  Grant: Estancias Breves FPU (Ministerio de Educación)
  Advisor: Dr. Marie-Christine Boiron

- Instituto Geológico y Minero de España (Tres Cantos, España)
  Mineral separation and U-Pb TIMS geochronology
  Stay: 01/07/2011 - 01/08/2011
  Advisor: Dr. Pablo Valverde

Chapter 3: THE LOGROSÁN GRANITE

SUMMARY:

A complete characterization of the Logrosán granite is developed in this chapter. The field and petrographic features, whole-rock and rock-forming mineral chemistry are summarized here. The zircon U–Pb CA-ID-TIMS and LA-ICP-MS geochronology results allow constraining the age of the Logrosán granite emplacement. In this chapter, there is also a compilation and discussion of the results obtained from several isotopic methods (Sr-Nd-O in whole-rock and Lu-Hf-in zircon).

THE LOGROSÁN GRANITE

3.1. General features

3.1.1. Macroscopic observations

The Logrosán granite (a.k.a. San Cristóbal hill) occupies an outcropping area of about 4 km^2. The intrusion is surrounded by a landscape of contact metamorphic rocks in which the high granitic relief stands out. It is a dome-shape hill with two twin summits, the highest of which, at the west, attains an altitude of 681 m, while the eastern top reaches 677 m. This body shows a sub-ellipsoidal shape elongated in the NE-SW direction, and a hidden larger volume of granite rocks may be assumed by the extent of the contact-metamorphic aureole. The granitic body corresponds mainly to a coarse- to medium-grained two-mica-leucogranite (Main Unit), while more fractionated units (Evolved Units) are found principally on the summits of the San Cristóbal hill (Fig. 3.1).

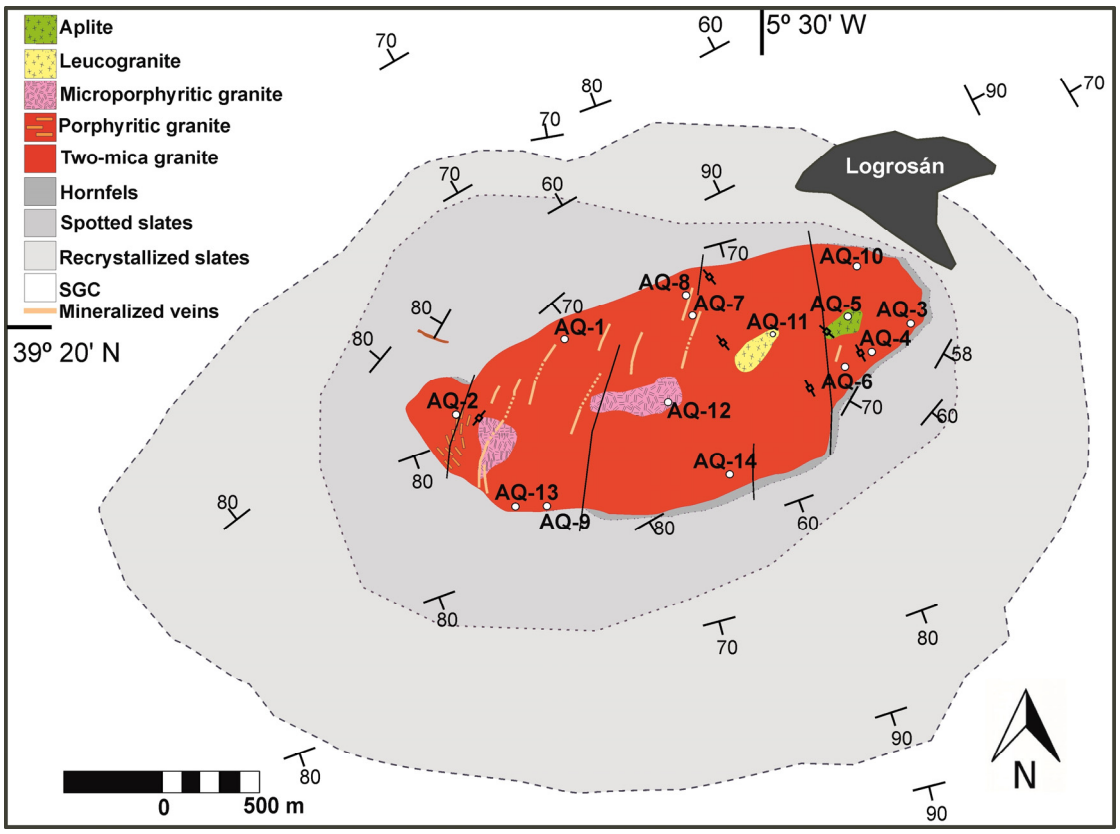

Fig. 3.1: Detailed map of the Logrosán granite. Sampling points for whole rock analyses are indicated by open circles.

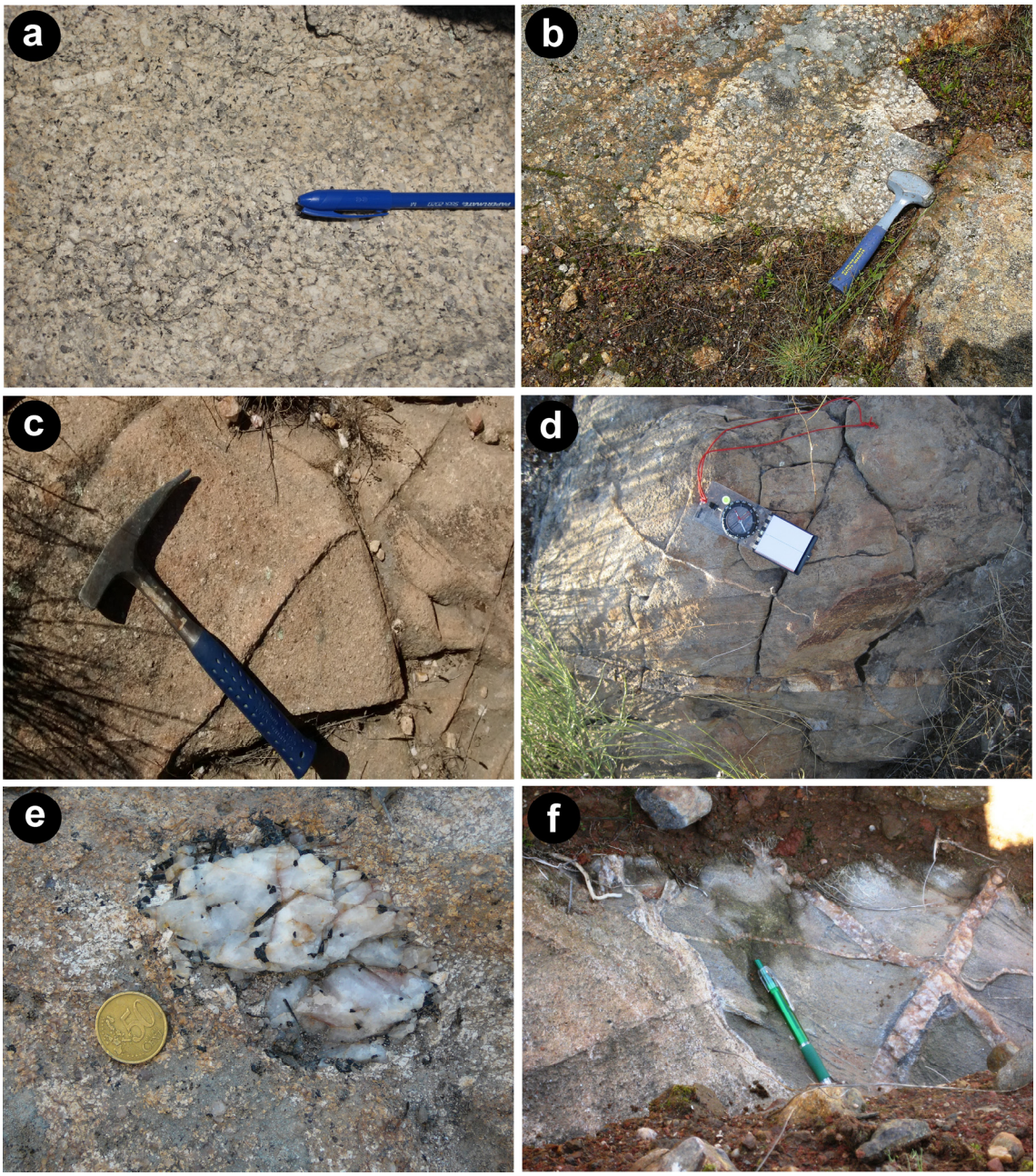

Fig. 3.2: Field features of the Logrosán granite. **a)** Two-mica granite with coarse to medium grain from the Main Unit. **b)** Porphyritic sectors within the Main Unit granite. **c)** Microporphyritic (two-texture) granite. **d)** Aplite from the Evolved Units and barren quartz veins cutting through it. **e)** Pegmatitic miarole within the Main Unite granite. **f)** Sharp granite-SGC metasediment contact. Quartz-tourmaline veins within both units.

The Logrosán pluton is mainly composed of a coarse- to medium-grained two-mica leucogranite (Main Unit) (Fig. 3.2a) which grades to fine-grained or porphyritic varieties (Fig. 3.2b). Where K-feldspar megacrysts appear, flow textures are visible with a N130 main trend, following the contact of the granitic pluton in the most external areas. The two summits of the hill defined by the Logrosán granite are composed of a microporphyritic (two-texture) granite (Fig. 3.2c) and an aplitic granite (Evolved Units) (Fig. 3.2d). No sharp contacts between the Evolved Units and the Main Unit were observed. Pegmatitic and fine-grained leucocratic bodies of variable size

are frequent, usually showing sharp contacts with the Main Unit. Micaceous, mostly biotitic enclaves are occasionally found, as well as schlieren structures. Tourmaline appears as an accessory phase within most of the Logrosán granite units, and within pegmatitic miaroles (Fig. 3.2e). Tourmaline is also associated with all types of quartz-veining systems that cross-cut the granite body. Tourmaline also occurs as quartz-tourmaline veins within the granite-metasediment contact (Fig. 3.2f). The Logrosán granite was affected by complex hydrothermal events which are identified by the presence of sectors with a dense network- of quartz-rich veining (cm-scale in thickness of barren-, tourmaline-, cassiterite- rich varieties). Therefore, greisen-type alteration zones are found in the sectors with a high proportion of mineralized veins and veinlets. Greisen alteration is not only restricted to the selvages, but also affects some parts of the granitic body. This alteration is characterized by high contents of muscovite and the presence of disseminated cassiterite. A 'sandy granite' is very common adjacent to the Sn-(W) veins and greisen alteration, and in most cases is a result of old mining activity (processing/panning for mineral recovery).

3.1.2. Microscopic characteristics

The Logrosán granite shows a holocrystalline, seriate inequigranular, medium-grained texture. The mineralogy consists of quartz, plagioclase, K-feldspar, muscovite, biotite and accessory minerals (tourmaline, apatite, zircon, beryl, monazite, ilmenite and rutile). The modal amounts indicated below have been taken from Rossi (1975).

Quartz occurs as subeuhedral grains of about 300 μm with undulatory extinction and local pressure solution grain contacts (Fig. 3.3a). Quartz may contain tiny inclusions of other minerals, such as muscovite and tourmaline. Minor quartz is found as rounded small inclusions within K-feldspar, plagioclase and biotite. Quartz makes 30.4–39.7 % modal.

K-feldspar occurs as euhedral to anhedral large sized crystals (up to several centimeter), reaching a modal amount of 24.1-30.2 %. It shows flame-shaped albite lamellae perthitic textures, usually coincident with micro-shear zones. Micrographic textures between quartz and K-feldspar are also found (Fig. 3.3b). K-feldspar phenocrysts often have poikilitic textures, hosting small quartz, plagioclase, muscovite, zircon, monazite, apatite, and tourmaline crystals.

Plagioclase is commonly euhedral, polysynthetic twinned, and sized usually between 1 to 3 mm, although reaching occasionally the cm scale. It is normally zoned, with cores slightly more

anorthitic than rims (see Fig. 3.4). The inner part of plagioclase is often altered to muscovite or sericite (Fig. 3.3c). Plagioclase modal amount ranges from 26.1 to 32.8%.

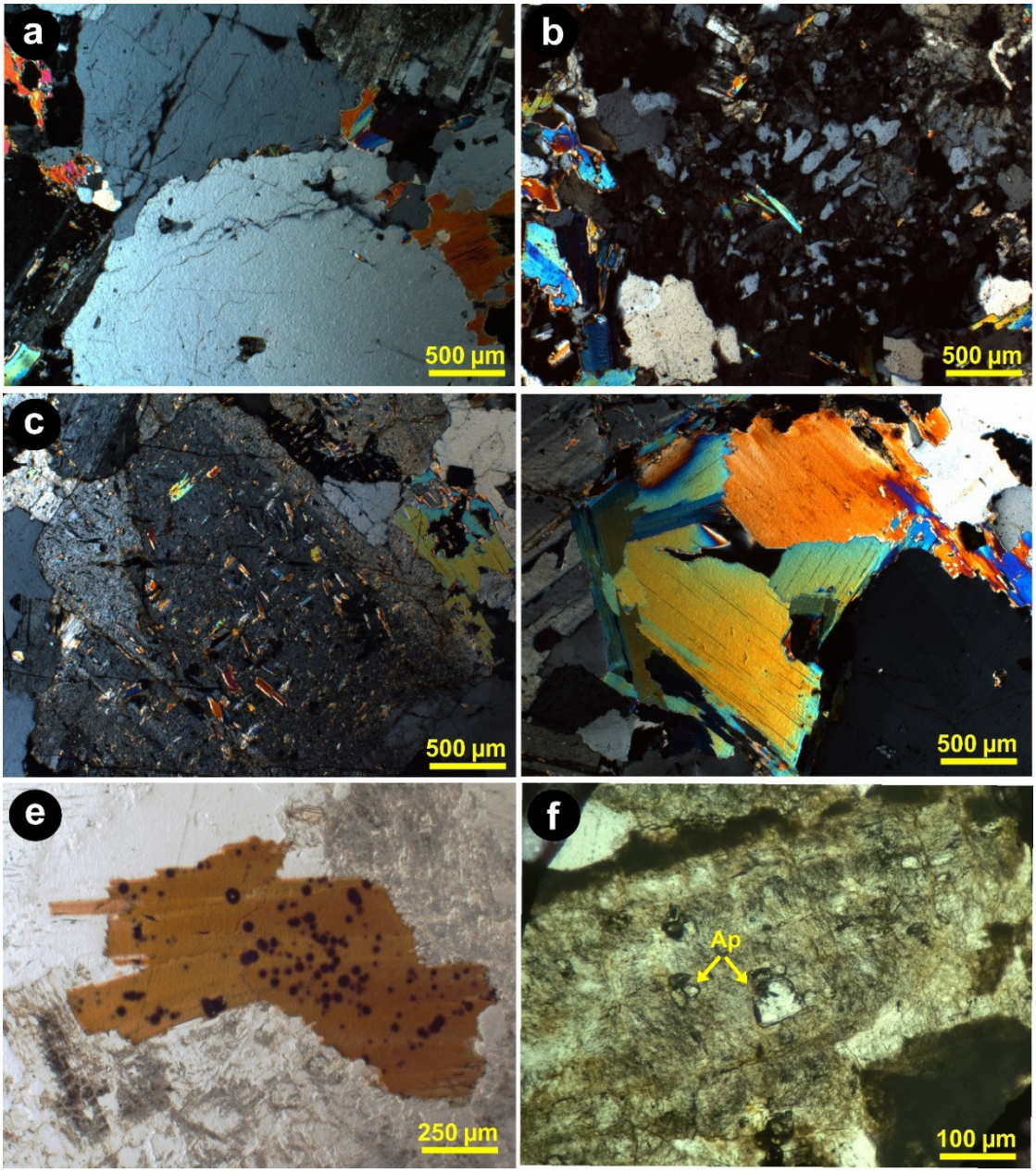

Fig. 3.3: Microscopic features of the Logrosán granite under transmitted light. **a)** Quartz grains showing pressure-solution contacts (NX). **b)** Micrographic textures between quartz and K-feldspar (NX). **c)** Zoned plagioclase altered by muscovite (NX). **d)** Igneous muscovite crystal aggregate (NX). **e)** Strongly pleochroic biotite with several decrepitation halos around zircon inclusions. **f)** Magmatic apatite included in K-feldspar.

Muscovite is a main mineral in the leucogranite with a modal value of 2.0-8.1 %. Magmatic muscovite is silver-colored platy under naked eye, subeuhedral, and with sizes ranging from 300 µm to about 1 mm (Fig. 3.3d). Igneous muscovite often show undulatory extinction, indicating plastic deformation processes. Besides, secondary muscovite is also abundant, especially in altered granites. Secondary muscovite tends to be smaller in size (100-200 µm) and replaces

magmatic minerals within the Normal and Evolved Units. In strongly altered granites and vein selvages, post-magmatic or hydrothermal muscovite has larger sizes (up to several millimeters) and usually shows a yellowish tonality.

Biotite occurs mostly as euhedral to subeuhedral large crystals (> 1mm). Its color is reddish brown and shows a strong pleochroism from brown to olive green. Biotite represents 1.2–3.3 modal and appears isolated, or forming micaceous aggregates with muscovite. It usually hosts inclusions of other minerals, such as zircon or rutile. Pleochroic halos around small zircon inclusions are very often observable within biotite (Fig. 3.3e).

The most ubiquitous accessory minerals (0.3−2.1 % of the modal abundance) are tourmaline, apatite, monazite, (Nb-Ta) rutile, ilmenite and zircon. Igneous tourmaline occurs disseminated throughout the granite, in micropegmatitic nodules or miaroles, and in lenticular clots (< 2 cm) associated with quartz, muscovite, K-feldspar and apatite. It forms medium to large grained, subeuhedral to anhedral, yellowish-brown to green-colored, usually weakly zoned or unzoned crystals. Some tourmaline crystals show irregularly shaped embayment, which indicates crystals were unstable in the melt prior to the magmatic crystallization. Since is not associated with tourmaline veinlets, it is interpreted to have formed very soon after crystallization of the pluton, probably as a result of metasomatic processes. Tourmaline occurs in muscovite aggregates associated with minor beryl. The abundance of tourmaline in the rock increases with proximity to the mineralized veins, suggesting that a significant amount of tourmaline within the granite is somehow related to the hydrothermal event responsible for the Sn-(W) mineralization. Apatite is relatively abundant, and occurs as small euhedral inclusions mostly included in plagioclase and K-feldspar (Fig. 3.3f). The Logrosán granite is moderately rich in zircon, which appears preferentially within biotite and quartz crystals. Other accessory minerals are the rutile needles, which are found mostly in quartz and biotite. Ilmenite occurs associated with mica aggregates. Ilmenite is the main opaque mineral identified, as well as minor arsenopyrite. Monazite is rare, but appears as subeuhedral mostly included within the main rock-forming minerals.

3.2. Mineral geochemistry

The whole dataset of major and trace-element composition of selected mineral phases from the Logrosán granite are shown in the electronic supplementary material (Supplementary Table 1 and Supplementary Table 2).

3.2.1. Feldspars

K-feldspar composition is close to pure orthoclase (average $Or_{95}Ab_5$). The composition of K-feldspar from the Main Unit (MU) and the Evolved Units (EU) are very similar. Thus, K-feldspar from the MU has a compositional range of $Or_{86\text{-}99}Ab_{1\text{-}14}$, whereas K-feldspar from the EU is $Or_{87\text{-}99}Ab_{1\text{-}13}$ (Table 3.1).

Table 3.1: Major (wt.%; EMPA) and trace (ppm; LA-ICP-MS) composition of representative K-feldspar from the Logrosán granite.

	Main Unit (MU)						**Evolved Unit (EU)**					
Sample	**111912**	**111974**	**111978**	**112463**	**112470**	**112470**	**177**	**111976**	**111976**	**111979**	**111979**	**111979**
Analysis	**79**	**5**	**158**	**71**	**2**	**46**	**99**	**1**	**9**	**18**	**64**	**85**
SiO_2	65.3	64.7	63.6	64.2	64.0	63.3	62.8	64.3	62.9	63.9	62.9	64.6
Al_2O_3	19.2	18.5	18.4	18.6	19.0	19.2	18.7	18.3	18.9	18.7	18.7	18.3
CaO	0.00	0.01	0.03	0.01	0.00	0.00	0.02	0.00	0.00	0.00	0.00	0.01
Na_2O	0.15	0.35	0.14	0.15	1.53	1.25	0.73	0.90	0.37	0.54	0.57	0.15
K_2O	14.8	15.0	16.1	15.1	14.8	15.2	16.0	15.3	15.7	15.7	16.2	15.5
P_2O_5	0.04	0.72	0.03	0.07	0.47	1.04	0.97	0.09	0.72	0.36	0.62	0.07
F	0.05	0.01	0.04	0.01	0.04	0.02	0.02	0.01	0.00	0.00	0.01	0.00
Total	99.5	99.3	98.3	98.1	99.8	100	99.2	98.9	98.6	99.3	99.0	98.6
% Or	98.5	96.5	98.6	98.5	86.4	88.8	93.5	91.8	96.6	95.0	94.9	98.6
% Ab	1.51	3.46	1.27	1.45	13.57	11.16	6.44	8.23	3.44	4.98	5.07	1.40
% An	0.00	0.05	0.16	0.04	0.00	0.00	0.10	0.01	0.00	0.00	0.00	0.03
Nº ions in formula on the basis of 8 oxygens												
Si	2.997	2.973	2.985	2.994	2.946	2.916	2.924	2.984	2.938	2.967	2.939	3.007
Al	1.036	1.004	1.020	1.020	1.034	1.039	1.027	1.003	1.042	1.025	1.030	1.006
Ca	0.000	0.000	0.002	0.000	0.000	0.000	0.001	0.000	0.000	0.000	0.000	0.000
Na	0.013	0.031	0.012	0.013	0.136	0.112	0.066	0.081	0.033	0.049	0.052	0.013
K	0.863	0.878	0.962	0.898	0.868	0.891	0.951	0.903	0.937	0.930	0.967	0.923
P	0.001	0.028	0.001	0.003	0.018	0.041	0.038	0.004	0.029	0.014	0.025	0.003
F	0.007	0.001	0.005	0.002	0.006	0.003	0.003	0.001	0.000	0.000	0.002	0.000

	Main Unit				**Evolved Units**							
Sample	**111978**	**111978**	**111978**	**111911**	**177**	**177**	**177**	**177**	**111979**	**111979**	**111979**	**111979**
Spot	17a04	17a06	17a09	17b03	17c12	17c15	17d04	17d05	17d08	17d11	17d12	17e03
Li	6.78	b.d.l	b.d.l	b.d.l	89.60	26.90	35.50	54.10	11.70	7.09	14.00	9.06
Be	b.d.l	b.d.l	b.d.l	b.d.l	b.d.l	b.d.l	b.d.l	12.30	1.45	b.d.l	b.d.l	2.61
B	29.20	25.60	26.20	b.d.l	b.d.l	b.d.l	12.80	b.d.l	b.d.l	b.d.l	b.d.l	41.10
Rb	889	1010	971	804	640	518	599	505	582	468	489	747
Sr	2.12	40.30	2.30	11.20	97.00	110	46.50	92.40	72.00	53.60	50.60	69.80
Cs	175	138	125	102	106	31.90	33.70	87.80	53.80	16.10	6.57	77.00
Ba	361	297	362	537	1350	1660	171	465	399	488	123	408
Eu	0.06	b.d.l	b.d.l	b.d.l	0.18	0.53	0.25	0.28	0.43	0.41	0.29	0.09
Zn	b.d.l	b.d.l	b.d.l	b.d.l	91.10	2.77	b.d.l	3.70	b.d.l	b.d.l	b.d.l	2.38
Sc	15.20	14.00	14.20	12.40	15.30	14.70	14.00	13.80	12.60	14.50	14.90	13.90
Hf	b.d.l	b.d.l	b.d.l	b.d.l	b.d.l	b.d.l	b.d.l	b.d.l	b.d.l	b.d.l	b.d.l	b.d.l
Pb	2.01	12.60	1.23	2.08	83.40	123	58.00	55.90	99.30	50.60	56.80	24.50
Nb	b.d.l	0.03	b.d.l	b.d.l	7.00	b.d.l	b.d.l	b.d.l	b.d.l	b.d.l	b.d.l	b.d.l
Ta	b.d.l	b.d.l	b.d.l	0.03	1.73	b.d.l	b.d.l	b.d.l	0.03	b.d.l	b.d.l	0.03
Sn	b.d.l	4.99	2.54	b.d.l	7.72	8.93	12.70	13.90	20.50	11.80	14.00	13.30
W	0.41	0.36	0.16	b.d.l	1.94	0.49	b.d.l	0.27	b.d.l	b.d.l	b.d.l	0.30
Rb/Sr	419	25.06	422	71.79	6.60	4.71	12.88	5.47	8.08	8.73	9.66	10.70

Plagioclase is predominantly albite (average of $Ab_{95}Or_1An_3$) and F-rich (up to 0.11 wt.% for the MU, and 0.17 wt.% for the EU). Plagioclase from the MU is $Ab_{85\text{-}100}An_{0\text{-}11}Or_{0\text{-}4}$, and plagioclase

from the EU is compositionally more heterogeneous $Ab_{82-99}An_{0-14}Or_{0-18}$ (Table 3.2). Two different plagioclase generations may be recognized both in the Main Unit, and in the Evolved Units (Fig. 3.4). The first generation consists of an idiomorphic fairly homogeneous plagioclase (> 1mm), with composition of An_{11} to An_{05}. The second generation is characterized by smaller (less than 1 mm) interstitial, no-zoned plagioclase, which is compositionally a very pure albite, with an Ab component always above 95%. Moreover, among the plagioclase from the Evolved Units, the plagioclase belonging to the phenocrysts of the microporphyritic granite is, in general, poorer in the Ab component (Fig. 3.5).

Table 3.2: Major (wt.%; EMPA) and trace (ppm; LA-ICP-MS) composition of representative plagioclase from the Logrosán granite.

	Main Unit (MU)						Evolved Unit (EU)						
Sample	**111911**		**111974**	**111978**	**112466**	**112470**	**177**				**111976**	**111979**	
Analysis	**193**	**221**	**12**	**139**	**36**	**23**	**97**	**105**	**114**	**92**	**2**	**23**	**69**
Gen.	**I**	**II**	**II**	**I**	**I**	**II**	**I**	**I**	**I**	**II**	**I**	**II**	**II**
SiO_2	65.2	68.6	68.6	64.9	64.5	66.5	65.1	65.2	64.4	66.6	66.9	68.1	68.5
Al_2O_3	21.5	18.9	19.4	20.9	22.4	20.6	20.8	21.1	21.8	20.3	20.3	19.8	19.7
CaO	2.39	0.28	0.04	2.29	1.09	0.60	2.14	1.86	2.89	0.04	0.80	0.59	0.14
Na_2O	9.94	11.6	11.4	9.9	11.1	11.3	10.3	10.1	9.89	10.7	11.2	11.3	11.6
K_2O	0.57	0.10	0.10	0.48	0.52	0.24	0.40	0.49	0.25	0.01	0.19	0.16	0.08
P_2O_5	0.42	0.17	0.02	0.39	0.38	1.02	0.36	0.42	0.24	0.72	0.09	0.02	0.21
F	0.00	0.00	0.00	0.01	0.11	0.00	0.04	b.d.l.	b.d.l.	b.d.l	b.d.l.	0.02	0.04
Total	100.0	99.7	99.5	99.0	100.1	100.1	99.1	99.1	99.4	98.4	99.4	100.0	100.3
% Or	3.20	0.54	0.58	2.73	2.85	1.36	2.25	2.80	1.43	4.22	1.07	0.92	0.47
% Ab	85.4	98.2	99.2	86.3	92.2	95.8	87.7	88.3	84.9	95.6	95.2	96.3	98.9
% An	11.35	1.28	0.18	11.0	4.99	2.81	10.1	8.95	13.71	0.2	3.78	2.78	0.67
Nº ions in formula on the basis of 8 oxygens													
Si	2.868	3.004	3.002	2.882	2.831	2.902	2.887	2.885	2.850	2.959	2.945	2.974	2.981
Al	1.113	0.973	0.999	1.095	1.156	1.058	1.086	1.100	1.137	1.063	1.053	1.022	1.010
Ca	0.113	0.013	0.002	0.109	0.051	0.028	0.102	0.088	0.137	0.002	0.038	0.028	0.007
Na	0.848	0.989	0.970	0.855	0.946	0.952	0.886	0.871	0.849	0.919	0.954	0.958	0.974
K	0.032	0.005	0.006	0.027	0.029	0.013	0.023	0.028	0.014	0.041	0.011	0.009	0.005
P	0.016	0.006	0.001	0.015	0.014	0.038	0.013	0.016	0.009	0.000	0.003	0.001	0.008
F	0.000	0.000	0.003	0.002	0.015	0.000	0.005	0.000	0.000	0.000	0.000	0.003	0.005

	Main Unit (MU)						Evolved Units (EU)						
Sample	**112470**	**111911**			**111978**		**177**			**111979**			
Spot	17b17	17a16	17b05	17a15	17a07	17a11	17c08	17d03	17d06	17e05	17d09	17d14	17d17
Gen.	I	I	I	II	II	II	I	I	I	II	II	II	II
Li	b.d.l.	b.d.l.	b.d.l.	b.d.l.	b.d.l.	b.d.l.	5.30	13.60	b.d.l.	b.d.l.	23.90	b.d.l.	b.d.l.
Be	b.d.l.	2.51	3.45	b.d.l.	b.d.l.	2.19	1.98	1.40	b.d.l.	4.29	3.08	3.15	1.56
B	b.d.l.	b.d.l.	b.d.l.	b.d.l.	b.d.l.	b.d.l.	b.d.l.	b.d.l.	b.d.l.	22.00	b.d.l.	b.d.l.	b.d.l.
Rb	3.14	1.63	2.57	0.21	0.42	1.20	1.92	1.69	0.61	8.63	3.11	1.55	0.46
Sr	105	36.90	98.20	20.60	18.90	24.80	101	100	130	39.90	33.60	35.40	29.20
Cs	b.d.l.	b.d.l.	b.d.l.	0.13	0.24	0.62	0.11	0.34	b.d.l.	2.85	0.81	0.55	0.15
Ba	24.10	13.30	29.80	2.06	1.97	4.13	18.80	22.10	22.00	7.71	9.76	3.89	2.44
Eu	0.69	0.23	0.58	b.d.l.	b.d.l.	b.d.l.	0.65	0.71	0.69	b.d.l.	0.10	b.d.l.	b.d.l.
Zn	b.d.l.	b.d.l.	b.d.l.	b.d.l.	b.d.l.	b.d.l.	b.d.l.	b.d.l.	b.d.l.	3.75	10.40	b.d.l.	b.d.l.
Sc	13.90	13.90	13.80	14.60	14.80	14.70	13.70	15.10	13.70	14.50	16.50	13.90	14.30
Hf	b.d.l.	b.d.l.	b.d.l.	b.d.l.	b.d.l.	b.d.l.	b.d.l.	b.d.l.	b.d.l.	b.d.l.	b.d.l.	b.d.l.	b.d.l.
Pb	27.50	18.30	30.20	5.97	5.53	6.55	28.30	31.40	36.10	3.81	13.60	4.29	6.10
Nb	b.d.l.	b.d.l.	b.d.l.	b.d.l.	b.d.l.	b.d.l.	b.d.l.	b.d.l.	0.02	b.d.l.	b.d.l.	b.d.l.	b.d.l.
Ta	b.d.l.	b.d.l.	b.d.l.	b.d.l.	b.d.l.	b.d.l.	b.d.l.	b.d.l.	b.d.l.	b.d.l.	b.d.l.	b.d.l.	b.d.l.
Sn	5.43	11.90	3.62	2.18	b.d.l.	3.93	4.70	4.70	5.35	3.94	b.d.l.	b.d.l.	b.d.l.
W	b.d.l.	b.d.l.	b.d.l.	b.d.l.	b.d.l.	b.d.l.	b.d.l.	b.d.l.	b.d.l.	0.48	0.77	b.d.l.	b.d.l.

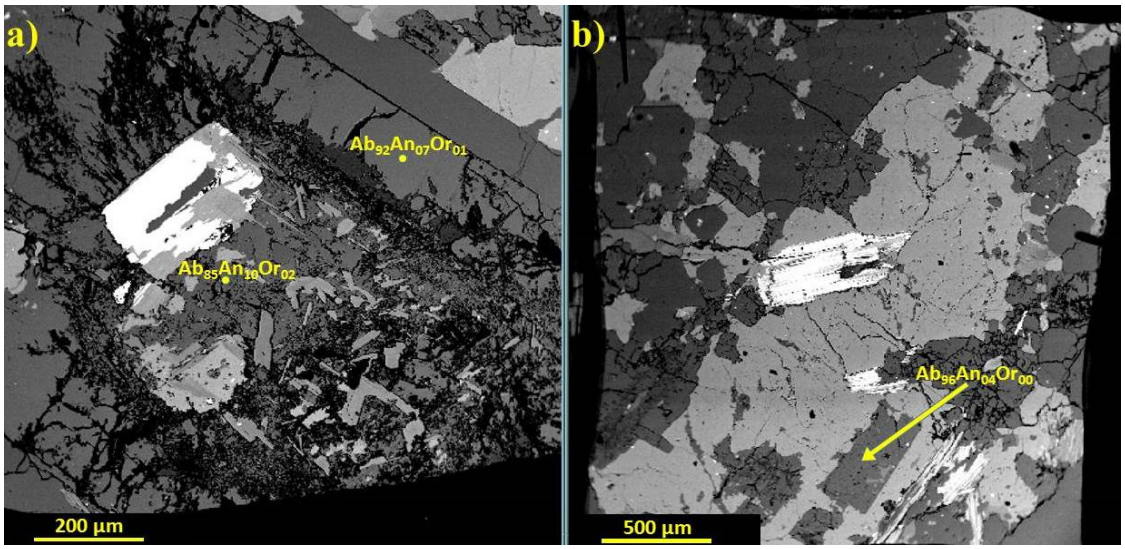

Fig. 3.4: BSE images of plagioclase. **a)** Slightly zoned plagioclase-I from the Main Unit ($Ab_{85}An_{10}Or_{02}$→$Ab_{92}An_{07}Or_{01}$). The core is altered to muscovite, K-feldspar and chlorite. **b)** Interstitial plagioclase-II from the Evolved Units ($Ab_{96}An_{04}Or_{00}$).

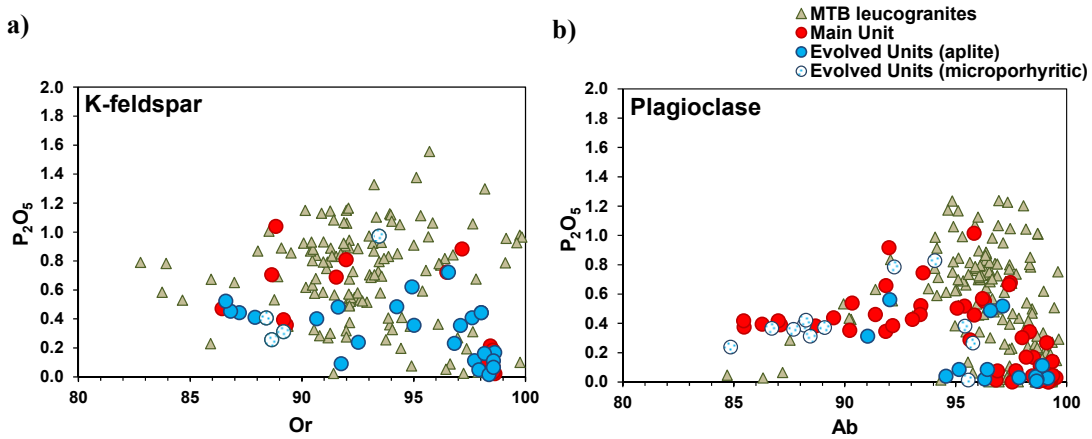

Fig. 3.5: P_2O_5 variation diagrams for feldspars from the Logrosán granite and Montes de Toledo Batholith leucogranites (Merino, 2014). **a)** P_2O_5 (wt.%) vs. ortochlase component (%) in K-fedspar. **b)** P_2O_5 (wt.%) vs. ortochlase (%) component in plagioclase.

Plagioclase and K-feldspar are relatively phosphorous-rich, having contents of P_2O_5 up to 1.04 wt.% in K-feldspar, and up to 1.02 wt.% in plagioclase. These values are similar to those found in feldspars from other phosphorous-rich leucogranites in the Central Iberian Zone (e.g., Belvís de Monroy granite, Merino, 2014) (Fig. 3.5). Nevertheless, P_2O_5 contents in Logrosán are much higher than in the feldspars from other granitoids from the CIZ (e.g., SCS granitoids, Villaseca et al., 2008; most of MTB granitoids, Merino, 2014; Pedrobernardo pluton, Bea et al., 1994). K-feldspars from the MU has, in general, slightly higher P_2O_5 contents than K-feldspar from the EU (Table 3.1 and 4.2). Plagioclase tends to have the highest P_2O_5 contents when Ab component is around 95-96 mol.% (Fig. 3.5). Moreover, feldspar crystals hosting apatite inclusions are usually depleted in P_2O_5 close to the apatite inclusions.

Most trace elements in feldspars yield values below detection limits. K-feldspar and plagioclase minor chemistry is summarized in Table 3.1 and Table 3.2. First and second plagioclase generations show differences in trace element chemistry; Pl-I is enriched in Ba, Sr, and Sn when comparing to Pl-II. The Ab-rich Pl-II shows higher variations in the Rb content and a slight positive correlation between Rb and (Sr+Ba); while Pl-I has little variations in the Rb content and almost constant (Sr+Ba) values, except for some outliers (Fig. 3.6a). K-feldspar and plagioclase from the Evolved Units are enriched in Li, Be, Sr, Ba, Zn, Pb, Nb, Ta, Sn, and W with respect to feldspars from the Main Unit (Table 3.1, Table 3.2 and Fig. 3.6b). Some differences in LILE behavior between K-feldspar and plagioclase from the Logrosán granite are found; K-feldspar shows lower Rb and Cs contents in the EU, while plagioclase tends to have higher Rb and Cs contents in the EU, compared with plagioclase from the MU (Fig. 3.6b). The presence of abundant muscovite in the late-magmatic stages might have been contributed to a decrease of the Rb mineral partition in the K-feldspar, given that Rb contents of K-feldspar from the EU are low. Moreover, the noteworthy drop in Cs in the K-feldspar might be associated with alteration or weathering processes, as Cs is very sensitive to fluid mobilization. However, taking into consideration the associated drop in Rb contents (and Sr, Ba increase) an alternative uncommon magmatic fractionation could be proposed. Rb/Sr ratios appear to decrease significantly in the Evolved Unit K-feldspar from the Logrosán granite (Table 3.1), a behavior not expected for a regular fractionation process. Similarly, the fact that Sr and Ba in K-feldspar and plagioclase increase from the Main Unit to the Evolved Units does not fit a regular fractionation process.

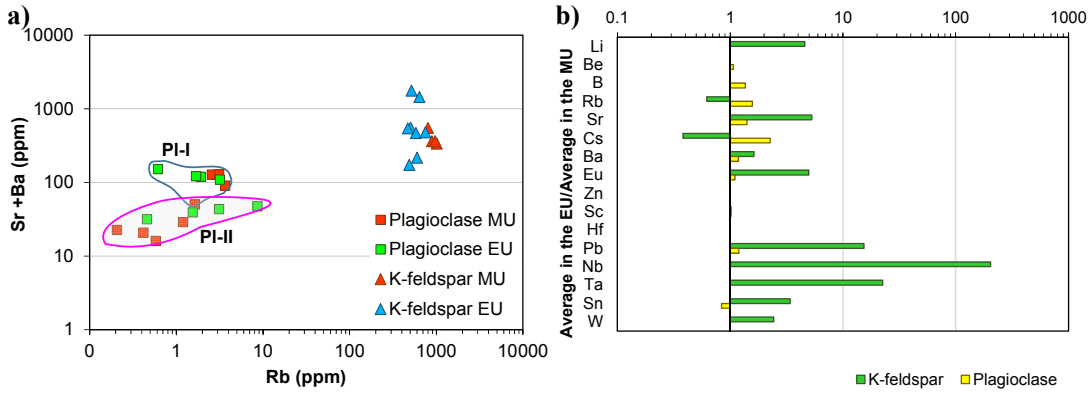

Fig. 3.6: a) Rb (ppm) vs. (Sr+Ba) compositional plot of feldspars from the Logrosán granite. **b)** Trace element relative enrichment and depletion from Main Unit to Evolved Units of feldspar from the Logrosán granite.

3.2.2. Micas

White mica from the Logrosán granite, either from the MU, or from the EU is compositionally muscovite (Table 3.3).

Table 3.3: Major (wt.%; EMPA) and trace (ppm; LA-ICP-MS) composition of representative muscovite from Logrosán.

	Main Unit (MU)						Evolved Units (EU)					
	111974	112470	112466	112463	111980	111975	111979	111979	111979	177	177	177
	19	**9**	**37**	**64**	**18**	**18**	**66**	**80**	**81**	**101**	**117**	**127**
SiO_2	45.1	43.2	45.4	46.3	44.1	46.2	46.0	46.3	46.3	44.8	45.3	45.2
TiO_2	0.94	0.05	0.67	0.04	0.51	0.38	0.27	0.00	0.04	0.03	0.40	0.64
Al_2O_3	34.3	30.2	35.6	36.3	34.7	29.8	34.5	33.8	36.2	35.1	33.9	34.0
FeO	1.15	9.24	1.07	1.33	0.85	3.27	1.75	1.88	0.99	1.30	1.43	1.29
MnO	0.02	0.10	0.05	0.03	0.00	0.00	0.01	0.01	0.00	0.00	0.02	0.05
MgO	0.69	1.65	0.60	0.15	0.54	2.16	0.91	0.70	0.25	0.73	0.93	0.80
CaO	0.00	0.05	0.00	0.03	0.00	0.00	0.00	0.00	0.00	0.02	0.00	0.01
Na_2O	0.48	0.20	0.85	0.25	0.70	0.29	0.75	0.41	0.47	0.83	0.75	0.56
K_2O	10.14	7.91	10.54	10.21	9.58	10.72	10.47	10.94	10.80	10.31	10.46	10.57
F	0.43	0.25	0.40	0.43	0.51	1.43	0.46	0.38	0.25	0.21	0.19	0.18
Cl	0.00	0.01	0.00	0.01	0.00	0.00	0.00	0.01	0.00	0.00	0.00	0.00
Total	93.2	92.8	95.2	95.0	91.6	94.2	95.1	94.4	95.3	93.3	93.4	93.3
Li_2O*	0.06	0.00	0.05	0.06	0.08	0.37	0.04	0.00	0.00	0.00	0.00	0.44
H_2O*	4.19	4.12	4.29	4.30	4.09	3.67	4.24	4.38	4.30	4.30	4.30	3.55
par	6.66	3.67	10.96	3.64	10.02	3.89	9.85	5.40	6.22	10.89	9.84	7.46
mus	93.3	96.3	89.0	96.4	90.0	96.1	90.1	94.6	93.8	89.1	90.2	92.5
Nº ions in formula on the basis of 22 oxygens												
Si	6.149	6.106	6.083	6.162	6.109	6.373	6.182	6.265	6.168	6.111	6.183	6.169
Al iv	1.851	1.894	1.917	1.838	1.891	1.627	1.818	1.735	1.832	1.889	1.817	1.831
Al vi	3.662	3.135	3.694	3.860	3.775	3.212	3.641	3.668	3.847	3.752	3.640	3.646
Ti	0.097	0.005	0.067	0.004	0.054	0.039	0.027	0.000	0.004	0.003	0.041	0.066
Fe	0.131	1.093	0.120	0.148	0.098	0.378	0.196	0.213	0.110	0.148	0.164	0.147
Mn	0.002	0.012	0.005	0.003	0.000	0.000	0.002	0.002	0.000	0.000	0.003	0.006
Mg	0.139	0.347	0.120	0.030	0.110	0.444	0.182	0.141	0.049	0.147	0.190	0.164
Li*	0.033	0.000	0.026	0.031	0.047	0.205	0.036	0.023	0.001	0.000	0.000	0.000
Ca	0.000	0.008	0.000	0.004	0.000	0.000	0.000	0.000	0.000	0.002	0.000	0.002
Na	0.126	0.054	0.221	0.066	0.188	0.076	0.196	0.108	0.122	0.219	0.199	0.148
K	1.764	1.426	1.799	1.735	1.692	1.885	1.795	1.890	1.835	1.794	1.821	1.841
OH*	3.813	3.888	3.831	3.819	3.775	3.376	3.806	3.835	3.894	3.910	3.917	3.921
F	0.187	0.110	0.168	0.180	0.225	0.624	0.193	0.162	0.106	0.090	0.082	0.078
Cl	0.000	0.002	0.000	0.001	0.000	0.000	0.001	0.003	0.000	0.000	0.001	0.001

	Main Unit (MU)						Evolved Units (EU)					
	P	**P**	**P**	**P**	**S**	**S**	**P**	**P**	**S**	**S**	**S**	**S**
	111978	111911	111911	111911	111978	111911	177	111979	177	177	111979	111979
Spot	17a05	17a14	17b07	17b09	17a10	17b10	17c14	17d10	17c16	17c17	17d15	17e06
Li	787	917	977	803	1020	3720	415	653	428	847	1100	511
Be	9.28	21.2	15.3	6.90	19.2	21.3	3.43	17.2	b.d.l.	3.10	15.1	6.01
B	61.1	62.6	65.5	49.8	107	33.6	142	73.7	103	73.2	111	26.8
MgO	0.71	0.93	0.94	0.85	0.86	3.75	0.73	0.79	0.86	2.64	1.48	0.83
Al_2O_3	36.7	37.4	37.7	35.9	34.3	29.3	36.4	36.1	35.7	34.3	28.1	37.3
SiO_2	45.5	45.8	46.2	45.3	45.3	46.2	44.8	45.7	45.7	46.0	46.3	46.5
Sc	15.8	12.1	12.3	12.6	12.8	20.8	13.1	10.9	85.5	66.6	13.2	25.2
TiO_2	0.39	0.19	0.12	0.60	0.22	0.70	0.04	0.17	0.82	1.59	0.19	0.82
V	13.7	7.07	6.45	8.01	4.59	99.0	0.77	5.69	172	215	8.76	23.9
Co	0.25	b.d.l.	0.39	0.55	b.d.l.	b.d.l.	b.d.l.	1.10	0.45	2.85	1.17	0.70
Zn	125	93.9	82.7	91.6	99.0	239	50.7	135	74.9	442	95.4	88.7
Rb	1750	927	936	1010	1200	1630	664	802	877	1150	926	870
Sr	0.53	1.29	1.74	1.24	1.01	0.56	2.32	2.01	1.84	1.55	1.99	1.37
Zr	1.23	0.94	0.80	1.02	0.24	b.d.l.	0.44	1.13	2.27	1.56	1.63	2.44
Nb	126	20.7	18.4	25.8	34.7	7.18	4.11	10.9	116	171	23.9	72.1
Sn	175	369	346	215	469	472	215	179	100	107	136	39.7
Cs	108	289	281	268	285	505	83.3	106	43.7	136	325	16.0
Ba	50	136	226	178	197	216	437	207	178	156	251	67.1
Hf	0.21	b.d.l.	b.d.l.	b.d.l.	b.d.l.	b.d.l.	b.d.l.	0.09	0.30	0.26	b.d.l.	0.27
Ta	24.5	2.80	2.10	6.89	6.57	0.31	0.47	1.88	12.0	22.0	2.86	5.76
W	45.6	69.0	57.8	47.9	61.5	58.4	54.3	10.4	128	94.1	17.0	39.0
Pb	1.30	2.32	2.59	1.65	2.19	1.92	2.03	1.94	2.06	2.28	2.46	1.80
U	b.d.l.	0.30	0.45	b.d.l.	0.20	b.d.l.	b.d.l.	0.18	0.25	0.19	1.03	b.d.l.

*LiO_2 calc. from Monier and Robert (1986).

P: primary muscovite; **S**: secondary muscovite.

Muscovite from the Logrosán granite has an average formula $K_{0.88}Na_{0.05}Fe_{0.11}Mg_{0.11}Ti_{0.01}Al_{2.66}Si_{3.12}O_{10}(OH_{1.85}F_{0.15})$, which differs from the ideal stoichiometry ($KAl_3Si_3O_{10}[OH]_2$). This is a typical feature of plutonic muscovite (Miller et al., 1981).

Muscovite from the Logrosán granite defines a trend from the muscovite end member to protolitholite (lithian syderophyllite) in the case of MU white mica, and to syderophyllite for the EU white mica (Fig. 3.7a). Due to the widespread alteration of the granite, it is expected that numerous muscovite crystals show secondary-looking and plot within the secondary muscovite field (Fig. 3.7b). The variations in FeO, Li_2O and F are positively correlated with MgO (Fig. 3.8). Higher contents in MgO, FeO, Li_2O, and F usually correspond with secondary-looking muscovite crystals. Fresh muscovite samples fit fundamentally the muscovite end member, while secondary-looking muscovite are enriched mainly in Li, Fe, Mg (and F), plotting close to the protolithonite and syderophyllite fields (Fig. 3.7a). In any case, most of the muscovite crystals do not reach high levels of Li. Li_2O attains up to 0.82 wt.% for the MU muscovite, and up to 0.52 wt.% for the EU muscovite. Igneous muscovite (taking an estimated value of < 1wt.% MgO) from the MU is richer in Li_2O, and F, and impoverished in Na_2O, when compared to muscovite from the EU (Fig. 3.8).

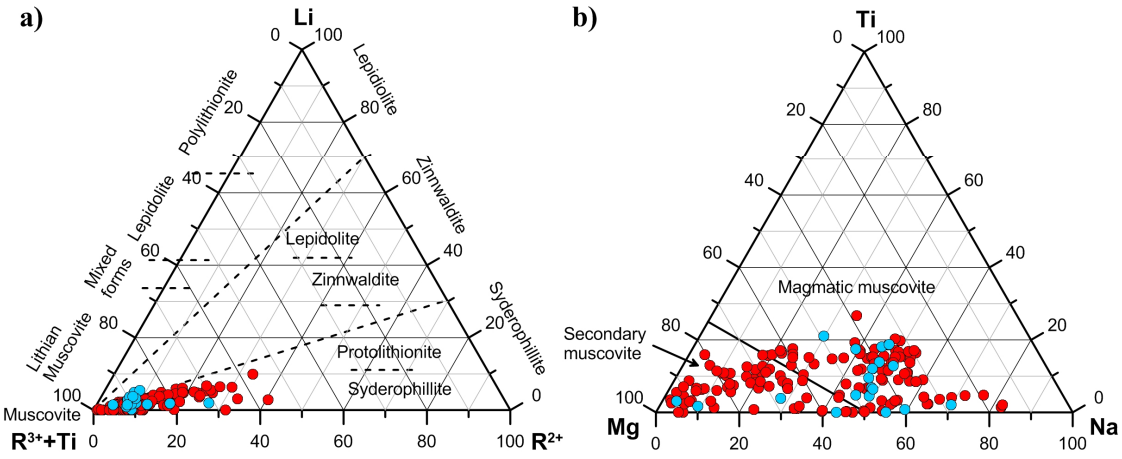

Fig. 3.7: a) Li–R^{2+}–R^{3+}+Ti diagram, according to the classification of Foster (1960) slightly modified by Rieder et al. (1999), with $R^{3+}=Al^{VI}$, $R^{2+}=(Fe_t^{2+}+Mn^{2+}+Mg)$. **b)** Mg–Ti–Na (atoms per 22O) diagram for muscovite. Magmatic and secondary muscovite fields are taken from Miller et al. (1981).

Trace elements have been analyzed in muscovite from the Logrosán granite. Primary muscovite from granitic samples have in general higher Li and Rb contents than secondary muscovite, no further discriminant chemical features are found (Table 3.3). Granitic muscovite has a good correlation in the Rb/Sr plot, showing a negative trend (Fig. 3.9a). Muscovite from the EU are richer in Sr and poorer in Rb than the MU muscovite. Lithium and tin correlates well, in general.

Muscovite with the higher Li contents has respectively higher Sn contents (Fig. 3.9b). Muscovite from the MU is richer in Sn (Fig. 3.9c), while EU muscovite shows higher contents in Nb, Ta and W (Fig. 3.9d, 4.13d and 4.13f). There is an anomalous data in the MU muscovite (17b10; Table 3.3), which corresponds to a Li-rich secondary muscovite narrow rim with a high Nb/Ta ratio and a low Al_2O_3 content.

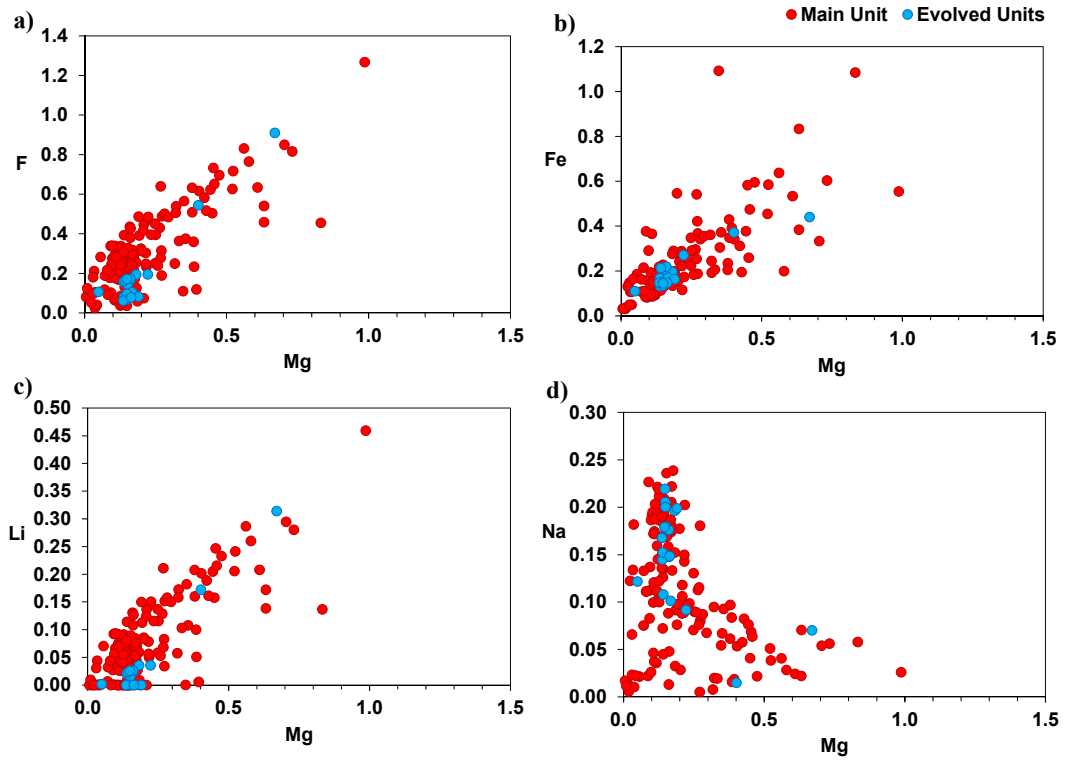

Fig. 3.8: Mg variation diagrams for muscovite from the Logrosán granite (apfu on the basis of 22 oxygens). **a)** Mg vs. Fe (apfu). **b)** Mg vs. F (apfu). **c)** Mg vs. Li (apfu). **d)** Mg vs. Na (apfu).

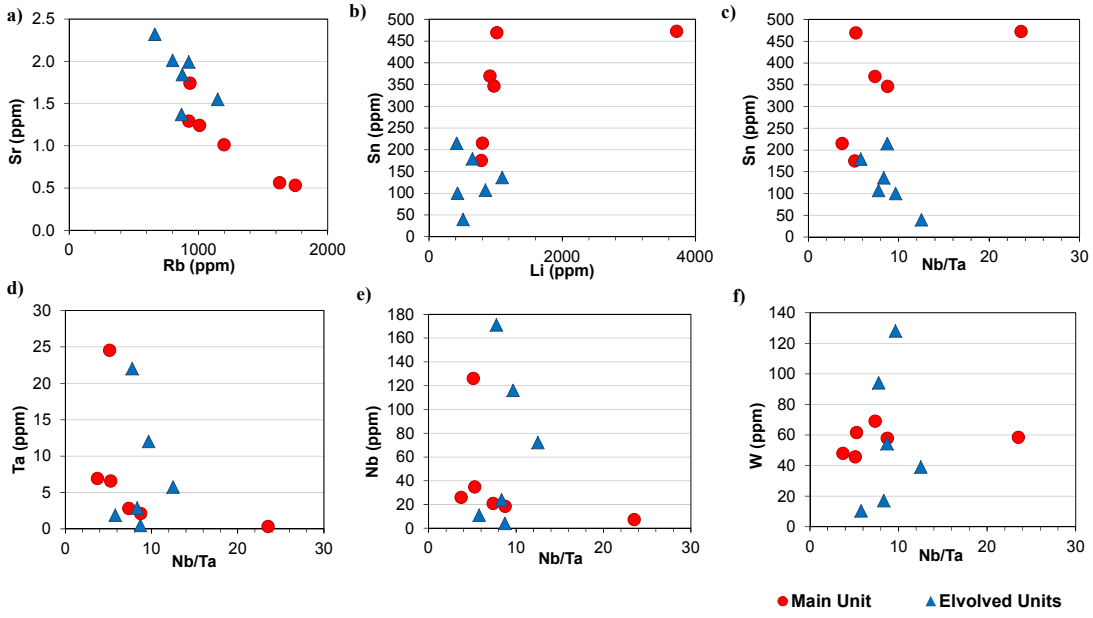

Fig. 3.9: Binary compositional diagrams of muscovite from the Logrosán granite. **a)** Rb vs. Sr. **b)** Li vs. Sn. **c)** Nb/Ta vs. Sn. **d)** Nb/Ta vs. Ta. **e)** Nb/Ta vs. Nb. **f)** Nb/Ta vs. W.

Biotite from the Logrosán granite is Al-rich (19.21-22.18 wt.% Al_2O_3) (Table 3.4), plotting in the aluminum-potassic family of magmatic biotite in the Mg vs. Al_{total} diagram by Nachit et al. (1985) (Fig. 3.10a). Biotite from other granitoids from the CIZ also plot in this field, such us biotite from the S-type SCS granites (Villaseca and Barbero, 1994), and biotite from the MTB granitoids (Merino, 2014). Biotite and muscovite coexistence in a granite is a good indicator of highly peraluminous composition.

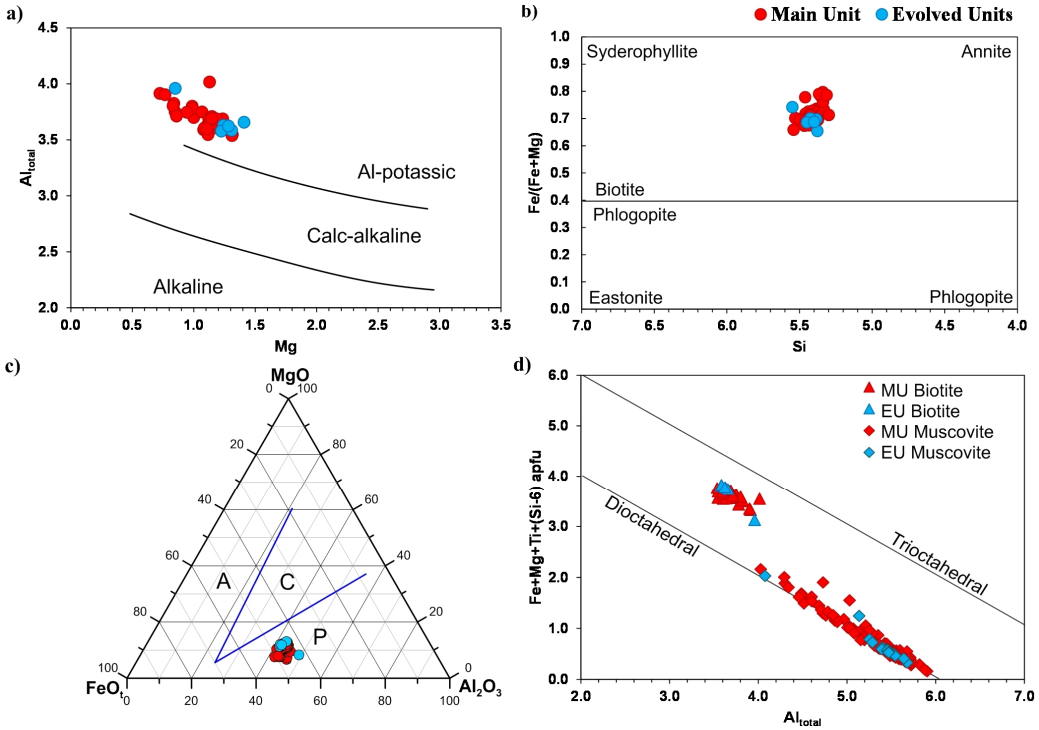

Fig. 3.10: a) Al_{total} vs. Mg (apfu, atoms per 22O) diagram for biotite. Compositional fields from different magmatic series are taken from Nachit et al. (1985). **b)** Classification of Logrosán biotite. Fields after Rieder et al. (1999) (apfu, atoms per 22O). **c)** Composition of biotite plotted in the FeO-MgO-Al_2O_3 (wt.%) diagram proposed by Abdel-Rahman (1994) to discrimine biotite from (A) anorogenic alkaline suites; (P) peraluminous suites, including S-type; (C) and orogenic calc-alkaline suites. **d)** Biotite and muscovite compositions in terms of octahedral-site occupancy (Conrad et al., 1988).

Accordingly to the mica classification of Rieder et al. (1999), the Logrosán biotite is close to the Fe-rich siderophyllite-annite end member with high Fe/(Fe+Mg) ratios between 0.654 and 0.797 (Fig. 3.10b). The EU biotite is depleted in Mg with respect to the MU biotite. The biotite composition depends on the nature of the magmas from which it crystallizes (Abdel-Rahman, 1994). Accordingly, the Logrosán biotite matches with the chemical characteristics of biotite from peraluminous suites in the triangular FeO–MgO–Al_2O_3 diagram (Fig. 3.10c). Biotite compositions deviate significantly from trioctahedral stoichiometry suggesting substantial octahedral site vacancies, which is related with low crystallization temperatures (Conrad et al., 1988) (Fig. 3.10d). On the contrary, muscovite follows the dioctahedral trend, which indicates that magmatic equilibrium crystallization between muscovite and the melt exists (Conrad et al., 1988).

Table 3.4: Major (wt.%; EMPA) and trace (ppm; LA-ICP-MS) composition of representative biotite from Logrosán. *LiO_2 calc. from Tindle and Webb (1990).

	Main Unit (MU)						**Evolved Units (EU)**					
	111974	**111975**	**112466**	**112470**	**112470**	**112476**	**11979**	**177**	**177**	**177**	**177**	**177**
	18	**28**	**41**	**24**	**30**	**78**	**78**	**87**	**91**	**106**	**112**	**123**
SiO_2	34.6	33.5	35.5	36.1	34.7	34.6	36.0	34.7	34.3	34.5	35.0	34.5
TiO_2	2.83	3.29	2.73	2.83	2.28	3.21	2.54	2.47	2.48	2.50	1.82	2.31
Al_2O_3	19.5	20.4	20.5	20.9	20.0	20.1	21.8	19.8	19.2	19.9	19.5	19.6
FeO	20.6	23.0	21.5	20.9	23.0	20.8	18.9	22.0	21.6	20.4	21.9	21.6
MnO	0.28	0.22	0.25	0.36	0.28	0.07	0.14	0.25	0.29	0.32	0.23	0.33
MgO	5.06	3.52	4.95	5.54	3.67	5.12	3.70	5.37	5.20	6.07	5.63	5.49
CaO	0.01	0.00	0.00	0.02	0.00	0.00	0.09	0.03	0.02	0.00	0.00	0.00
Na_2O	0.23	0.20	0.13	0.11	0.12	0.12	0.15	0.13	0.13	0.08	0.08	0.13
K_2O	8.62	9.14	9.37	9.35	9.00	9.48	7.73	9.31	9.38	9.36	9.47	9.43
F	0.00	1.23	0.91	0.77	0.49	0.99	0.70	0.50	0.61	0.50	0.48	0.90
Cl	0.94	0.03	0.02	0.02	0.02	0.03	0.04	0.03	0.04	0.03	0.01	0.03
Total	92.7	94.5	95.8	96.9	93.6	94.5	91.9	94.6	93.4	93.7	94.1	94.3
Li_2O*	0.38	0.07	0.64	0.80	0.41	0.37	0.79	0.40	0.30	0.35	0.48	0.34
H_2O*	3.56	3.19	3.50	3.64	3.58	3.38	3.55	3.62	3.50	3.60	3.61	3.39
Nº ions in formula on the basis of 22 oxygens												
Si	5.459	5.313	5.412	5.393	5.461	5.373	5.549	5.384	5.425	5.377	5.449	5.399
Al iv	2.541	2.687	2.588	2.607	2.539	2.627	2.451	2.616	2.575	2.623	2.551	2.601
Al vi	1.082	1.114	1.098	1.079	1.173	1.060	1.509	1.015	1.002	1.034	1.034	1.022
Ti	0.335	0.392	0.313	0.318	0.269	0.375	0.294	0.288	0.295	0.292	0.213	0.272
Fe	2.722	3.051	2.734	2.616	3.020	2.704	2.438	2.858	2.861	2.665	2.855	2.825
Mn	0.037	0.029	0.033	0.046	0.037	0.009	0.018	0.033	0.039	0.042	0.030	0.044
Mg	1.189	0.832	1.123	1.236	0.860	1.187	0.850	1.243	1.224	1.410	1.309	1.282
Li*	0.239	0.046	0.393	0.480	0.262	0.230	0.491	0.249	0.192	0.219	0.303	0.215
Ca	0.002	0.000	0.000	0.002	0.000	0.000	0.016	0.005	0.004	0.000	0.000	0.000
Na	0.071	0.062	0.039	0.031	0.037	0.036	0.046	0.038	0.039	0.025	0.024	0.039
K	1.734	1.846	1.822	1.784	1.806	1.879	1.518	1.845	1.890	1.860	1.883	1.885
OH*	3.749	3.375	3.556	3.629	3.753	3.505	3.648	3.745	3.686	3.747	3.758	3.547
F	0.000	0.618	0.440	0.365	0.241	0.486	0.342	0.246	0.303	0.246	0.239	0.445
Cl	0.251	0.007	0.005	0.006	0.006	0.009	0.011	0.009	0.011	0.007	0.004	0.008
Si	5.459	5.313	5.412	5.393	5.461	5.373	5.549	5.384	5.425	5.377	5.449	5.399

	Mean Unit		**Evolved Units**		
	111911	**111911**	**177**	**177**	**111979**
	jn17a13	**jn17b06**	**jn17c07**	**jn17c10**	**jn17d13**
Li	3710	3500	1870	1800	2580
Be	4.90	5.12	3.53	4.01	6.32
B	10.2	b.d.l.	b.d.l.	b.d.l.	b.d.l.
Sc	9.65	32.9	47.9	27.9	12.6
V	8.82	208	236	144	435
Co	4.93	15.1	7.04	27.10	14.6
Zn	1120	1400	1120	952	1640
Rb	1930	1130	1050	970	623
Sr	0.15	0.30	0.45	0.41	2.36
Y	b.d.l.	b.d.l.	0.10	0.50	0.13
Zr	0.25	1.01	1.54	15.6	0.89
Nb	58.1	107	114	76.9	36.9
Mo	b.d.l.	b.d.l.	b.d.l.	b.d.l.	0.48
Sn	274	133	81.6	65.7	110
Cs	3370	57.1	62.7	35.5	22.30
Ba	152	88.8	96.3	222	1770
Hf	b.d.l.	0.16	0.14	0.41	b.d.l.
Ta	17.9	7.52	8.01	4.46	1.10
W	11.1	2.86	3.14	2.98	0.41
Pb	1.62	2.59	2.57	2.22	1.99
Th	b.d.l.	0.10	b.d.l.	0.32	0.03
U	b.d.l.	0.47	0.11	1.18	0.86

Trace elements in biotite are included in Table 3.4. Biotite from the Logrosán granite has high contents in Rb (623–1930 ppm), Li (1800–3700 ppm), Sn (65.7–274 ppm), and Nb (36.9–114 ppm). The mineral chemistry of biotite from the Logrosán granite is similar to this found for biotite from similar granites or granitic units from the Krušné hory-Smrčiny batholith in the west Bohemian Massif, and the Cornubian batholith in England (Stone et al., 1997). High Rb and Li contents in Logrosán biotite are similar to them of the 2-mica monzogranite units from the Cornubian batholith. Tin content in biotite from Logrosán is more alike the Sn biotite content from the younger and more evolved Czech granites. Niobium is enriched over Ta and is highly enriched in the biotite from the highly fractionated Logrosán granite. This agrees well with the Nb enrichment in the residue during partial melting of crustal rocks (Stepanov and Hermann, 2013).

3.2.3. Tourmaline

Tourmaline is an accessory mineral within the Logrosán granite. Tourmaline from the granite shows small compositional variations (Table 3.5) for SiO_2 (35.52–36.42 wt.%), MnO (0.00 to 0.13 wt.%), CaO (0.01 to 0.16 wt.%) and Na_2O (1.43 to 2.52 wt.%) contents. While Al_2O_3 (31.04–35.05 wt.%), MgO (1.64–4.49 wt.%), TiO_2 (0.19–0.85 wt.%), and FeO_t (9.38–12.53 wt.%) contents are more heterogeneous. The K_2O contents are generally low (<0.08 wt.%). F contents vary from 0.15–0.65 wt.%. Moreover, Fe/(Fe+Mg) values in the tourmaline from the Logrosán granite vary from 0.55 to 0.81. The high Fe/(Fe+Mg) values are related to granite environments, more especially, to associated tin mineralization (Henry and Guidott, 1985; Pirajno and Smithies, 1992; Mlynarczyk and Williams-Jones, 2006). Tourmaline from pegmatites and from eary quartz-tourmaline veins have also been analyzed, showing a composition quite similar to this of the granite tourmaline, agreeing their magmatic origin (Table 3.5) (Roda-Robles et al., 2004; Roda-Robles et al., 2011).

The structural formulae of tourmaline were calculated by normalizing to 24.5 oxygens (Table 3.5). Lithium and boron were not analyzed by electron microprobe; boron is assumed to be 3 apfu; and lithium was calculated on stoichiometry. Fe^{2+} and Fe^{3+} values were calculated by assuming a charge balance between cations and anions. Even though a systematic error on Fe^{2+} and Fe^{3+} calculation may be introduced by the boron approach, the uncertainty introduced by the lithium approximation is negligible for schorl–dravite tourmaline series.

Studied tourmaline samples within the Logrosán granite, pegmatites, and early quartz-tourmaline veins belong to the alkali group and, occasionally, to the vacancy or alkali-free group (Fig. 3.11a), corresponding with the schorl and foitite end-members, respectively (Fig 4.11b).

Tourmaline plots generally on the Li-poor granitoids and their associated pegmatites and aplites field in the Al–Fe_t–Mg diagram and in the Ca–Fe_t–Mg diagram of Henry and Guidotti (1985) (Fig. 3.11c and d). Tourmaline from the granite plots occasionally on the metapelite or quartz-tourmaline fields, possibly related to the circulation and assimilation of metamorphic fluids within the granite. The deficiency of cations in position X corresponds with a percent range of 17−52 % in tourmaline from granite and pegmatite, while this range is slightly higher (27−58 %) for tourmaline from quartz-tourmaline veins. According to the vacancy percentage two groups can be recognized in zoned tourmaline from quartz-tourmaline veins (Fig. 3.11b). Variations from core to rim comprise a decrease in the vacancy percentage, FeO, Si_2O and Al_2O_3; and an increase in TiO_2, Na_2O MgO, FeO (due to Fe^{2+} rise), and F (Fig. 3.12).

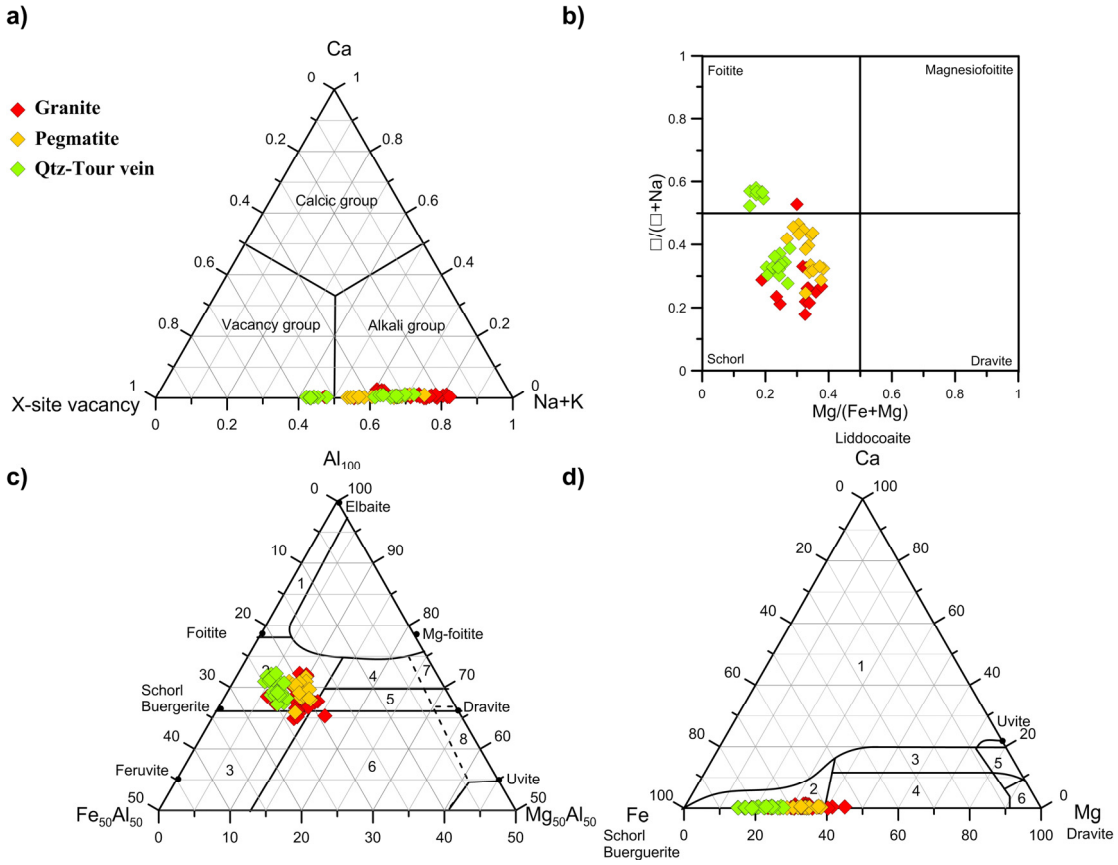

Fig. 3.11: a) X-site occupancy diagram for the tourmaline from the Logrosán granite (Hawthorne and Henry, 1999) **b)** Nomenclature diagram of tourmaline based on X-site vacancy/(X-site vacancy + Na) vs. Mg/(Mg + Fe) plot after Henry et al. (2003). **c)** Al–Fe–Mg ternary plot for tourmalines **d)** Granitic tourmaline analyses on Ca-Fe-Mg ternary diagram.
Labelled fields in c) and d) after Henry and Guidotti (1985): 1. Li-rich granitoid pegmatites and aplites; 2. Li-poor granitoids, pegmatites and aplites; 3. Fe^{3+}-rich quartz–tourmaline rocks (altered granitoids); 4. metapelites and metapsammites with Al-saturating phase, 5. metapelites and metapsammites lacking Al-saturating phase; 6. Fe^{3+}-rich quartz–tourmaline rock, calc-silicate rocks and metapelites; 7. low-Ca metaultramafic rocks and Cr-V-rich metasediments; 8. metacarbonates and metapyroxenites.

Table 3.5: Representative major (wt.%; EMPA) composition of tourmaline from the Logrosán granite.

	Granite									Pegmatite			Qtz-Tour veins		
Sample	**112463**			**112464**			**111978**			**L179**			**L108**		
Element	**55**	**56**	**78**	**44**	**48**	**45**	**166**	**170**	**177**	**72**	**78**	**89**	**100**	**104**	**111**
SiO_2	34.52	36.42	36.06	35.81	36.14	35.69	35.76	34.85	35.56	36.50	36.40	36.47	35.87	36.44	35.75
TiO_2	0.69	0.70	0.85	0.23	0.36	0.46	0.23	0.82	0.73	0.40	0.28	0.71	0.75	0.18	0.76
Al_2O_3	32.97	31.93	32.41	35.05	31.67	34.90	33.22	31.04	31.87	33.43	35.37	33.39	33.00	35.65	33.56
FeO	11.53	12.29	11.75	9.46	9.77	9.38	10.57	11.11	12.53	10.80	10.49	10.25	12.85	12.35	12.18
MgO	3.39	3.35	3.45	2.85	4.49	2.77	2.54	3.14	1.64	3.16	2.76	3.47	2.32	1.62	2.03
MnO	0.01	0.12	0.06	0.01	0.05	0.06	0.06	0.12	0.13	0.01	0.09	0.07	0.06	0.02	0.06
CaO	0.06	0.03	0.02	0.11	0.04	0.11	0.02	0.07	0.02	0.01	0.01	0.07	0.02	b.d.l.	0.06
Na_2O	2.45	2.41	2.52	1.86	2.44	1.94	1.43	2.16	2.13	2.07	1.74	2.20	2.09	1.37	1.96
K_2O	0.04	0.03	0.03	0.05	0.04	0.04	0.02	0.04	0.04	0.03	0.02	0.02	0.02	0.01	0.01
F	0.50	0.55	0.44	0.20	0.57	0.31	0.15	0.48	0.55	0.22	0.09	0.35	0.46	0.04	0.38
O=F,Cl	0.21	0.23	0.19	0.08	0.24	0.13	0.06	0.20	0.23	0.09	0.04	0.15	0.19	0.02	0.16
Total	85.96	87.60	87.42	85.54	85.33	85.53	83.94	83.62	84.96	86.52	87.22	86.85	87.23	87.67	86.57
Nº ions in formula on the basis of 24.5 oxygens															
B*	3	3	3	3	3	3	3	3	3	3	3	3	3	3	3
Si total	5.810	6.024	5.961	5.926	6.058	5.915	6.055	6.010	6.062	6.023	5.928	5.994	5.957	5.940	5.950
Al total	6.542	6.226	6.314	6.837	6.258	6.818	6.629	6.309	6.405	6.502	6.791	6.468	6.459	6.851	6.583
Al z	6.074	5.860	5.898	6.036	5.881	6.008	5.906	5.849	5.813	5.912	6.028	5.889	5.918	6.030	5.923
Ti z	0.088	0.087	0.106	0.028	0.046	0.058	0.030	0.106	0.094	0.050	0.034	0.088	0.093	0.023	0.095
Si z	-0.190	0.024	-0.039	-0.074	0.058	-0.085	0.055	0.010	0.062	0.023	-0.072	-0.006	-0.043	-0.060	-0.050
Al y	0.469	0.366	0.416	0.800	0.377	0.809	0.724	0.460	0.592	0.590	0.763	0.579	0.541	0.822	0.660
Fe	1.624	1.700	1.625	1.309	1.369	1.300	1.497	1.602	1.786	1.491	1.429	1.409	1.785	1.683	1.696
Mn	0.002	0.016	0.009	0.001	0.007	0.008	0.009	0.017	0.019	0.001	0.013	0.010	0.008	0.003	0.008
Mg	0.851	0.827	0.849	0.702	1.121	0.685	0.641	0.808	0.416	0.777	0.671	0.850	0.574	0.393	0.504
Li*	0.055	0.091	0.101	0.188	0.126	0.198	0.130	0.113	0.187	0.141	0.124	0.151	0.092	0.099	0.132
Y total	3.000	3.000	3.000	3.000	3.000	3.000	3.000	3.000	3.000	3.000	3.000	3.000	3.000	3.000	3.000
Ca	0.011	0.005	0.004	0.020	0.008	0.020	0.004	0.013	0.003	0.001	0.002	0.012	0.004	0.000	0.010
Na	0.800	0.774	0.808	0.597	0.792	0.623	0.468	0.722	0.703	0.661	0.549	0.702	0.672	0.432	0.632
K	0.009	0.006	0.007	0.011	0.009	0.007	0.004	0.009	0.010	0.006	0.004	0.003	0.005	0.003	0.001
X total	0.820	0.785	0.819	0.628	0.809	0.650	0.476	0.743	0.716	0.667	0.555	0.717	0.681	0.435	0.642
Vac X	0.180	0.215	0.181	0.372	0.191	0.350	0.524	0.257	0.284	0.333	0.445	0.283	0.319	0.565	0.358
OH*	3.732	3.712	3.769	3.898	3.698	3.839	3.919	3.739	3.705	3.884	3.952	3.818	3.760	3.977	3.801
F	0.268	0.288	0.231	0.102	0.302	0.161	0.081	0.261	0.295	0.116	0.048	0.182	0.240	0.023	0.199
Fe^{2+}	1.313	1.435	1.341	1.047	1.146	1.078	1.167	1.346	1.621	1.190	1.078	1.152	1.497	1.293	1.427
Fe^{3+}	0.311	0.265	0.284	0.261	0.223	0.222	0.330	0.256	0.165	0.301	0.351	0.257	0.288	0.390	0.269
Fe/(Fe+Mg)	0.656	0.673	0.657	0.651	0.550	0.655	0.700	0.665	0.811	0.658	0.680	0.624	0.757	0.811	0.771
Na/(Na+Ca)	0.987	0.994	0.995	0.967	0.990	0.969	0.992	0.983	0.995	0.998	0.996	0.984	0.994	1.000	0.985

* Calculated or estimated (see text)

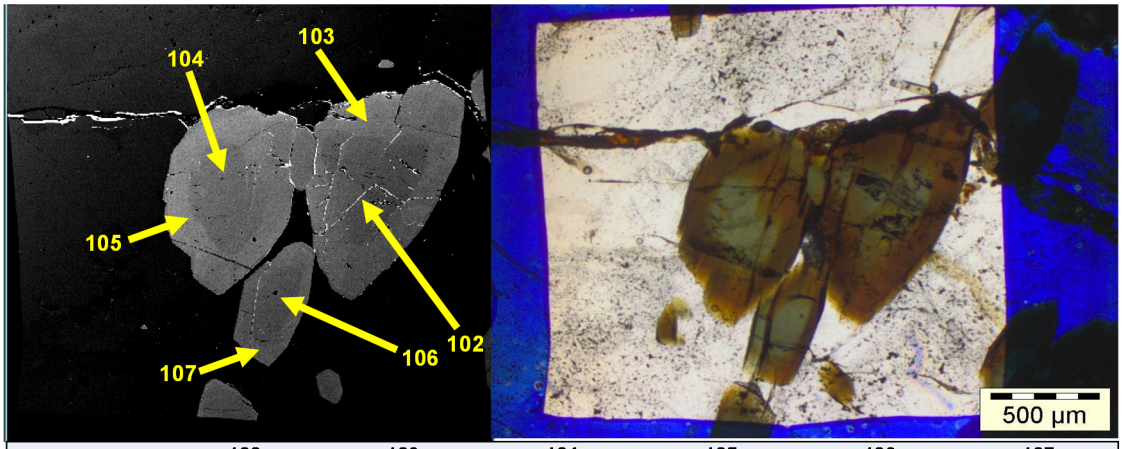

	102	103	104	105	106	107
SiO_2	37.03	35.71	36.44	36.09	36.88	36.15
TiO_2	0.177	0.617	0.184	0.744	0.116	0.666
Al_2O_3	34.75	33.21	35.65	33.82	35.42	33.66
FeO	12.18	11.77	12.35	12.15	12.62	12.28
MgO	1.406	2.130	1.618	2.266	1.453	2.179
Na_2O	1.379	2.109	1.366	2.053	1.326	2.076
F	0.071	0.374	0.044	0.307	0.071	0.296
Fe^{2+}	1.357	1.417	1.293	1.377	1.351	1.409
Fe^{3+}	0.314	0.232	0.390	0.297	0.366	0.286
VacX	55%	30%	57%	33%	58%	32%

Fig. 3.12: Zoned tourmaline of the late magmatic quart-tourmaline veins from the Logrosán granite, showing the composition from core to rim. Left: back-scattered image; Right: transmitted light.

The common substitution for the analyzed tourmaline is the alkali deficiency substitution (Fig. 3.13a), which indicates a main availability of water in the system according to Gallagher (1988). A certain degree of proton-loss substitution is also recognized, suggesting that the tourmaline crystallization process was buffered by both, alkalis and H_2O. In addition, tourmaline from the Logrosán granite defines a preferential trend following the schorl ↔ dravite vector in the Mg-Fe diagram; the trend toward the alkali-deficient tourmaline is also recognized (Fig. 3.13b).

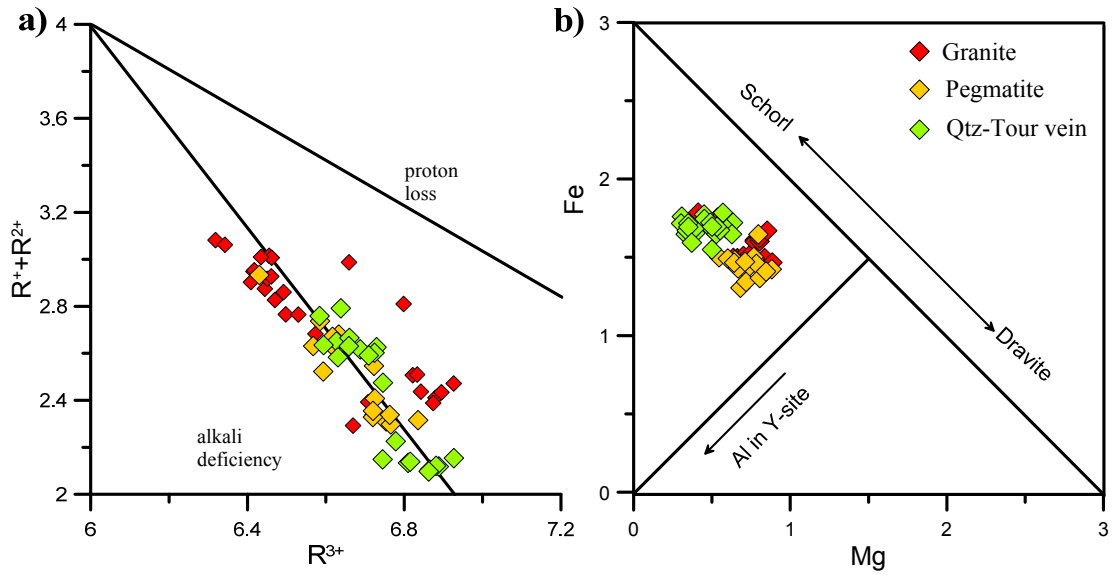

Fig. 3.13: a) R^{3+} (Al + 4/3 Ti) vs. $R^{+}+R^{2+}$ (Na + 2Ca + K + Mg + Mn) for granitic tourmalines. Substitution trends from Gallagher (1988). **b)** Mg vs. Fe diagram for tourmaline from the Logrosán granite. Mg^{2+} ↔ Fe^{2+} vector after Burt (1989).

Table 3.6: Representative trace (ppm; LA-ICP-MS) composition of tourmaline from the Logrosán granite. (MgO, Al_2O_3, SiO_2 and TiO_2 in wt.%)

	Granite	**Pegmatite**									**Qtz-Tour veins**											
	111978	**L179**									**L108**											
Spot	**17a12**	**18b09**	**18b10**	**18b11**	**18b12**	**18b13**	**18b14**	**18b15**	**18b16**	**18b17**	**18a12**	**18a13**	**18a14**	**18a15**	**18a16**	**18a17**	**18b03**	**18b04**	**18b05**	**18b06**	**18b07**	**18b08**
	-	**C**	**R**	**R**	**C**	**C**	**R**	**R**	**C**	**R**	**C**	**C**	**R**	**R**	**C**	**R**	**C**	**R**	**C**	**R**	**C**	**R**
Li	148	127	170	110	45.2	44.4	97.3	105	43.7	163	121	41.5	193	182	174	150	41.7	278	39.8	184	42.7	281
Be	4.56	4.30	b.d.l.	21.50	2.28	3.36	20.9	35.6	3.69	b.d.l.	5.96	b.d.l.	4.53	5.38	3.19	5.05	b.d.l.	5.58	3.30	3.73	3.53	5.98
B	20200	21400	22400	21800	22700	22300	21600	22100	21500	21600	24400	22700	23400	22900	22600	21800	20900	20000	21400	21400	21300	21000
MgO	2.66	3.92	3.31	2.72	2.52	2.62	2.66	3.10	3.07	3.16	1.66	1.19	1.95	2.60	2.22	2.52	1.56	2.20	1.53	2.26	1.61	2.21
Al_2O_3	33.1	36.8	36.0	35.9	36.5	35.4	35.2	36.4	35.8	35.1	36.5	35.0	34.6	33.7	34.4	34.6	37.7	34.7	36.7	34.6	36.9	35.8
SiO_2	35.6	36.5	36.6	36.4	36.7	36.7	36.5	36.8	36.3	36.5	36.6	35.6	35.7	35.6	35.9	37	36.4	35.9	37	35.7	36.8	35.8
Sc	11.2	35.1	11.4	22.9	34.6	39.1	22.9	25.7	50.2	11.8	9.60	11.3	8.75	7.60	8.34	8.59	8.34	7.98	8.50	8.35	9.62	7.83
TiO_2	0.75	1.00	0.46	0.29	0.26	0.28	0.26	0.27	0.32	0.52	0.35	0.18	0.60	0.86	0.71	0.64	0.17	0.97	0.16	0.89	0.17	1.03
V	16.8	44.8	24.6	38.6	45.1	25.7	18.6	23.4	31.5	31.4	30.9	28.4	35.0	16.8	31.0	35.6	24.7	30.6	24.5	25.3	29.9	27.7
Co	b.d.l.	0.73	1.08	2.03	2.14	0.62	0.78	0.59	0.59	1.51	2.51	2.88	b.d.l.	4.20	3.67	1.76	3.03	3.81	3.07	4.08	5.69	3.93
Zn	1110	856	850	798	799	728	719	767	791	878	855	768	923	1130	995	1030	800	1090	741	984	805	938
Sr	12.6	11.3	6.92	4.91	3.61	3.38	4.50	5.17	4.42	8.09	6.72	3.76	13.3	16.7	14.6	7.41	3.72	13.6	3.69	17.1	3.34	14.9
Zr	b.d.l.	b.d.l.	b.d.l.	b.d.l.	0.37	1.33	3.07	0.65	0.67	4.66	b.d.l.	b.d.l.	b.d.l.	b.d.l.	b.d.l.	b.d.l.	b.d.l.	b.d.l.	b.d.l.	b.d.l.	b.d.l.	b.d.l.
Nb	2.47	0.69	0.17	0.71	0.29	0.46	1.17	1.53	1.02	0.25	b.d.l.	0.42	1.27	0.56	0.95	0.40	0.18	0.73	0.20	0.82	0.16	0.56
Sn	124	182	64.4	109	138	291	180	154	323	65.2	17.4	41.7	51.4	25.0	38.4	24.1	13.9	35.8	14.3	41.8	13.2	29.0
Ta	4.30	1.84	0.16	1.12	2.25	4.10	2.40	2.85	7.61	0.13	b.d.l.	0.87	0.51	0.27	0.28	0.19	0.23	0.45	0.19	0.35	0.12	0.32
Pb	3.87	3.35	1.92	1.22	0.75	0.98	1.24	1.19	0.99	2.40	b.d.l.	0.43	2.01	2.51	2.11	1.22	b.d.l.	1.95	b.d.l.	2.67	0.39	2.22

C: core; **R**: rim

Trace element chemistry in tourmaline has been analyzed predominantly on zoned tourmaline from pegmatites, and late-magmatic quartz-tourmaline veins (Table 3.6). A concentric zonation develops from green cores to brown rims (Fig. 3.12). Zonation is more observable in tourmaline from veins than in tourmaline from pegmatites. Tourmaline is enriched in Li in cores, being higher in rims from quartz-tourmaline veins. Beryllium is generally low, except for some tourmaline rims from pegmatites. Zn and MgO display a positive correlation trend, with higher Zn contents toward rims, especially in tourmaline from veins. Tin displays no variation in tourmaline from veins and, although Sn contents are much higher in pegmatitic tourmalines, it decreases from cores to rims. Scandium behaves similarly to Sn. This Sc evolution is contrary to that found in some pegmatite-granite association from nearby areas (Roda-Robles et al., 2012). Strontium has a positive correlation with MgO, being enriched in rims (Fig. 3.14).

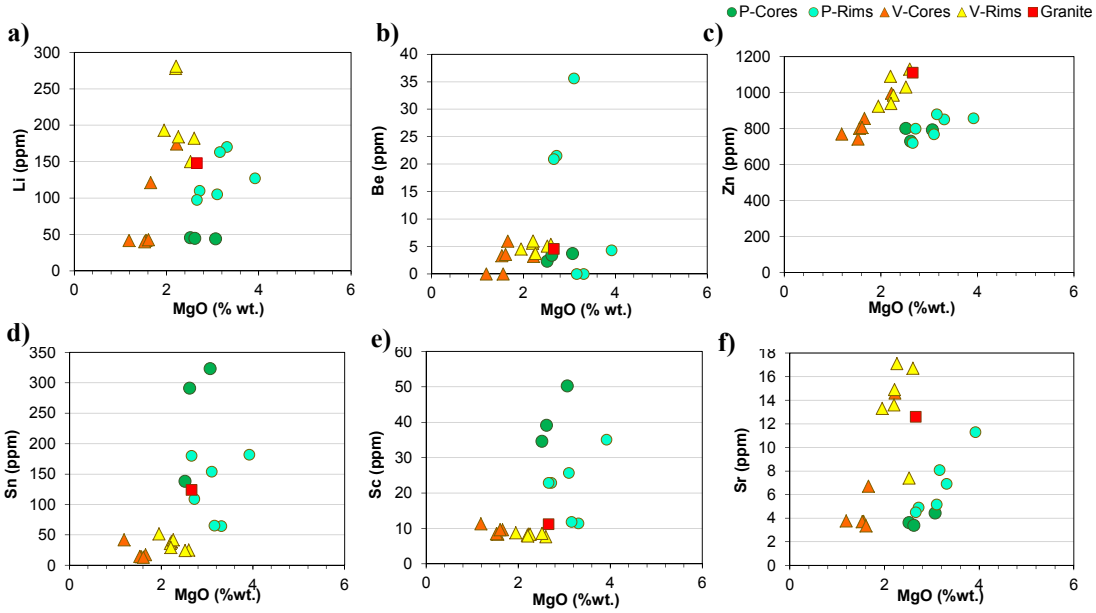

Fig. 3.14: Chemical variation diagrams of tourmalines from pegmatite (P), veins (V) and granite. **a)** MgO vs. Li. **b)** MgO vs. Be. **c)** Mg.O vs. Zn. **d)** Mg.O vs. Sn. **e)** MgO vs. Sc. **f)** Mg.O vs. Sr.

3.2.4. Zircon

The trace element composition of zircon from the Logrosán granite is summarized in Table 3.7. The magmatic or inherited (xenolithic) condition is indicated in the Table 3.7. In general, euhedral elongated bipyramidal primatic crystals are generally magmatic Variscan-age zircons, while inherited zircons are mainly stubby.

Logrosán zircon shows relatively high REE (647-2435 ppm), Nb (1.17-5.24 ppm), Ta (0.31-3.92 ppm), Sc (157-939 ppm) and Hf (7631-11800 ppm) contents, characteristic of zircon from granitoid rocks (Hoskin and Schaltegger, 2003; Belousova et al., 2002). Zircon REE abundances normalized to chondrite values (McDonough and Sun, 1995) show steeply-rising slopes from

the LREE to the HREE, and negative Eu anomalies (Eu/Eu*<0.3). Variscan-age zircon is generally richer in Hf than inherited zircon (Fig. 3.15). This is in agreement with the fact that the abundance of Hf in igneous zircon is considered as a marker of the magma differentiation degree (Hoskin and Schaltegger, 2003). Hf correlates positively with P, Y, Th, U, Nb, Ta, HREE and LREE, whilst it shows a negative correlation with Zr/Hf (Fig. 3.15). The positive correlation of P, Y and HREE with Hf reveals that "xenotime" substitution mechanism is the dominant substitution in the Logrosán zircon (Speer, 1982). Experiments on Zr/Hf fractionation in zircon-crystallizing melts unravel a decrease of the Zr/Hf ratio of the residual melt related to an increase of the abundance of HfO_2 in zircon for fractional crystallization of peraluminous granitic melts (Linnen and Keppler, 2002). Then, the decrease in Zr/Hf with increasing Hf observed in the Logrosán zircon can be explained by crystal fractionation. Likewise, the behavior of incompatible elements, such as Th, U, Nb and Ta, which increase correlatively with Hf in zircon, denotes an enrichment of these elements in the melt as the magma evolves.

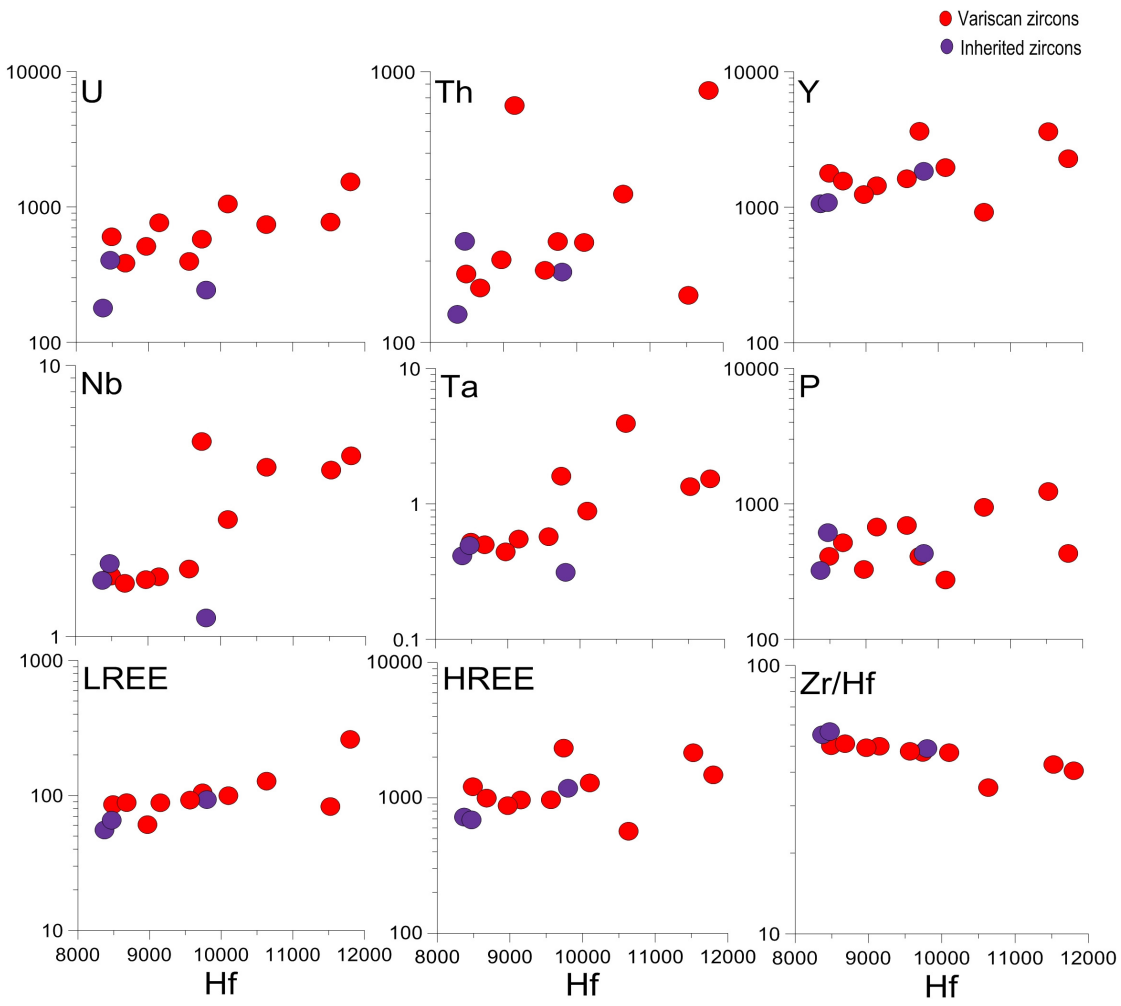

Fig. 3.15: Selected trace elements plotted versus Hf content (ppm) of Variscan-age and inherited zircons from the Logrosán granite.

Table 3.7: LA-ICP-MS trace element composition and REE (ppm) of zircons from the Logrosán granite.

Sample	L30-27	L24-17	L24-1	L24-20	L30-30	L24-19	L24-16	L24-6	L24-20	L30-31	L24-10	L24-9	L30-28	L24-12
Age*	V	V	V	V	V	V	V	V	V	V	V	O-I	PO-I	PO-I
P	409	274	516	409	430	674	328	1233	692	613	585	322	430	942
Sc	244	392	222	556	381	157	323	939	564	625	627	157	253	580
Ti	19.78	18.40	22.84	7.37	12.65	11.21	21.04	5.89	19.14	61.60	12.34	56.71	22.96	15.70
Y	1780	1960	1560	3630	2280	1440	1240	3612	1622	1082	934	1060	1840	917
Nb	1.67	2.70	1.57	5.24	4.64	1.66	1.62	4.11	1.77	1.86	1.75	1.61	1.17	4.21
Ta	0.52	0.88	0.50	1.60	1.53	0.55	0.44	1.34	0.57	0.49	0.46	0.41	0.31	3.92
Hf	8490	10100	8680	9740	11800	9150	8970	11524	9565	10633	7631	8370	9800	8471
Pb	6.54	8.47	4.53	6.37	39.50	21.50	5.94	5.30	5.64	8.32	5.08	4.07	5.30	15.72
Th	179	234	159	236	852	750	202	149	185	236	148	127	182	353
U	601	1050	384	577	1530	763	511	772	395	403	568	179	243	740
La	0.24	1.07	0.11	b.d.l.	2.21	b.d.l	b.d.l	0.513	0.224	0.25	0.39	0.303	b.d.l	2.37
Ce	4.41	9.28	4.53	5.18	33.6	7.12	3.06	5.18	4.79	3.70	4.21	3.46	2.61	19.9
Pr	0.51	1.44	0.65	0.22	8.37	0.59	0.32	0.39	0.77	0.60	0.68	0.43	0.49	4.68
Nd	7.22	11.7	9.79	3.81	68.1	9.26	5.74	4.36	11.1	7.6	7.24	6.26	8.27	33.4
Sm	14.7	16.0	15.6	12.0	46.3	15.1	11.3	9.83	15.6	11.8	8.92	9.21	15.8	21.8
Eu	0.45	1.07	0.74	0.83	2.03	0.43	0.39	0.62	0.77	0.34	0.40	0.55	0.55	1.19
Gd	58.20	59.10	57.10	82.60	99.60	55.80	40.00	61.93	59.12	41.23	33.21	35.30	65.50	44.28
Tb	18.60	19.80	17.30	29.90	27.50	15.80	12.20	23.48	16.34	11.17	9.32	10.40	18.80	11.66
Dy	206	209	179	366	262	163	128	312	180	117	98.2	114	197	108
Ho	65.8	68.1	54.6	127	78.8	53.2	42.7	113	55.65	37.58	31.61	37.6	65.3	30.9
Er	260	284	229	549	319	218	186	505	222	156	130	161	277	119
Tm	55.10	58.30	45.00	110.0	66.20	44.60	40.50	104	43.72	31.43	26.91	33.10	54.60	25.31
Yb	531	568	413	1000	626	412	406	935	390	286	254	315	485	236
Lu	72.00	82.00	58.30	148	100	58.50	60.90	160	60.49	49.18	41.88	50.50	79.60	36.53
LREE	85.72	99.66	88.53	104.6	260.2	88.30	60.82	82.82	92.37	65.56	55.05	55.52	93.22	127.6
HREE	1209	1289	996	2330	1480	965	876	2154	968	688	592	722	1177	567
Zr/Hf	50.19	47.32	51.11	47.39	40.53	49.98	49.35	42.74	47.86	45.18	55.40	55.16	49.06	44.01
T (ºC)**	872	863	889	766	821	808	879	744	868	1024	818	1012	890	845

* V Variscan-age zircon, PO-I pre-Ordovician inheritance, O-I Ordovician inheritance.
** Temperatures estimated using the Ti-in-zircon geothermometer recalibrated by Ferry and Watson (2007). Temperatures uncertainty for each data is ±4.5%.

3.2.5. Apatite

Apatite is a widespread accessory phase in igneous rocks and may incorporate significant amounts of trace elements, Sr, Th, U and rare earth elements (REE) (e.g., Belousova et al., 2002; Rønsbo, 2008; Chu et al., 2009). Major and trace element compositions of selected apatite from the Logrosán granite are summarized in Table 3.8. There are no significant differences in major element compositions between MU and EU apatites.

Table 3.8: Major (wt.%; EMPA) and trace-element (ppm; LA-ICP-MS) composition of representative apatite from the Logrosán granite.

	Main Unit								**Evolved Units**	
Sample	**112476**				**111911**		**112469**		**111979**	
	1	**10**	**19**	**24**	**41**	**36**	**62**	**64**	**29**	**31**
P_2O_5	41.30	41.81	42.26	42.30	42.00	42.40	42.06	42.20	42.16	43.32
SiO_2	0.02	b.d.l.	0.03	0.02	0.00	b.d.l.	0.04	0.01	0.02	0.00
FeO	0.05	0.17	0.59	0.68	0.63	0.93	0.26	0.71	0.95	0.92
MnO	0.38	0.45	1.11	1.30	0.74	1.25	0.49	1.17	0.59	0.75
MgO	b.d.l.	b.d.l.	b.d.l.	0.02	0.01	0.02	b.d.l.	b.d.l.	0.01	b.d.l.
CaO	55.79	55.47	54.01	53.24	54.06	52.48	54.47	53.29	54.09	54.11
Na_2O	0.01	b.d.l.	b.d.l.	b.d.l.	b.d.l.	0.02	0.01	0.03	0.07	0.02
SrO	0.13	0.04	0.06	0.16	0.12	0.10	0.11	0.13	0.09	0.12
F	3.55	3.37	3.38	3.46	3.80	3.76	3.58	3.45	3.43	3.23
Cl	0.01	b.d.l.	0.01	b.d.l.	0.01	0.01	0.01	b.d.l.	b.d.l.	b.d.l.
Sum	101.2	101.3	101.4	101.2	101.4	b.d.l.	101.0	101.0	101.4	102.5
H_2O*	0.08	0.18	0.18	0.14	0.00	0.00	0.08	0.14	0.16	0.28
O=F,Cl	1.50	1.42	1.43	1.46	1.60	1.58	1.51	1.45	1.44	1.36
Total	99.82	100.1	100.2	99.85	99.77	99.37	99.59	99.68	100.1	101.4
Nº ions on the basis of 25 oxygens										
P	5.919	5.960	6.010	6.033	6.004	6.068	6.009	6.030	6.003	6.065
Si	0.004	0.000	0.005	0.003	0.001	0.000	0.007	0.002	0.003	0.000
Fe	0.007	0.024	0.082	0.096	0.089	0.131	0.037	0.101	0.134	0.128
Mn	0.054	0.064	0.157	0.185	0.105	0.180	0.069	0.167	0.084	0.105
Mg	0.000	0.000	0.000	0.004	0.003	0.004	0.000	0.000	0.003	0.000
Ca	10.12	10.01	9.720	9.611	9.780	9.504	9.847	9.637	9.746	9.589
Na	0.004	0.000	0.000	0.000	0.000	0.006	0.002	0.011	0.023	0.005
Sr	0.012	0.004	0.006	0.016	0.012	0.010	0.011	0.013	0.008	0.011
OH*	0.095	0.206	0.202	0.157	0.000	0.000	0.089	0.157	0.178	0.311
F	1.902	1.794	1.795	1.843	2.029	2.007	1.909	1.843	1.822	1.689
Cl	0.004	0.000	0.003	0.000	0.002	0.001	0.003	0.000	0.000	0.000
Be	b.d.l.	0.25	1.70	b.d.l.	1.30	b.d.l.	1	b.d.l.	b.d.l.	b.d.l.
B	7.04	8.02	30.10	b.d.l.	1.87	1.91	6.18	5.93	42.60	5.04
Sc	b.d.l.	1.46	6.20	1.68	636	2.98	0.85	0.93	24.00	1.63
Sr	375	249	247	1032	15.05	430	437	607	178	169
Y	56.20	510	40.90	14.59	b.d.l.	23.60	74.60	19.33	66.00	82.20
Zr	0.28	4.40	7.60	0.10	b.d.l.	b.d.l.	b.d.l.	b.d.l.	267	2.90
Nb	b.d.l.	0	b.d.l.	b.d.l.	163	b.d.l.	0.11	b.d.l.	2.50	b.d.l.
La	142	149	89.5	113	289	193	352	423	125	272
Ce	288	389	170	199	32.20	358	676	631	251	519
Pr	32.8	53.3	17.4	19.1	100	39.9	71.9	55.8	27.2	53.5
Nd	117	218	62.3	66.4	17.50	136	258	180	108	182
Sm	25.8	75.0	14.6	11.8	26.7	25.2	44.10	20.6	30.8	35.5
Eu	18.1	23.1	14.7	20.9	11.3	30.7	48.1	38.0	15.7	34.0
Gd	18.8	86.0	9.60	7.39	1.21	15.0	26.4	10.4	16.8	25.3
Tb	2.54	15.6	1.59	0.8	4.87	1.39	2.93	0.98	3.50	3.25
Dy	11.7	96.0	7.90	3.32	0.57	5.18	14.0	4.54	16.8	15.1
Ho	1.74	16.0	1.05	0.47	1.06	0.70	2.14	0.63	2.60	2.02
Er	3.68	41.0	2.83	1.01	0.10	1.67	5.78	1.40	6.80	4.62
Tm	0.60	5.70	0.41	0.12	0.53	0.27	0.90	0.19	0.95	0.62
Yb	4.26	34.60	3.55	0.92	0.07	2.25	7.00	1.43	5.00	4.67
Lu	0.52	3.71	0.37	0.12	b.d.l.	b.d.l.	0.94	0.19	0.35	0.60
Hf	0.01	0.10	0.21	b.d.l.	b.d.l.	b.d.l.	b.d.l.	b.d.l.	5.70	0.08
Ta	b.d.l.	0.09	0.00	b.d.l.	36	b.d.l.	0.02	b.d.l.	0.12	b.d.l.
Pb	34.9	27.3	45.9	50.4	49.5	24.9	27.6	29.2	25.7	43.0
Th	19.8	10.1	9.6	25.8	64.0	25.3	40.9	28.4	8.7	22.3
U	56.6	50.0	44.8	71.2	b.d.l.	125	34.9	75.3	36.7	164

The magmatic apatite from the Logrosán granite is fluorapatite (3.06-4.94 wt.% F). High F and low Cl contents are characteristic of apatite from S-type granites (Sha and Chappell, 1999). Major constituents of apatite, CaO and P_2O_5, show little variation. Values range from 49.9 to 55.8 wt.% CaO, and 40.5 to 43.8 wt.% P_2O_5; Na_2O and MgO contents are extremely low and mostly below the detection limit. FeO and MnO values are relatively high (average value of 0.59 wt.% FeO and 1.0 wt.% MnO). Nevertheless, the apatite FeO and MnO contents are lower than in the highly fractionated Belvís granite, where apatite reaches contents up to 4.0 and 4.2 wt.%, respectively (Merino, 2014). Sr contents vary noticeably from 15.1 to 1032 ppm. Total REE contents range from 698 to 5765 ppm. Thorium and U contents show variable amounts Th: 2.61-126 ppm, and U: 18.2 to 164 ppm.

Chondrite-normalized REE patterns of representative apatite are shown in Fig. 3.16. The Logrosán magmatic apatite displays relatively LREE enriched patterns. The magmatic apatite has certain degree of REE fractionation with $(Ce/Yb)_n$ values always above 1 (1.3−115.9). The chondrite-normalized REE patterns of magmatic Logrosán apatite generally have marked positive Eu/Eu* anomalies. However, apatite from the MU occasionally shows prominent negative Eu/Eu* anomalies, similar to those found for the whole-rock granite. Magmatic apatite with positive Eu anomalies is uncommon in granites but has been also found in other leucogranites from the nearby Montes de Toledo batholith (Merino, 2014).

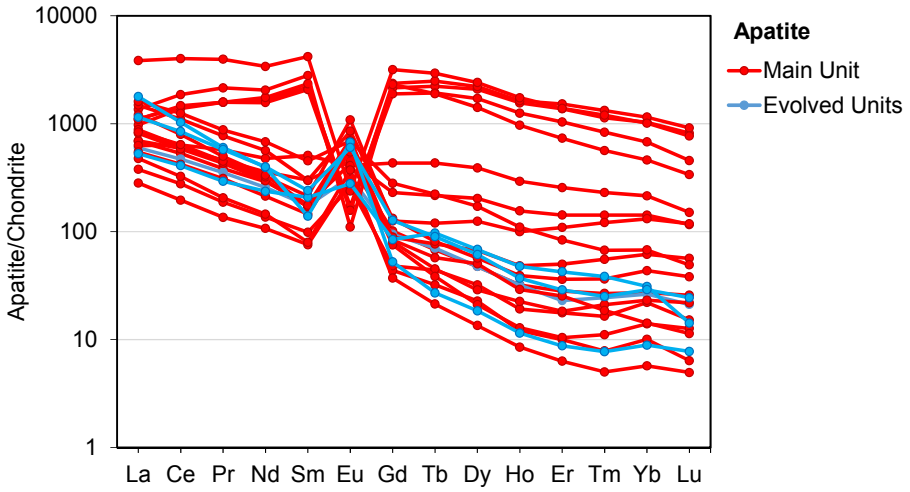

Fig. 3.16: Chondrite-normalized REE patterns of magmatic apatite from the Logrosán granite. Normalizing values from McDonough and Sun (1995).

3.2.6. Monazite

Monazite is an accessory mineral in the Logrosán granite. It occurs as isometric light greenish crystals, usually smaller than 100 µm. The monazite crystals are fairly homogenous in BSE

images, showing no zonation pattern or aureoles. Representative electron microprobe analyses of monazite separates from the Logrosán granite are summarized in Table 3.9. Monazite may be classified as (Ce) monazite, since Ce is generally higher than (La, Nd).

Monazite chemistry from the Logrosán granite displays variable UO_2 and ThO_2 contents (0.32−3.95 wt.% UO_2; and 4.21−12.59 wt.%ThO_2). Yttrium reaches relatively high values (0.29−2.12 wt.%). Monazite is highly enriched in LREE (average of 55.08 wt.%) with respect to HREE (average of 3.29 wt.%). Since there is a strong correlation between $(Th^* + U)^{4+}$ and Ca^{2+} (Fig. 3.17a), it is suggested the involvement of a cheralite substitution mechanism: $(Th,U)^{4+} + Ca^{2+} = 2(Y, REE)^{3+}$. This type of substitution mechanism is typical of S-type granites (Förster, 1998a, 1998b; Broska and Petrík, 2008; Hoshino et al., 2010). LREE and (HREE + Y) have a good positive correlation accordingly to the UO_2 contents (Fig. 3.17b). Ca and LREE display a good negative correlation independently of the uranium content (Fig. 3.17c). However, correlations between Ca and Th* with LREE and (HREE+Y) are dependent of the UO_2 content (Fig. 3.17d, 3.17e and 3.17f). Uranium displays a weak correlation with the LREE, and negative correlations with the (HREE + Y) (Fig. 3.17g, 3.17h). This may indicate that the role of the U for the cheralite substitution is minor. As proposed for monazite from the perphosphorous Belvís de Monroy pluton by Pérez-Soba et al. (2014), the cheralite substitution favors the entrance of Ca and Th, and this substitution is charge-compensated on the basis of the uranium content.

Table 3.9: Major composition (wt.%; EMPA) of monazite from the Logrosán granite.

Sample	**111911/111912**										
Element	**1**	**2**	**3**	**4**	**5**	**6**	**7**	**8**	**10**	**11**	**12**
P_2O_5	30.19	30.65	30.15	30.76	31.18	29.01	30.14	30.23	29.43	29.55	30.16
SiO_2	b.d.l.	0.12	0.09	0.02	0.14	0.12	0.19	0.15	0.22	0.13	0.14
UO_2	3.95	0.89	0.46	3.46	0.40	0.39	0.70	0.68	0.32	1.06	0.78
ThO_2	8.88	4.38	4.21	6.65	5.10	8.91	9.13	12.59	4.25	8.27	9.69
Y_2O_3	1.46	1.19	0.38	2.12	0.40	0.45	0.83	0.29	0.47	1.95	0.49
La_2O_3	10.50	14.25	11.83	11.67	13.10	12.63	11.60	10.30	12.37	11.14	11.26
Ce_2O_3	24.68	28.55	27.73	25.18	28.66	27.58	27.12	25.92	28.88	25.41	26.52
Pr_2O_3	1.54	1.65	1.84	1.47	1.77	1.70	1.79	1.77	1.58	1.76	1.68
Nd_2O_3	11.50	12.37	16.07	10.98	14.09	13.02	13.00	13.12	13.97	13.27	12.27
Sm_2O_3	1.65	1.38	2.30	1.51	1.49	1.09	1.23	1.19	1.60	1.70	1.63
Eu_2O_3	n.d.	n.d.	n.d.	n.d.	n.d.	n.d.	n.d.	n.d.	n.d.	n.d.	n.d.
Gd_2O_3	2.98	3.28	3.45	3.07	2.91	2.73	2.85	2.46	3.37	2.92	2.94
Tb_2O_3	b.d.l.	b.d.l.	b.d.l.	b.d.l.	b.d.l.	b.d.l.	b.d.l.	b.d.l.	b.d.l.	b.d.l.	b.d.l.
Dy_2O_3	0.59	0.69	0.26	0.67	0.05	0.09	0.37	0.14	0.22	0.78	0.22
Ho_2O_3	b.d.l.	b.d.l.	b.d.l.	0.01	b.d.l.	0.06	b.d.l.	b.d.l.	0.02	0.00	0.00
Er_2O_3	b.d.l.	b.d.l.	b.d.l.	b.d.l.	b.d.l.	b.d.l.	b.d.l.	b.d.l.	b.d.l.	b.d.l.	b.d.l.
Tm_2O_3	0.14	0.16	b.d.l.	0.14	0.03	0.07	b.d.l.	b.d.l.	0.03	0.11	b.d.l.
Yb_2O_3	0.12	0.07	0.04	0.10	0.10	0.10	0.18	0.07	0.09	0.16	0.11

(Cont.)

(Cont.)

Sample	**111911/111912**										
Element	**1**	**2**	**3**	**4**	**5**	**6**	**7**	**8**	**10**	**11**	**12**
Lu_2O_3	0.01	0.04	0.01	0.04	b.d.l.	0.04	b.d.l.	0.03	0.03	0.02	b.d.l.
ZrO_2	b.d.l.	b.d.l.	0.08	b.d.l.	b.d.l.	b.d.l.	b.d.l.	0.02	0.36	b.d.l.	b.d.l.
HfO_2	b.d.l.	b.d.l.	b.d.l.	b.d.l.	b.d.l.	b.d.l.	b.d.l.	b.d.l.	b.d.l.	b.d.l.	b.d.l.
CaO	2.61	1.08	0.89	2.09	1.04	1.58	1.85	2.28	0.42	1.43	1.99
MnO	b.d.l.	b.d.l.	b.d.l.	b.d.l.	b.d.l.	b.d.l.	b.d.l.	b.d.l.	b.d.l.	b.d.l.	b.d.l.
PbO	0.23	0.06	0.04	0.21	0.06	0.09	0.10	0.08	0.04	0.07	0.09
Total	101.0	100.8	99.8	100.1	100.5	99.6	101.1	101.3	97.7	99.7	100.0
Htn	0.000	0.000	0.000	0.000	0.000	0.000	0.001	0.001	0.000	0.000	0.001
Mnz	0.754	0.863	0.898	0.775	0.911	0.853	0.836	0.834	0.902	0.815	0.840
Xnt	0.085	0.082	0.060	0.103	0.052	0.052	0.065	0.046	0.063	0.099	0.058
Crl	0.239	0.096	0.084	0.192	0.101	0.160	0.178	0.240	0.063	0.154	0.196
Nº ions in formula on the basis of 4 oxygens											
Si	0.000	0.005	0.004	0.001	0.005	0.005	0.007	0.006	0.009	0.005	0.005
Al	0.002	0.004	0.002	0.002	0.000	0.003	0.000	0.001	0.030	0.001	0.003
Ca	0.109	0.044	0.037	0.086	0.043	0.068	0.077	0.095	0.018	0.060	0.083
U	0.034	0.008	0.004	0.030	0.003	0.003	0.006	0.006	0.003	0.009	0.007
Th	0.079	0.038	0.038	0.058	0.045	0.081	0.081	0.111	0.038	0.074	0.086
Pb	0.002	0.001	0.000	0.002	0.001	0.001	0.001	0.001	0.000	0.001	0.001
Zr	0.000	0.000	0.001	0.000	0.000	0.000	0.000	0.000	0.007	0.000	0.000
Hf	0.000	0.000	0.000	0.000	0.000	0.000	0.000	0.000	0.000	0.000	0.000
P	0.994	1.001	1.001	1.007	1.015	0.981	0.992	0.995	0.988	0.989	0.999
Y	0.030	0.024	0.008	0.044	0.008	0.010	0.017	0.006	0.010	0.041	0.010
La	0.151	0.203	0.171	0.166	0.186	0.186	0.166	0.148	0.181	0.162	0.162
Ce	0.351	0.403	0.398	0.356	0.403	0.403	0.386	0.369	0.419	0.368	0.380
Pr	0.022	0.023	0.026	0.021	0.025	0.025	0.025	0.025	0.023	0.025	0.024
Nd	0.160	0.170	0.225	0.152	0.193	0.186	0.181	0.182	0.198	0.187	0.171
Pm	0.000	0.000	0.000	0.000	0.000	0.000	0.000	0.000	0.000	0.000	0.000
Sm	0.022	0.018	0.031	0.020	0.020	0.015	0.017	0.016	0.022	0.023	0.022
Eu	0.000	0.000	0.000	0.000	0.000	0.000	0.000	0.000	0.000	0.000	0.000
Gd	0.038	0.042	0.045	0.039	0.037	0.036	0.037	0.032	0.044	0.038	0.038
Tb	0.000	0.000	0.000	0.000	0.000	0.000	0.000	0.000	0.000	0.000	0.000
Dy	0.007	0.009	0.003	0.008	0.001	0.001	0.005	0.002	0.003	0.010	0.003
Ho	0.000	0.000	0.000	0.000	0.000	0.001	0.000	0.000	0.000	0.000	0.000
Er	0.000	0.000	0.000	0.000	0.000	0.000	0.000	0.000	0.000	0.000	0.000
Tm	0.002	0.002	0.000	0.002	0.000	0.001	0.000	0.000	0.000	0.001	0.000
Yb	0.001	0.001	0.001	0.001	0.001	0.001	0.002	0.001	0.001	0.002	0.001
Lu	0.000	0.000	0.000	0.000	0.000	0.000	0.000	0.000	0.000	0.000	0.000
Si	0.000	0.005	0.004	0.001	0.005	0.005	0.007	0.006	0.009	0.005	0.005
Al	0.002	0.004	0.002	0.002	0.000	0.003	0.000	0.001	0.030	0.001	0.003

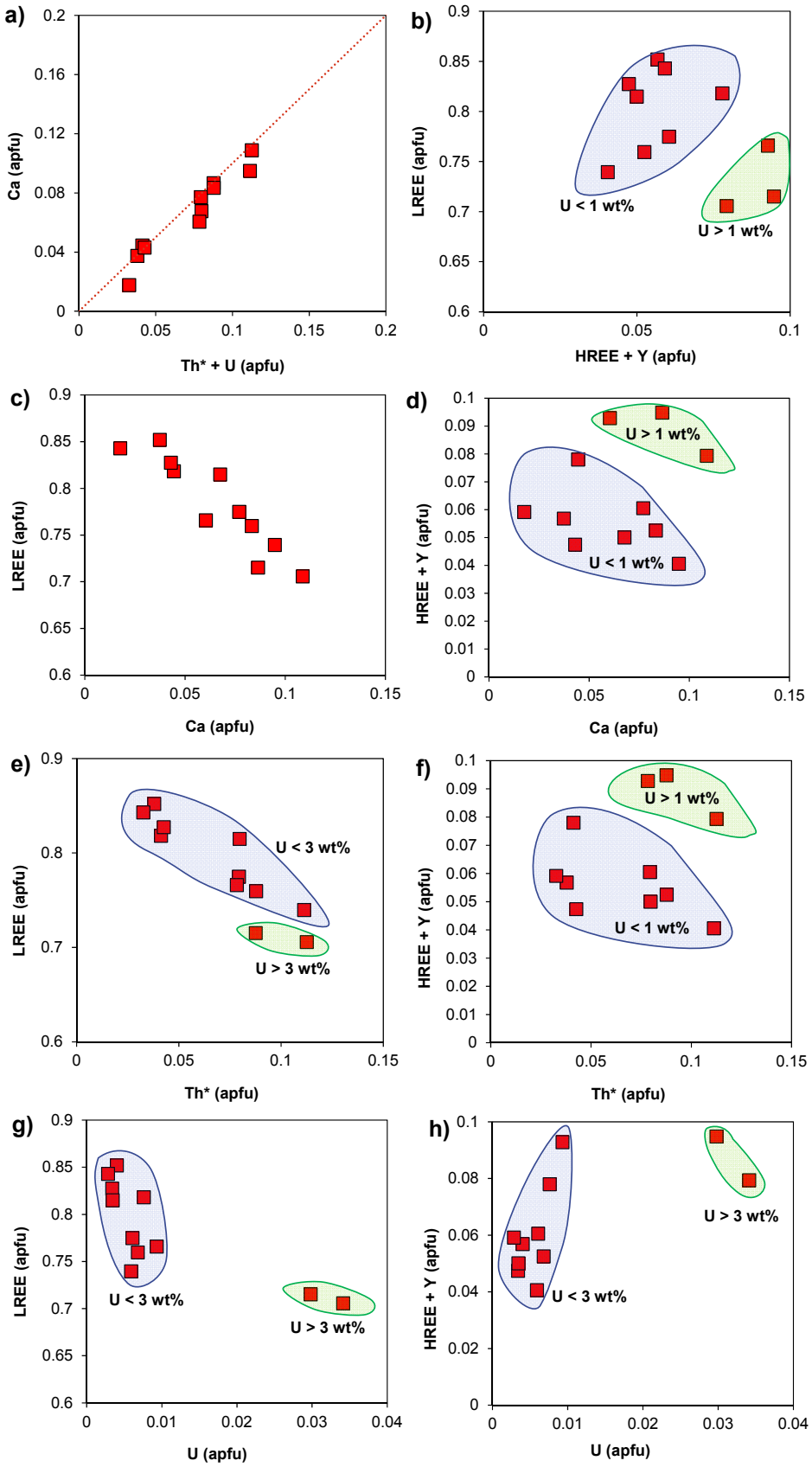

Fig. 3.17: Chemical composition of monazite from the Logrosán granite. **a)** Cheralite substitution mechanism. The 1:1 vector is represented by the red dotted line. **b)** (HREE + Y) *vs.* LREE. **c)** Ca *vs.* LREE. **d)** Ca *vs.*. (HREE + Y). **e)** Th* *vs.* LREE. **f)** Th* *vs.* (HREE + Y). **g)** U *vs.*. LREE. **h)** U *vs.* (HREE + Y).
Th* is the Th content after subtracting the equivalent of the Si content.

3.3. Whole-rock geochemistry

The results of major, minor and trace element analyses of nine granite samples are presented in Table 3.10. The Logrosán granite shows high SiO_2 (63.59-74.03 wt.%), P_2O_5 (0.42-0.78 wt.%) and Al_2O_3 (14.42-15.38 wt.%), but very low CaO (0.25-0.69 wt.%) contents. Some granite samples have concentrations of certain elements below detection limits (V: 5 ppm, Cr: 20 ppm, Sc: 1 ppm, Co: 10 ppm) and almost all the granites have Ni < 20 ppm and Mo < 2 ppm.

The Logrosán granite is classified as a monzogranite in the QAPF diagram of Streckeisen (1976) (Fig. 3.18a) using the modal data of Rossi (1975). Moreover, the low color index (CI < 5%) of the Logrosán granite allow defining it as a leucogranite. The Logrosán stock has a strong peraluminous character, with an alumina-saturation index ranging from 1.22 to 2 and high normative corundum contents (3.55-8.42%). In the A-B multicationic diagram of Debon and LeFort (1983) (modified by Villaseca et al., 1998a), the Logrosán granite plot similarly to other leucogranites from the Central Iberian Zone (Fig. 3.18b). They display a trend together with other Central Extremadura Batholith (CEB) granites, where most evolved units plot in the highly felsic peraluminous field, close to the extremely high peraluminous field.

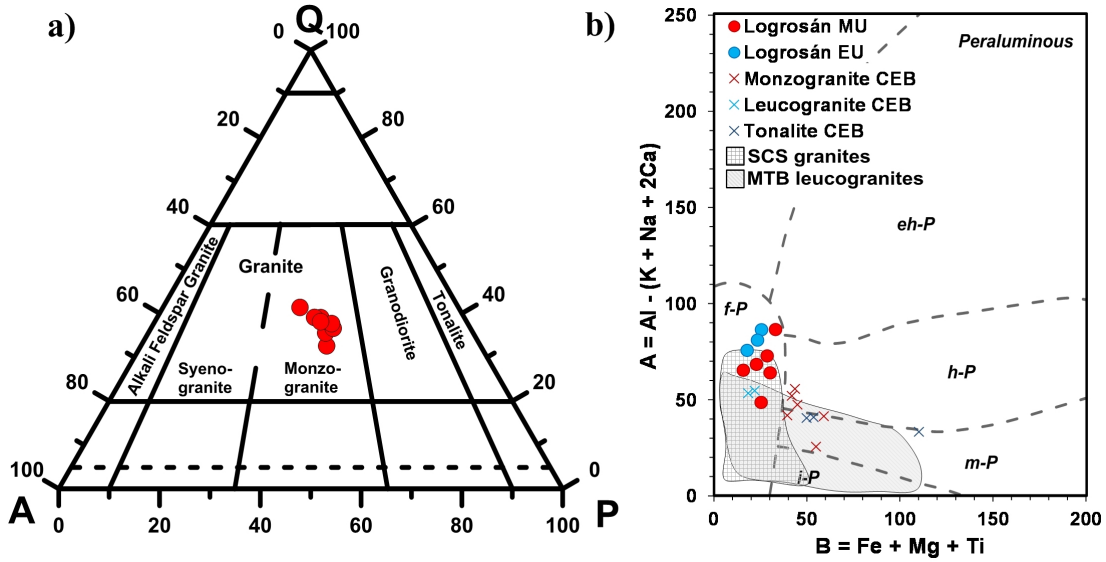

Fig. 3.18: a) Modal composition of Logrosán granite samples plotted in the QAPF classification diagram of Streckeisen (1976). **b)** A-B diagram (Debon and LeFort, 1983; modified from Villaseca et al., 1998a) showing the phosphorous-rich Logrosán granite and the compositional fields of other granitoids from the Central Iberian Zone (Villaseca et al., 1998b, Castro et al. 1999, Merino, 2014). Peraluminous fields are: ehP: extremely high peraluminous; hP: highly peraluminous; mP: moderately peraluminous; lP: low peraluminous; fP: highly felsic peraluminous.

Table 3.10: Whole-rock major (wt. %), trace-element and REE (ppm) compositions of the Logrosán granite.

	Main granites						Evolved granites		
	AQ1 111911	**AQ2 111912**	**AQ4 111976**	**AQ6 111978**	**AQ13 178**	**AQ14 179**	**AQ5 111979**	**AQ11 174**	**AQ12 177**
SiO_2	72.46	72.26	72.53	73.93	73.12	74.03	72.94	72.73	74.01
Al_2O_3	14.43	14.76	15.24	15.14	14.92	14.94	15.30	14.42	14.83
FeOt	1.250	1.710	1.330	0.820	1.370	1.140	0.780	1.450	1.170
MnO	0.017	0.019	0.021	0.021	0.023	0.019	0.011	0.021	0.016
MgO	0.280	0.330	0.380	0.160	0.330	0.240	0.220	0.220	0.260
CaO	0.590	0.450	0.690	0.500	0.540	0.510	0.460	0.250	0.460
Na_2O	3.680	2.670	3.310	3.870	3.310	3.420	3.270	2.950	2.950
K_2O	4.460	4.750	4.880	4.190	4.420	4.530	4.830	4.350	4.630
TiO_2	0.182	0.228	0.269	0.103	0.213	0.168	0.167	0.126	0.151
P_2O_5	0.500	0.470	0.570	0.570	0.490	0.460	0.540	0.510	0.550
LOI	1.330	2.550	1.620	1.510	1.470	1.080	1.950	1.980	1.740
Total	99.16	100.2	100.8	100.8	100.2	100.5	100.5	99.00	100.8
Sc	3.00	4.00	2.00	3.00	3.00	2.00	2.00	2.00	3.00
Be	15.00	23.00	16.00	11.00	14.00	18.00	7.00	19.00	9.00
V	7.00	12.00	10.00	< 5	13.00	10.00	< 5	10.00	9.00
Cr	< 20	< 20	< 20	< 20	< 20	< 20	< 20	280	180
Co	2.00	4.00	3.00	3.00	2.00	2.00	2.00	2.00	2.00
Ni	< 20	< 20	< 20	< 20	< 20	< 20	< 20	< 20	< 20
Cu	< 10	20.00	< 10	< 10	20.00	< 10	< 10	< 10	< 10
Zn	30.00	50.00	60.00	30.00	40.00	70.00	< 30	70.00	< 30
Ga	21.00	23.00	25.00	20.00	22.00	21.00	20.00	24.00	20.00
Ge	2.20	2.10	1.70	2.30	2.30	2.10	1.50	3.40	2.50
As	60.00	51.00	137	94.00	137	64.00	123	44.00	103
Rb	288	301	338	317	311	238	270	362	317
Sr	44.00	41.00	57.00	39.00	44.00	38.00	52.00	32.00	57.00
Y	6.90	5.20	7.60	5.50	7.60	9.60	5.40	3.30	6.60
Zr	76.00	80.00	118.00	43.00	82.00	77.00	74.00	60.00	62.00
Nb	8.70	11.70	10.10	13.60	11.40	9.00	9.60	15.90	11.10
Mo	< 2	< 2	< 2	< 2	< 2	< 2	< 2	< 2	< 2
Ag	< 0.5	0.50	< 0.5	< 0.5	< 0.5	< 0.5	0.70	< 0.5	< 0.5
In	< 0.1	0.10	< 0.1	< 0.1	< 0.1	< 0.1	< 0.1	0.10	< 0.1
Sn	50.00	67.00	33.00	35.00	49.00	11.00	37.00	29.00	53.00
Sb	0.50	0.40	< 0.2	0.70	< 0.2	0.30	0.90	< 0.2	0.50
Cs	59.50	88.00	74.40	50.20	54.60	26.70	70.30	51.60	145
Ba	224	241	290	138	226	178	219	152	225
La	13.80	16.10	21.80	6.53	15.10	13.00	11.40	8.81	9.67
Ce	31.40	35.60	50.20	14.80	33.10	27.70	27.80	19.20	20.70
Pr	3.58	3.85	6.42	1.74	3.95	3.34	3.25	2.17	2.48
Nd	13.30	14.50	25.80	6.40	15.60	12.90	12.50	8.06	10.00
Sm	2.96	3.05	5.18	1.56	3.25	2.94	2.92	1.73	2.47
Eu	0.32	0.32	0.47	0.21	0.33	0.30	0.32	0.19	0.36
Gd	2.24	2.21	3.35	1.44	2.54	2.52	2.22	1.26	2.24
Tb	0.33	0.29	0.46	0.25	0.36	0.40	0.35	0.18	0.35
Dy	1.52	1.35	1.85	1.20	1.64	1.87	1.50	0.84	1.75
Ho	0.24	0.21	0.26	0.19	0.25	0.32	0.22	0.12	0.24
Er	0.60	0.52	0.60	0.51	0.66	0.86	0.46	0.30	0.51
Tm	0.09	0.07	0.08	0.07	0.09	0.12	0.06	0.05	0.06
Yb	0.56	0.49	0.44	0.53	0.52	0.71	0.37	0.30	0.38
Lu	0.08	0.07	0.06	0.07	0.08	0.11	0.05	0.05	0.06
Hf	2.20	2.40	3.00	1.50	2.60	2.50	2.50	1.70	2.10
Ta	2.26	3.08	2.50	4.76	3.73	1.97	1.98	4.00	2.30
W	24.60	82.10	74.20	36.00	23.90	9.00	131.00	1.60	376
Tl	1.84	1.98	2.02	1.99	1.87	1.40	1.77	1.56	1.79
Pb	28.00	22.00	29.00	21.00	24.00	28.00	26.00	21.00	29.00
Bi	0.30	< 0.1	0.60	1.50	0.30	2.60	0.40	< 0.1	0.60
Th	7.59	8.28	19.90	3.07	8.70	6.65	8.67	5.30	4.45
U	7.91	7.25	10.90	8.49	7.04	11.00	10.50	9.04	7.23
F		2003	1611	1150			1053		
Li		290	303	141			210		
T (ºC)	738	755	777	699	752	746	744	734	733

*Temperatures estimated using the saturation zircon temperature of Watson and Harrison (1983)

Geochemical and mineralogical variations of the Logrosán granite have been represented using different parameters as iso-concentration curves on the granite outcrop surface (Fig. 3.19). Only the whole-rock analyses from fresh granite samples have been considered for this purpose. The parameters used are: the Q and B parameters of De la Roche (1964) which indicate the free silica (quartz amount), and separate the color and colorless minerals, respectively; the Mu, Or and Pl parameters of Saavedra (1977); and the Ab parameter of Karayeva (1968), which represents the Na entering together with the Ca into the albite structure. Owing to the relatively simple mineralogy of the Logrosán granite, these parameters represent the quartz (Q), biotite, tourmaline and/or rutile (B), muscovite (Mu), K-feldspar (Or), plagioclase (Pl) and albite (Ab).

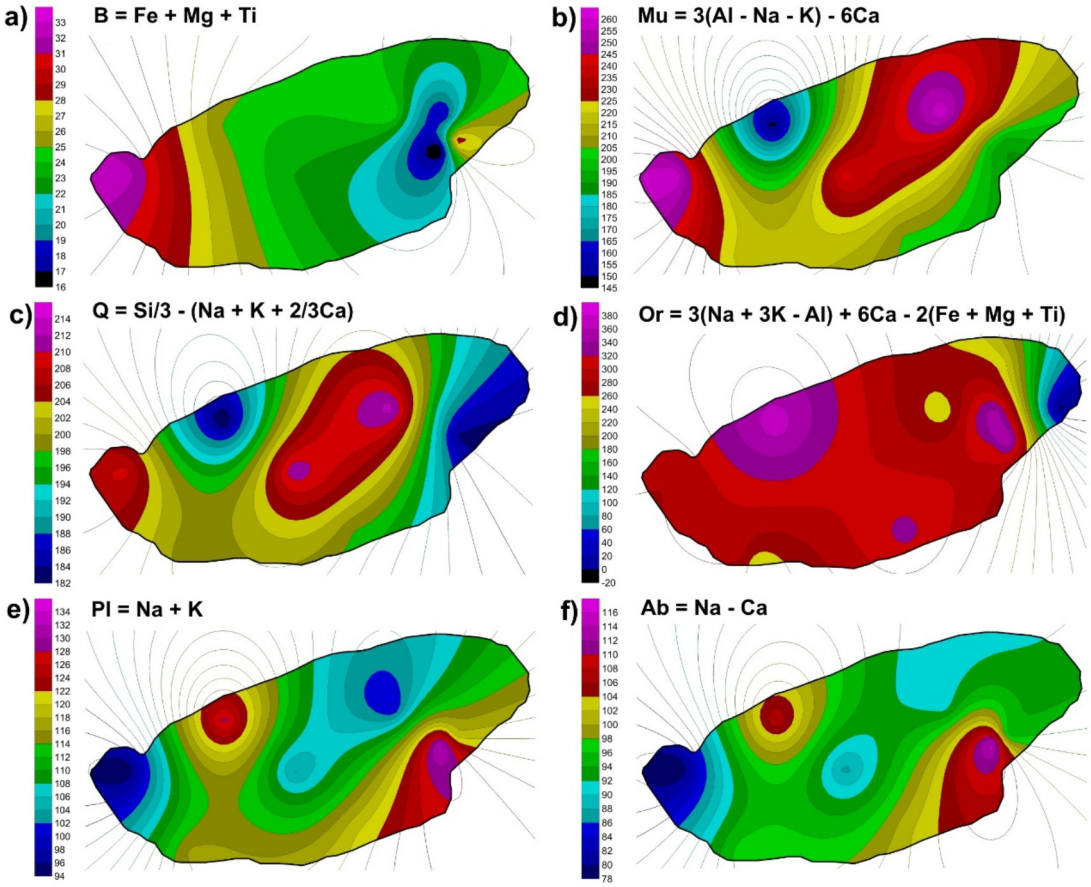

Fig. 3.19: Iso-concentration maps: **a)** B parameter. **b)** Mu parameter. **c)** Q parameter. **d)** Or parameter. **e)** Pl parameter. **f)** Ab parameter.

The parameter B is in general low (Fig. 3.19a). The lowest B values are associated with the aplitic sectors. On the other hand, the highest B values correspond with the western part of the pluton, where the Sn-(W) mineralization is preferentially found. These high values may be related with a higher content of rutile and tourmaline, rather than biotite. This would be in agreement with the analogous high Mu values in this specific area (Fig 3.19b). The Mu parameter reaches also high values at the highest topographic points, corresponding with the

Evolved Units. Q parameter maximum values are associated with the Evolved Units and the Sn-(W) mineralization zone (Fig. 3.19). This Q high parameter together with the high Mu and B values at the western part of the stock, allow determining the greisen alteration and mafic mineral concentration within the granite associated with the Sn-(W) ores. The Or values are in general high and quite homogeneous (Fig. 3.19d). A low Or parameter value in the eastern part of the cupola is associated with low Q and medium values of B, Pl and Ab. This corresponds with the two mica medium-grained granite of the Main Unit, but in an area with less porphyritic or aplitic sectors, and low alteration (lack of silicification or muscovitization). Pl and Ab parameters show very similar iso-concentration curves (Fig. 3.19e and 3.19f) because plagioclase found in the Logrosán granite is fundamentally albite. Highest Ab values associated with the highest Or values and the lowest Mu values correspond with less altered sectors.

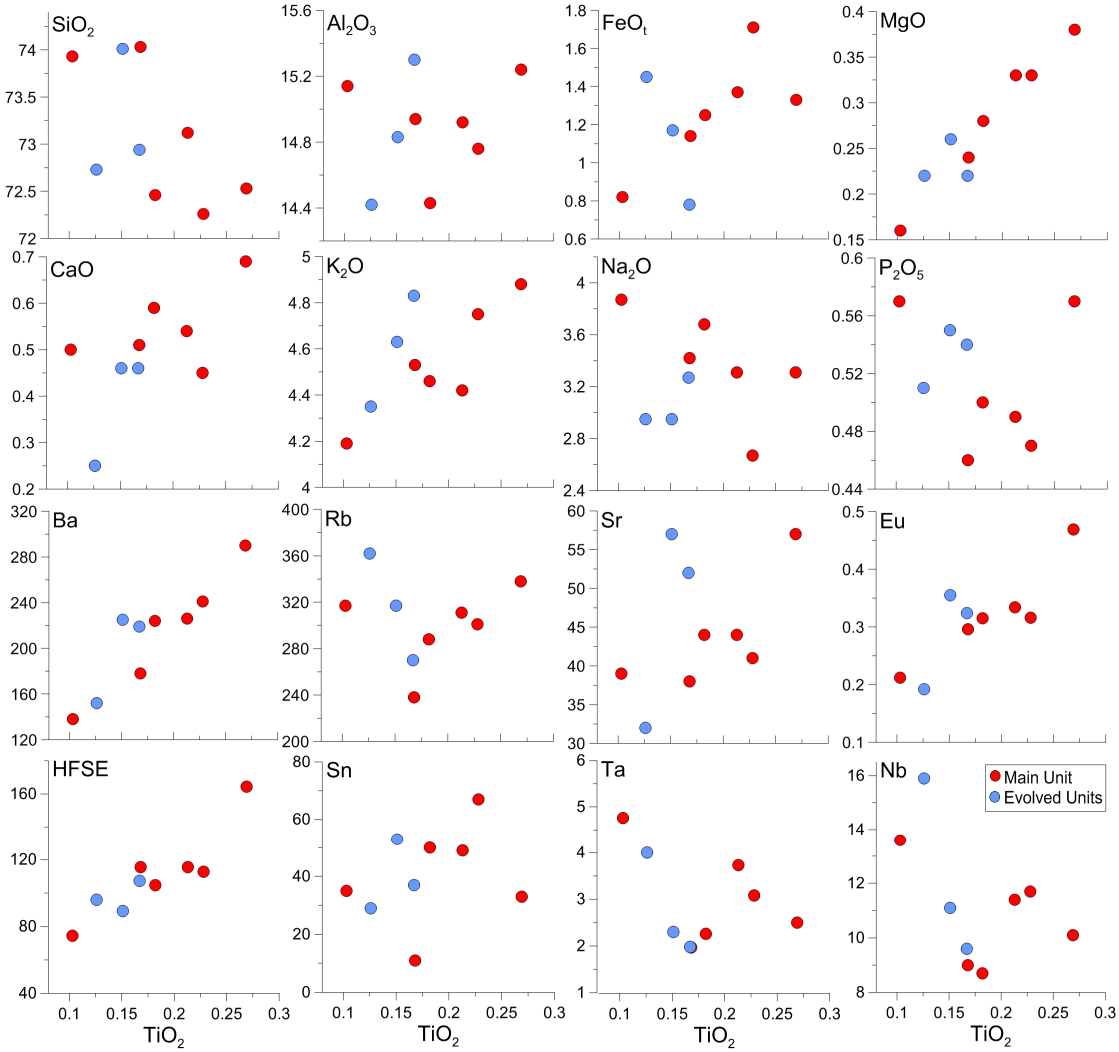

Fig. 3.20: Selected major (wt. %) and trace (ppm) element variation diagrams versus TiO_2 of the Logrosán granite. *HFSE: Zr+Hf+Nb+Ta+Th+U

In variation diagrams using TiO_2 as a differentiation index, Logrosán samples do not define clear fractional crystallization trends, except for the MgO, which markedly decreases toward the more

evolved samples (Fig. 3.20). Although there is some scatter in the plots, generally the Al_2O_3, FeOt, MgO, CaO and K_2O contents decrease while the SiO_2, Na_2O and P_2O_5 contents increase. Scatter is mainly caused by a slightly albitized sample which behaves discordantly to other samples from the Main Unit (AQ6 sample in Table 3.10). However, more evolved granites (Evolved Units) seem to form discrete trends for certain major elements such as CaO and K_2O. Their depletion would be consistent with plagioclase and alkali feldspar fractionation, but the Main and Evolved Units show different evolution trends.

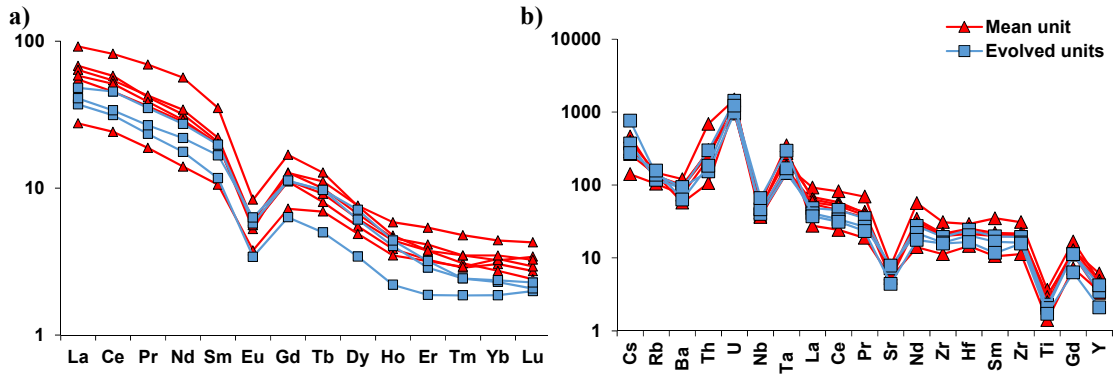

Fig. 3.21: a) Chondrite-normalized REE diagram, and **b)** chondrite-normalized multi-trace element diagram of the Logrosán granite.

Granite REE patterns show a variable fractionation (La_N/Yb_N= 8.37–33.6) but are generally highly fractionated, with a negative Eu anomaly for granites from the Main Unit (Eu/Eu*=0.32-0.42) and slightly more negative toward granites from the Evolved Units (Eu/Eu*=0.37-0.45) (Fig. 3.21). In trace-element chondrite normalized diagrams, the Logrosán samples show negative anomalies in Ba, Nb, Sr and Ti (Fig. 3.21). The negative Eu anomaly and the low Sr contents of the granite suggest that plagioclase fractionation has occurred for both, the Main Unit and the Evolved Units. In variation diagrams Ba, Rb, Sr, Eu, Cs, Y, Th, HREE and LREE become depleted with increasing degree of fractionation (Fig. 3.20). As with major elements, granite samples from the Evolved Units show different trends for some elements (e.g., Rb, Fig. 3.20) compared to the Main Unit set of samples. The HFSE (Zr+Hf+Nb+Ta+Th) show no clear trend with granite differentiation. A slight tendency of increasing Nb and Ta can be recognized, while Sn exhibits a wider scatter (Fig. 3.20). High Sn contents are found in this granite with respect to the crustal average (i.e., granites with Sn > 10 ppm, as defined by Flinter, 1971) allowing its classification as a stanniferous granite. Ga and Hf data display trends where more fractionated samples show the lowest contents. The overall range for Ga and Hf concentration is quite restricted (Ga: 20-25 ppm and Hf: 1.5-3.0).

3.4. Oxygen isotopes

Whole rock $\delta^{18}O$ results of Logrosán granite gave a narrow range between 14.1 and 15.0 ‰ (vs. SMOW), showing a positive correlation with SiO_2 of the rock (Table 3.11). $\delta^{18}O$ values higher than 10 ‰ have been observed in many Variscan granites from western Europe (Tartèse and Boulvais, 2010; Hoefs and Emmermann, 1983) and are typical of high-SiO_2 peraluminous granites (Taylor, 1978). Similar $\delta^{18}O$ values have been found in other granites from the southern CIZ (e.g., Castelo Branco Batholith: 12.2−13.7‰, Antunes et al., 2008). Nevertheless, these values are significantly higher than those found in the peraluminous S-type granites from the Spanish Central System, which mostly range from 8.3 to 10.2‰ (Recio et al., 1992; Villaseca and Herreros, 2000).

Table 3.11: O-D isotopic data of the Logrosán granite.

Sample	Rock type	SiO_2	$\delta^{18}O_{SMOW}$	δD_{SMOW}	H_2O %
AQ2	main granite	72.26	14.1	-84.7	1.4
AQ5	evolved granite	72.94	14.5	-77.9	1.3
AQ12	evolved granite	74.01	15.0	-77.0	1.2

3.5. Sr-Nd isotopes

The measured Sr and Nd isotope ratios were recalculated back to 308 Ma based on the intrusion age determined by U-Pb geochronology (Table 3.12). The Sm-Nd model ages were calculated using the equation of Liew and Hofmann (1988) (Table 3.13). The obtained model ages (1.31-1.67 Ga) are similar to those given for other peraluminous monzogranites and leucogranites from the Central Extremadura Batholith (e.g., Antunes et al., 2008; Castro et al., 1999, Merino et al., 2014). The Logrosán granite is characterized by a large variation in initial $^{87}Sr/^{86}Sr$ ratios (from 0.7125 to 0.7286), whereas εNd is much less variable (between -4.3 and -4.0) (Fig. 3.22).

Table 3.12: Rb-Sr isotopic data of the Logrosán granite.

Sample	Rock type	Age (Ma)	Rb	Sr	$^{87}Rb/^{86}Sr$	$^{87}Sr/^{86}Sr$	±2σ	$(^{87}Sr/^{86}Sr)_t$
AQ2	main granite	308	301	41	21.487	0.822394	4	0.728213
AQ6	main granite	308	317	39	23.806	0.829387	6	0.725042
AQ13	main granite	308	311	44	20.657	0.807511	3	0.716966
AQ3	altered granite	308	411	28	43.362	0.918694	6	0.728633
AQ10	altered granite	308	361	77	13.658	0.774096	4	0.714232
AQ12	evolved granite	308	317	57	16.216	0.783536	3	0.712459

Table 3.13: Sm-Nd isotopic data of the Logrosán granite.

Sample	Rock type	Age (Ma)	Sm (ppm)	Nd (ppm)	$^{147}Sm/^{144}Nd$	$^{143}Nd/^{144}Nd$	±2σ	$(^{143}Nd/^{144}Nd)_t$	ε^t_{Nd}	TDM
AQ2	main granite	308	3.05	14.5	0.1272	0.512294	2	0.512037	-4.0	1.32
AQ6	main granite	308	1.56	6.40	0.1474	0.512321	2	0.512024	-4.2	1.62
AQ13	main granite	308	3.25	15.6	0.1259	0.51229	1	0.512036	-4.0	1.31
AQ3	altered granite	308	2.76	11.1	0.1503	0.512325	1	0.512022	-4.3	1.67
AQ10	altered granite	308	4.90	19.5	0.1519	0.512343	1	0.512036	-4.0	1.67
AQ12	evolved granite	308	2.47	10.0	0.1493	0.512327	2	0.512026	-4.2	1.65

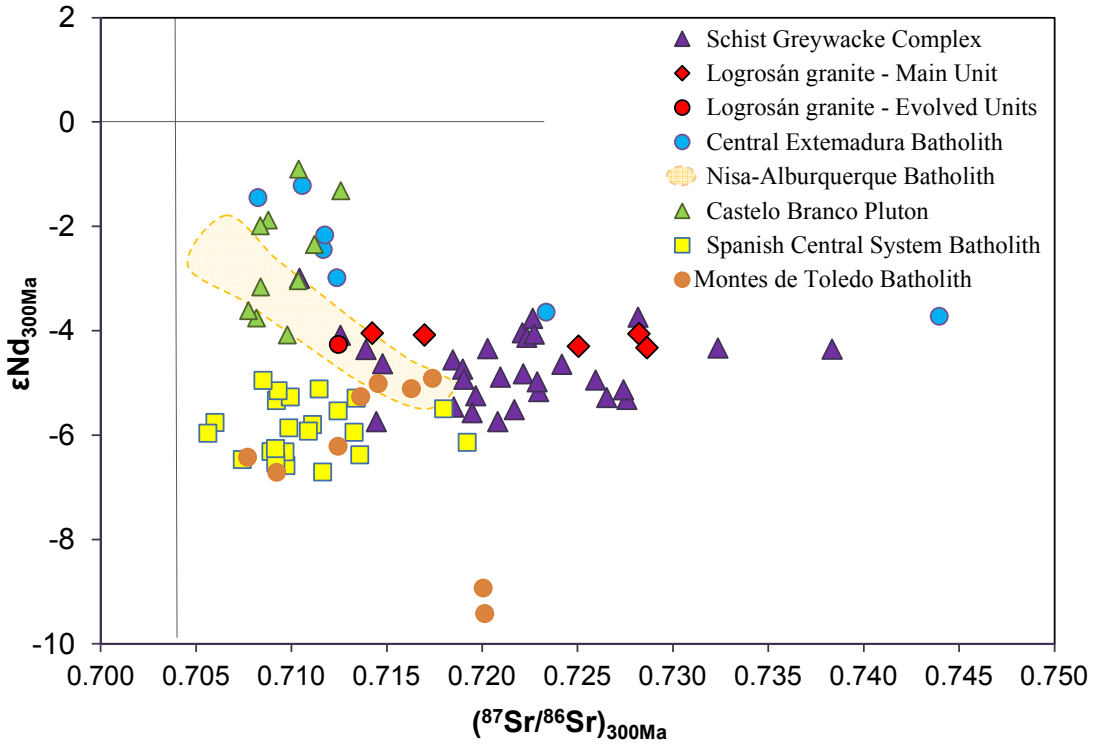

Fig. 3.22: Initial Sr-Nd composition of the Logrosán granite and representative samples of other granites from the Central Extremadura Batholith (Castro et al., 1999; Antunes et al., 2008; González-Menéndez and Bea, 2004), the Spanish Central System (Villaseca et al., 1998b) and crustal protoloiths of the Central Iberian Zone (Beetsma, 1995; López-Guijarro et al., 2008; Ugidos et al., 1997; Villaseca et al., 2014). All data have been recalculated to a reference age of 300 Ma.

3.6. Hf isotope zircon composition

From a total of 68 zircon grains selected, 37 grains were dated by U-Pb and 28 were analyzed for their Hf-isotope composition. Based on the morphology, two groups of zircon grains have been distinguished: (1) euhedral elongated bipyramidal prisms and (2) stubby prisms. Most of the analyzed grains (about 67%) belong to the first group. This population is characterized by sizes ranging from 100 to 200 µm and aspect ratios ranging from 1:6 to 1:2, being dominantly 1:2 (Fig. 3.23; e.g., L24-20 and L30-31). The second zircon type comprises stubby prisms (1:1 aspect ratio) of usually smaller grain size (average size of 100 µm) (Fig. 3.23, e.g., L24-12).

The BSE images show that most zircon grains have homogeneous or sector-zoned inner cores with dark thin rims (Fig. 3.23, e.g., L24-01). Stubby zircon crystals sometimes present texturally discordant dark cores and/or fine euhedral oscillatory zoning (Fig. 3.23, e.g., L30-22).

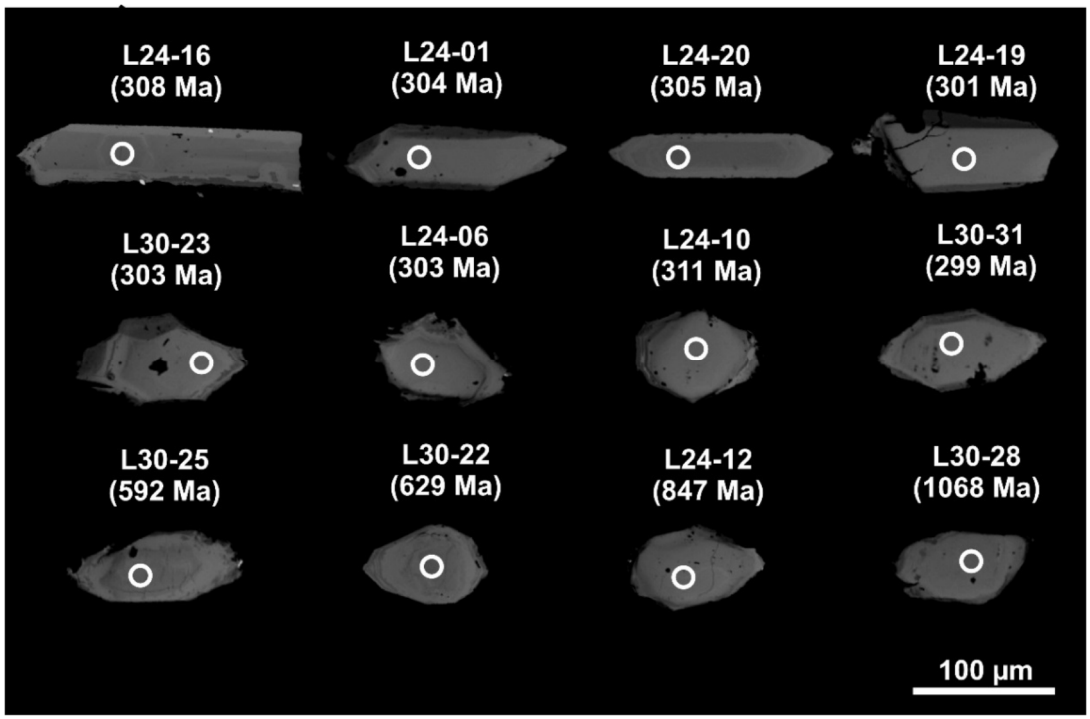

Fig. 3.23: Back-scattered electron (BSE) images of representative zircon crystals from the Logrosán granite. Spot numbers and ages are listed in Table 3.7.

The zircon Lu-Hf isotopic data collected during this study are summarized in Table 3.14. Depleted-mantle model ages (T_{DM}) are useful to estimate the crustal residence age of the granite protolith (Andersen et al., 2002). T_{DM} were calculated using the measured $^{176}Lu/^{177}Hf$ ratios, referred to a model depleted mantle with a present-day $^{176}Hf/^{177}Hf = 0.28325$ and $^{176}Lu/^{177}Hf = 0.0384$ (Griffin et al., 2000; 2002). These T_{DM} ages represent only a minimum age of the source of the host magma. Thus, a more realistic two-stage model (T_{DM2}) has been used to estimate model ages of the source of the Logrosán granite. T_{DM2} were calculated assuming a $^{176}Lu/^{177}Hf$ ratio of 0.015 for the average continental crust (Griffin et al., 2000).

The Variscan zircon population yields initial $^{176}Hf/^{177}Hf$ ratios of 0.282299-0.282758 which correspond to εHf(t) varying from +5.7 to -10.5, a range well outside of analytical uncertainties. The T_{DM2} range for Variscan zircon is accordingly wide, and ranges from 928 to 1957 Ma but mostly between 1179 and 1594 Ma with an average value of 1368 Ma. This average value encompasses the ages given by the whole rock Nd depleted model age (1.31-1.67 Ga). Neoproterozoic inherited zircons show initial $^{176}Hf/^{177}Hf$ ratios of 0.281549 to 0.282735 which corresponds to $\varepsilon Hf_{(t)}$ of +14.7 to -29.7, with more frequent εHf(t) between +6.0 and –3.2. Meso-

to Paleoproterozoic zircons have $^{176}Hf/^{177}Hf$ initial ratios of 0.281326-0.282007, and εHf(t) between -3.4 and -7.6.

Tabla 3.14: Lu-Hf LA-MC-ICPMS data of zircon from the Logrosán granite

Sample	$^{176}Hf/^{177}Hf$	1SE	$^{176}Lu/^{177}Hf$	$^{176}Yb/^{177}Hf$	Age (Ma)	Hf_i	εHf	1SE	T_{DM} (Ga)	T_{DM2}(Ga)
L24-1	0.282745	0.000039	0.00110	0.0295	308	0.282739	5.0	1.4	0.72	0.98
L24-2	0.282761	0.000059	0.00060	0.0166	308	0.282758	5.7	2.1	0.69	0.93
L24-6	0.282555	0.000057	0.00030	0.0087	308	0.282553	-1.5	2.0	0.97	1.39
L24-10	0.282466	0.000052	0.00080	0.0221	308	0.282462	-4.8	1.8	1.11	1.60
L24-16	0.282516	0.000041	0.00060	0.0171	308	0.282512	-3.0	1.5	1.03	1.49
L24-17	0.282496	0.000053	0.00050	0.0146	308	0.282493	-3.7	1.9	1.06	1.53
L24-19	0.282653	0.000029	0.00110	0.0318	308	0.282647	1.8	1.0	0.85	1.18
L24-20	0.282601	0.000033	0.00130	0.0359	308	0.282594	-0.1	1.2	0.93	1.30
L24-21	0.282304	0.000140	0.00080	0.0219	308	0.282299	-10.5	5.0	1.33	1.96
L24-23	0.282488	0.000035	0.00080	0.0239	308	0.282483	-4.0	1.2	1.08	1.55
L24-26	0.282614	0.000032	0.00020	0.0059	308	0.282613	0.6	1.1	0.88	1.26
L24-27	0.282591	0.000035	0.00110	0.0313	308	0.282585	-0.4	1.2	0.94	1.32
L24-31	0.282502	0.000160	0.00140	0.0378	308	0.282494	-3.6	5.7	1.07	1.53
L24-36	0.282651	0.000050	0.00100	0.0295	308	0.282645	1.7	1.8	0.85	1.19
L24-24	0.282489	0.000110	0.00230	0.0654	447	0.282469	-1.2	3.9	1.12	1.49
L24-3	0.282557	0.000046	0.00090	0.0214	518	0.282549	3.2	1.6	0.98	1.27
L24-7	0.281758	0.000052	0.00040	0.0103	545	0.281753	-24.4	1.8	2.07	3.02
L24-4	0.282528	0.000048	0.00100	0.0263	550	0.282518	2.8	1.7	1.03	1.32
L24-9	0.282586	0.000036	0.00120	0.0299	563	0.282573	5.1	1.3	0.95	1.18
L24-32	0.282610	0.000049	0.00160	0.0425	576	0.282592	6.0	1.7	0.93	1.13
L24-25	0.282338	0.000032	0.00140	0.0400	592	0.282322	-3.2	1.1	1.31	1.73
L24-22	0.281564	0.000069	0.00130	0.0314	629	0.281549	-29.7	2.5	2.38	3.42
L24-11	0.282687	0.000034	0.00080	0.0217	648	0.282677	10.6	1.2	0.80	0.89
L24-33	0.282749	0.000040	0.00100	0.0237	736	0.282735	14.7	1.4	0.71	0.70
L24-12	0.282264	0.000057	0.00110	0.0330	847	0.282246	-0.2	2.0	1.40	1.74
L24-28	0.282034	0.000032	0.00130	0.0352	1068	0.282007	-3.6	1.1	1.73	2.14
L24-05	0.281340	0.000051	0.00040	0.0097	1950	0.281326	-7.6	1.8	2.63	3.09
L24-35	0.281449	0.000057	0.00050	0.0140	1975	0.281428	-3.4	2.0	2.49	2.84

3.7. U-Pb geochronology

Seven zircon fractions and one monazite fraction were analyzed by ID-TIMS. All zircon fractions were pre-treated to remove Pb loss before final dissolution, with the chemical abrasion (CA) method of Mattison (2005). Only one zircon fraction (Z7), a single grain, plots in a discordant position which could be attributed to partial secondary Pb-loss (see Krogh, 1982). The remaining data are either concordant or scattered owing to the presence of older xenocrystic zircon.

Five fractions (zircon fractions Z3, Z5, Z8, Z6 and monazite fraction M1) are concordant and plot between 307 and 310 Ma. The remaining zircon fractions (Z1, Z2 and Z4) are discordant owing to the presence of inherited zircon. These are multigrain (made up of 25 crystals) to some single crystal fractions (Table 3.15). The concordant fractions Z3 and Z5 and the discordant fractions Z2 and Z4 define a mixing line (Line 1; Fig 3.24a) which has an upper intercept of ca.

1.1 Ga, suggesting a Mesoproterozoic inheritance. The concordant fractions Z3 and Z5 and the discordant fraction Z1 also define a mixing line (Line 2; Fig 3.24a) which has an upper intercept of ca. 550-560 Ma, pointing to an additional Late Neoproterozoic inherited component. These are very long projections, so the validity of the age of the inherited component has been constrained by in-situ U-Pb ages (see LA-ICP-MS below).

Table 3.15: U-Pb ID-TIMS data of zircon and monazite fractions from the Logrosán granite.

Sample	Weight (mg)	Concentration			Isotopic ratios								Apparent ages (Ma)		
		U (ppm)	Pb (ppm)	Common Pb (pg)	$^{206}Pb^*/^{204}Pb$	$^{206}Pb/^{238}U$	%(2s)	$^{207}Pb/^{235}U$	%(2s)	$^{207}Pb/^{206}Pb$	% (2s)	Rho	$^{206}Pb/^{238}U$	$^{207}Pb/^{235}U$	$^{207}Pb/^{206}Pb$
Z4 (A9)20smpr	120	101	8.0	231	134	0.05183	0.46	0.3895	0.91	0.05451	0.76	0.56	325.7	334.0	392.0
Z1(A5)25smpr	100	81	4.4	33	583	0.05005	0.25	0.3651	0.44	0.05291	0.35	0.60	314.8	316.0	324.7
Z2(A7)11medpr	80	125	6.6	38	617	0.04952	0.31	0.3602	0.80	0.05276	0.73	0.40	311.6	312.4	318.4
Z3 (A8)3larpr	60	111	8.5	93	154	0.04889	0.44	0.354	1.04	0.05251	0.90	0.52	307.7	307.7	307.5
Z5(L1)3xtls	30	57	2.9	4.0	1063	0.04882	0.19	0.354	0.75	0.05250	0.69	0.44	307.3	307.3	307.2
Z6(L4)Single	30	61	3.2	6.0	724	0.04936	0.43	0.3586	0.56	0.05269	0.35	0.78	310.6	311.1	315.3
Z7(L2)2xtls+1fra	60	63	3.0	4.0	1542	0.04771	0.43	0.3465	0.60	0.05266	0.41	0.73	300.5	302.0	314.3
Z8(L3)Single	30	92	4.6	7.0	918	0.04907	0.42	0.3557	0.50	0.05257	0.27	0.85	308.8	309.0	310.1
M1(X7)2xtls	20	5849	548	412	784	0.04883	0.24	0.354	0.25	0.05258	0.08	0.95	307.3	307.7	310.9

Z, zircon, number of crystals; sm., small (ca. 80µm); med., medium (100-120µm); lar., large (120-180µm); pr., euhedral prisms (1:5 width/length ratio);el.; elongated (1:7 width/length ratio); s.xtl., single crystal (>180µm). All zircon fractions were chemically abraded (CA technique after Mattinson (2005). M, monazite. * Ratio corrected for mass fractionation (0.11 ± 0.02 % AMU Pb; 0.10± 0.02 % AMU U), spike contribution and analytical blank (6 pg Pb; 0.1 pg U). The other isotopic ratios are also corrected for initial common Pb after the model of Stacey and Kramers (1975). Rho, error OREJ correlation coefficient of the $^{207}Pb/^{235}U$ and $^{206}Pb/^{238}U$ ratios. Data reduced with PbMacDat (Isachsen *et al.* 2007; www.earth-time.org).

The age of the intrusion of the Logrosán granite is constrained by the cluster of analyses on the Concordia curve between 307 and 310 Ma (fractions Z3, Z5, Z8, Z6, and M1; Table 3.15). Fraction Z6, a single zircon, is slightly older, suggesting the possible presence of an inherited component. Zircon fractions Z3, Z8, and Z5 and the monazite fraction M1 overlap at 307-308 Ma (Fig. 3.24a). These four fractions provide a combined "Concordia" age of 307.88±0.86 Ma, with an MSWD of 1.8 (decay constant errors included). This age is considered the age of zircon and monazite crystallization, and therefore the most accurate estimate for the age of the granite intrusion.

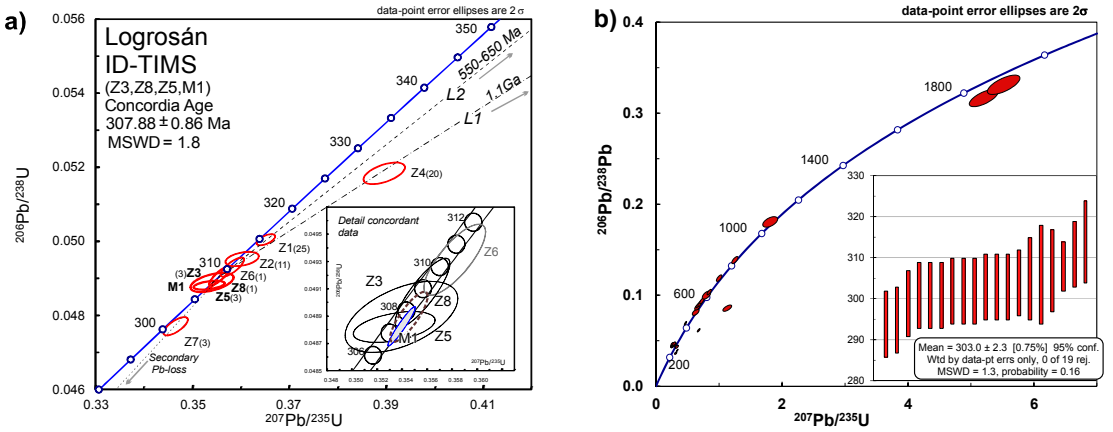

Fig. 3.24: a) Concordia diagram of the ID-TIMS data. Zircon (Z) and monazite (M) fractions, respectively; within brackets, number of crystals in each fraction. **b)** U–Pb LA-ICP-MS data showing weighted average $^{206}Pb/^{238}U$ ages and concordia plots.

Table 3.16: U-Pb LA-ICP-MS data of zircon from the Logrosán granite.

	Common ^{206}Pb (%)	U (ppm)	Th (ppm)	Th/U	Radiogenic ratios							Age (Ma)				Disc (%)
					$^{207}Pb/^{235}U$	σ	$^{206}Pb/^{238}U$	σ	ρ	$^{207}Pb/^{206}Pb$	σ	$^{206}Pb/^{238}U$	σ	$^{207}Pb/^{206}Pb$	σ	
L20-34	1.02	1590	330	0.207	0.3450	0.0117	0.0468	0.0007	0.38	0.0534	0.0020	295	4	347	85	18
L20-35	0.19	330	281	0.851	5.5353	0.1042	0.3311	0.0043	0.36	0.1213	0.0023	1844	21	1975	34	7
L20-36	0	245	141	0.577	0.3577	0.0082	0.0480	0.0007	0.29	0.0540	0.0012	302	4	371	53	23
L24-1	0	635	318	0.500	0.3596	0.0062	0.0483	0.0006	0.44	0.0540	0.0009	304	4	372	38	22
L24-2	0	291	226	0.777	0.3720	0.0091	0.0479	0.0007	0.32	0.0563	0.0014	302	4	464	55	54
L24-3	0	1088	50	0.046	0.7040	0.0196	0.0837	0.0014	0.33	0.0610	0.0017	518	8	641	60	24
L24-4C	0	339	174	0.513	0.7413	0.0162	0.0891	0.0011	0.20	0.0604	0.0014	550	7	618	50	12
L24-4R	0	281	166	0.593	0.3788	0.0103	0.0499	0.0008	0.31	0.0550	0.0015	314	5	414	62	32
L24-5	0.39	113	73	0.646	5.2215	0.0922	0.3168	0.0038	0.29	0.1196	0.0022	1774	19	1950	33	10
L24-6	0	490	165	0.336	0.3510	0.0073	0.0481	0.0007	0.39	0.0529	0.0011	303	4	324	46	7
L24-9	0	539	272	0.505	0.7521	0.0117	0.0912	0.0011	0.44	0.0598	0.0009	563	7	597	33	6
L24-10	0	154	136	0.879	0.3634	0.0084	0.0494	0.0007	0.28	0.0534	0.0012	311	4	344	53	11
L24-11	-0.16	328	209	0.637	0.9244	0.0140	0.1058	0.0013	0.42	0.0634	0.0009	648	7	721	32	11
L24-12	0	116	54	0.470	1.3287	0.0207	0.1405	0.0016	0.34	0.0686	0.0011	847	9	888	34	5
L24-13	0.43	2539	146	0.057	0.3778	0.0116	0.0488	0.0008	0.26	0.0561	0.0019	307	5	457	78	49
L24-16	0.1	485	241	0.497	0.3776	0.0062	0.0489	0.0006	0.33	0.0560	0.0009	308	3	452	38	47
L24-17	0	185	144	0.778	0.3632	0.0156	0.0487	0.0009	0.16	0.0541	0.0024	306	6	376	101	23
L24-19	0	233	212	0.910	0.3538	0.0090	0.0477	0.0007	0.29	0.0538	0.0014	301	4	362	58	20
L24-20	0	218	146	0.668	0.3579	0.0110	0.0484	0.0008	0.22	0.0536	0.0017	305	5	355	72	16
L24-32	0	320	159	0.496	0.7701	0.0148	0.0935	0.0013	0.41	0.0598	0.0011	576	7	595	41	3
L24-33	0	272	163	0.597	1.0815	0.0183	0.1210	0.0015	0.38	0.0648	0.0011	736	8	769	36	4
L30-21	0	306	240	0.784	0.3597	0.0092	0.0481	0.0007	0.30	0.0542	0.0014	303	4	380	58	25
L30-22	0	920	63	0.068	0.8833	0.0264	0.1024	0.0018	0.29	0.0626	0.0019	629	10	694	65	10
L30-23	-0.44	672	344	0.512	0.3666	0.0080	0.0481	0.0007	0.37	0.0553	0.0012	303	4	423	48	40
L30-24	0	925	99	0.107	0.5643	0.0081	0.0717	0.0009	0.48	0.0571	0.0008	447	5	494	30	11
L30-25	0	2028	2046	1.009	0.8096	0.0148	0.0962	0.0013	0.47	0.0610	0.0010	592	8	641	37	8
L30-26	0	542	166	0.307	0.3563	0.0080	0.0480	0.0007	0.34	0.0539	0.0012	302	4	366	51	21
L30-27	0	440	311	0.709	0.3534	0.0069	0.0479	0.0006	0.37	0.0535	0.0010	301	4	351	44	17
L30-28	0	176	342	1.944	1.8804	0.0465	0.1819	0.0024	0.15	0.0750	0.0020	1078	13	1068	54	-1
L30-29	-0.38	2448	2228	0.910	0.3715	0.0075	0.0479	0.0007	0.41	0.0563	0.0011	301	4	463	44	54
L30-30	0.83	9542	250	0.026	0.3463	0.0078	0.0467	0.0006	0.35	0.0538	0.0014	294	4	361	61	23
L30-31	0	591	618	1.045	0.3494	0.0091	0.0475	0.0007	0.30	0.0534	0.0014	299	4	344	60	15

The LA-ICP-MS data set is listed in Table 3.16 and plotted in a concordia diagram (Fig. 3.24b). Ages younger than 1.000 Ma are 204-corrected $^{206}Pb/^{238}U$, whereas older ages are 204-corrected $^{207}Pb/^{206}Pb$. Thirty seven analyses were performed, 32 of which yielded concordant ages ranging from 294 to 1975 Ma. Five analyses were rejected due to high common-Pb or degree of discordance. Nineteen analyses yielded Variscan ages and 13 analyses yielded older-than-Variscan ages. A total set of 19 Variscan zircon crystals provide a weighted average $^{206}Pb/^{238}U$ age of 303.0 ± 2.3 Ma (Fig. 3.24b). This weighted average age is similar to that calculated using ID-TIMS data (307.88 ± 0.86 Ma) within uncertainty. The ID-TIMS age of 307.88 ± 0.86 Ma is considered as the most accurate estimate for the age of the intrusion.

The thirteen older-than-Variscan ages represent 40% of inheritances. These ages are mostly Upper Neoproterozoic (from 550 to 847 Ma) (n = 8), and have been measured in dark anhedral to subeuhedral cores of stubby zircon (type-2) crystals; one of them was measured in a homogeneous dark core overgrown by a Variscan-age rim (L24-4, Table 3.16). Two youngest inherited zircon crystals show Cambrian (518 Ma) and Ordovician (447 Ma) ages (spots L24-18 and L30-30, Table 3.16) and are homogeneous stubby crystals. One Mesoproterozoic age of 1068 Ma was obtained in a homogenous dark core of a stubby zircon crystal (spot L30-28, Table 3.16 and Fig. 3.23). The two oldest inherited zircons are Paleoproterozoic, 1950 and 1975 Ma (spot L24-5 and L20-35, respectively; Table 3.16), and correspond to stubby zircon crystals.

3.8. Zircon saturation and Ti-in-zircon thermometries

Zircon saturation thermometry has been calculated based on the relationship between zircon solubility, temperature, and major element composition of the melt (Watson and Harrison, 1983; Hanchar and Watson, 2003). Zircon saturation thermometry of the Logrosán granite ranges from 699ºC to 777ºC and yields an average temperature of 742ºC (Table 3.10). Apparent temperatures for zircon crystallization have been also estimated using the Ti-in-zircon thermometer (Ferry and Watson, 2007). The Logrosán granite petrography suggests simultaneous crystallization of quartz, zircon and ilmenite; thus, $aSiO_2 = 1$ and $aTiO_2 < 1$. An activity of TiO_2 value of 0.6 based on the presence of ilmenite has been assumed. This would lead to underestimation of zircon crystallization temperatures by ≤50 °C (Watson and Harrison, 2005). Ti-in-zircon thermometry yields values from 744ºC to 1024ºC with an average temperature of 836ºC (Table 3.7), these values are markedly higher than the ones obtained by zircon saturation thermometry.

3.9. Discussion

3.9.1. Granite fractional crystallization

The whole-rock geochemistry described above provides no evidence for a unique fractional crystallization trend to link the main granite suite (Main Unit) with the evolved leucogranite units (Evolved Units). Hence, the Main and the Evolved Units are not related by a simple crystal fractionation process. Sequential restite fractionation can be dismissed as mafic xenoliths are absent in the Logrosán granite and most elements do not vary linearly with SiO_2 contents (Chappell et al., 1987). The low Ba and Sr contents together with the high Rb concentrations found in the granites suggest that they have undergone some fractional crystallization (Breaks and Moore, 1992), which is consistent with a cupola stockwork scenario. Source-rock heterogeneities could explain the compositional evolution of the Logrosán granite since a significant number of major and trace elements do not show any linear correlations (Fig. 3.20). Moreover, the great variability in the whole-rock initial Sr isotopic ratios ($^{87}Sr/^{86}Sr$: 0.7125-0.7286) and the Hf-isotope composition of the Variscan-age zircons from the Logrosán granite (from +5.7 to -10.5) indicate a heterogeneous magmatic system. The variation of more than 15 εHf units (Table 3.14) is the maximum range obtained in zircon samples from the Iberian Variscan granites (Teixeira et al., 2011; Villaseca et al., 2012; Merino, 2014; Merino et al., 2014). Besides, the lack of a single evolutionary path in terms of Sr, Ba, Rb, Eu and CaO between the Main and the Evolved Units indicates that fractional crystallization of plagioclase and K-feldspar did not occur in a simple closed magmatic system. Magmatic recharge from a deeper and chemically heterogeneous magma reservoir could produce the more residual and evolved granites of the Logrosán cupola. Thus, a complex multi-pulse granite system inefficiently mixed, formed by isotopically heterogeneous fractionated magmas that episodically replenish the Logrosán cupola is more likely than a single magma batch following closed *in situ* fractional crystallization processes.

3.9.2. Zircon saturation and Ti-in-zircon thermometries

The average temperatures obtained for the Logrosán Variscan-age zircon crystallization is 836 ºC, similar to other temperature estimates on S-type granites of the Central Iberian Zone (788 to 844ºC after Orejana et al., 2012; Merino et al., 2014). Lower temperature estimates (699-777 ºC, Table 3.10) have been obtained based on whole-rock zircon saturation. The average whole-rock zircon saturation temperature (742ºC) is below the average Ti-in zircon temperature (836ºC) for the Logrosán granite. Granitoids rich in zircon inheritances are probably

undersaturated with respect to zircon at the source. Consequently, the calculated zircon saturation temperatures are most likely underestimations of the actual temperature of crystallization (Miller et al., 2003). The zircon inheritances of the Logrosán granite may yield unrealistic zircon saturation temperatures. Hence, the average Ti-in-zircon temperature (836ºC) provides a better estimation of the temperature of the magma from which the zircon crystallized.

3.9.3. Inheritances and source constraints

Mineralogical and geochemical features of the Logrosán granite (e.g., high peraluminosity and low CaO contents) and the absence of mafic microgranular enclaves suggest a crustal-derived melt origin with a major contribution of aluminous metasedimentary sources (Dias et al., 2002; Chappell et al., 1991). Likewise, high whole rock $\delta^{18}O$ values point to an ^{18}O-enriched sedimentary or metasedimentary protolith. Phosphorous-rich character may be inherited from a P-rich source (Rodríguez-Alonso et al., 2004; Villaseca et al., 2008) as indicated in other P-rich granites from the area (Antunes et al., 2008; Villaseca et al., 2008; Ramírez and Menéndez, 1999). This P-rich character is also consistent with the presence of phosphate mineralization surrounding the granite, and with dispersed phosphate mineralization in the regional Schist Greywacke Complex (Vindel et al., 2014; Chapter 5, this volume).

Zircon crystals from the Logrosán granite have Zr/Hf ratios ranging 41-55 with an average value of 48. According to Pupin (2000), the estimated signature of zircon from the continental crust is 36-45. However, Pérez-Soba et al. (2007) estimated the Zr/Hf ratios of zircon crystals from migmatites and augen orthogneisses from the Spanish Central System and suggested a slightly higher range (Zr/Hf = 36-56) for pure crustal signatures. Hence, Zr/Hf ratios of the Logrosán zircon fit well with crustal signatures. It is expected that the Zr/Hf ratio in a single magma series should be approximately constant (Wang et al., 2010). Therefore, the wide range of Zr/Hf values for such a small granitic body may indicate not only a different degree of differentiation but also a participation of several magma inputs.

The high initial $^{87}Sr/^{86}Sr$ ratios of the Logrosán samples are attributed to a significant participation of the Sr derived from crustal material as established for similar granitoids of the CIZ (Ruiz et al., 2008; Castro et al., 1999; Villaseca et al., 1998b). Variability in $^{87}Sr/^{86}Sr$ data of the Logrosán granite (Fig. 3.22) may well indicate an origin by partial melting of a compositionally heterogeneous continental crust. The $^{87}Sr/^{86}Sr$ ratios of the Logrosán granite plot in an intermediate position on the Sr-Nd isotopic field from other monzogranites and leucogranites from the Central Extremadura Batholith. The large variability in $^{87}Sr/^{86}Sr$ data at almost constant εNd values can hardly indicate mixing of different proportions of mantle-

derived magmas with crustal sources (Castro et al., 1999). The low negative initial Nd isotope ratios of the Logrosán granite (around -4.2), typical of other Central Extremadura Batholith granites (e.g., Castelo Branco, Antunes et al., 2008; Alburquerque, González Menéndez and Bea, 2004; Montes de Toledo, Villaseca et al., 2008; Merino et al., 2014), contrasts with other S-type granites from northern areas of the CIZ (Fig. 3.22). The metasediments of the SGC also show low Nd isotope signatures (at Variscan times) and might be the most appropriate protolith of the Logrosán granite (Fig. 3.22).

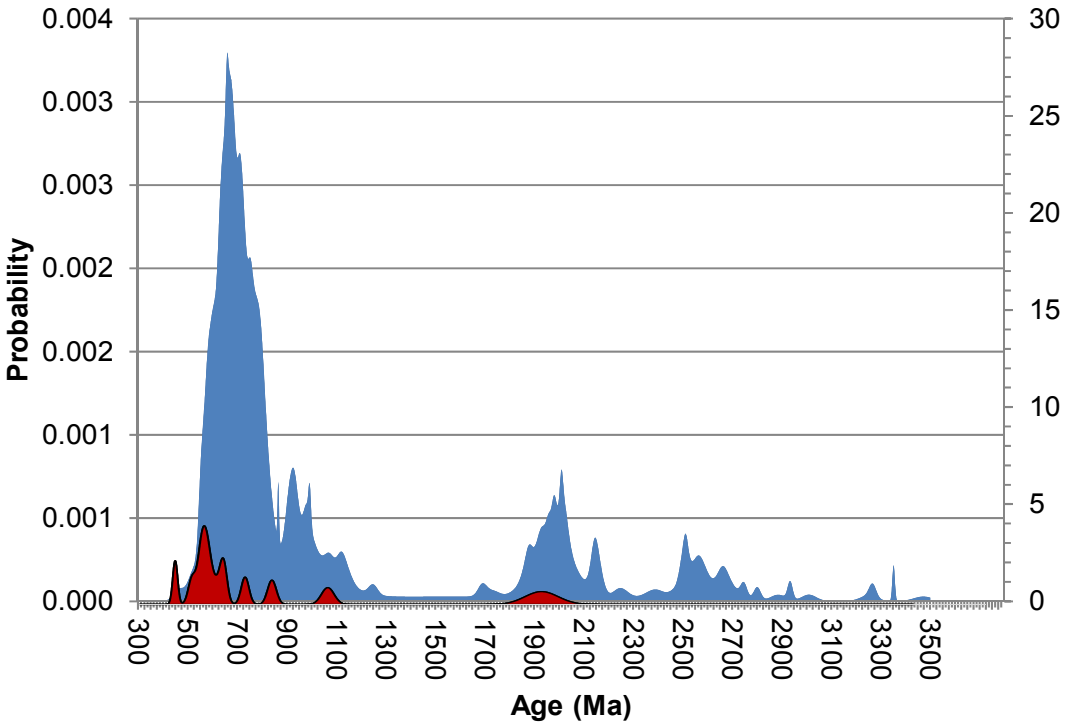

Fig. 3.25: Relative probability plots of the inherited zircon U-Pb ages of the Logrosán granite (red fields) compared to the data available of the CIZ metasediments from the Schist Greywacke Complex (blue fields): samples ZD1 and ZD2 (Gutiérrez-Alonso et al., 2003), sample of the Sabugal area (Teixeira et al., 2011), samples PNC1 and PNC2 (Pereira et al., 2012), and sample Ctc67 (Talavera et al., 2012).

Inherited zircon crystals from the Logrosán granite define an age range of ca. 447-1975 Ma displaying predominant Neoproterozoic populations (Table 3.16). Despite the limited dataset (13 inherited zircons), it is still possible to distinguish two main groups: (1) Cambro-Ordovician and Neoproterozoic ages and (2) Meso- and Paleoproterozoic ages (Fig. 3.25). The first group of inheritance (Early Paleozoic and Neoproterozoic) is the most abundant and fits well with materials derived from the Cadomian orogeny. The minor amount of Mesoproterozoic zircon inheritances, and the distribution of Nd and Hf model ages (around 1.45 ± 0.2 Ga), either in Variscan granites and Neoproterozoic metasediments, have been attributed to the Saharan and Arabian-Nubian shields as possible supplying provinces for the Central Iberian Zone (e.g., Pereira et al., 2012; Villaseca et al., 2011; Bea et al., 2010; Henry et al., 2009). The only zircon

inheritance of Ordovician age (ca. 447 Ma) could be related to the Ordovician magmatism described along the Central Iberian Zone (e.g., Rubio-Ordóñez et al., 2012; Neiva et al., 2009; Solá et al., 2008; Bea et al., 2007). In general, the probability density curve of the Logrosán granite inheritances shows a broad overlap with the zircon U–Pb age distribution previously reported for the Schist Greywacke Complex ages (Talavera et al., 2012; Teixeira et al., 2011; Gutiérrez-Alonso et al., 2003) (Fig. 3.25). This comparison again points to the Schist Greywacke Complex as the most probable protolith of the Logrosán granite.

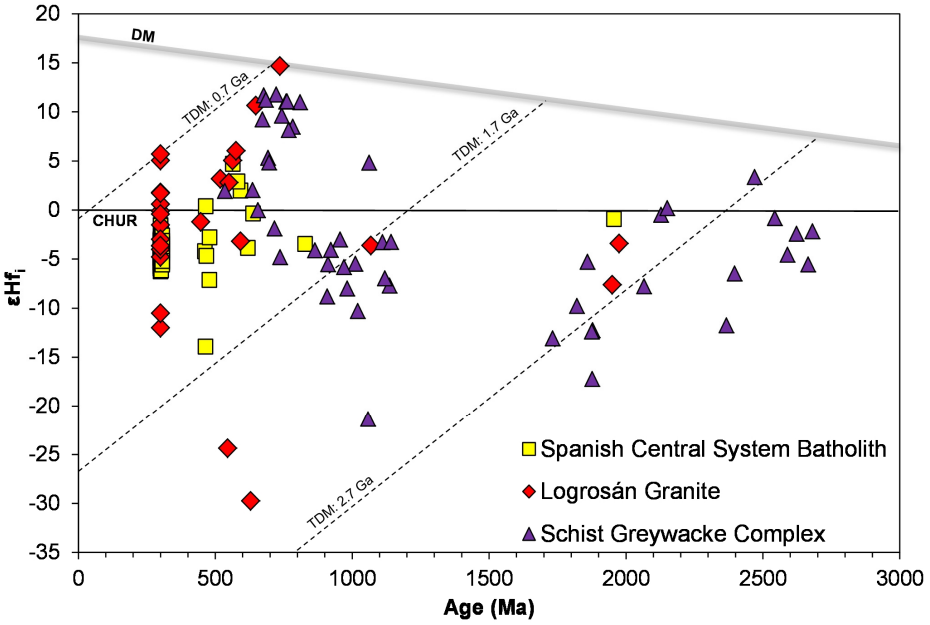

Fig. 3.26: Initial epsilon Hf vs. U–Pb age plot of the zircon crystals from the Logrosán granite. Data from the SGC (represented by the Sabugal sample from Teixeira et al., 2011) and the Spanish Central System granitoids (Villaseca et al., 2012) are given for comparison. Dotted lines indicate the crustal evolution paths at 0.7 Ga ($^{176}Lu/^{177}Hf$ = 0.0010), 1.7 Ga ($^{176}Lu/^{177}Hf$ = 0.0013) and 2.7 Ga ($^{176}Lu/^{177}Hf$ = 0.0006).

Magmatic zircon crystals from the Logrosán granite have a significant wide range of $\varepsilon Hf_{(t)}$ values showing variations up to 15 εHf units, similar to those observed in samples of Variscan S-type granites from northern Portugal (Teixeira et al., 2011). The large range of negative $\varepsilon Hf_{(t)}$ values is in agreement with the S-type nature of the granite, but there is also a significant proportion of positive $\varepsilon Hf_{(t)}$ values (Fig. 3.26). The large range of negative $\varepsilon Hf_{(t)}$ values denotes an origin by partial melting of heterogeneous crustal sources or by crustal contamination of a mantle-derived parental magma as proposed for other Variscan S-type granites from the Central Iberian Zone (Teixeira et al., 2011; Neiva et al., 2013). Although positive $\varepsilon Hf_{(t)}$ values tend to be interpreted as mantle-derived, this cannot be easily applied to the Logrosán granite. The absence of coeval mafic magmatism and the clearly peraluminous and phosphorous-rich character of the Logrosán cupola is more in agreement with the involvement of recycled juvenile material in the genesis of this granite. From this prospective, εHf values of Neoproterozoic

zircons from the SGC metasediments (sample from Sabugal area, spots 21 and 70 of Teixeira et al., 2011; see also Orejana et al., 2015), recalculated at the age of the Logrosán granite emplacement, yield positive values (up to +4.5) that overlap with those found in Variscan-age zircons from the Logrosán granite. Moreover, some inherited Neoproterozoic zircon crystals within the Logrosán granite show strong positive $\varepsilon Hf_{(t)}$ values (up to +14.7, e.g., L24-33, Table 6) similar to zircon populations found in metasediments from the SGC (up to +11.7, spot Malcl-21 of Teixeira et al., 2011). Such correlation reinforces the genetic relationship with this probable protolith (Fig. 3.26) and is in agreement with the presence of a recycled mantle-derived component in the granite crustal source.

3.9.4. Geochronological comparison

Widespread granite generation occurred across the Central Iberian Zone over 325-300 Ma time interval (e.g., Dias et al., 1998; Fernández Suárez et al., 2000; Bea et al., 2003; Orejana et al., 2012; Merino et al., 2014). Most of the felsic magmatism in the CIZ is syn- to post-tectonic with respect to the last ductile deformation phase (D_3) (Dias et al., 1998) with a bulk of data peaks at 320 (mainly syn-D_3 leucogranites of Galicia and northern Portugal), 308-306 and 301 Ma (Dias et al., 1998; Orejana et al., 2012; Merino et al., 2014). The U-Pb results here presented indicate that the Logrosán intrusion occurred at ca. 308 Ma, thus in a post-tectonic Variscan stage.

When compared with granites from the southern CIZ (those of the CEB), there is a good overlap in age with this determined for the Logrosán rocks: 310 Ma for Castelo Branco (Antunes et al., 2008), 308 Ma for Nisa-Alburquerque (Solá et al., 2009), 311-298 Ma for the Montes de Toledo (Orejana et al., 2011; Merino et al., 2014), and 309 Ma for the Cabeza de Araya and Trujillo plutons (Gutiérrez-Alonso et al., 2011). It is also similar to the age of the emplacement of the Los Pedroches batholith (314-304 Ma, Carracedo et al., 2009), which limits the southern edge of the CIZ. The age range of emplacement of the Spanish Central System batholith is also similar: 311-298 Ma (Bea et al., 2003; Zeck et al., 2007; Díaz-Alvarado et al., 2011; Orejana et al., 2012); and so is the age of emplacement of the Montes de Toledo batholith: 316-297 Ma (Merino et al., 2014). Thus, the granite batholiths and plutons from central Spain and the southern CIZ are practically coeval.

Chapter 4: Sn-(W) MINERALIZATION

SUMMARY:

The Logrosán Sn-(W) ore deposits represent the perfect case-study granite-related ore deposit, owing to its petrographical features and close relationship to the granite intrusion. Field interpretation, mineralogy, paragenetic studies, geochronology, fluid inclusion and isotope studies provide further constraints on the ore formation. Most outstanding results are derived from the fluid inclusion study, and its combination with geochemical and geochronological data have been essential to unravel the origin and evolution of metal-bearing fluids. The common presence of N_2-CH_4-rich fluids indicates that assimilation of nearby organic-rich components from the country metasedimentary host-rocks took place during the final stages of the granite consolidation and emplacement. Thus, metamorphic fluids seem to have played an important role in cassiterite transportation under reduced conditions. Mixing of metamorphic and post-magmatic fluids is likely to be responsible for the Logrosán Sn-(W) ore deposit development and for the cassiterite precipitation.

Sn-(W) MINERALIZATION

4.1. General features

The Logrosán tin ore deposits consist of a network of Sn-(W) cm to dm-size veins, stockworks, and disseminated ores in altered host rocks, as well as secondary alluvial, eluvial and colluvium deposits. The Logrosán tin ore area comprises two different sectors (Fig. 4.1): (1) the Cerro de San Cristóbal sector: intragranitic veins and disseminated mineralization in greisen within the Logrosán granite; and (2) the El Serranillo sector: veins and disseminated mineralization hosted by muscovitized and tourmalinized Neoproterozoic metasediments from the Schist Greywacke Complex (SGC).

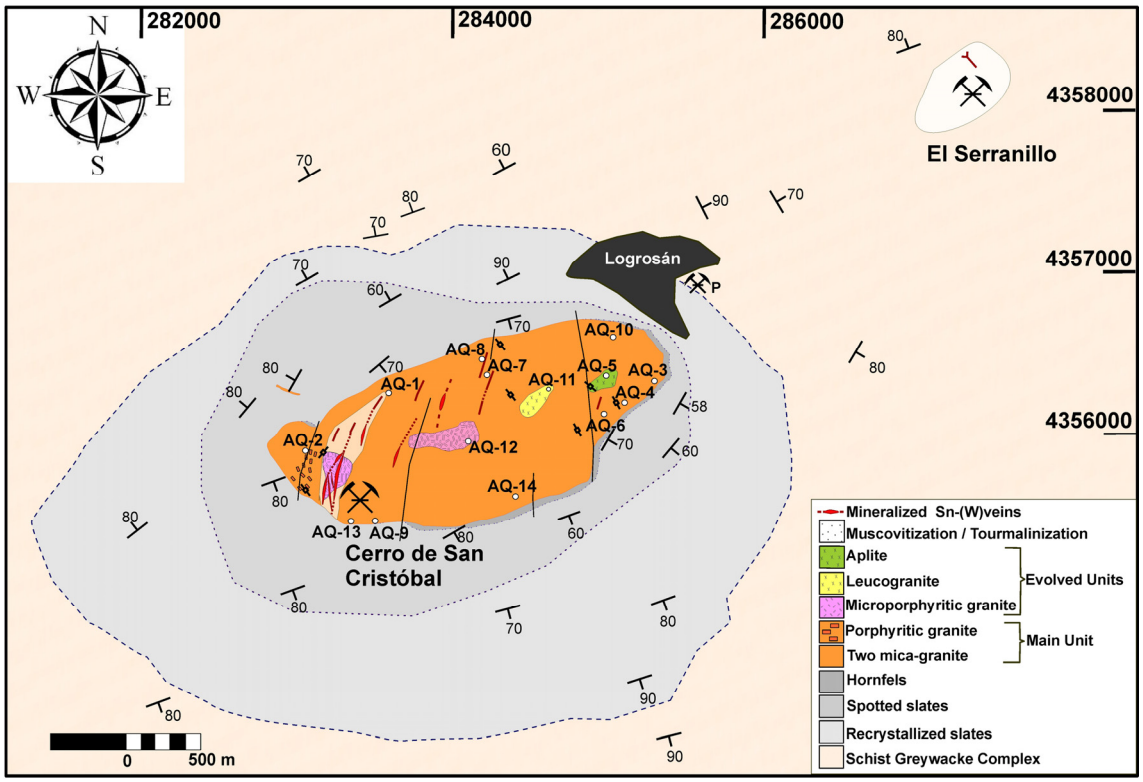

Fig. 4.1: Geological map showing the Logrosán ore deposits. Granite and greisen sampling points are indicated by open circles.

4.1.1. Cerro de San Cristóbal sector

The Cerro de San Cristóbal sector (Fig. 4.1) includes the Logrosán granite and its contact metamorphic aureole. The Logrosán cupola (~ 4 km^2) displays a sub-elliptical form elongated in the NE–SW axis, and corresponds to a coarse- to medium-grained two-mica-leucogranite. This is a tin-rich S-type late Variscan pluton with a felsic, phosphorous-rich and strongly peraluminous character. More evolved units are located in the summits of the San Cristóbal hill, and are related

to later intrusions from deeper magmatic reservoirs (Chicharro et al., 2013; 2014). Further description of the Logrosán granite is found in Chapter 3.

Distinct episodes of alteration and veining are recognized in the Logrosán granite. The granite is triggered by numerous barren and mineralized veins. Similarly to Rossi (1975) and Guijarro (1985b), four main vein systems have been recognized. Crosscutting field relationships allow stablishing a relative vein chronology. (i) In the first place, there is a well-represented system of narrow (~2 cm) barren quartz-tourmaline veins with diverse directions. This system corresponds to the quartz-tourmaline veins predating the mineralization stage. As they have different strikes throughout the granite, it is probable that there were more than one episode of tourmaline-bearing veins, some of them maybe overlapping the ore deposition. Moreover, relatively thick (~ 10 cm) quartz-tourmaline veins have been found nearby the granite-SGC contact, within the granite and the Neoproterozoic metasedimentary SGC rocks. They display a N165 strike within the granite, being locally parallel to some granitic structures (e.g., pegmatite dikes); hence, they may be interpreted as coeval (Fig. 4.2a). Tourmaline needle-like crystals are disposed here along the vein strike (Fig. 4.2b). However, quartz-tourmaline veins within the hornfels from the metamorphic aureole have usually a N30 strike and do not visibly cut the granite. Tourmaline crystals sometimes fill tension gashes-like structures within these veins, following a N165 strike (Fig. 4.2c). Tension gash-like geometries indicate the torn and stretching of the early N30 quartz veins, with the tourmaline needles filling fractures that are parallel to the maximum stretching direction (σ_1), and perpendicular to the minimum compressive stress (σ_3) (Fig. 4.2d). The tension gash-like directions are coincident with the early quartz-tourmaline veins found in the granite nearby the granite-SGC contact (N165). This suggests that the release of volatiles (at least, of boron) is significant, even reaching the metamorphic aureole, in a late-magmatic and early fracture stage, prior to the cassiterite precipitation. (ii) Quartz-tourmaline veins are cut by quartz-cassiterite veins, which have strikes ranging from N20 to N40, but preferentially N35 (Fig. 4.3a). Quartz-cassiterite veins usually are 10-20 cm thick; thinner crosscutting quartz-cassiterite veins are also often found in mineralized areas resulting in relatively wide stockwork zones. Quartz-cassiterite veins show a 2-10 cm greisenized selvage with quartz, muscovite, tourmaline, and disseminated cassiterite. Mineralized veins and greisen in the Logrosán granite are generally found in the western sector of the hill. (iii) Quartz-sulfide veins are commonly 20-50 cm thick, but may reach up to 1 m thick. They usually lack of selvage and cut the quartz-cassiterite veins (Fig. 4.3b). They have N-S to N10 directions. (4) The late vein system ranges from N110 to N130 strikes. This system comprises thin barren veins (~2 cm) consisting of milky quartz. They cut every other vein system.

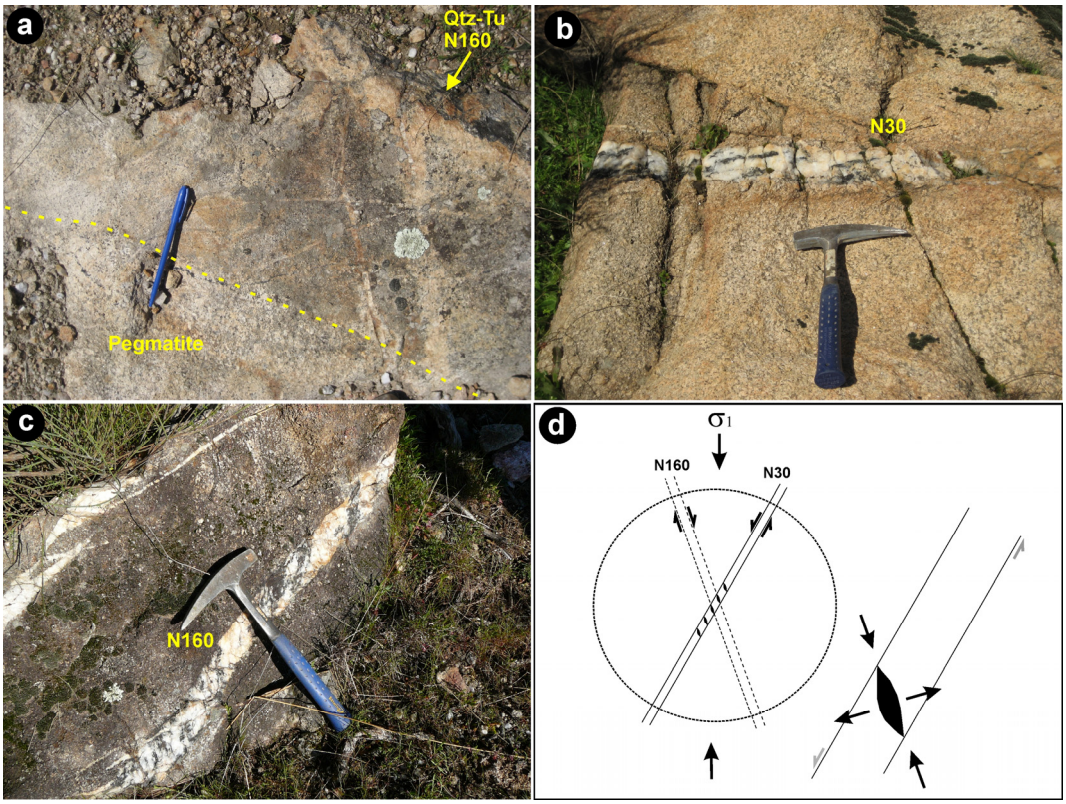

Fig. 4.2: a) N160 quartz-tourmaline vein within the granite. Note that quartz-tourmaline vein and pegmatite body directions are parallel. **b)** N160 quartz tourmaline vein within the Logrosán granite. **c)** N30 quartz-tourmaline vein hosted by the SGC, displaying tension gash-like tourmaline filling. **d)** Schematic drawing of the tension gash-like structures, motion and stress vectors.

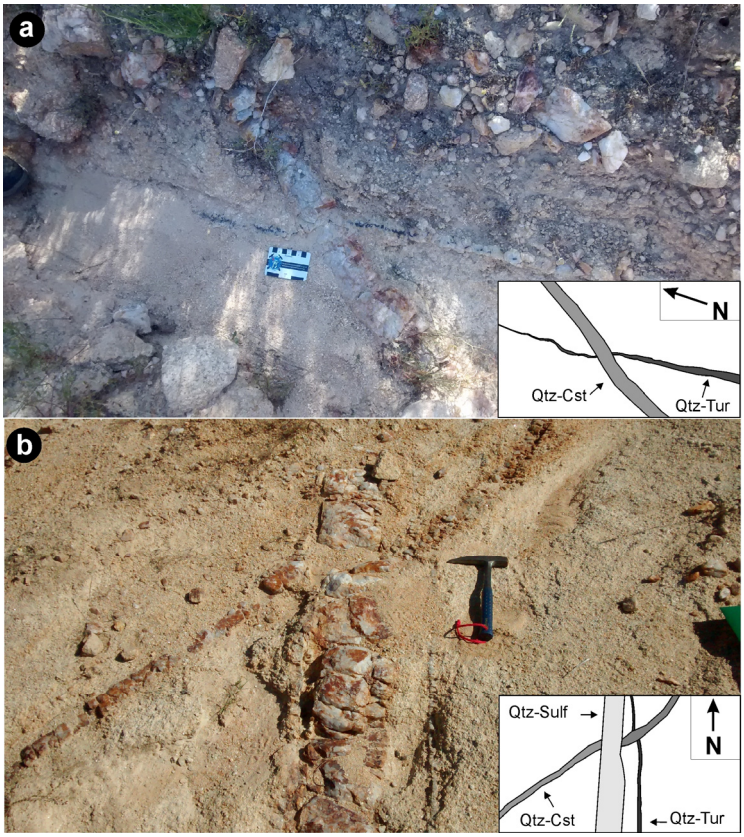

Fig. 4.3: Crosscutting relationships between different veins from the Logrosán granite.

Wall rock hydrothermal alteration in the granite mainly consists of tourmalinization, greisen alteration, and kaolinization. Tourmalinization is represented by the multiple quartz-tourmaline veins, and the pervasive tourmalinization of the wall-rocks, which may be associated with silicification. Greisen alteration is found in the first 2 to 10 cm around the veins (Figs. 4.4a). The extension of the alteration zone increases where major proportion of crosscutting veins occur, affecting wider areas (Fig. 4.4b). Disseminated cassiterite is usually found in small cavities within the selvages and greisen zones (Fig. 4.4b). However, cassiterite mainly occurs close to the walls in the quartz-cassiterite veins, which may have different sizes, mainly from decimeter (Fig. 4.4c) to centimeter (Fig. 4.4d).

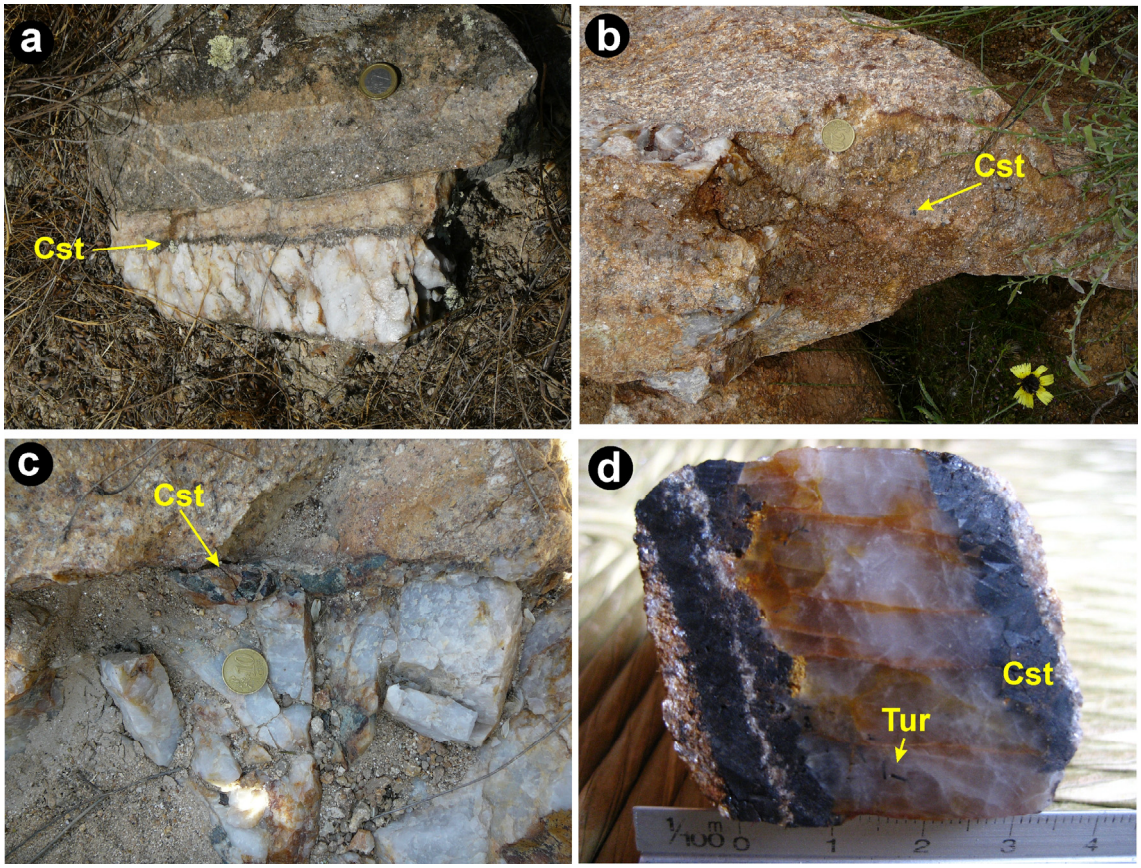

Fig.4.4: a) Quartz-cassiterite (Cst) vein with greisen selvage. **b)** Intense greisenization of the Logrosán granite and disseminated cassiterite. **c)** Quartz-cassiterite vein, with visible cassiterite crystals, and a narrow greisen selvage. **d)** Photograph of a typical quartz-cassiterite veinlet, with a muscovite (Ms) selvage and late tourmaline (Tur) needles.

Several faults and fault zones have been observed in the Cerro de San Cristóbal hill, with N40-N60 strikes. Slickensides indicate a right-lateral (dextral) sense of motion along the fault (Fig. 4.5a and 4.5b). Kaolinitation may be very intense around vein swarms, affecting relatively wide areas (Fig. 4.5c). Faults play an important role providing zones of high permeability; the flow of fluids increases and the feldspars are partly crushed, increasing the reactive surface.

Consequently, the hydrolysis of feldspars and the kaolin formation become faster and more efficient. The hydrolisis of K-feldspar to kaolinite is described by the following equations, including (i) the formation of sericite/illite from feldspars, and subsequently, (ii) the hydrolysis of sericite/illite to kaolinite:

i. $3KAlSi_3O_8 + 2H^+ \rightarrow KAl_3Si_3O_{10}(OH)_2 + 6SiO_2 + 2K^+$

ii. $2KAl_3Si_3O_{10}(OH)_2 + 2H^+ + 3H_2O \rightarrow 3Al_2Si_2O_5(OH)_4 + 2K^+$

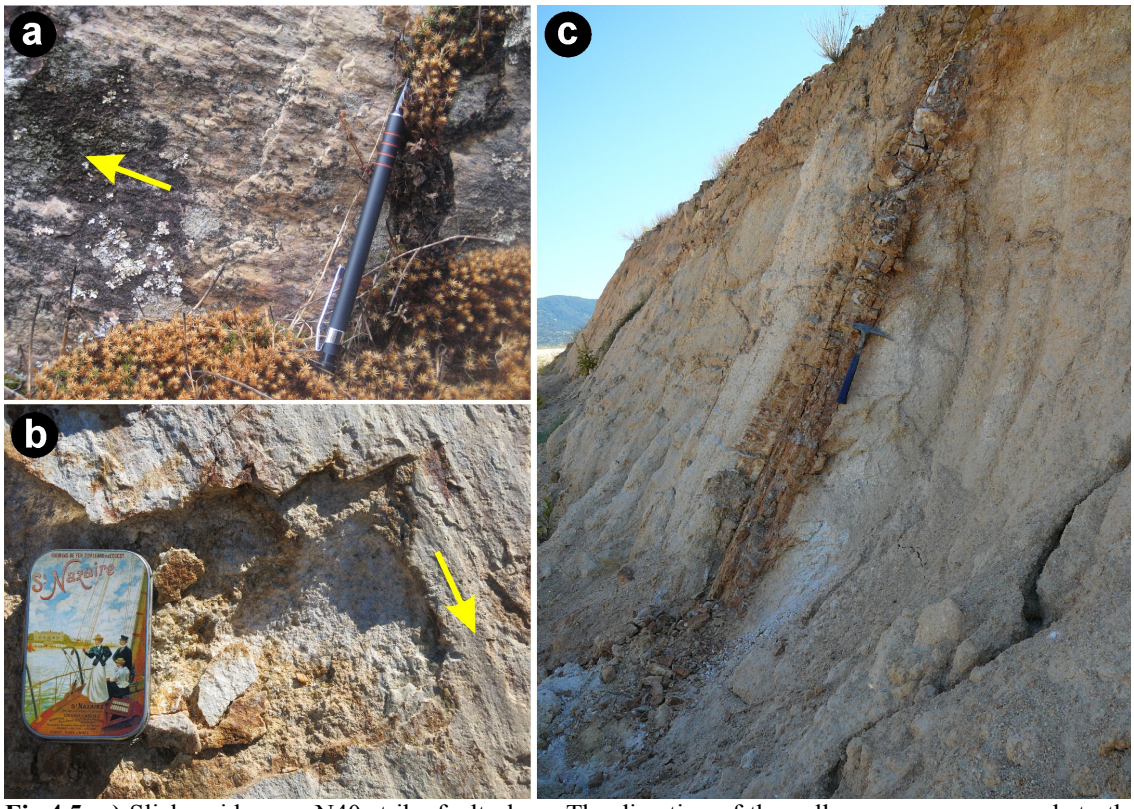

Fig.4.5: a) Slickenside on a N40 strike fault plane. The direction of the yellow arrow corresponds to the movement of the missing block, indicating a sinistral sense of movement. **b)** Slickenside on a N60 strike fault plane within a fracture swarm zone. Note the kaolin formation. **c)** Intense kaolinized granite in a fault zone.

4.1.2. El Serranillo sector

Sn-(W) mineralized veins crosscut the metasedimentary sequence of the SGC in the El Serranillo sector, about 3 km to the NE from the Logrosán granite outcrop (Fig. 4.1). These mineralized veins strike in several directions, with dips ranging from subvertical to subhorizontal forming a stockwork area of approximately 500 m in diameter, where the system is nonetheless dominated by N30 veins (Fig. 4.6a). The stockwork host rocks are strongly tourmalinized and, to a lesser extent, silicified and muscovitized (Fig. 4.6b). The widespread alteration of these rocks is noticeable up to 500 m southwest of the El Serranillo mine. Silicification and recrystallization of the SGC metasediments give these rocks a similar aspect to that of the recrystallized slates of the

outer zone of the metamorphic aureole. In this regard, a SW–NE transect from the Cerro de San Cristóbal sector to the El Serranillo indicates that the mineralization from the latter is probably located away from the metamorphic aureole. Arsenopyrite, molybdenite, cassiterite, columbite and rutile are disseminated in the altered zone.

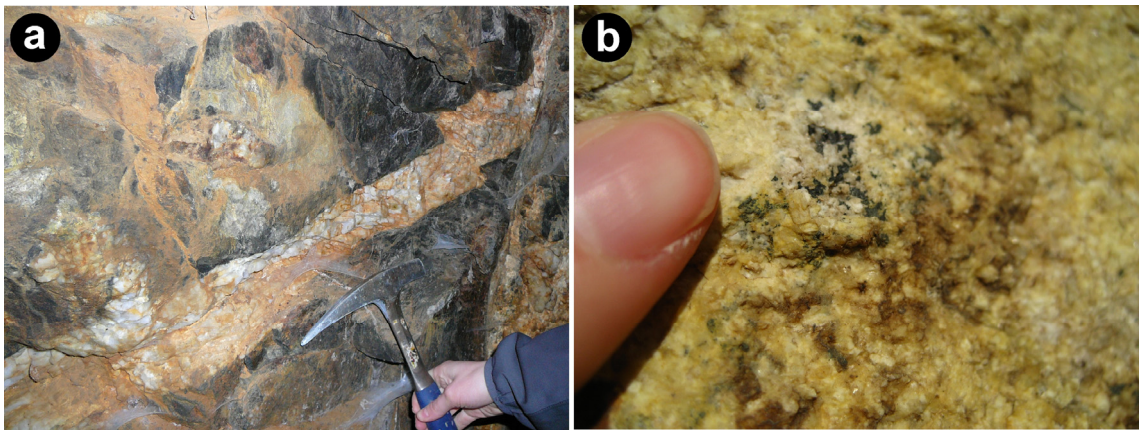

Fig.4.6: a) Quartz-cassiterite stockwork in the El Serranillo gallery. **b)** Disseminated Nb-Ta mineralization within silicified and muscovitized SGC host-rocks.

4.2. Paragenetic sequence

The mineral paragenesis of the Logrosán ore deposits is shown in Fig. 4.7. Two main ore stages and one alteration stage have been recognized.

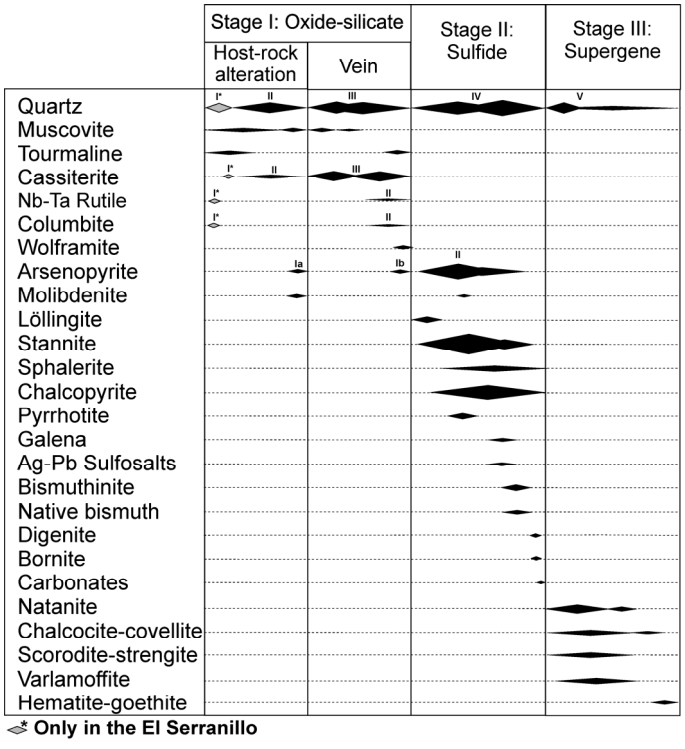

Fig.4.7: Paragenetic sequence of the Logrosán ore deposits.

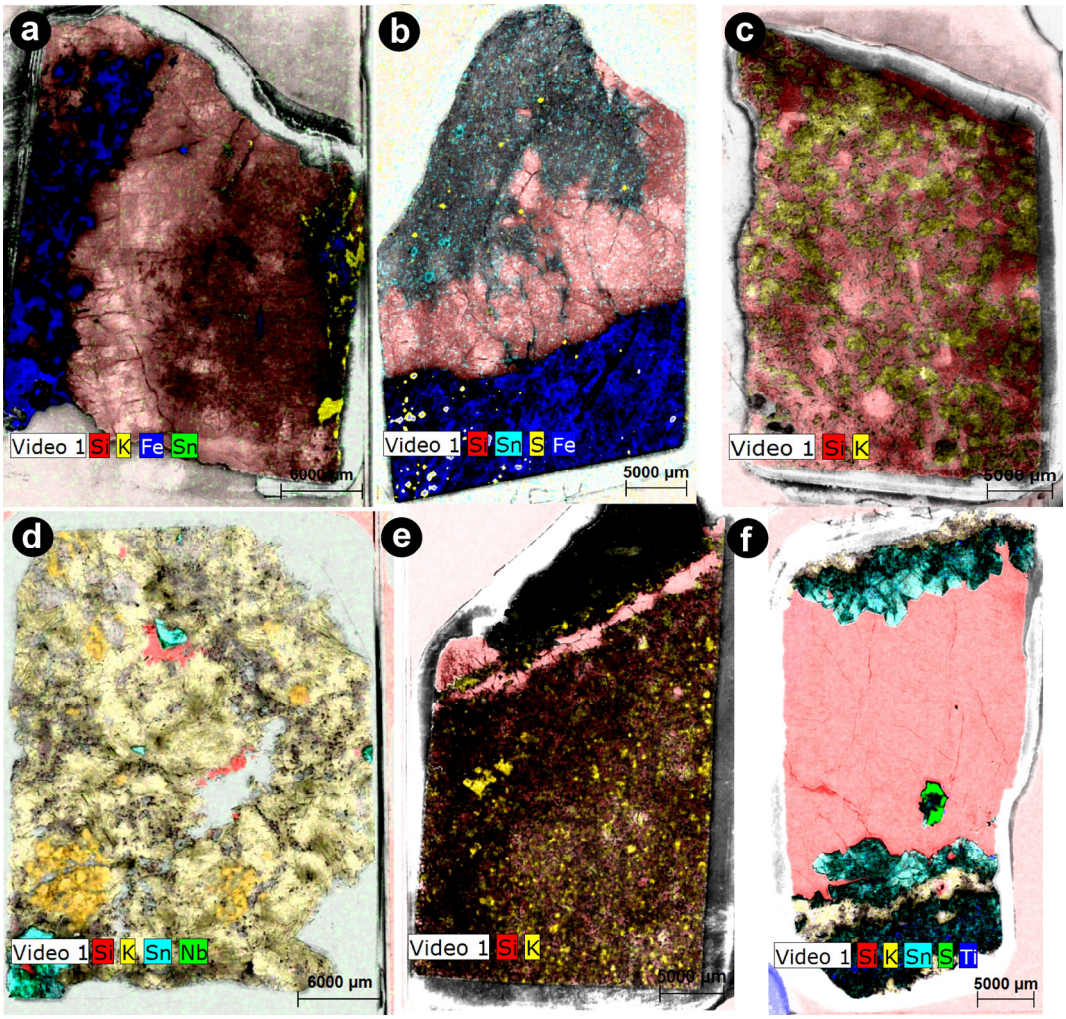

Fig.4.8: Micro-FRX images. **a)** Quartz-tourmaline vein and greisen selvage: tourmaline (dark blue), quartz (red), muscovite (yellow). **b)** Mineral association in altered SGC metasediments: tourmaline (dark blue), cassiterite (light blue), quartz (red), arsenopyrite and molybdenite (yellow). **c)** Greisen-like altered granite: muscovite (yellow), quartz (red). **d)** Mineral association in greisen altered granite: cassiterite (blue), muscovite (yellow), quartz (red). **e)** Quartz-cassiterite vein and greisenized selvage; cassiterite (black, at the top), quartz (red), muscovite (yellow). **f)** Mineral association in a Qtz-Cst vein: cassiterite (blue), arsenopyrite (green), quartz (red), muscovite (light yellow).

- *Stage I: Oxide-silicate stage*

The earliest ore stage is characterized by the precipitation of the economic minerals (i.e. cassiterite, columbite, Nb-Ta rutile and minor wolframite) (Fig. 4.7). Two substages are recognized: (i) a first host-rock alteration substage (Fig. 4.8a, 4.8b, 4.8c, and 4.8d); and (ii) a second vein substage (Fig. 4.8e and 4.8f). (i) The host-rock alteration substage is a pervasive alteration of the wall-rocks, resulting in complete muscovitization (Ms I) of the rocks. Columbite (Cb I) and Nb-Ta rutile (Nb-Ta Rt I) intergrowths are found disseminated within the muscovitized metasedimentary wall rocks in the El Serranillo sector, and are locally associated with zircon. A first generation of cassiterite (Cst) has been found bordering the columbite and Nb-Ta rutile

earlier phases. However, the host-rock alteration substage is mostly characterized by disseminated, zoned subhedral to euhedral cassiterite crystals without inclusions (Cst II). Cst II occurs within granite and metasedimentary altered wall rocks (Fig. 4.9a). Minor early arsenopyrite (Apy I) and molybdenite are also present. (2) The vein substage started with mica (Ms II) selvages. Quartz, euhedral cassiterite (Cst III) (Fig. 4.9b) and minor euhedral wolframite and arsenopyrite (Apy II) crystals were subsequently deposited. Subhedral columbite (Cb II) and Nb-Ta rutile (Nb-Ta Rt II) are found in cassiterite. Tourmaline needles appear as a later phase concentrated toward the center of the veins.

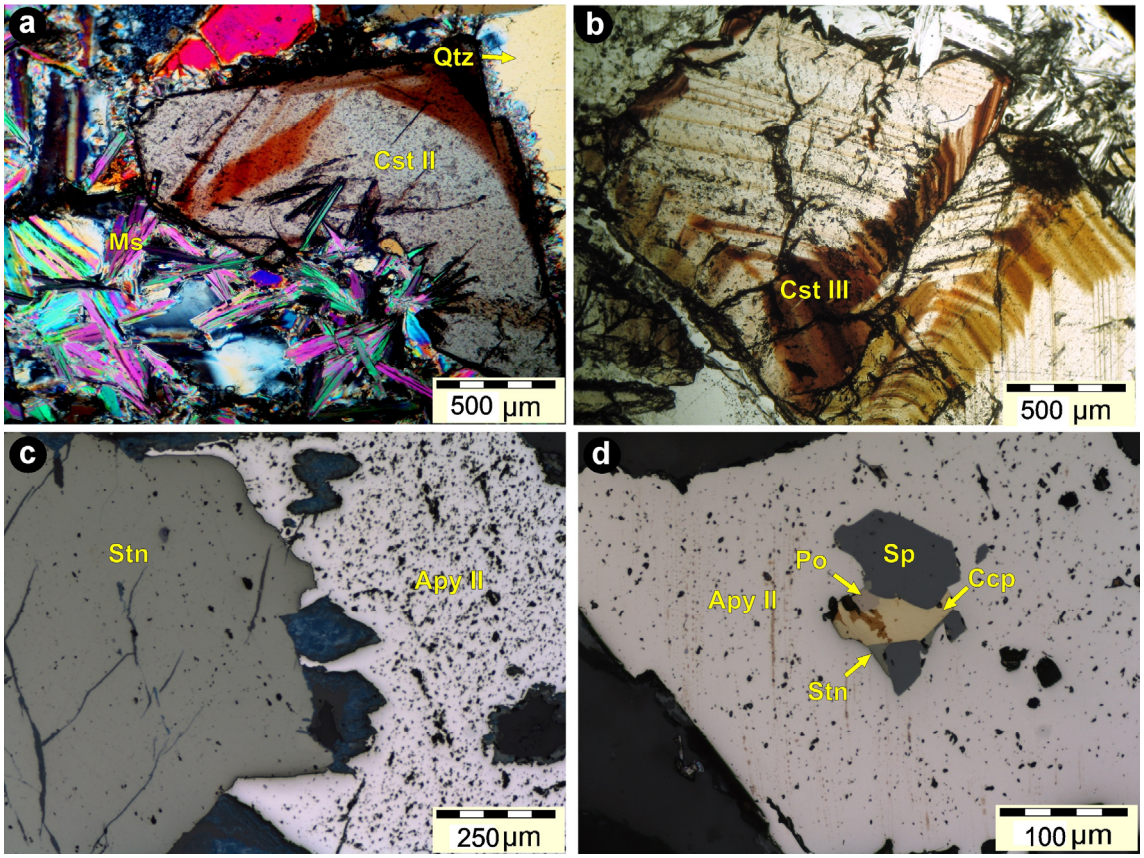

Fig. 4.9: **a)** Greisen-type alteration with zoned cassiterite (Cst II), muscovite (Ms) and quartz (Qtz). Transmitted light, crossed nicols (NX). **b)** Microphotography in transmitted light of zoned cassiterite (Cst III) and selvage of a quartz-cassiterite vein. **c)** Arsenopyrite (Apy II) and stannite (Stn) intergrowth. Reflected light. **d)** Arsenopyrite (Apy II) crystal containing inclusions of stannite (Stn), sphalerite (Sph), chalcopyrite (Cpy) and minor pyrrhotite (Po). Reflected light.

- *Stage II: Sulfide stage*

Arsenopyrite and stannite are the dominant minerals in the Sulfide Stage (Fig. 4.9c). Most arsenopyrite in this stage (Apy II) precipitates early in the paragenetic sequence, and presents usually euhedral to subeuhedral habits. Löllingite has been recognized in the cores of Apy II. Arsenopyrite forms intergrowths and curvilinear equilibrium grain boundaries with stannite. Arsenopyrite II also contains rounded crystals of stannite, sphalerite, chalcopyrite and minor

pyrrhotite, suggesting co-precipitation of these phases (Fig. 4.9d). The presence of stannite, sphalerite and chalcopyrite as replacement patches, and along fractures in Apy II, indicates that they are formed continually at different times of the Sulfide Stage. These sulfides also occur as large crystals penecontemporaneous with each other. Moreover, sphalerite single crystals include minute blebs of chalcopyrite. Similarly, stannite occurs as small blebs of exsolution-type in sphalerite, and vice-versa. Galena and Ag-Pb sulfosalts are rare, they appear coprecipitated with sphalerite inclusions within stannite crystals. Minor native bismuth and bismuthinite intergrowths are found as inclusions within arsenopyrite, and also, within sphalerite enclosed in Apy II. Bismuthinite and native bismuth intergrowths are also found as isolated crystals. Other minor sulfides, such as molybdenite, tetrahedrite, digenite and bornite have been found locally. Calcite and siderite occur as a very late phase.

- *Stage III: Supergene stage*

Natanite replaces cassiterite, resulting in a partial or complete replacement of the original ore; hematite and goethite are also found in these oxidizing zones. Primary sulfides are partly altered to chalcocite-covellite; developed particularly along fractures and grain boundaries. Scorodite-strengite and varlamoffite locally replace stannite and arsenopyrite.

4.3. Mineral chemistry

The whole dataset of major and trace-element composition of selected mineral phases from the Logrosán Sn-(W) ore deposits are in electronic supplementary material (Supplementary Table 3, Table 4, Table 5, Table 6 and Table 7).

4.3.1. Cassiterite

About 200 analyses of cassiterite were performed, and a representative selection is summarized in Table 4.1. Cassiterite (Cst I) occurs bordering Nb-Ta rutile (Nb-Ta Rt I) and columbite (Cbt I) intergrowths (Fig. 4.10a). Cst I is scarce, but stands out because its chemical difference with the later cassiterite generations. Cst I has lower Sn, higher Nb+Ta and higher Fe+Mn contents than Cst II and III. Disseminated single cassiterite crystals in the altered wall rocks (Cst II) show compositional zoning in transmitted light, with darker zones exhibiting strong pleochroism from red to colorless. No inclusions have been found within Cst II. Cassiterite from quartz veins (Cst III) is characterized by euhedral (> 5 mm) zoned crystals, hosting Nb-Ta rutile and columbite intergrowths as inclusions (Fig. 4.10c). Cst II and III chemical compositions are very similar, although they belong to different stages in the paragenetic sequence. Most cassiterite crystals

consist of nearly pure SnO_2, and are richer in Fe than in Mn. Although Cst II and Cst III may contain up to 2.09 wt.% Nb_2O_5 and 1.30 wt.% Ta_2O_5, the Nb_2O_5 and Ta_2O_5 average is of 0.19 and 0.18 wt.%, respectively (Table 4.1). Cst I contains relatively higher Nb_2O_5 (0.00 – 1.73 wt.%; average of 0.88 wt.%) and higher Ta_2O_5 (1.73 – 6.92 wt.%; average of 2.69 wt.%) than Cst II and Cst III (Table 4.1). Cassiterite from the Logrosán ore deposits plots close to the (Sn, Ti, W) corner and following the (Sn,Ti,W)-(Fe,Mn)$(Nb,Ta)_2$ trend (Fig. 4.11a and 4.11b). Cassiterite dark zones tend to be depleted in Sn and enriched in Fe, Nb and Ti. Tantalum content among dark zones is heterogeneous, with the red zones slightly enriched in Ta as compared to the brown zones.

Table 4.1: Representative electron microprobe analysis (%wt) of disseminated cassiterite in altered host rocks (Cst I and Cst II) and quartz veins (Cst III) from El Serranillo (SER) and Cerro de San Cristóbal (L) sectors. Calculated number of ions on the basis of 2 oxygens.

	Cst I		Cst II					Cst III					
	SER5		SER2	SER2	L43	L106	L107	SER4	8697	L42	L42	L58	L110A
	22	65	30	31	11	60	37	27	17	30	21	34	111
FeO	1.04	0.98	0.12	0.22	0.03	0.24	0.09	0.35	0.28	0.32	0.03	0.03	0.06
MnO	0.03	0.42	0.00	0.00	0.00	0.00	0.00	b.d.l.	b.d.l.	b.d.l.	0.02	b.d.l.	b.d.l.
MgO	b.d.l.	0.01	b.d.l.	b.d.l.	b.d.l.	0.02	0.00	b.d.l.	b.d.l.	b.d.l.	b.d.l.	b.d.l.	0.02
TiO_2	0.63	0.18	0.51	0.84	0.52	0.92	0.63	0.07	0.75	0.74	0.20	0.93	0.46
Nb_2O_5	1.02	1.73	0.11	0.22	0.03	0.36	0.32	b.d.l.	1.09	0.45	0.13	0.05	0.00
Ta_2O_5	3.68	1.73	0.20	0.14	0.22	0.42	0.00	0.18	0.01	0.56	0.21	0.34	0.17
SnO_2	93.7	94.4	99.2	98.1	98.8	98.0	99.0	99.5	98.3	96.9	99.3	98.7	99.2
WO_3	0.07	0.12	0.03		0.04	0.01	0.09	b.d.l.	0.01	0.07	0.00	0.00	0.00
Total	100.1	99.6	100.2	99.5	99.7	100.0	100.1	100.1	100.4	99.0	99.9	100.1	100.0
Fe	0.022	0.020	0.003	0.004	0.001	0.005	0.002	0.007	0.006	0.007	0.001	0.001	0.001
Mn	0.001	0.009	0.000	0.000	0.000	0.000	0.000	0.000	0.000	0.000	0.000	0.000	0.000
Mg	0.000	0.000	0.000	0.000	0.000	0.001	0.000	0.000	0.000	0.000	0.000	0.000	0.001
Ti	0.012	0.003	0.009	0.016	0.010	0.017	0.012	0.001	0.014	0.014	0.004	0.017	0.009
Nb	0.011	0.019	0.001	0.002	0.000	0.004	0.004	0.000	0.012	0.005	0.001	0.001	0.000
Ta	0.025	0.012	0.001	0.001	0.001	0.003	0.000	0.001	0.000	0.004	0.001	0.002	0.001
Sn	0.931	0.941	0.986	0.978	0.996	0.971	0.982	0.994	0.968	0.961	1.002	0.979	0.989
W	0.000	0.001	0.000	0.000	0.000	0.000	0.001	0.000	0.000	0.000	0.000	0.000	0.000
Total	1.002	1.006	1.001	1.001	1.008	1.001	1.000	1.003	1.000	0.991	1.009	1.000	1.001

4.3.2. Nb-Ta rutile and columbite

Nb-Ta rutile and columbite intergrowths (Nb-Ta Rt I and Cb I) occur in altered metasedimentary rocks in the El Serranillo. They may reach up to 200 μm in size, and show patchy zoned crystals (Fig. 4.10b). Single oscillatory zoned columbite crystals are found locally (Fig. 4.10c). Nb-Ta rutile from El Serranillo (Nb-Ta Rt I) contains up to 14.15 wt.% Nb_2O_5 and 20.63 wt.% Ta_2O_5. Ta and Sn usually dominate over Nb and W, respectively (Table 4.2). The Nb-Ta rutile I composition aligns along the (Sn,Ti,W)-(Fe,Mn)$(Nb,Ta)_2$ trend (Fig. 4.11c). Columbite I is a ferrocolumbite with an average composition of $(Fe_{0.78}Mn_{0.17})(Nb_{1.48}Ta_{0.31}Ti_{0.23})O_6$. Cb I contains up to 61.35 wt.% Nb_2O_5, and 28.01 wt.% Ta_2O_5 (Table 4.2). In oscillatory single zoned columbite crystals, rims are enriched with Nb and Ti, and depleted in Ta.

In the cassiterite veins, Nb-Ta rutile (Nb-Ta Rt II) and columbite (Cb II) have not been found together. Nb-Ta rutile and columbite inclusions are randomly distributed within cassiterite

crystals; they occur in both, the dark and light cassiterite zones, and no chemical variations around the inclusions in the host cassiterite have been recognized. Nb-Ta rutile and columbite inclusions are small (50–100 μm), and display oscillatory zoning (Fig. 4.10d). Nb-Ta rutile of cassiterite veins is compositionally heterogeneous, with variable TiO_2 content from 59.14 to 92.55 wt.% and Nb>Ta contents (Table 4.2). This Nb-Ta rutile II differs compositionally from Nb-Ta rutile I by showing lower Nb+Ta contents (Fig. 4.11c). Nb_2O_5 reaches up to 24.88 wt.% and Ta_2O_5, 11.11 wt.%. Columbite II and columbite I show similar compositions in the (Sn,Ti,W)-(Fe,Mn)-(Nb,Ta) diagram. Both of them are ferrocolumbite, and fit well along the (Sn,Ti,W)-(Fe,Mn)$(Nb,Ta)_2$ trend (Fig. 4.11d). However, Cb II has a higher Nb content (from 57.12 to 72.42 wt.% Nb_2O_5) than the highest Nb content found in Cb I and considerably lower Ta contents (Table 4.2). Columbite II has an average composition of $(Fe_{0.76}Mn_{0.18})(Nb_{1.69}Ta_{0.09}Ti_{0.22})O_6$.

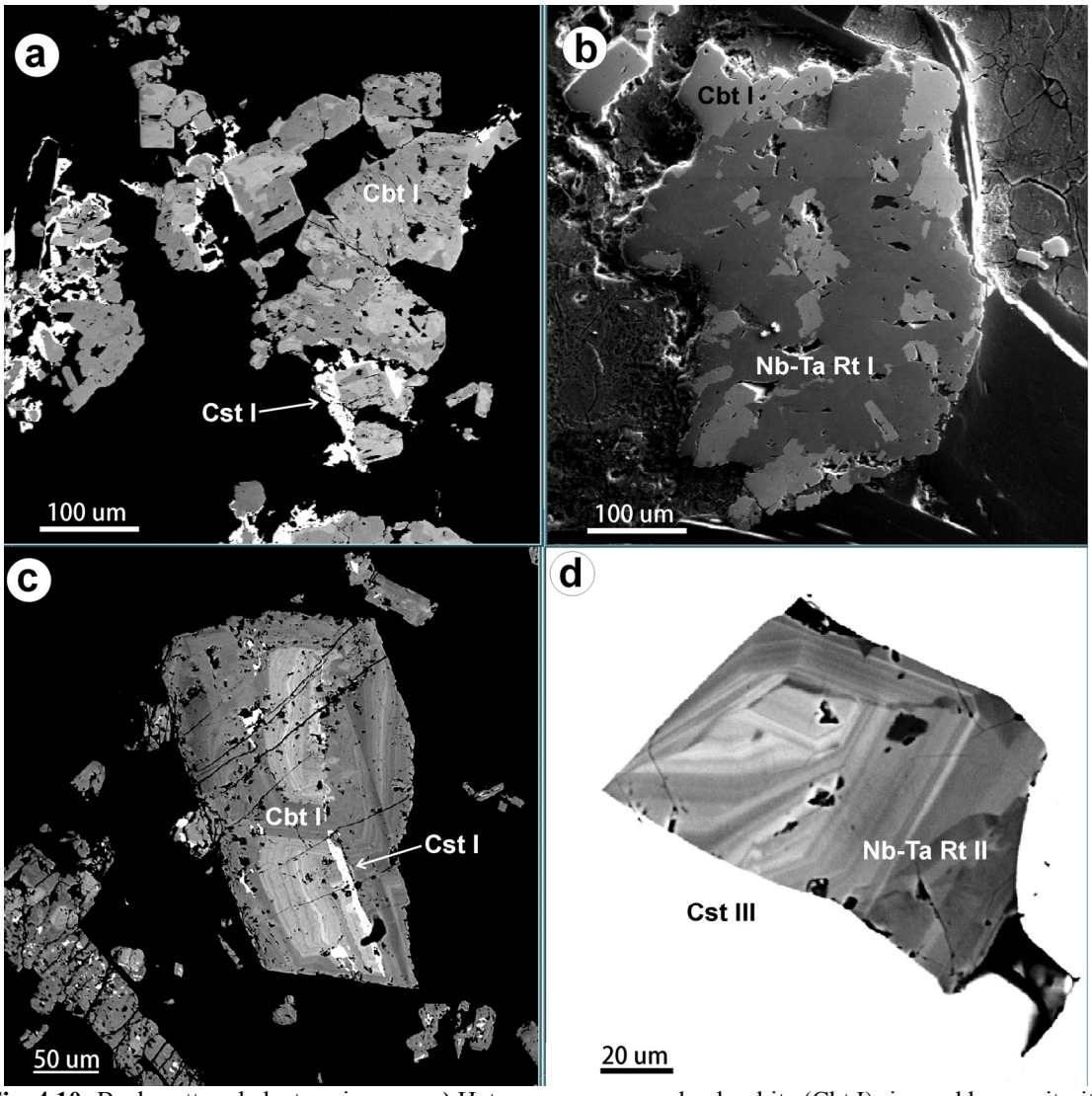

Fig. 4.10: Backscattered electron images. **a)** Heterogeneous zoned columbite (Cbt I) rimmed by cassiterite (Cst I). **b)** Columbite (Cbt I) and Nb-Ta rutile (Nb-Ta Rt I) intergrowth. **c)** Oscillatory zoned columbite (Cbt I) and cassiterite (Cst I). **d)** Oscillatory zoned Nb-Ta rutile inclusion (Nb-Ta Rt II) in cassiterite (Cst III).

Table 4.2: Representative electron microprobe analysis (wt.%) of disseminated Nb-Ta rutile and columbite in altered host rocks (Nb–Ta Rt I and Cb I) and inclusions within cassiterite (Nb–Ta Rt II and Cb II) from El Serranillo (SER) and Cerro de San Cristóbal (SC) sectors.

	Nb-Ta Rt I				Nb-Ta Rt II				Cb I				Cb II			
Samples	**SER**	**SER**	**SER**	**SER**	**SER**	**SER**	**SC**	**SC**	**SER**	**SER**	**SER**	**SER**	**SER**	**SER**	**SC**	**SC**
Element	**57**	**60**	**69**	**70**	**13**	**14**	**26**	**80**	**10**	**23**	**68**	**71**	**47**	**1**	**35**	**84**
FeO	4.78	5.70	7.62	5.34	1.43	5.14	5.93	8.37	9.07	15.72	16.56	16.97	18.08	19.86	19.51	19.44
MnO	0.04	0.04	0.04	0.05	b.d.l.	0.00	0.00	0.02	10.11	2.35	1.74	1.85	0.86	0.07	0.12	0.62
MgO	0.00	0.00	0.00	0.00	b.d.l.	0.01	0.00	0.00	0.14	0.00	0.05	0.04	0.02	0.00	0.01	0.03
TiO_2	69.6	67.7	57.4	69.7	92.6	71.9	68.4	59.1	3.06	3.85	4.71	3.98	6.78	4.76	6.55	4.11
Nb_2O_5	6.90	9.40	14.15	8.19	2.31	15.3	12.8	24.9	54.2	47.2	56.5	56.0	65.1	67.9	63.9	72.4
Ta_2O_5	17.1	15.0	17.6	15.5	1.61	2.38	11.0	4.65	20.93	28.01	18.17	18.42	4.98	2.58	5.54	2.48
SnO_2	1.87	2.05	2.44	1.01	1.56	4.38	1.63	2.67	0.68	0.34	1.27	1.05	1.70	0.80	1.71	0.86
WO_3	0.06	0.08	0.10	0.07	0.19	0.41	0.40	0.16	2.17	1.46	0.25	0.23	2.42	3.01	2.19	0.26
Total	100.3	100.0	99.4	99.8	99.6	99.5	100.1	99.9	100.3	98.9	99.3	98.5	100.0	99.0	99.6	100.2
Fe	0.061	0.074	0.103	0.069	0.016	0.064	0.076	0.108	0.898	0.833	0.831	0.863	0.853	0.946	0.929	0.908
Mn	0.000	0.000	0.001	0.001	0.000	0.000	0.000	0.000	0.031	0.126	0.089	0.095	0.041	0.003	0.006	0.029
Mg	0.000	0.000	0.000	0.000	0.000	0.000	0.000	0.000	0.004	0.000	0.005	0.004	0.002	0.000	0.001	0.003
Ti	0.804	0.787	0.700	0.804	0.957	0.800	0.783	0.684	0.218	0.184	0.212	0.182	0.288	0.204	0.280	0.172
Nb	0.048	0.066	0.104	0.057	0.014	0.102	0.088	0.173	1.439	1.351	1.533	1.540	1.662	1.749	1.646	1.828
Ta	0.071	0.063	0.078	0.065	0.006	0.010	0.045	0.019	0.386	0.483	0.297	0.305	0.076	0.040	0.086	0.038
Sn	0.011	0.013	0.016	0.006	0.009	0.026	0.010	0.016	0.011	0.009	0.030	0.026	0.038	0.018	0.039	0.019
W	0.000	0.000	0.000	0.000	0.001	0.002	0.002	0.001	0.016	0.024	0.004	0.004	0.035	0.044	0.032	0.004
Total	0.997	1.003	1.001	1.001	1.003	1.003	1.004	1.001	3.002	3.009	3.001	3.018	2.996	3.005	3.019	3.001

Calculated number of ions on the basis of 2 oxygens for Nb-Ta rutile, and 6 oxygens for columbite.

4.3.3. Substitution mechanisms in the Sn–Nb–Ta–Ti mineral phases

Nb-Ta-Ti bearing phases (Nb-Ta rutile I and Cb I) occur as single crystals or intergrowths, and are the first ores to precipitate. An early and scarce cassiterite generation (Cst I) is found in the rims of the early Nb-Ta phases. This cassiterite contains relatively high Nb, Ta and Fe contents, compared to the later generations (Fig. 4.11, Table 4.1).

A comparison of the geochemistry of Logrosán cassiterite to samples from similar Portuguese tin ore deposits (Neiva, 1996; 2008) has been accomplished. Cassiterite zoning from Logrosán resembles cassiterite zoning from Portuguese Sn>W-bearing quartz veins. In both cases, lighter zones are nearly pure SnO_2, whereas the darker zones are enriched with Ta, Fe and Nb, as also described in other tin ore deposits from the Central Iberian Zone (Murciego et al., 1997). The entrance of these elements in the cassiterite suggests the coupled substitution: $3Sn^{4+} \leftrightarrow (Fe,Mn)^{2+} + 2(Nb,Ta)^{5+}$. This mechanism has been described as dominant in cassiterite from pegmatites, high-temperature quartz veins and for the dark zones of cassiterite from similar ore deposits (Murciego et al., 1997; Neiva, 1996; 2008). Cst I shows a more complex behavior, probably associated with the presence of some Fe^{3+} in its structure. Moreover, the Ti content is also higher in darker zones than in nearly pure SnO_2 lighter zones of the cassiterite from Logrosán (Cst II). The incorporation of Ti in cassiterite can be explained by the direct substitution $Ti^{4+} \leftrightarrow Sn^{4+}$. On the basis of textural and chemical features, the Nb-Ta phases (columbite II and Nb-Ta rutile II) have been interpreted as inclusions within the Logrosán cassiterite. This is

consistent with the occurrence of an earlier Nb-Ta rutile and columbite predating the cassiterite precipitation. The mechanism $3(Sn,Ti)^{4+} \leftrightarrow (Fe,Mn)^{2+} + 2(Nb,Ta)^{5+}$ is the dominant one for cassiterite, Nb-Ta rutile, and columbite.

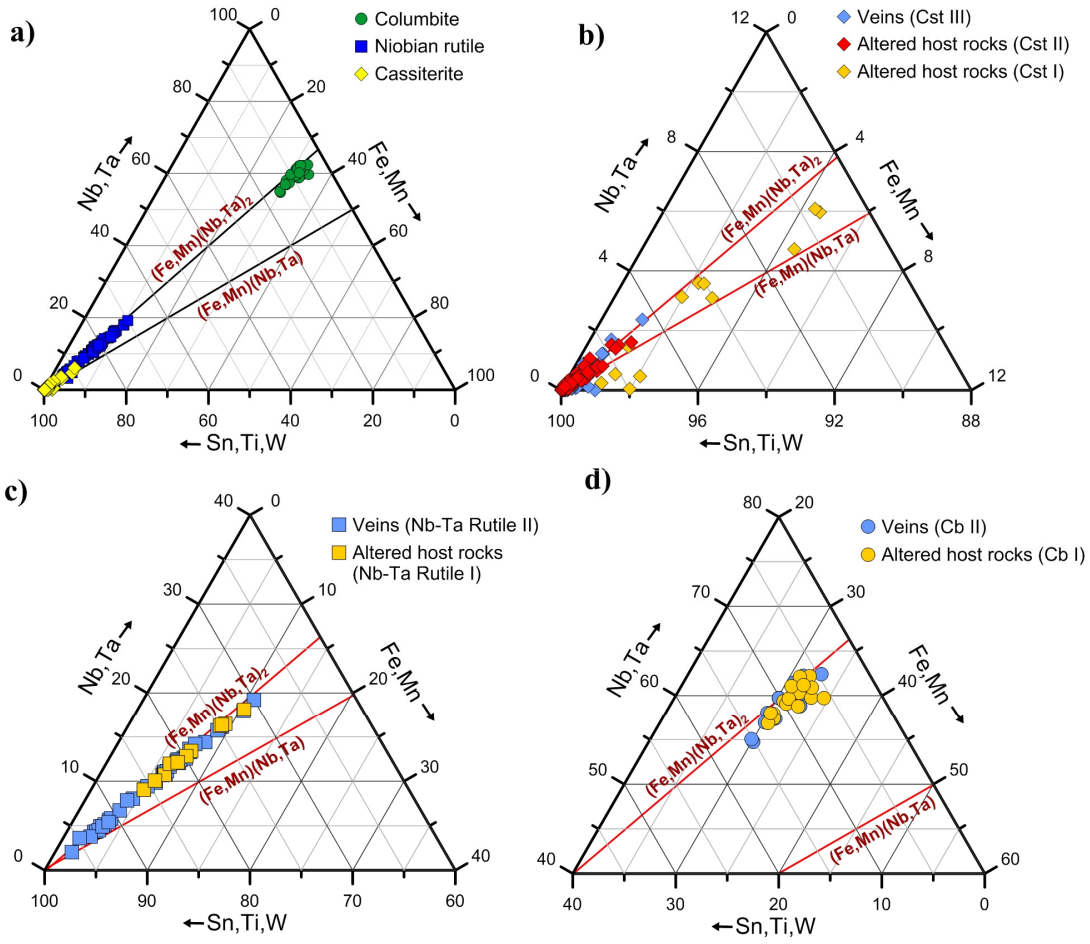

Fig. 4.11: Compositional diagrams of (Sn,Ti,W)–(Nb,Ta)–(Fe,Mn) for: **a)** Sn–Nb–Ta–Ti mineral phases **b)** cassiterite, **c)** Nb-Ta rutile and **d)** columbite.

4.3.4. Sulfides

Representative sulfide compositions from the Logrosán veins are given in Table 4.3. Arsenopyrite is the most common and ubiquitous sulfur in the Logrosán ore deposits, appearing in both the Oxide and the Sulfide stages. A total of 99 analyses have been performed on arsenopyrite from greisen, quartz-cassiterite and quartz-sulfide samples. Arsenopyrite from the Oxide Stage (Apy I) is characterized by small (~ 200 µm), isolated euhedral crystals. The proportion of Fe ranges from 34.06 to 34.69 at.%. The proportion of As (32.70–34.41 at.%) varies inversely with S (31.03–32.80 at.%). In the Sulfide Stage, arsenopyrite (Apy II) appears as euhedral to subeuhedral grains, up to few mm across, co-precipitating first with löllingite, and subsequently, with pyrrhotite,

sphalerite, stannite and chalcopyrite. Arsenopyrite individual crystals are mostly homogeneous, though some show zoning, with variations higher than 1 at.% As from core to rim. The Fe content ranges from 32.91 to 35.19 at.%. The As and the S contents are inversely correlated. Sulfur varies from 30.13 to 33.79 at.%, while As shows a wide range of variation from 31.62 to 35.11 at.%. The composition of stannite is characterized by appreciable variations of Zn and Fe contents (0.27–11.04 at.% Zn; 1.94-14.17 at.% Fe). The contents in Sn, Cu and S are homogeneous (11.63–14.30 at.% Sn; 22.80–27.65 at.% Cu; 48.62–51.42 at.% S). The chemical composition of sphalerite shows variations in Zn and Fe (38.72–48.06 at.% Zn; 0.98–10.39 at.% Fe) and constant S content (50.16-51.60 at.% S). Stannite enriched in Zn and sphalerite enriched in Fe are associated with pyrrhotite inclusions.

Table 4.3: Average composition of sulfide minerals from the Logrosán ore deposits (wt.%; EMPA) (Apy: arsenopyrite, Stn: stannite; Sp: sphalerite, Ccp: chalcopyrite, Po: pyrrhotite). (L, LOG = Logrosán, SER = Serranillo)

	Apy I (oxide stage)			Apy II (sulfide stage)			Stn			Sph		Cpy		Po
	L105	L111	L111	LOG5	L4.2	SER7	LOG12	LOG13	SER4	LOG4.3	L4.2	LOG4.3	SER4	LOG4.3
Element	**42**	**80**	**81**	**27**	**133**	**59**	**53**	**85**	**46**	**7**	**103**	**6**	**67**	**5**
Zn wt.%	b.d.l.	b.d.l.	b.d.l.	b.d.l.	b.d.l.	b.d.l.	6.11	2.11	2.62	53.52	63.87	b.d.l.	b.d.l.	0.18
Ag	b.d.l.	b.d.l.	b.d.l.	0.01	b.d.l.	b.d.l.	0.01	0.09	0.00	b.d.l.	0.54	0.05	0.01	b.d.l.
Co	b.d.l.	b.d.l.	b.d.l.	0.03	b.d.l.	b.d.l.	b.d.l.	b.d.l.	0.00	0.03	b.d.l.	0.04	0.03	0.07
Bi	b.d.l.	b.d.l.	b.d.l.	0.06	b.d.l.	b.d.l.	0.10	0.07	0.10	0.05	b.d.l.	0.10	0.14	0.12
Ni	b.d.l.	b.d.l.	b.d.l.	b.d.l.	b.d.l.	b.d.l.	b.d.l.	b.d.l.	b.d.l.	b.d.l.	b.d.l.	b.d.l.	b.d.l.	b.d.l.
Fe	35.3	35.3	35.0	34.8	34.7	35.7	8.01	8.52	11.2	11.1	1.40	30.0	30.4	58.5
Mn	b.d.l.	b.d.l.	b.d.l.	b.d.l.	b.d.l.	b.d.l.	b.d.l.	b.d.l.	b.d.l.	b.d.l.	0.04	b.d.l.	b.d.l.	b.d.l.
Cu	b.d.l.	b.d.l.	b.d.l.	b.d.l.	b.d.l.	b.d.l.	28.5	29.6	27.6	0.02	b.d.l.	33.1	34.8	0.10
Cd	b.d.l.	b.d.l.	b.d.l.	0.05	b.d.l.	b.d.l.	0.11	0.07	0.12	0.86	b.d.l.	0.04	0.00	0.03
Sn	0.01	b.d.l.	b.d.l.	0.01	b.d.l.	b.d.l.	26.67	30.35	28.51	b.d.l.	b.d.l.	0.05	0.17	b.d.l.
Sb	b.d.l.	b.d.l.	b.d.l.	0.07	b.d.l.	b.d.l.	b.d.l.	b.d.l.	b.d.l.	0.06	b.d.l.	0.05	0.01	0.05
Pb	0.15	0.10	0.16	0.13	0.04	0.15	0.17	0.10	0.11	0.16	0.13	0.19	0.14	0.22
As	45.9	45.6	46.7	45.7	46.8	44.3	b.d.l.	b.d.l.	b.d.l.	b.d.l.	b.d.l.	b.d.l.	b.d.l.	0.03
S	18.9	19.3	18.6	18.9	18.3	19.9	29.6	28.6	29.1	34.1	33.2	35.3	33.7	39.9
Total	100.3	100.3	100.4	99.7	99.8	99.9	99.2	99.6	99.3	99.9	99.6	98.9	99.4	99.1
Zn at.%	0.00	0.00	0.00	0.00	0.00	0.00	5.09	1.79	2.19	39.2	47.6	0.00	0.00	0.12
Ag	0.00	0.00	0.00	0.00	0.00	0.00	0.00	0.04	0.00	0.00	0.27	0.02	0.00	0.00
Co	0.00	0.00	0.00	0.03	0.00	0.00	0.00	0.00	0.00	0.02	0.00	0.03	0.03	0.05
Bi	0.00	0.00	0.00	0.02	0.00	0.00	0.02	0.02	0.03	0.01	0.00	0.02	0.03	0.02
Ni	0.00	0.00	0.00	0.00	0.00	0.00	0.00	0.00	0.00	0.00	0.00	0.00	0.00	0.00
Fe	34.5	34.3	34.3	34.1	34.2	34.5	7.81	8.46	11.0	9.50	1.23	24.8	25.3	45.5
Mn	0.00	0.00	0.00	0.00	0.00	0.00	0.00	0.00	0.00	0.00	0.04	0.00	0.00	0.00
Cu	0.00	0.00	0.00	0.00	0.00	0.00	24.4	25.9	23.8	0.02	0.36	24.1	25.5	0.07
Cd	0.00	0.00	0.00	0.02	0.00	0.00	0.05	0.03	0.06	0.37	0.00	0.02	0.00	0.01
Sn	0.01	0.00	0.00	0.00	0.00	0.00	12.2	14.2	13.2	0.00	0.00	0.02	0.07	0.00
Sb	0.00	0.00	0.00	0.03	0.00	0.00	0.00	0.00	0.00	0.02	0.00	0.02	0.00	0.02
Pb	0.04	0.02	0.04	0.03	0.01	0.04	0.04	0.03	0.03	0.04	0.03	0.04	0.03	0.05
As	33.4	33.0	34.0	33.4	34.4	31.9	0.00	0.00	0.00	0.00	0.00	0.00	0.00	0.02
S	32.1	32.6	31.7	32.3	31.4	33.5	50.3	49.6	49.8	50.8	50.4	50.9	49.0	54.1

4.3.5. Muscovite

White mica from greisen and quartz-cassiterite vein selvages shows a major chemical composition equivalent to this of white mica from the granite. Major and trace element composition of greisen/muscovitized host rocks, and vein muscovite is summarized in Table 4.4.

Table 4.4: Major (wt.%; EMPA) and trace (ppm, LA-ICP-MS) composition of muscovite from the Logrosán ore deposits

	65.1	65.1	L44	L107	L107	L107	L107	L113	L113	L113	L113	L113	57A	57A	SER2	SER2
	23	106	63	27	32	33	35	2	4	5	18	19	38	39	95	100
SiO_2	46.9	45.1	47.6	47.0	46.6	47.0	46.6	46.5	46.5	46.1	47.5	46.5	46.7	46.1	46.9	45.0
TiO_2	0.66	0.37	0.98	0.46	0.05	0.29	0.56	0.50	0.49	0.01	0.05	0.43	0.02	0.47	0.11	0.08
Al_2O_3	33.5	34.5	35.7	32.5	35.1	33.1	32.9	31.7	32.8	35.3	35.9	32.0	34.9	32.1	36.0	35.1
FeO	2.52	1.32	1.25	2.30	0.94	1.99	2.23	2.87	2.36	1.41	0.57	2.62	1.34	2.41	1.12	1.32
MnO	0.03	0.04	0.01	0.13	0.06	0.03	0.03	0.06	b.d.l.	0.01	0.02	b.d.l.	0.06	0.03	0.07	b.d.l.
MgO	1.31	0.61	0.79	1.21	0.28	0.77	1.02	1.48	1.12	0.75	0.21	1.14	0.76	1.35	0.44	0.39
CaO	0.01	0.03	0.02	0.02	0.01	b.d.l.	0.03	0.02	0.00	b.d.l.	0.01	b.d.l.	0.01	0.02	b.d.l.	b.d.l.
Na_2O	0.46	0.51	0.94	0.42	0.11	0.20	0.49	0.35	0.37	0.84	0.05	0.38	0.76	0.43	0.53	0.57
K_2O	10.1	10.7	9.40	10.1	9.71	10.0	10.0	9.92	10.25	9.73	8.33	10.1	10.1	10.2	10.40	10.7
F	0.99	0.76	0.53	1.05	0.39	0.67	0.88	1.23	0.91	0.67	0.24	1.15	0.76	1.11	0.46	0.33
Cl	n.d.	0.01	b.d.l.	0.01	b.d.l.	b.d.l.	0.02	0.03	0.01	b.d.l.	0.01	b.d.l.	0.01	b.d.l.	b.d.l.	b.d.l.
Total	96.7	94.0	97.3	95.3	93.3	94.0	94.8	94.6	94.9	94.8	92.8	94.4	95.5	94.2	96.3	93.7
Li_2O*	0.23	0.16	0.09	0.25	0.05	0.13	0.20	0.31	0.21	0.13	0.00	0.28	0.16	0.27	0.07	0.03
H_2O*	4.05	4.04	4.36	3.96	4.26	4.11	4.02	3.82	4.00	4.16	4.37	3.86	4.14	3.87	4.33	4.25
Par	6.37	6.68	13.14	5.89	1.72	2.92	6.89	5.09	5.16	11.65	0.89	5.45	10.28	6.05	7.15	7.57
Mus	93.6	93.3	86.9	94.1	98.3	97.1	93.1	94.9	94.8	88.3	99.1	94.5	89.7	94.0	92.9	92.4
Nº ions in formula on the basis o 22 oxygens																
Si	6.234	6.144	6.191	6.329	6.287	6.360	6.291	6.324	6.286	6.180	6.345	6.333	6.223	6.294	6.186	6.132
Al iv	1.766	1.856	1.809	1.671	1.713	1.640	1.709	1.676	1.714	1.820	1.655	1.667	1.777	1.706	1.814	1.868
Al vi	3.476	3.683	3.666	3.486	3.875	3.635	3.526	3.403	3.515	3.748	3.993	3.473	3.716	3.452	3.780	3.761
Ti	0.066	0.038	0.096	0.047	0.005	0.029	0.057	0.051	0.050	0.001	0.005	0.044	0.002	0.049	0.010	0.008
Fe	0.280	0.150	0.136	0.258	0.106	0.226	0.252	0.326	0.267	0.158	0.063	0.298	0.149	0.275	0.123	0.151
Mn	0.003	0.004	0.001	0.014	0.007	0.004	0.003	0.007	0.000	0.002	0.002	0.000	0.007	0.003	0.007	0.000
Mg	0.260	0.124	0.153	0.243	0.056	0.155	0.205	0.299	0.225	0.150	0.043	0.231	0.151	0.274	0.087	0.078
Li*	0.123	0.087	0.047	0.136	0.025	0.071	0.108	0.167	0.113	0.072	0.000	0.154	0.086	0.148	0.036	0.014
Ca	0.001	0.004	0.003	0.003	0.001	0.000	0.004	0.003	0.000	0.000	0.002	0.000	0.001	0.004	0.000	0.000
Na	0.117	0.134	0.236	0.109	0.029	0.052	0.128	0.092	0.096	0.219	0.013	0.101	0.198	0.114	0.135	0.152
K	1.723	1.867	1.559	1.745	1.672	1.726	1.725	1.722	1.768	1.662	1.420	1.758	1.724	1.776	1.749	1.852
OH*	3.586	3.673	3.782	3.552	3.831	3.715	3.620	3.466	3.608	3.715	3.897	3.505	3.680	3.520	3.807	3.860
F	0.414	0.325	0.218	0.447	0.168	0.285	0.376	0.527	0.390	0.284	0.101	0.495	0.319	0.480	0.193	0.140
Cl	0.000	0.002	0.000	0.001	0.000	0.000	0.004	0.007	0.002	0.001	0.002	0.000	0.001	0.000	0.000	0.000

Zoning*	L	L	L	L	L	D	D	D	D
	L113 jn18c03	L113 jn18c05	L113 jn18c10	L113 jn18c04	57A jn18c16	L113 jn18c08	L113 jn18c06	L113 jn18c09	57A jn18c17
Li	758	835	694	796	754	1750	1510	1750	1600
Be	b.d.l.	4.97	b.d.l.	3.55	7.43	21.6	20.8	24.7	22.0
B	56.5	72.7	47.7	61.8	65.4	92.3	86.4	78.3	62.0
MgO	0.79	0.98	0.85	0.79	0.97	1.41	1.29	1.57	1.45
Al_2O_3	38.8	38.8	37.6	39.6	40.3	35.6	36.1	36.2	36.2
SiO_2	45.6	46.1	46.0	46.6	46.7	46.6	46.5	47.6	46.1
Sc	13.4	9.0	86.4	10.1	11.2	11.9	12.1	12.6	16.0
TiO_2	0.50	0.01	0.83	0.37	0.03	0.59	0.58	0.73	0.66
V	2.5	b.d.l.	22.2	19.10	2.03	22.6	24.6	25.7	56.7
Co	0.61	0.60	0.78	0.40	0.83	b.d.l.	b.d.l.	b.d.l.	b.d.l.
Zn	81.0	71.8	79.5	90.2	64.5	328	288	362	366
Rb	918	798	998	914	782	1440	1440	1460	1380
Sr	2.09	1.11	1.64	1.61	2.08	3.12	2.69	3.03	2.78
Zr	0.90	0.48	2.63	0.74	0.59	b.d.l.	0.37	0.88	0.43
Nb	28.9	1.11	182	20.0	4.40	34.0	39.0	47.9	45.7
Sn	110	249	80.9	161	162	951	916	971	1010
Cs	121	248	31.3	170	115	621	557	627	315
Ba	85.6	95.1	60.9	120	273	338	588	633	407
Hf	b.d.l.	b.d.l.	0.37	b.d.l.	b.d.l.	b.d.l.	b.d.l.	b.d.l.	b.d.l.
Ta	5.22	0.14	13.50	3.41	0.38	0.36	0.31	0.57	0.82
W	34.8	17.8	66.1	40.4	13.8	62.5	62.8	67.5	66.8
Pb	1.72	1.48	1.86	1.52	2.34	2.70	2.42	2.59	2.38
U	b.d.l.	b.d.l.	0.066	b.d.l.	b.d.l.	b.d.l.	b.d.l.	0.12	b.d.l.
Nb/Ta	5.54	8.10	13.48	5.87	11.46	94.71	126.62	84.63	55.53

* L: lighter zone; D: darker zone

The calculated average formula of quartz-cassiterite vein selvage muscovite and greisen muscovite is $K_{0.86}Na_{0.06}Fe_{0.08}Mg_{0.08}Ti_{0.02}Al_{2.72}Si_{3.12}O_{10}(OH_{1.85},F_{0.15})$; the main difference with the granite mica is the Fe and Mg content, which are higher for the granite white mica (0.11 Fe apfu; 0.11 Mg apfu). Similarly, Caruzzo (2003) describes these chemical similarities for muscovite from greisen and muscovite from ore related granites from Nova Scotia. Similar to the Main Unit granite muscovite, greisen/vein muscovite defines a trend from the muscovite end member to protolithionite; although displaying a more restricted composition, closer to the muscovite end member (Fig. 4.12a). Moreover, most of the greisen/vein muscovite plots in the 'magmatic' muscovite field (Fig. 4.12b). This is indicative of crystallization in the presence of melt, which suggests that first mineralization stages might be contemporaneous to the granite emplacement. There is for granite and greisen/vein muscovite an evolution through the 'secondary' muscovite field, with an increase of the phengite component.

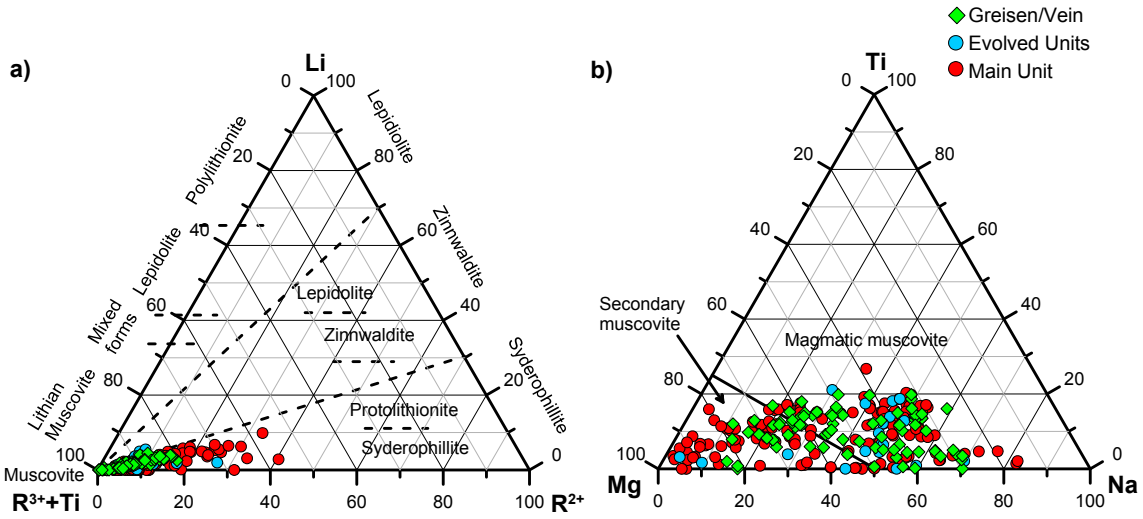

Fig. 4.12: a) Li–R^{2+}–R^{3+}+Ti diagram, according to the classification of Foster (1960), slightly modified by Rieder et al. (1999), with $R^{3+}=Al^{VI}$, $R^{2+}=(Fe_t^{2+}+Mn^{2+}+Mg)$. **b)** Mg–Ti–Na (atoms per 22O) diagram for muscovite. Magmatic and secondary muscovite fields are taken from Miller et al. (1981).

Although major composition of granite muscovite and greisen/vein muscovite is very similar, some differences have been found in the trace element chemistry. Trace element composition of muscovite from quartz-cassiterite selvage veins and greisen show two clusters (Fig. 4.13). Back scattered electron images unravel that hydrothermal greisen/vein muscovite sometimes displays darker replacement patches (Fig. 4.14). These darker zones correspond with the clusters showing higher Nb/Ta ratios, higher Sr, Rb, Sn, Li, B, Be, MgO, TiO_2, Zn, Pb, and Cs contents, and are impoverished in Al_2O_3 (Fig. 4.13 and Table 4.4). Moreover, Sn correlates relatively well with Li, B, Be, W and Nb/Ta in the greisen/vein samples. These late intergrowths indicate that an increase in fluid infiltration richer in volatile (B, Li) and metal-bearing components (Sn, W, Nb) occurred during the hydrothermal event in relation to the cassiterite precipitation.

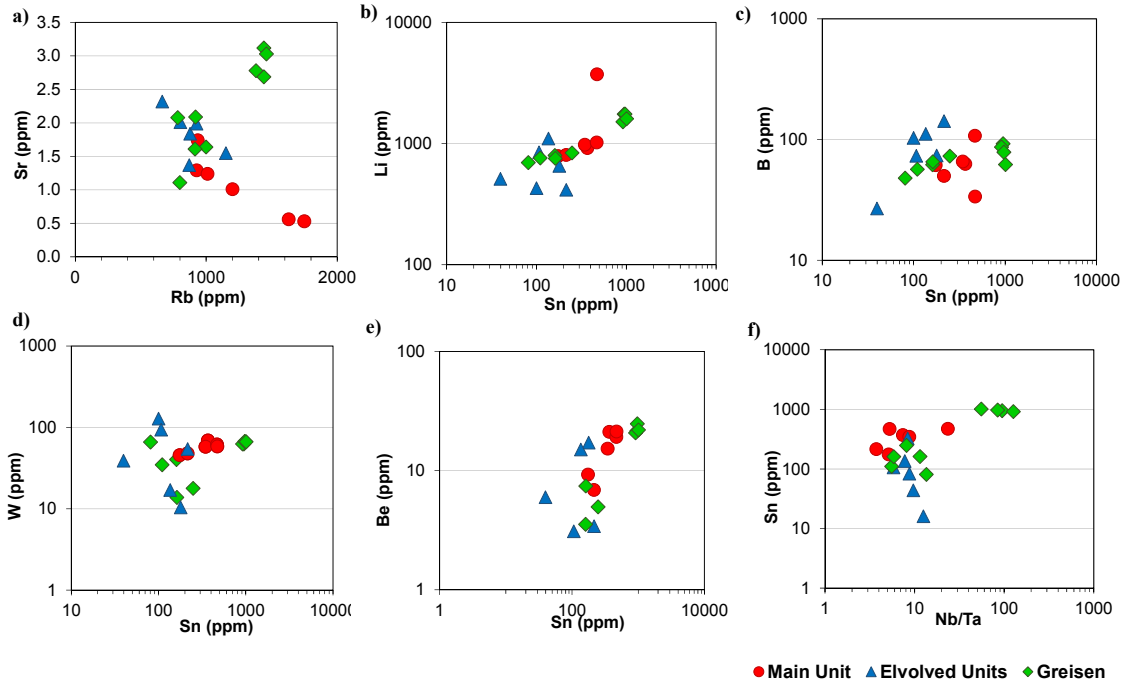

Fig. 4.13: Binary compositional diagrams of muscovite from the Logrosán granite (Table 3.3) and from greisen-like selvages (Table 4.4). **a)** Rb vs. Sr. **b)** Sn vs.Li. **c)** Sn vs. B. **d)** Sn vs. W. **e)** Sn vs. Be. **f)** Sn vs. Nb/Ta.

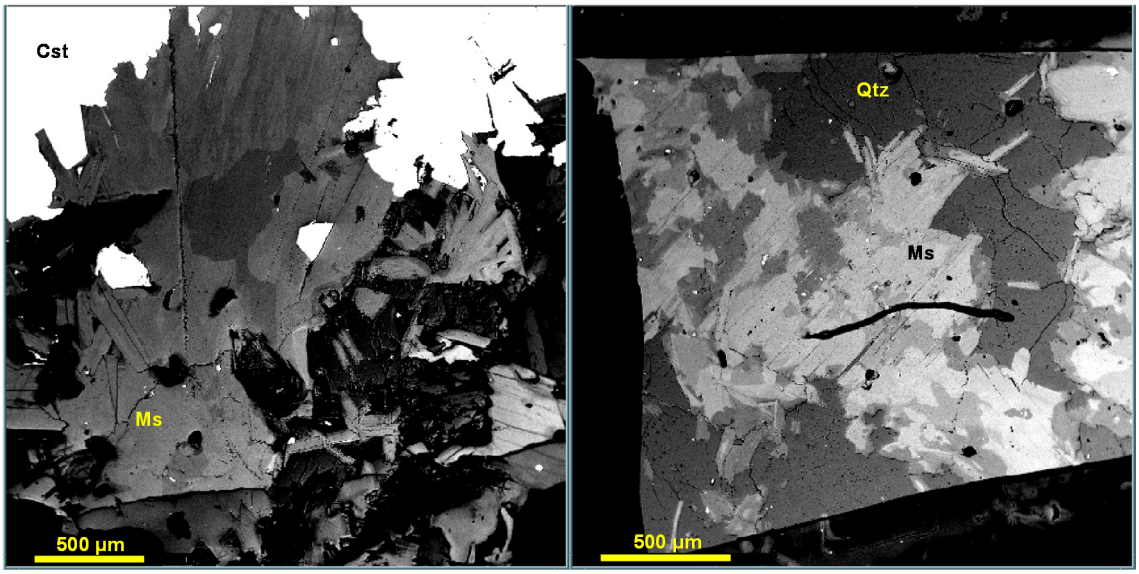

Fig. 4.14: Back scattered images of muscovite intergrown with cassiterite and being replaced by a darker muscovite phase (left), and of muscovite from a quartz-muscovite greisenized selvage with darker replacement patches and a darker rim (right).

4.3.6. Tourmaline

Most tourmaline in the Logrosán ore deposits predates the mineralization, but some quartz-tourmaline veins, isolated tourmaline crystals, and tourmaline alteration haloes are directly related to the early, or even to the late, stages of the quartz-cassiterite veins. Tourmaline, as most minerals described, occurs either in the intra- (San Cristóbal) as well as in the extragranitic (El Serranillo)

ore deposits. Contrarily to other studied minerals, tourmaline does show compositional particularities when associated with the intra- or the extra-granitic ore deposits (Table 4.5). Tourmaline form both ore deposits belongs to the alkali group (Fig. 4.15a). Tourmaline associated with the extragranitic Sn-(W) ore deposits is classified as a dravite, while tourmaline related to the intragranitic ore deposits is a schorl (Fig. 4.15b). Due to the host rock assimilation, tourmaline from the extragranitic ore deposits is richer in MgO (e.g., Roda-Robles et al., 2011). Therefore, it plots mostly in the metapelites and metapsammites field, and also in the Fe^{3+}-rich quartz–tourmaline rock field. Hydrothermal intragranitic tourmaline plots in the Li-poor granitoids, pegmatites and aplites field (Fig. 4.15c and Fig. 4.15d) (e.g., Roda-Robles et al., 2004). Both tourmalines follow the alkali deficiency substitution trend (Fig. 4.16a). They also display a preferential trend following the schorl ↔ dravite vector (Fig. 4.16b).

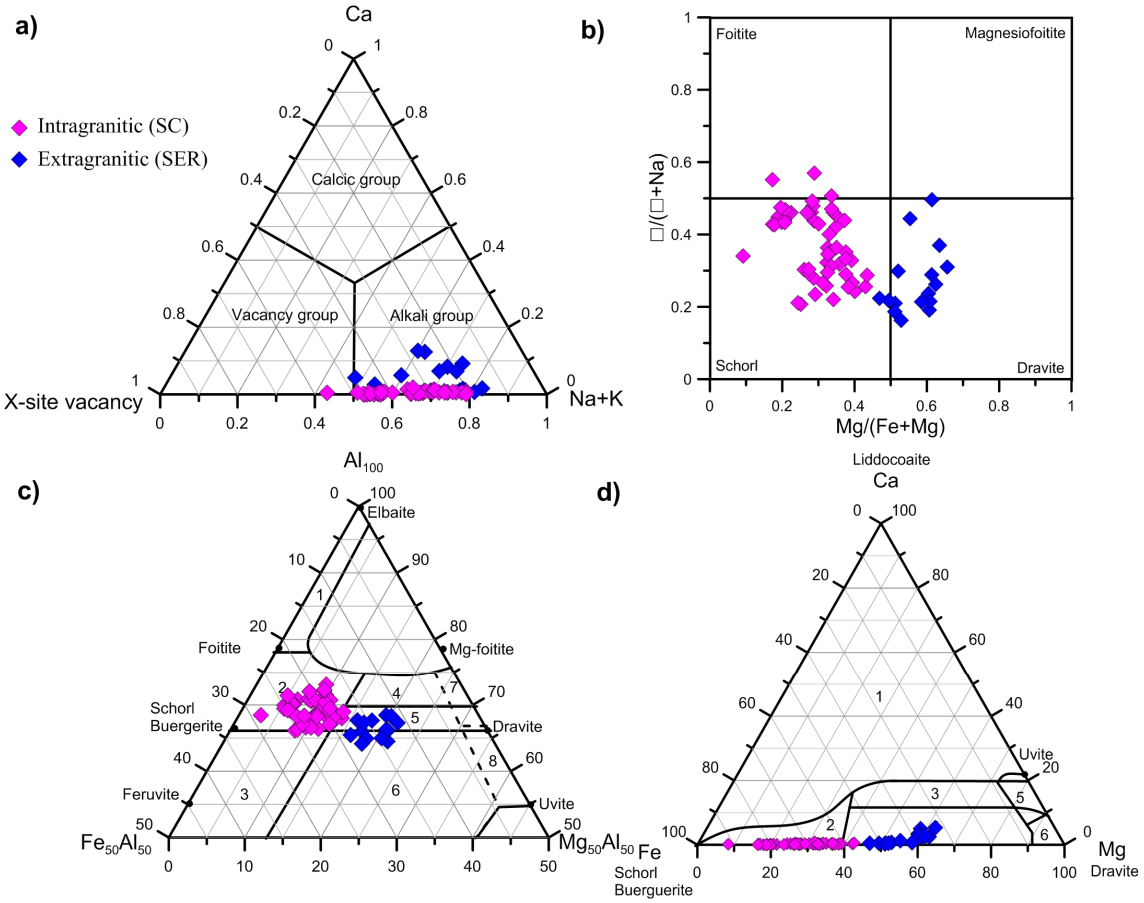

Fig. 4.15: a) X-site occupancy diagram of tourmaline from the Logrosán altered host-rocks, selvages and quartz-cassiterite veins (Hawthorne and Henry, 1999) **b)** Nomenclature diagram of tourmaline based on X-site vacancy/(X-site vacancy + Na) vs. Mg/(Mg + Fe) plot after Henry et al. (2003). **c)** Al–Fe–Mg ternary plot for tourmalines **d)** Hydrothermal tourmaline analyses on Ca-Fe-Mg ternary diagram.
Labelled fields in c) and d) after Henry and Guidotti (1985): 1. Li-rich granitoid pegmatites and aplites; 2. Li-poor granitoids, pegmatites and aplites; 3. Fe^{3+}-rich quartz–tourmaline rocks (altered granitoids); 4. metapelites and metapsammites with Al-saturating phase, 5. metapelites and metapsammites lacking Al-saturating phase; 6. Fe^{3+}-rich quartz–tourmaline rock, calc-silicate rocks and metapelites; 7. low-Ca metaultramafic rocks and Cr-V-rich metasediments; 8. metacarbonates and metapyroxenites.

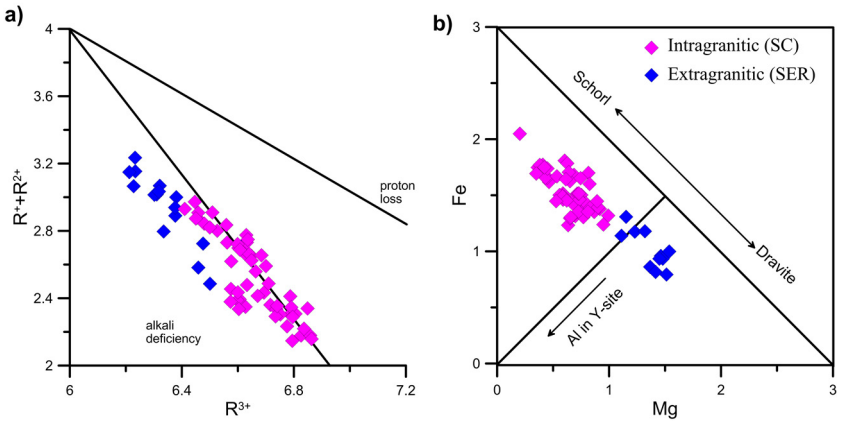

Fig. 4.16: a) R^{3+} (Al + 4/3 Ti) vs. $R^{+}+R^{2+}$ (Na + 2Ca + K + Mg + Mn) of granitic tourmalines. Substitution trends from Gallagher (1988). **b)** Mg vs. Fe diagram for tourmaline from the Logrosán quartz-cassiterite veins and alteration. $Mg^{2+} \leftrightarrow Fe^{2+}$ vector after Burt (1989).

Table 4.5: Major composition (wt.%; EMPA) of representative tourmaline and average composition of late- and early tourmaline from the Logrosán intra- and the extragranitic ore deposits.

	Late tourmaline (Intra-)					Early tourmaline (Intra-)					Early tourmaline (Extra-)					
Sample	**L57A**		**L57B**		**Aver.**	**65.2**	**65.3**			**Aver.**	**SER8A**					**Aver.**
Element	**40**	**42**	**64**	**80**		**49**	**120**	**121**	**63**		**41**	**42**	**48**	**50**	**52**	
SiO_2	35.92	36.51	36.89	36.94	36.53	36.03	36.51	36.33	35.35	35.98	37.26	37.21	37.68	37.40	37.21	37.35
TiO_2	0.28	0.22	0.22	0.22	0.30	0.89	0.40	0.75	0.65	0.47	0.38	0.41	0.22	0.25	0.38	0.39
Al_2O_3	33.79	35.00	33.77	33.66	33.66	33.18	34.68	32.95	31.61	33.52	32.55	32.25	33.25	32.66	31.86	32.55
FeO	12.52	11.83	12.67	11.97	12.40	10.73	11.07	10.93	12.54	10.64	7.03	8.56	5.87	6.85	9.20	7.51
MgO	1.73	1.92	1.49	1.77	1.79	2.88	3.13	2.91	2.48	2.83	6.03	5.04	6.29	5.98	5.40	5.61
MnO	0.06	0.09	0.05	0.06	0.04	0.05	0.07	0.05	0.09	0.07	0.00	0.00	0.00	0.04	0.02	0.03
CaO	0.01	0.01	0.02	0.00	0.01	0.03	0.03	0.03	0.04	0.03	0.47	0.07	0.75	0.39	0.04	0.28
Na_2O	1.73	1.69	1.77	1.65	1.77	2.08	2.04	2.28	2.09	1.96	2.20	2.42	1.91	2.30	2.52	2.18
K_2O	0.04	0.02	0.03	0.03	0.03	0.04	0.04	0.03	0.01	0.03	0.03	0.05	0.02	0.02	0.05	0.03
F	0.22	0.10	0.05	0.09	0.15	0.41	0.26	0.26	0.54	0.28	0.42	0.54	0.21	0.33	0.55	0.38
Total	86.29	87.38	86.97	86.38	86.69	86.30	88.22	86.52	85.40	85.80	86.37	86.57	86.19	86.23	87.21	86.30
Subtotal	86.29	87.38	86.97	86.38	86.69	86.30	88.22	86.52	85.40	85.80	86.37	86.57	86.19	86.23	87.21	86.30
O=F,Cl	0.092	0.041	0.023	0.037	0.064	0.173	0.110	0.109	0.227	0.120	0.176	0.229	0.090	0.137	0.232	0.158
Total	86.20	87.34	86.95	86.34	86.62	86.13	88.11	86.41	85.18	85.68	86.20	86.34	86.10	86.09	86.98	86.14
Si total	5.994	5.974	6.089	6.113	6.053	5.987	5.926	6.021	6.019	5.995	6.079	6.110	6.097	6.097	6.095	6.103
Al total	6.646	6.750	6.570	6.566	6.575	6.499	6.635	6.438	6.344	6.581	6.259	6.242	6.340	6.277	6.150	6.269
Al z	5.958	5.989	5.874	5.850	5.897	5.865	6.008	5.856	5.871	5.926	5.859	5.822	5.867	5.862	5.843	5.833
Ti z	0.036	0.028	0.027	0.028	0.037	0.111	0.049	0.093	0.083	0.059	0.047	0.051	0.027	0.031	0.047	0.048
Si z	-0.006	-0.026	0.089	0.113	0.053	-0.013	-0.074	0.021	0.019	-0.005	0.079	0.110	0.097	0.097	0.095	0.103
Al y	0.687	0.761	0.695	0.717	0.678	0.634	0.626	0.582	0.472	0.655	0.400	0.421	0.473	0.415	0.307	0.436
Fe	1.747	1.618	1.748	1.657	1.719	1.491	1.503	1.515	1.785	1.484	0.959	1.176	0.794	0.935	1.260	1.027
Mn	0.008	0.013	0.007	0.008	0.006	0.007	0.009	0.006	0.012	0.009	0.000	0.000	0.000	0.006	0.002	0.005
Mg	0.431	0.468	0.367	0.436	0.442	0.714	0.756	0.719	0.630	0.701	1.467	1.234	1.517	1.453	1.318	1.365
Li*	0.126	0.140	0.182	0.182	0.155	0.154	0.106	0.177	0.100	0.151	0.173	0.169	0.216	0.191	0.113	0.167
Y total	3.000	3.000	3.000	3.000	3.000	3.000	3.000	3.000	3.000	3.000	3.000	3.000	3.000	3.000	3.000	3.000
Ca	0.001	0.002	0.004	0.000	0.002	0.005	0.005	0.006	0.008	0.006	0.082	0.012	0.130	0.069	0.007	0.050
Na	0.561	0.536	0.566	0.529	0.568	0.669	0.641	0.733	0.690	0.632	0.696	0.772	0.598	0.727	0.799	0.690
K	0.008	0.004	0.005	0.006	0.006	0.008	0.008	0.006	0.003	0.006	0.006	0.011	0.004	0.005	0.010	0.005
X total	0.570	0.543	0.576	0.534	0.576	0.682	0.653	0.745	0.700	0.644	0.784	0.795	0.731	0.801	0.816	0.745
OH*	3.884	3.949	3.972	3.953	3.920	3.783	3.866	3.865	3.710	3.850	3.784	3.718	3.891	3.832	3.715	3.805
F	0.116	0.051	0.028	0.047	0.080	0.217	0.134	0.135	0.290	0.150	0.216	0.282	0.109	0.168	0.285	0.195
B*	3.000	3.000	3.000	3.000	3.000	3.000	3.000	3.000	3.000	3.000	3.000	3.000	3.000	3.000	3.000	3.000
Fe/ (Fe+Mg)	0.802	0.776	0.827	0.792	0.796	0.676	0.665	0.678	0.739	0.679	0.395	0.488	0.344	0.391	0.489	0.429
Na/ (Na+Ca)	0.998	0.996	0.993	1.000	0.996	0.993	0.993	0.992	0.988	0.990	0.894	0.985	0.822	0.914	0.991	0.932

In addition to the compositional differences found between intra- and extragranitic tourmaline there are some other minor features attending to early- or late- precipitation and zonation patterns.

Late tourmaline found in quartz-cassiterite veins post-dating the cassiterite is fairly homogeneous, and has the highest average FeO content, and the least vacancy percentages (Table 4.5). Early metasomatic tourmaline, either from the intra- or extra- ore deposits, is zoned. Zonation consists of a decrease in the vacancy percentage, FeO, Si_2O and Al_2O_3; and an increase in TiO_2, Na_2O, FeO, and F from core to rim. However, the MgO decreases from core to rim in the extragranitic tourmaline, while it increases in the intragranitic tourmaline. Although tourmaline associated with the ore deposits hosted by metasediments could have assimilated some Mg from the nearby rocks, it shows high Fe contents and an evolution to higher Fe contents toward the rim. Similarly, Fe is also enriched from early to late tourmaline phases. The Fe enrichment is a common feature of tourmaline associated with granite-related tin deposits (Henry and Guidotti, 1985). Trace elements in tourmaline have been analyzed in those crystals associated with Sn-(W) intragranitic ore deposits (Table 4.6). No significant compositional differences or chemical trends have been obtained when comparing core to rim, early to late or magmatic to hydrothermal tourmaline types. Iron, magnesium and the degree of vacancy sites are the only components which vary markedly with the fluid evolution. This agrees with an oxidizing fluid (probably of magmatic origin) causing the saturation of Fe-rich tourmaline (Mlynarczyk and Williams-Jones, 2006).

Table 4.6: Trace element composition (ppm; LA-ICP-MS) of representative tourmaline from the Logrosán ore deposits.

	Early tourmaline									Late tourmaline			
	65.3									57A			
Spot	jn18a03	jn18a04	jn18a05	jn18a06	jn18a07	jn18a08	jn18a09	jn18a10	jn18a11	jn18c12	jn18c13	jn18c14	jn18c15
	C	C	R	C	R	R	C	R	R				
Li	81.30	213	63.00	119	160	162	617	123	166	164	83.70	140	122
Be	b.d.l.	4.55	13.9	b.d.l.	b.d.l.	6.58	b.d.l.	b.d.l.	b.d.l.	b.d.l.	16.8	7.16	20.9
B	27100	26200	25900	25600	24900	24600	24300	21500	24200	22400	22300	23600	23100
MgO	2.41	3.06	3.23	3.64	3.65	3.78	0.65	2.80	2.85	2.51	1.91	2.18	2.15
Al_2O_3	36.40	34.10	35.30	34.70	34.00	36.20	35.20	31.20	34.80	33.60	34.90	36.10	37.60
SiO_2	36.50	36.30	36.10	36.50	36.50	36.70	36.10	31.80	36.30	36.00	36.40	36.90	36.50
Sc	7.41	8.49	18.40	10.20	8.23	7.49	8.18	12.50	10.10	8.21	8.21	7.78	9.06
TiO_2	0.17	0.88	0.26	0.54	0.61	0.33	0.62	0.40	0.74	1.00	0.25	0.49	0.29
V	9.69	39.40	100	13.70	21.70	12.40	11.30	30.60	20.00	25.80	19.90	23.60	24.80
Co	4.2	0.6	3.2	b.d.l.	0.6	b.d.l.	1.1	0.6	b.d.l.	b.d.l.	b.d.l.	0.3	b.d.l.
Zn	1180	1200	907	821	874	882	1420	791	2860	2280	1870	2020	2170
Sr	5.45	20.5	29.6	12.2	15.7	17.1	20.5	7.97	28.4	28.6	9.84	12.2	12.5
Zr	b.d.l.	b.d.l.	0.99	0.20	b.d.l.	b.d.l.	b.d.l.	b.d.l.	b.d.l.	b.d.l.	0.37	b.d.l.	0.41
Nb	b.d.l.	0.63	0.77	0.81	b.d.l.	0.34	b.d.l.	<0.157	0.28	0.40	1.04	0.53	1.64
Sn	57.80	113	196	174	68.00	89.70	14.10	61.10	40.90	131	164	94.30	181
Ta	0.20	0.92	1.71	1.60	0.11	0.27	b.d.l.	0.19	0.18	b.d.l.	b.d.l.	b.d.l.	b.d.l.
Pb	1.09	3.36	1.48	3.55	3.11	3.75	4.42	2.28	4.07	6.71	2.07	2.47	2.11

*C: core; *R: rim.

4.4. Altered granite and greisen geochemistry

Whole rock-analyses of granite, altered granites, and greisen are summarized in Table 4.7. Altered granites and greisen show significant geochemical differences with regard to the Main and Evolved Units (Table 4.7) (Fig. 4.17) (see Chapter 3).

Table 4.7: Whole-rock major (wt.%) and trace-element (ppm) compositions of the Logrosán granite.

	Main Unit						Evolved Units			Altered granites			Greisen
	AQ1	AQ2	AQ4	AQ6	AQ13	AQ14	AQ5	AQ11	AQ12	AQ3	AQ9	AQ10	AQ7
	111911	111912	111976	111978	178	179	111979	174	177	111970	112688	112690	111918
SiO_2	72.46	72.26	72.53	73.93	73.12	74.03	72.94	72.73	74.01	70.49	66.79	63.59	49.75
Al_2O_3	14.43	14.76	15.24	15.14	14.92	14.94	15.30	14.42	14.83	16.58	17.67	19.38	31.61
FeO_t	1.25	1.71	1.33	0.82	1.37	1.14	0.78	1.45	1.17	1.38	2.18	1.00	1.83
MnO	0.02	0.02	0.02	0.02	0.02	0.02	0.01	0.02	0.02	0.03	0.03	0.01	0.04
MgO	0.28	0.33	0.38	0.16	0.33	0.24	0.22	0.22	0.26	0.35	0.48	0.23	0.75
CaO	0.59	0.45	0.69	0.50	0.54	0.51	0.46	0.25	0.46	0.31	0.30	0.40	0.07
Na_2O	3.68	2.67	3.31	3.87	3.31	3.42	3.27	2.95	2.95	2.30	3.04	4.28	1.37
K_2O	4.46	4.75	4.88	4.19	4.42	4.53	4.83	4.35	4.63	4.04	5.46	5.09	8.50
TiO_2	0.18	0.23	0.27	0.10	0.21	0.17	0.17	0.13	0.15	0.17	0.33	0.16	0.24
P_2O_5	0.50	0.47	0.57	0.57	0.49	0.46	0.54	0.51	0.55	0.42	0.63	0.78	0.04
LOI	1.33	2.55	1.62	1.51	1.47	1.08	1.95	1.98	1.74	3.29	2.90	4.09	5.86
Total	99.16	100.2	100.8	100.8	100.2	100.5	100.5	99.00	100.8	99.37	99.80	99.01	100.0
Sc	3.00	4.00	2.00	3.00	3.00	2.00	2.00	2.00	3.00	3.00	6.00	1.00	5.00
Be	15.00	23.00	16.00	11.00	14.00	18.00	7.00	19.00	9.00	7.00	12.00	10.00	15.00
V	7.00	12.00	10.00	< 5	13.00	10.00	< 5	10.00	9.00	8.00	21.00	7.00	15.00
Cr	< 20	< 20	< 20	< 20	< 20	< 20	< 20	280	180.0	< 20	< 20	< 20	< 20
Co	2.00	4.00	3.00	3.00	2.00	2.00	2.00	2.00	2.00	2.00	2.00	1.00	1.00
Ni	< 20	< 20	< 20	< 20	< 20	< 20	< 20	< 20	< 20	< 20	< 20	< 20	< 20
Cu	< 10	20.00	< 10	< 10	20.00	< 10	< 10	< 10	< 10	< 10	20.00	50.00	10.00
Zn	30.00	50.00	60.00	30.00	40.00	70.00	< 30	70.00	< 30	< 30	100	60.00	100
Ga	21.00	23.00	25.00	20.00	22.00	21.00	20.00	24.00	20.00	34.00	34.00	26.00	91.00
Ge	2.20	2.10	1.70	2.30	2.30	2.10	1.50	3.40	2.50	2.70	2.90	2.20	3.80
As	60.00	51.00	137	94.00	137.0	64.00	123	44.00	103	1470	307	102	36.00
Rb	288	301	338	317	311	238	270	362	317	411	425	361	918
Sr	44.00	41.00	57.00	39.00	44.00	38.00	52.00	32.00	57.00	28.00	36.00	77.00	26.00
Y	6.90	5.20	7.60	5.50	7.60	9.60	5.40	3.30	6.60	7.00	6.00	7.40	13.10
Zr	76.00	80.00	118.00	43.00	82.00	77.00	74.00	60.00	62.00	79.00	101	94.00	42.00
Nb	8.70	11.70	10.10	13.60	11.40	9.00	9.60	15.90	11.10	11.60	21.30	10.40	21.00
Mo	< 2	< 2	< 2	< 2	< 2	< 2	< 2	< 2	< 2	< 2	< 2	< 2	< 2
Ag	< 0.5	0.50	< 0.5	< 0.5	< 0.5	< 0.5	0.70	< 0.5	< 0.5	1.00	< 0.5	< 0.5	< 0.5
In	< 0.1	0.10	< 0.1	< 0.1	< 0.1	< 0.1	< 0.1	0.10	< 0.1	0.20	0.10	< 0.1	2.20
Sn	50.00	67.00	33.00	35.00	49.00	11.00	37.00	29.00	53.00	244	66.00	32.00	>1000
Sb	0.50	0.40	< 0.2	0.70	< 0.2	0.30	0.90	< 0.2	0.50	0.90	< 0.2	0.30	0.30
Cs	59.50	88.00	74.40	50.20	54.60	26.70	70.30	51.60	145.00	95.00	76.10	58.70	275.0
Ba	224	241	290	138.0	226.0	178.0	219.0	152	225	82.00	237	237	161.0
La	13.80	16.10	21.80	6.53	15.10	13.00	11.40	8.81	9.67	12.50	19.90	17.20	14.40
Ce	31.40	35.60	50.20	14.80	33.10	27.70	27.80	19.20	20.70	28.00	44.50	39.20	31.70
Pr	3.58	3.85	6.42	1.74	3.95	3.34	3.25	2.17	2.48	3.08	5.50	5.20	4.02
Nd	13.30	14.50	25.80	6.40	15.60	12.90	12.50	8.06	10.00	11.10	19.00	19.50	15.00
Sm	2.96	3.05	5.18	1.56	3.25	2.94	2.92	1.73	2.47	2.76	3.92	4.90	3.44
Eu	0.32	0.32	0.47	0.21	0.33	0.30	0.32	0.19	0.36	0.15	0.28	0.58	0.35
Gd	2.24	2.21	3.35	1.44	2.54	2.52	2.22	1.26	2.24	2.28	2.38	3.64	2.73
Tb	0.33	0.29	0.46	0.25	0.36	0.40	0.35	0.18	0.35	0.35	0.32	0.54	0.44
Dy	1.52	1.35	1.85	1.20	1.64	1.87	1.50	0.84	1.75	1.64	1.47	2.13	2.22
Ho	0.24	0.21	0.26	0.19	0.25	0.32	0.22	0.12	0.24	0.25	0.21	0.26	0.34
Er	0.60	0.52	0.60	0.51	0.66	0.86	0.46	0.30	0.51	0.64	0.50	0.59	0.84
Tm	0.09	0.07	0.08	0.07	0.09	0.12	0.06	0.05	0.06	0.10	0.07	0.08	0.10
Yb	0.56	0.49	0.44	0.53	0.52	0.71	0.37	0.30	0.38	0.66	0.42	0.45	0.57
Lu	0.08	0.07	0.06	0.07	0.08	0.11	0.05	0.05	0.06	0.09	0.07	0.06	0.08
Hf	2.20	2.40	3.00	1.50	2.60	2.50	2.50	1.70	2.10	2.50	3.10	3.10	1.20
Ta	2.26	3.08	2.50	4.76	3.73	1.97	1.98	4.00	2.30	3.27	5.70	2.06	3.07
W	24.60	82.10	74.20	36.00	23.90	9.00	131	1.60	376	155	27.90	29.40	51.50
Tl	1.84	1.98	2.02	1.99	1.87	1.40	1.77	1.56	1.79	2.25	2.87	2.43	4.69
Pb	28.00	22.00	29.00	21.00	24.00	28.00	26.00	21.00	29.00	10.00	31.00	40.00	8.00
Bi	0.30	< 0.1	0.60	1.50	0.30	2.60	0.40	< 0.1	0.60	3.30	7.70	0.50	0.70
Th	7.59	8.28	19.90	3.07	8.70	6.65	8.67	5.30	4.45	5.99	12.10	13.20	7.02
U	7.91	7.25	10.90	8.49	7.04	11.00	10.50	9.04	7.23	12.80	8.51	15.50	5.62
F		2003	1611	1150			1053			3063		1657	5495
Li		290	303	141			210			269		123	780

Altered granites and greisen are impoverished in SiO_2 and highly enriched in Al_2O_3, due to muscovitization and sericitization processes (Fig 4.17a). Altered granites and greisen are Rb-

enriched, which probably denotes the substitution of K during the hydrolysis of feldspars. They have significantly higher loss on ignition values (LOI: 2.90−5.86 %) (Fig 4.17b), suggesting elevated volatile contents (i.e. water, boron, and fluorine). The samples with the higher F contents correspond to the higher Sn contents (Fig 4.17c and 4.17d). Sn even reaches values above the upper limit of detection in greisen samples (in Table 4.7 see AQ7: Sn > 1000 ppm). Although F minerals have not been found, fluorine contents are high in the Logrosán granite and greisen. F is hosted in minerals such as muscovite, biotite and apatite. The F content of the granite ranges between 1053 and 2003 ppm, whereas in the greisen it may reach up to 5500 ppm (Table 4.7).

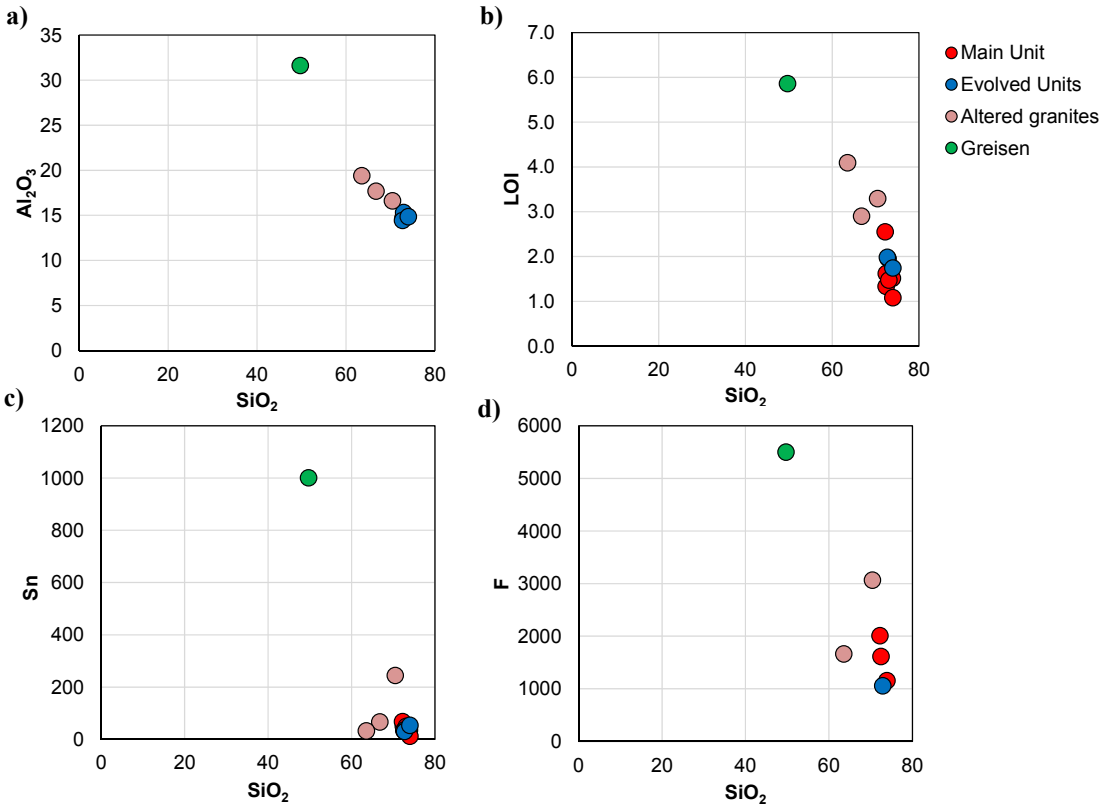

Fig. 4.17: Selected major (wt. %) and trace (ppm) element variation diagrams versus SiO_2 for the Logrosán granite.

4.5. Ar-Ar thermochronology data

Ar-Ar analyses for five muscovite samples from altered host-rocks and selvages related to cassiterite mineralization were performed (Table 4.8). The samples produced relatively undisturbed spectra and well-defined plateaux (Fig. 4.18). The plateau ages vary from 303±3 to 311±3 Ma, with MSWD values from 0.86 to 2.47, representing reliable crystallization ages for the muscovite from the altered host-rocks and vein samples. The isochron ages are consistent with these results, giving ages from 290±20 to 308±3 Ma (Fig. 4.18).

Table 4.8: Argon release data of muscovite from the Logrosán samples

Sample	J	$^{40}Ar/^{39}Ar$	1σ	$^{36}Ar/^{39}Ar$	1σ	$^{37}Ar/^{39}Ar$	1σ	$^{38}Ar/^{39}Ar$	1σ	^{39}Ar (mol)	^{40}Ar (%)	Age (Ma)	
L104	0.0061	33.84	0.25	0.0247	0.0009	2.637	0.872	0.0228	0.0015	5.1E-17	78.81	272.7	± 4.2
	0.0061	33.50	0.21	0.0140	0.0003	0.332	0.256	0.0163	0.0005	1.1E-16	87.64	297.5	± 2.8
	0.0061	33.02	0.20	0.0081	0.0001	-0.089	0.075	0.0137	0.0001	3.3E-16	92.68	309.1	± 2.3
	0.0061	32.63	0.20	0.0059	0.0000	-0.060	0.039	0.0131	0.0001	5.9E-16	94.55	311.4	± 2.1
	0.0061	31.97	0.19	0.0040	0.0001	0.069	0.065	0.0130	0.0002	6.8E-16	96.31	310.8	± 2.0
	0.0061	31.77	0.19	0.0036	0.0000	0.174	0.052	0.0131	0.0002	6.0E-16	96.64	310.0	± 2.0
	0.0061	31.64	0.19	0.0034	0.0001	0.220	0.064	0.0132	0.0002	7.4E-16	96.85	309.5	± 1.9
	0.0061	31.33	0.19	0.0033	0.0001	0.630	0.116	0.0142	0.0004	7.5E-16	96.99	307.2	± 2.0
	0.0061	31.15	0.19	0.0032	0.0001	0.822	0.149	0.0146	0.0005	7.5E-16	97.16	306.1	± 2.0
	0.0061	31.22	0.19	0.0036	0.0001	0.843	0.148	0.0147	0.0004	8.2E-16	96.76	305.6	± 2.0
	0.0061	31.27	0.19	0.0029	0.0001	0.407	0.080	0.0136	0.0003	9.0E-16	97.37	307.7	± 1.9
	0.0061	31.12	0.19	0.0030	0.0001	0.704	0.124	0.0143	0.0004	8.3E-16	97.27	306.1	± 1.9
	0.0061	31.05	0.19	0.0033	0.0001	0.835	0.140	0.0147	0.0004	8.3E-16	97.05	304.9	± 2.0
	0.0061	31.03	0.19	0.0035	0.0001	0.950	0.156	0.0150	0.0005	8.0E-16	96.86	304.2	± 2.0
L105	0.0062	48.16	0.54	0.1252	0.0023	0.175	1.544	0.0433	0.0035	7.6E-17	22.44	116.4	± 9.0
	0.0062	36.30	0.29	0.0560	0.0012	0.526	0.960	0.0288	0.0022	1.2E-16	54.03	206.1	± 5.1
	0.0062	37.21	0.23	0.0347	0.0008	-0.536	0.670	0.0212	0.0016	1.7E-16	72.08	276.1	± 3.7
	0.0062	37.17	0.18	0.0258	0.0005	-0.513	0.420	0.0177	0.0010	2.7E-16	79.16	300.8	± 2.8
	0.0062	35.12	0.16	0.0129	0.0005	-1.624	0.361	0.0128	0.0008	2.9E-16	88.67	316.7	± 2.3
	0.0062	34.30	0.17	0.0091	0.0006	-1.979	0.483	0.0114	0.0011	2.2E-16	91.64	319.3	± 2.6
	0.0062	34.11	0.16	0.0096	0.0005	-1.224	0.397	0.0129	0.0009	2.8E-16	91.29	316.7	± 2.3
	0.0062	33.33	0.15	0.0081	0.0004	-0.658	0.310	0.0133	0.0007	3.6E-16	92.57	314.2	± 2.0
	0.0062	32.59	0.18	0.0065	0.0003	-0.798	0.207	0.0123	0.0005	5.2E-16	93.84	311.6	± 1.9
	0.0062	32.09	0.15	0.0057	0.0003	0.093	0.256	0.0143	0.0007	6.0E-16	94.69	310.0	± 1.7
	0.0062	31.75	0.14	0.0049	0.0002	-0.036	0.193	0.0137	0.0005	6.3E-16	95.40	309.1	± 1.6
	0.0062	31.69	0.13	0.0047	0.0002	0.060	0.178	0.0138	0.0004	7.0E-16	95.62	309.2	± 1.5
L107	0.0062	49.86	1.35	0.1372	0.0043	15.114	3.159	0.0759	0.0085	1.0E-16	20.26	111.6	± 9.0
	0.0062	37.57	0.69	0.0543	0.0018	9.744	2.186	0.0471	0.0062	1.6E-16	58.88	235.1	± 6.6
	0.0062	34.24	0.37	0.0260	0.0009	5.406	1.266	0.0310	0.0035	2.5E-16	78.62	281.5	± 4.1
	0.0062	32.57	0.27	0.0149	0.0006	3.667	0.903	0.0247	0.0027	3.9E-16	87.26	295.5	± 3.1
	0.0062	32.31	0.06	0.0059	0.0001	-0.203	0.036	0.0129	0.0001	4.9E-16	94.53	315.0	± 0.7
	0.0062	31.81	0.06	0.0040	0.0001	-0.339	0.044	0.0121	0.0001	3.9E-16	96.20	315.5	± 0.7
	0.0062	31.61	0.06	0.0041	0.0001	-0.227	0.036	0.0125	0.0001	5.0E-16	96.10	313.5	± 0.6
	0.0062	31.90	0.06	0.0062	0.0001	0.221	0.079	0.0139	0.0002	6.1E-16	94.30	310.7	± 0.7
	0.0062	30.91	0.08	0.0046	0.0001	0.923	0.160	0.0152	0.0005	6.8E-16	95.80	306.4	± 0.9
	0.0062	30.99	0.07	0.0045	0.0001	0.671	0.123	0.0146	0.0004	9.9E-16	95.84	307.3	± 0.8
	0.0062	31.09	0.07	0.0055	0.0001	0.819	0.101	0.0161	0.0006	9.2E-16	94.93	305.5	± 0.8
	0.0062	30.76	0.07	0.0045	0.0001	0.794	0.090	0.0159	0.0006	1.0E-15	95.82	305.1	± 0.8
	0.0062	30.86	0.07	0.0045	0.0000	0.729	0.082	0.0156	0.0005	1.2E-15	95.84	306.0	± 0.7
L111	0.0059	53.21	1.67	0.0848	0.0089	-1.442	4.723	0.0259	0.0090	3.3E-19	52.23	275.4	± 25.3
	0.0059	31.39	0.33	0.0591	0.0027	-0.006	1.489	0.0247	0.0028	1.0E-18	43.78	141.6	± 8.4
	0.0059	23.99	0.14	0.0352	0.0013	-0.110	0.742	0.0198	0.0014	2.1E-18	56.18	138.9	± 4.3
	0.0059	31.99	0.17	0.0373	0.0013	-0.157	0.709	0.0201	0.0013	2.2E-18	65.13	210.5	± 4.0
	0.0059	35.28	0.15	0.0326	0.0010	-0.218	0.545	0.0188	0.0010	2.8E-18	72.38	254.8	± 3.2
	0.0059	35.43	0.15	0.0249	0.0010	-0.147	0.547	0.0173	0.0010	2.8E-18	78.96	277.3	± 3.1
	0.0059	34.58	0.16	0.0173	0.0010	0.069	0.579	0.0163	0.0011	2.6E-18	85.08	290.6	± 3.2
	0.0059	34.27	0.15	0.0137	0.0010	0.052	0.569	0.0154	0.0011	2.7E-18	88.07	297.5	± 3.2
	0.0059	34.02	0.15	0.0121	0.0010	-0.065	0.546	0.0147	0.0010	2.8E-18	89.38	299.5	± 3.0
	0.0059	34.54	0.15	0.0135	0.0010	0.053	0.532	0.0154	0.0010	2.9E-18	88.32	300.5	± 3.0
	0.0059	34.86	0.12	0.0103	0.0007	-0.745	0.374	0.0130	0.0007	4.1E-20	91.03	311.4	± 2.1
	0.0059	33.84	0.13	0.0060	0.0008	-0.809	0.448	0.0123	0.0008	3.5E-20	94.52	313.7	± 2.5
	0.0059	33.69	0.13	0.0066	0.0008	-0.627	0.450	0.0127	0.0008	3.4E-20	94.00	310.9	± 2.5
	0.0059	34.86	0.12	0.0092	0.0007	-0.651	0.406	0.0129	0.0008	3.8E-20	91.98	314.4	± 2.3
	0.0059	33.31	0.13	0.0055	0.0008	-0.401	0.463	0.0131	0.0009	3.4E-20	94.97	310.6	± 2.5
	0.0059	33.03	0.12	0.0053	0.0008	-0.084	0.455	0.0136	0.0009	3.6E-20	95.17	308.8	± 2.4
	0.0059	33.10	0.11	0.0050	0.0007	-0.293	0.393	0.0132	0.0007	4.1E-20	95.46	310.3	± 2.1
	0.0059	33.14	0.11	0.0048	0.0007	-0.318	0.378	0.0130	0.0007	4.3E-20	95.58	310.9	± 2.1
	0.0059	33.17	0.12	0.0060	0.0007	0.192	0.410	0.0141	0.0008	4.3E-20	94.66	308.6	± 2.1
	0.0059	33.02	0.12	0.0056	0.0007	0.272	0.436	0.0143	0.0009	4.0E-20	95.01	308.4	± 2.2
	0.0059	32.85	0.13	0.0062	0.0007	0.584	0.433	0.0151	0.0009	4.3E-20	94.53	305.6	± 2.2
	0.0059	32.94	0.11	0.0050	0.0006	-0.043	0.368	0.0136	0.0007	4.5E-20	95.48	309.0	± 2.0
	0.0059	32.65	0.12	0.0055	0.0006	0.465	0.412	0.0147	0.0008	4.4E-20	95.09	305.5	± 2.1
	0.0059	32.64	0.11	0.0047	0.0006	0.150	0.376	0.0140	0.0007	4.7E-20	95.71	307.1	± 2.0
	0.0059	32.60	0.12	0.0054	0.0006	0.596	0.409	0.0150	0.0008	4.8E-20	95.23	305.4	± 2.0
	0.0059	32.66	0.10	0.0041	0.0006	-0.078	0.338	0.0134	0.0007	4.9E-20	96.20	308.7	± 1.8
	0.0059	32.38	0.11	0.0046	0.0006	0.425	0.374	0.0145	0.0007	4.9E-20	95.87	305.4	± 1.9
	0.0059	32.75	0.12	0.0054	0.0005	0.664	0.349	0.0150	0.0007	5.8E-20	95.25	306.8	± 1.8
	0.0059	32.86	0.12	0.0051	0.0005	0.774	0.339	0.0152	0.0007	6.2E-20	95.57	308.8	± 1.7
SER	0.0060	25.58	0.08	0.0484	0.0005	-0.388	0.272	0.0219	0.0005	1.5E-16	43.45	116.5	± 2.2
	0.0060	35.49	0.09	0.0313	0.0001	-0.053	0.068	0.0183	0.0002	6.4E-16	73.66	263.0	± 1.5
	0.0060	33.05	0.08	0.0107	0.0001	0.259	0.074	0.0148	0.0002	1.9E-15	90.37	297.6	± 1.0
	0.0060	31.64	0.10	0.0054	0.0001	0.754	0.173	0.0150	0.0005	7.6E-16	95.10	299.8	± 1.0
	0.0060	32.04	0.09	0.0056	0.0001	0.462	0.107	0.0143	0.0004	1.5E-15	94.92	302.7	± 0.9
	0.0060	31.76	0.09	0.0045	0.0001	0.511	0.113	0.0143	0.0004	1.4E-15	95.89	303.1	± 0.9
	0.0060	31.75	0.09	0.0041	0.0001	0.450	0.103	0.0140	0.0003	1.6E-15	96.28	304.1	± 0.9
	0.0060	31.33	0.15	0.0039	0.0002	1.203	0.402	0.0163	0.0013	1.2E-15	96.57	301.4	± 1.6
	0.0060	31.25	0.17	0.0042	0.0003	1.414	0.441	0.0170	0.0015	1.1E-15	96.33	300.1	± 1.8
	0.0060	31.25	0.17	0.0041	0.0003	1.372	0.443	0.0168	0.0014	1.1E-15	96.40	300.2	± 1.7

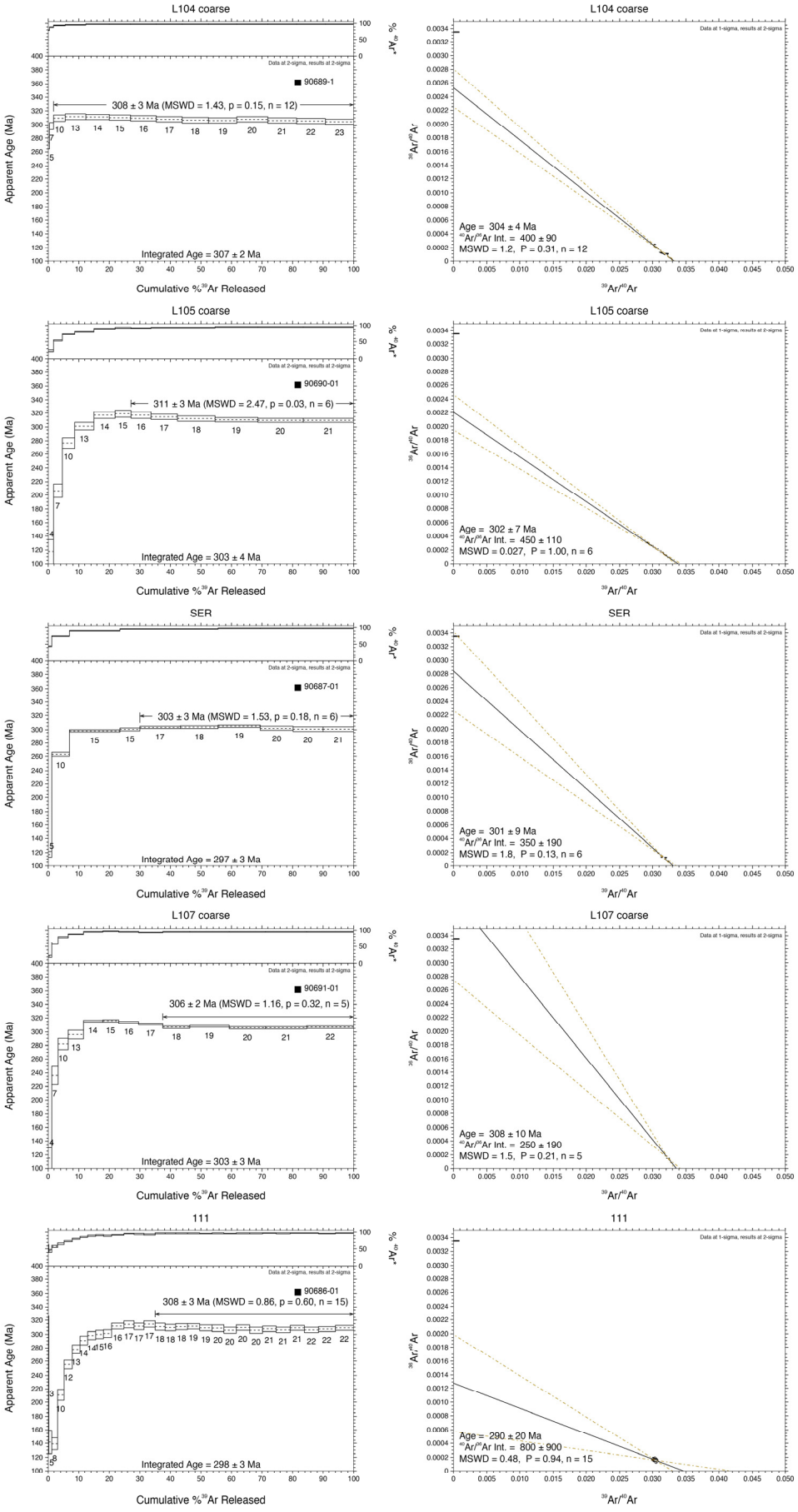

Fig. 4.18: $^{40}Ar/^{39}Ar$ step-heating age spectrum and isochron diagrams of analyzed muscovite samples.

4.6. Fluid inclusion study

Fluid inclusions suitable for microthermomety and Raman analyses have been found in quartz and cassiterite of quartz-cassiterite and quartz-sulfide veins. More than 250 microthermometric and 85 Raman measurements have been performed on four samples of quartz-cassiterite and quartz-sulfide veins from the Logrosán ore deposits. Based on phase association, microthermometric data and Raman spectroscopy results; the fluid inclusions may be classified as the following five compositional types:

- Type-I: Mixed N_2-CH_4 aqueous fluid inclusions, with low salinity.
- Type-II: Complex mixed N_2-CO_2-CH_4 aqueous fluid inclusion, with low to moderate salinity.
- Type-III: Low density N_2-rich vapor fluid inclusions.
- Type-IV: Low density CO_2-rich vapor fluid inclusions.
- Type-V: Aqueous fluid inclusions.

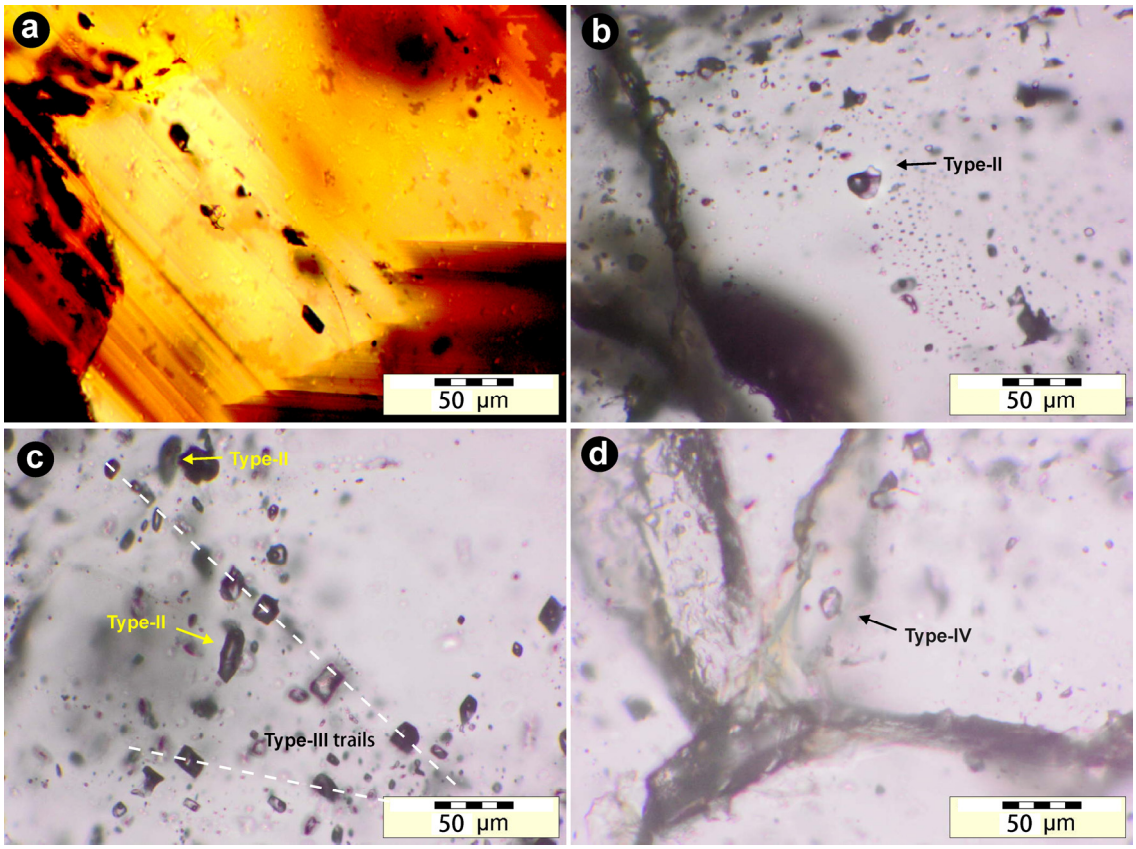

Fig. 4.19: a) Type-I primary fluid inclusions oriented along a crystal growth band in cassiterite. **b)** Type-II primary isolated fluid inclusion. **c)** Type-III secondary trails cutting type-II primary FIA's. **d)** Type-IV primary fluid inclusions in late quartz.

4.6.1. Fluid inclusion petrography

The fluid inclusions in the studied samples display a complex network. Fluid inclusions are numerous and widespread in quartz-cassiterite and quartz-sulfide vein samples. They occur mostly in quartz grains, but also in cassiterite grains. Samples from three distinct mineralized veins have been studied from Stage I (Oxide Stage) and/or Stage II (Sulfide Stage). Distinct fluid inclusion types frequently occur within the same quartz grain, but in separate isolated groups or along separate trails.

Type-I fluid inclusions appear only in quartz-cassiterite veins (Stage I). They occur exclusively in cassiterite, and are distributed along growth zones, indicating a primary origin, following the Roedder (1984) criteria. These mixed N_2-CH_4 aqueous fluid inclusions are rather dark in appearance, ranging from 5 to 40 μm in size. Visual estimations of the volumetric fraction of vapor phase range from 30 to 40 vol%. They feature irregular, elongated, and oblate shapes. Larger fluid inclusions are isolated, while smaller ones appear as trails, following crystal growth orientations (Fig. 4.19a). Primary type-I fluid inclusions, which belong to the Oxide Stage in the paragenetic sequence (i.e. cassiterite precipitation), predate the later CO_2-bearing fluid inclusions.

Type-II fluid inclusions are dominant and widespread in all studied samples, either from the quartz-cassiterite veins (Stage I) or quartz-sulfide veins (Stage II). Their sizes range generally from 20 to 50 μm. The volumetric fractions of vapor phase show wide variations from 30 to 80 vol%. They occur as isolated fluid inclusions in quartz-sulfide samples, suggesting a primary origin in these samples. These complex mixed N_2-CO_2-CH_4 type occurs mostly in clusters, and isolated fluid inclusions, randomly distributed within quartz of quartz-cassiterite veins and quartz-sulfide veins (Fig. 4.19b). Type-II fluid inclusions may punctually occur within cassiterite near the grain boundaries, but not following any crystallographic direction. More often, type-II fluid inclusions are found within quartz neighboring cassiterite and sulfide grains.

Type-III appears mainly in quartz-sulfide veins (Stage II). Low density N_2-rich vapor type-III fluid inclusions are rare. They usually occur along healed fractures, and are interspersed locally with type-II fluid inclusions (Fig. 4.19c). They range from 5 to 50 μm, with a high vapor phase fraction (FV from 97 to 100 vol%). They show rounded, elongated, and irregular shapes, as well as negative crystal shapes.

Type-IV is found predominantly in the Stage II (Sulfide Stage). Their sizes vary between 10 and 40 μm and they appear as negative crystals. The volumetric vapor fraction estimated visually is 100 vol%. They are confined mainly to vuggy parts of the quartz-sulfide veins, suggesting a late

origin (Fig. 4.19d). They may appear locally as intragranular trails in quartz of quartz-cassiterite veins.

Type-V aqueous fluid inclusions are secondary and occur broadly in all studied samples. Type-V aqueous fluid inclusions are found as transgranular trails. Their sizes vary between less than 5 µm and 50 µm, smaller fluid inclusions tend to have elongated shapes, while larger ones are rather irregular. The vapor phase is below 20 %.

4.6.2. Microthermometry and Raman spectroscopy: results and interpretation

Microthermometric and Raman data, bulk compositions, salinity, and densities of the Logrosán fluid inclusions are summarized in Table 4.9.

Table 4.9: Summary of microthermometric (°C) and Raman data for fluid inclusions in selected samples from the Logrosán ore deposits.

	Type I	**Type II**	**Type III**	**Type IV**	**Type V**
Phase stage	Stage I	Stage I / Stage II	Stage II	Stage II	Stage III
Mineral host	Cassiterite	Quartz	Quartz	Quartz	Quartz
Composition	N_2-CH_4	N_2-CO_2-CH_4	N_2-rich	CO_2-rich	H_2O
FV (%)	30 / 40	30 / 80	97 / 100	100	< 20
Microthermometry (ºC)					
Th_{N2-CH4}	-135.1 / -127.2	-135.5 / -101.7	-133.2 / -124.8	-128.4 / -92.2	–
Tm_{CO2}	–	-86.8 / -57.2	-68.5 / -62.3	-62.1 / -60.0	–
Tm_{cl}	4.9 / 9.6	4.1 / 15.2	11.2 / 12.2	–	–
Tm_{ice}	-3.6 / -0.2	-7.4 / -0.2	–	–	-2.7 / -1.2
Th_{CO2}	–	-34.2 / 7.5	–	-40.2 / -8.2	–
Th	336.9 / 397.6	280.0 / 389.8	–	–	152.2 / 258.5
Raman (mol.%)					
ZN_2	43.9 / 74.1	16.8 / 67.0	51.5 / 67.1		–
ZCO_2	–	13.7 / 65.3	18.9 / 33.2		–
ZCH_4	25.9 / 56.1	7.00 / 34.3	13.5 / 16.3		–
Bulk composition (mol.%)					
XH_2O	93.8 / 96.8	53.3 / 98.4	0.00 / 39.6	–	97.2 / 98.7
XN_2	1.4 / 4.1	0.3 / 27.4	36.8 / 57.7	15.9 / 37.5	–
XCO_2	–	0.9 / 15.6	13.1 / 31.4	52.3 / 79.7	–
XCH_4	1.1 / 2.8	0.3 / 12.5	8.3 / 16.3	4.5 / 10.1	–
Volatile phase type	H1	S2 / (H4)	S2	H4	–
NaCl (% equiv.)	2.1 / 4.5	0.4 / 11.0	–	–	2.1 / 4.5
Global density (g/cc)	**0.64 / 0.73**	**0.26 / 0.74**	**0.07 / 0.10**	**0.04 / 0.13**	**0.83 / 1.02**

Phase transitions were observed between -180 and +30 ºC by microthermometry. Van den Kerkhof (1988, 1990) and Van den Kerkhof and Thiéry (2001) proposed a division of volatile-rich fluid inclusions in H-type and S-type. This classification is based on phase transitions of volatile phases upon freezing and then, warming runs. H-type fluid inclusions have a homogenization as the final phase transition (Th > Tm) while in S-type fluid inclusions, sublimation or melting is the final phase transition (Th < Tm). We have followed this classification for the volatile phase of Logrosán fluid inclusions, owing to the N_2 and CH_4 high contents identified by Raman spectroscopy on the volatile phase.

Molar volumes have been estimated on the basis of binary N_2-CH_4 models (Van den Kerkhof 1988, 1990; Thiéry et al. 1994) for N_2-rich fluid inclusions (type-I, type-II and type-III), owing to the lack of ternary N_2-CH_4-CO_2 diagrams. The molar volume obtained for each fluid inclusion has been corrected, taking into account the CO_2 molar fraction in the volatile phase. For CO_2-rich fluid inclusions (type-II with H4 volatile phase, and type-IV), molar volumes have been taken from the Th_{CO2} and the binary CO_2-N_2 model (Thiéry et al., 1994). Global density was calculated from the molar volume and the vapor/liquid ratio visually estimated at room temperature. Bulk composition calculations have been done after the Ramboz et al. (1985) method. These calculations have been checked for N_2-rich fluid inclusions with Tm_{cl} measured, using the equation of state (EOS) of Duan et al. (1996) with the program NOSALT (Bakker, 2003), and obtaining similar results. Likewise, the program BULK (Bakker, 2003), using the Soave (1972), Lee and Kesler (1975), and Thiéry et al. (1994) EOS, also generates similar results to the obtained manually for CO_2-rich fluid inclusion calculations. Owing to the lack of experimental studies for complex N_2-CO_2-CH_4-H_2O-NaCl compositional fluid inclusion systems, the salinity calculations (expressed as wt.% NaCl equiv.) using the Bodnar (1993) equation are just a rough estimate. Isochores were calculated with the program ISOC (Bakker, 2003) using the EOS of Duan et al. (1992, 1996) for type-I and type-II fluid inclusions; using the EOS of Flowers (1979) and Holloway (1977) for type-III and type-IV fluid inclusions; and the H_2O–NaCl fluid inclusions were calculated from the EOS of Knight and Bodnar (1989).

- *Type-I: Mixed N_2-CH_4 aqueous fluid inclusions*

They consist of complex N_2-CH_4 aqueous inclusions. Vapor phase of these fluid inclusions is referred to as the H1 subtype inclusions proposed by Van den Kerkhof (1988). Accurate microthermometric observations in these fluid inclusions are difficult because of their opacity and the double reflection of the host cassiterite crystals. On warming, N_2-CH_4 homogenization ($Th_{N2\text{-}CH4}$) was observable only for a few specimens. Partial homogenization occurs to the liquid between -135.1 and -127.2 ºC. Ice melting temperatures (Tm_{ice}), when observable, range between -3.6 and -0.2 ºC. Melting clathrate temperatures (Tm_{cl}) yield values between 4.9 and 9.6 ºC. Total homogenization (Th) occurs to the liquid, and less frequently to the vapor, from 336.9 to 397.6ºC. Raman analyses indicate that the volatile phase has N_2 contents between 44 and 74 mol.%, and CH_4 contents between 26 and 56 mol.%. The bulk composition of type-I fluid inclusions is 93.8–96.8 mol.% H_2O, 1.4–4.1 mol.% N_2, and 1.1–2.8 mol.% CH_4. The bulk density of type-I fluid inclusions ranges from 0.64 and 0.73 g/cc. Salinity approaches range from 0.35 to 6 wt.% NaCl equiv.

- *Type-II: Complex mixed N_2-CO_2-CH_4 aqueous fluid inclusions*

Most N_2-CO_2-CH_4 volatile phase fluid inclusions may correspond to the S2 subtype (Th_{N2-CH4}→Tm_{CO2}) proposed by Van den Kerkhof (1988). The microthermometric data measured on warming yielded a N_2-CH_4 homogenization temperature (Th_{N2-CH4}) between -135.5 and -101.7 ºC. Melting or sublimation of the CO_2 solid (Tm_{CO2}) of -86.8 to -57.2 suggests the presence of other volatiles. Clathrate melting temperature (Tm_{cl}) range from 4.1 to 15.2 ºC. Ice melting temperatures (Tm_{ice}) were measured between -0.2 and -7.4 ºC, corresponding to salinities between 0.35 and 11 wt.% NaCl equiv., with an average value of 4.8 wt.% NaCl equiv. A few number of fluid inclusions included in type-II show homogenization of CO_2 (Th_{CO2}), observed to vapor phase in a large range of temperatures from -40.2 to 7.2 ºC. Their volatile phase should be classified as H4 (Th_{N2-CH4}→Tm_{CO2}→Th_{CO2}). The total homogenization (Th) of type-II fluid inclusions was either to liquid or vapor and, very frequently, the inclusions decrepitated. The total homogenization temperatures vary between 320.9 and 389.8 ºC, although fluid inclusions decrepitated from 280 ºC. Bulk composition is: 53.3–98.4 mol.% H_2O, 0.3–27.4 mol.% N_2, 0.8–15.6 mol.% CO_2, and 0.3–12.5 mol.% CH_4. Traces of H_2S have been recognized by Raman spectrometry. The global density ranges widely from 0.26 to 0.74 g/cc. Two groups can be distinguished, high-density and low-density type II, regarding the L/V ratio. The heterogeneity in the Type-II fluid inclusion suggests a possible process of immiscibility.

- *Type-III: N_2-rich vapor fluid inclusions*

The N_2>CO_2-CH_4 vapor fluid inclusions correspond to the S2 group defined by Van den Kerkhof (1988) (Th_{N2-CH4}→Tm_{CO2}). Under cooling, the N_2-CH_4 phase heterogenizes at about -100 ºC and homogenizes (Th_{N2-CH4}) between -133.2 and -124.8 ºC. Melting of CO_2 (Tm_{CO2}) has been recorded between -68.5 and -62.3 ºC, suggesting significant amounts of other volatile phases. Clathrate temperatures were only possible to measure for two fluid inclusions, yielding temperatures of 11.2 and 12.2 ºC. Type-III gaseous fluid inclusions have a very low density (0.07–0.11 g/cc). Bulk composition reveals H_2O contents between 0 and 53.7 mol.%; the volatile phases are characterized by high N_2 contents (28.8–57.7 mol.%), and moderate CO_2 (8.9–31.4 mol.%) and CH_4 (6.47–16.3 mol.%) contents.

- *Type-IV: CO_2-rich vapor fluid inclusions*

The CO_2>N_2-CH_4 monophasic fluid inclusions should be named as H4 after the Van den Kerkhof (1988) classification (Th_{N2-CH4}→Tm_{CO2}→Th_{CO2}). N_2-CH_4 homogenization (Th_{N2-CH4}) yields temperatures from -128.4 to -92.2 ºC, although it is not always identified in these fluid inclusions.

CO_2 melting temperatures (Tm_{CO2}) are in the range of -63.2 to -60.0 ºC, indicating the presence of other volatiles. The homogenization of CO_2 (Th_{CO2}) was observed to vapor in a varied range of temperatures from -40.2 to 8.2 ºC. These vapor-rich fluid inclusions have a very low bulk density (0.04–0.13 g/cc). The bulk composition is free of water and show high CO_2 contents (52.3–79.7 mol.%). N_2 ranges from 15.9 to 37.5 mol.% and CH_4 varies between 4.47 and 10.1 %mol.

- *Type-V: Secondary aqueous fluid inclusions*

The secondary liquid-rich H_2O±(N_2-CH_4-CO_2) inclusions has a volume percentage of the vapor phase lower than 20 %vol. Melting of ice (Tm_{ice}) is the only phase change observed, giving temperatures from -1.2 and -2.7 ºC (2.1 to 4.5 wt.% NaCl equiv.). Volatile phase traces have been recorded by Raman spectroscopy. However, clathrate phase nucleation is not recognized, indicating minor amounts (< 2.7 wt.%) of CO_2 (Hedenquist and Henley, 1985). Total homogenization temperatures (Th) were achieved between 152.2 and 258.5 ºC, showing a main pulse with a mode at 230 ºC, and a probable second minor pulse with a mode at 160 ºC, approximately (Fig. 4.20).

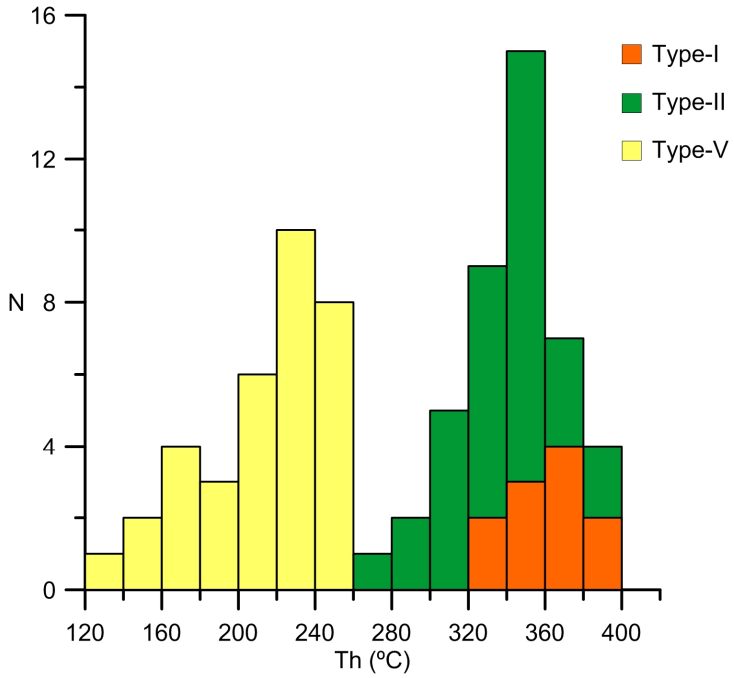

Fig. 4.20: Histograms of homogenization temperature for type-I, type-II and type-V fluid inclusions.

4.7. Stable isotope data and geothermometry

4.7.1. Oxygen and hydrogen isotopes

The $\delta^{18}O$ and δD values of whole rock, quartz, muscovite, cassiterite and tourmaline from SGC metasedimentary rocks, granite, pegmatite, early quartz-tourmaline veins, greisen, and quartz-cassiterite veins are presented in Table 4.10. Temperature estimates found in Table 4.10 have been calculated by a combination of isotope geothermometry (see 4.7.1.1. Isotope geothermometry below) and fluid inclusion homogenization temperatures; considering also a consistency with petrologic and mineralogical observations and associations. Thus, for late-magmatic and metasomatic episodes (i.e., pegmatite and quartz-tourmaline veins) a temperature range between 700 and 800 ºC is assumed; and for mineralization stages (altered host-rocks and quartz-cassiterite veins) temperature is confined between 450 and 540 ºC. A maximum temperature of 450 ºC and an arbitrary temperature of 350 ºC have been considered for the tourmaline isotopic calculations from quartz-cassiterite samples. Tourmaline is a late phase in quartz-cassiterite samples, appearing exclusively in the center of the veins and without any contact with the cassiterite. Therefore, lower crystallization temperatures should be expected.

Table 4.10: O/D stable isotope data for granite, metasediments and associated hydrothermal alteration and mineralization in Logrosán.

Mineral	Rock type	Sample	Parag. stage	$\delta^{18}O$ (‰SMOW)	$\delta^{18}D$ (‰SMOW)	$\%H_2O$	Tmin	Tmax	$\delta^{18}O$ fluid min	$\delta^{18}O$ fluid max	$\delta^{18}D$ fluid min	$\delta^{18}D$ fluid max
Whole rock	Metasediments	CEG-1		13.1	-52.6	3.8	-	-	-	-	-	-
		CEG-2		13.2	-67.3	1.7	-	-	-	-	-	-
		CEG-2		13.4	-67.3	1.7	-	-	-	-	-	-
	Granite	AQ2	Main	14.1	-84.7	1.4	-	-	-	-	-	-
		AQ-5	Evolved	14.5	-77.9	1.3	-	-	-	-	-	-
		AQ-12	Evolved	15.0	-77	1.2	-	-	-	-	-	-
Quartz	Pegmatite	L-179		14.3	-	-	700	800	14.1	13.4	-	-
	Qtz-Tur vein	L-108		13.7	-	-	700	800	13.5	12.8	-	-
	Greisen	SER-5	Qtz I	14.1	-	-	450	540	11.0	12.4	-	-
		SER-1	Qtz II	15.8	-	-	450	540	12.7	14.1	-	-
		L-104	Qtz II	16.5	-	-	450	540	13.4	14.8	-	-
		L-105	Qtz II	15.8	-	-	450	540	12.7	14.1	-	-
	Qtz-Cst vein	L-111	Qtz III	15.1	-	-	450	540	12.0	13.4	-	-
Muscovite	Granite	AQ1		12.9	-75.6	4.4	700	800	14.3	13.7	-71.4	-75.5
	Greisen	SER-1	Ms I	14.0	-76.6	3.5	450	540	13.3	14.3	-53.4	-62.3
		SER-1	Ms I	14.3	-76.6	3.5	450	540	13.6	14.6	-53.4	-62.3
		L-104	Ms I	13.5	-94.4	4.4	450	540	12.8	13.8	-71.2	-80.1
		L105	Ms I	13.7	-81.8	4.1	450	540	13.0	14.0	-58.6	-67.5
Cassiterite	Greisen	L-104	Cst II	8.2	-	-	450	540	12.4	12.4	-	-
	Qtz-Cst vein	L-111	Cst III	8.1	-	-	450	540	12.3	12.3	-	-
		L-111	Cst III	8.2	-	-	450	540	12.4	12.4	-	-
		L-165	Cst III	8.2	-	-	450	540	12.4	12.4	-	-
Tourmaline	Pegmatite	L-179		12.7	-94.5	3.3	700	800	13.3	13.4	-67.3	-72.6
	Qtz-Tur vein	L-108		12.4	-88.8	3.2	700	800	13.3	13.1	-61.6	-66.9
		L-108		12.3	-88.8	3.2	700	800	13.3	13.0	-61.6	-66.9
	Qtz-Cst vein	65.2	Tour II	13.2	-92.6	3.3	450	540	12.2	13.3	-70.1	-75.8

Accordingly to the specific range of temperature for each case, the following equations for the calculation of the fluid isotope signature have been selected. The $\delta^{18}O_{fluid}$ values from quartz, muscovite, cassiterite and tourmaline from altered host-rocks and quartz-cassiterite veins have been calculated using the equations of Clayton et al. (1972), O'Neil and Taylor (1967), Zheng (1991), and Zheng (1993), respectively. $\delta^{18}O_{fluid}$ calculations for quartz, muscovite and tourmaline from granites, pegmatites and quartz-tourmaline veins have been done after O'Neil (1986), Bottinga and Javoy (1973) and Zheng (1993) equations, respectively. δD_{fluid} for muscovite has been calculated using the Suzuoki and Epstein (1976) equation. δD_{fluid} values for tourmaline from pegmatites and quartz-tourmaline veins have been calculated after the equation of Guo Quian (1997), while the equation of Jiang (1998) has been used for δD_{fluid} calculations of tourmaline of quartz-cassiterite vein.

Whole rock SGC metasediment have $\delta^{18}O_{SMOW}$ values of 13.1 and 13.4 ‰, and δD_{SMOW} values of -67.3 and -52.6 ‰. These values are typical of low- to medium-grade metamorphosed sedimentary rocks (Sheppard, 1986, Hoefs, 2009). Whole rock granite samples studied correspond to one Main Unit sample ($\delta^{18}O_{SMOW}$ of 14.1 ‰, and δD_{SMOW} of -84.7 ‰), and two Evolved Unit samples. The Evolved Units display higher $\delta^{18}O_{SMOW}$ (14.5 and 15.0 ‰) and δD_{SMOW} values (-77.9 and -77.0 ‰). Quartz from a miarolitic pegmatite shows $\delta^{18}O_{fluid}$ values between 13.4 and 14.1 ‰, quartz from early quartz-tourmaline veins has lower $\delta^{18}O_{fluid}$ (12.8-13.5 ‰). $\delta^{18}O_{fluid}$ values of quartz from altered host rocks and quartz-cassiterite veins vary from 10.0 to 14.2 ‰. Quartz adjacent to the walls has been selected preferentially to quartz from the center of the veins, in order to select the quartz more likely in equilibrium with the muscovite from selvages. Vein and altered host-rocks samples show higher $\delta^{18}O_{quartz}$ than pegmatite and quartz-tourmaline veins, except for a specific sample, the SER-5 sample (Table 4.10). Muscovite from a granite sample in equilibrium with the fluid has $\delta^{18}O_{fluid}$ between 13.7 and 14.3 ‰, and δD_{fluid} between -75.5 and -71.4 ‰. Isotopic calculations of muscovite from altered host-rocks yield values ranging from 12.8 to 14.6 ‰ $\delta^{18}O_{fluid}$, and from -80.1 to -53.4 ‰ δD_{fluid}. Cassiterite from altered host-rocks and quartz-cassiterite veins has a very narrow $\delta^{18}O_{fluid}$ range, from 12.3 to 12.4 ‰. $\delta^{18}O_{fluid}$ values of tourmaline from pegmatite and quartz-tourmaline veins vary from 13.0 to 13.3 ‰, while δD_{fluid} varies from -61.6 to -72.6 ‰. Tourmaline of quartz-cassiterite veins shows very similar δD_{fluid} values (-60.7 to -70.1 ‰), but lower $\delta^{18}O_{fluid}$ (10.9 to 12.7 ‰).

4.7.1.1 Isotope geothermometry

Isotope geothermometers have been used to constraint the temperature of the magmatic and hydrothermal events in the Logrosán ore deposits. A quartz-tourmaline pair from a pegmatite yields a temperature of 716 ºC, using the Zheng (1993) equation (Table 4.11). Assuming an error

of 0.1‰ for δO_{quartz} and $\delta O_{tourmaline}$, the average error of the temperature calculation is ±82 ºC. This temperature is quite consistent with the calculated Logrosán granite saturation zircon temperatures (700-780 ºC) (Chicharro et al., 2014; Chapter 3, this volume). The granite crystallization yields an average temperature of 836 ºC for the parental magma (Ti-in-zircon geothermometry: Chicharro et al., 2014; Chapter 3, this volume). Tourmaline from quartz-tourmaline veins yields temperatures between 793 and 836 ºC (Table 4.11), agreeing with the granite crystallization temperature estimates. The quartz-tourmaline temperatures obtained are useful to relate these quartz-tourmaline veins to late-magmatic or metasomatic processes, rather than with hydrothermal processes. This implies an important release of boron during, or following, the granite emplacement.

Table 4.11: Stable isotope geothermometry estimated for minerals from the Logrosán ore deposits (*isotopic value of an equivalent sample)

Sample		Mineral pair	δ18OQtz	δ18Omineral	Temperature (°C)
					Chacko et al. (1996)
SER1	Altered host-rocks	Qtz-Ms	15.8	14.0	606 ± 52
SER1		Qtz-Ms	15.8	14.3	688 ± 70
L104		Qtz-Ms	16.5	13.5	410 ± 24
L105	Qtz-Cst vein	Qtz-Ms	15.8	13.7	542 ± 41
					Polyakov et al. (2005)
SER1	Altered host-rocks	Qtz-Cst	15.8	8.2*	530 ± 11
L104		Qtz-Cst	16.5	8.2	457 ± 10
L104		Qtz-Cst	15.8*	8.2	494 ± 11
L111	Qtz-Cst vein	Qtz-Cst	15.1	8.1	530 ± 12
L111		Qtz-Cst	15.1	8.2	536 ± 13
L165		Qtz-Cst	15.1*	8.2	536 ± 13
					Zheng (1993)
L179	Pegmatite	Qtz-Tur	14.3	12.7	716 ± 77
L108	Qtz-Tur vein	Qtz-Tur	13.7	12.4	836 ± 100
L108		Qtz-Tur	13.7	12.3	793 ± 91
					Kotzer et al. (1993)
65.2	Qtz-Cst vein	Qtz-Tur	15.1*	13.2	541 ± 60

The quartz-muscovite isotope thermometry using the equations of Chacko et al. (1996) provides a large range of temperatures. Assuming an error of 0.1‰ for δO_{quartz} and $\delta O_{muscovite}$, the average error of the temperature estimate is ±47ºC. These results vary from 410 to 688 ºC. The Cerro de San Cristóbal vein samples (L104 and L105) show temperatures (410 and 542 ºC) (Table 4.11) consistent with the quartz-cassiterite thermometry, the fluid inclusion estimates, and the arsenopyrite geothermometry. On the contrary, the exogranitic El Serranillo samples (SER-1) show higher temperatures (606 and 688 ºC) (Table 4.11). These high temperatures are most likely attributed to a disequilibrium relationship between the quartz and the analyzed muscovite.

Temperatures calculated for coexisting quartz and cassiterite using the fractionation factors of Polyakov et al. (2005) show a relatively narrow range between 457 and 536 ºC (average value of

514 ºC). The accompanying tourmaline gives an agreeing temperature of 450±60 ºC using the equation of Kotzer et al. (1993). As quartz and cassiterite have a large fractionation factor, these data might be considered as a good geothermometer. In fact, assuming an error of 0.1‰ for δO_{quartz} and $\delta O_{cassiterite}$, the average error of the temperature estimate is only ±12ºC. Therefore, a temperature between 450 and 530 ºC has been established as the best fit for the cassiterite precipitation. This range of temperature is in reasonable agreement with primary fluid inclusion homogenization temperatures recorded in cassiterite (<400 ºC) (Table 4.9), which represent the minor temperature of entrapment.

4.7.2. Sulfur isotopes

The sulfur isotope data are presented in Table 4.12 as conventional per mil values ($\delta^{34}S$‰) referenced to the Canyon Diable Troilite (CDT) standard, and calculated for the laser corrected factor. $\delta^{34}S_{CDT}$ values of arsenopyrite (from -2.5 to -5.5‰) and chalcopyrite (from -2.4 to -3.7 ‰) are in the same range (Table 4.12). The $\delta^{34}S_{H2S}$ composition of the fluid has been calculated for given temperatures determined on the basis of fluid inclusion studies, chemical geothermometry and paragenetic criteria for chalcopyrite. The $\delta^{34}S$ composition of the fluid of arsenopyrite cannot be calculated, as no fractionation factor exists for this mineral phase. The $\delta^{34}S_{H2S}$ composition of chalcopyrite samples varies between -2.3 and -3.6‰.

Table 4.12: Sulfur isotope data for sulfides from the Logrosán ore deposits.

Sample	Mineral	$\delta^{34}S_{CDT}$ (‰)	Laser correction factor (‰)	T (ºC)	$\delta^{34}SH_2S$ (‰)
L-4.2	Apy	-5.9	-5.5	430	-
L-4.2	Apy	-5.3	-4.9	430	-
L-5.1	Apy	-2.9	-2.5	430	-
L-5.1	Apy	-3.9	-3.5	430	-
SER-4	Cpy	-3.1	-2.4	370	-2.3
SER-4	Cpy	-4.5	-3.8	370	-3.6
SER-4	Cpy	-3.5	-2.8	370	-2.7

4.7.3. Arsenopyrite geothermometry

The dependence of arsenopyrite composition on equilibration conditions, such as temperature and S_2 activity, has been used as a geothermometer for temperatures higher than 300 ºC by Kretschmar and Scott (1976), and reexamined by Sharp et al. (1985). Iron arsenides, or other iron sulfides, have not been recognized accompanied the arsenopyrite (Apy I and Apy II) in the Logrosán Oxide Stage, making it impossible the application of the arsenopyrite geothermometer on this case. However, arsenopyrite from the Sulfide Stage (Apy II) has been identified enclosing remnants patches of löllingite, and pyrrhotite rounded crystals. Zoned arsenopyrite crystals with compositional variations in As higher than 1 at.% have not been considered for arsenopyrite

geothermometry. Accordingly, only 42 analyses of unzoned arsenopyrite crystals have been selected. An attempt was made to determine the ore forming conditions, assuming the equilibration of arsenopyrite, first with löllingite, and later, with pyrrhotite. The arsenopyrite compositions reflect the temperature of the early Sulfide Stage mineralization. The average compositions of arsenopyrite from different samples and the calculated temperatures are summarized in Table 4.13. Temperatures obtained range from 456 to 417 ºC, which represent the higher temperatures of the Sulfide Stage (Fig. 4.21). Moreover, the geothermometer of Nekrasov et al. (1979) has been applied to sphalerite-stannite pairs in samples where sphalerite and stannite are closely intergrown. A range of temperatures between 453 and 372 ºC for the following steps of the Sulfide Stage is estimated.

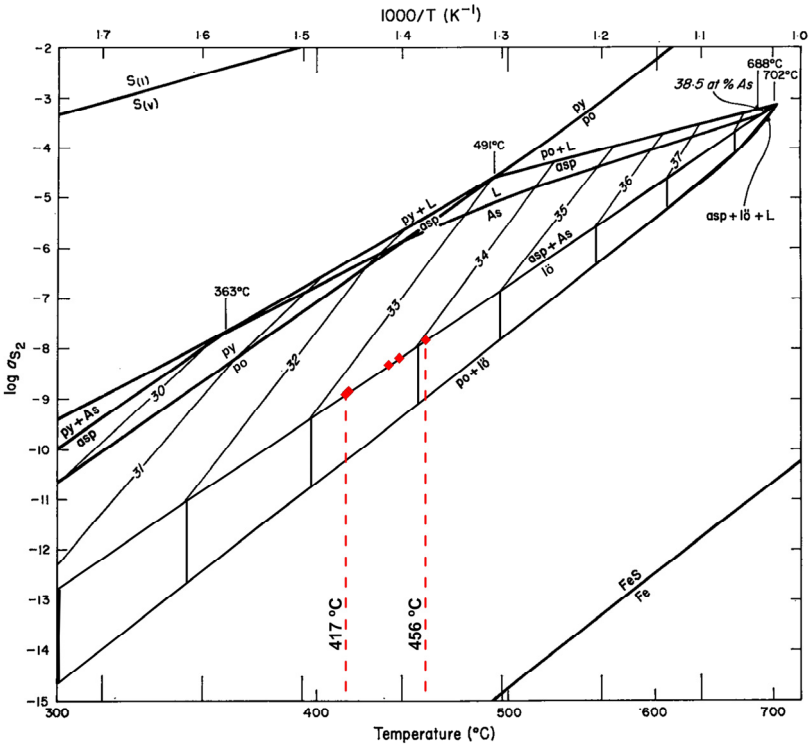

Fig. 4.21: Arsenopyrite geothermometry based on the T–X diagram of Kretschmar and Scott (1976). Arsenopyrite (Apy), native arsenic (As), liquid (L), löllingite (Lo), pyrhotite (Po), pyrite (Py).

Table 4.13: Average As (at.%) content and estimated temperature ranges from arsenopyrite geothermometry in arsenopyrite (Apy) from the Logrosán ore deposits.

Sample	At. %As			N	Estimated temperature (ºC)		
	Average	SD	Range				
L-4.2	34.08	0.35	33.42 – 34.74	11	456	±	10
L-13	33.90	0.54	33.03 – 34.82	12	442	±	10
L-4.3	33.73	0.58	32.67 – 34.45	7	438	±	10
L-5	33.35	0.88	32.09 – 34.04	4	416	±	20
L-5.3	33.34	0.60	32.69 – 34.16	5	415	±	10
L-12	33.37	0.60	32.70 – 33.86	3	417	±	10

4.8. Discussion

4.8.1. Timing of the Logrosán ore deposits

The Logrosán granite yields an U-Pb ID-TIMS age of 307.88±0.86 (2σ) Ma and a weighted average $^{206}Pb/^{238}U$ age of 303.0±2.3 (2σ) Ma (Chicharro et al., 2014; Chapter 3, this volume). In this work, the muscovite Ar-Ar ages obtained a range from 303 to 311 Ma, with 2-sigma errors of ±2-3 Ma. Muscovite from endogranitic mineralization (San Cristóbal) yield Ar-Ar ages from 306-311 Ma, in part anomalously older than the granite emplacement. The exogranitic sample (El Serranillo, SER) is slightly younger than the endogranitic samples (303 ± 3 Ma), although overlapping with analytical error. The El Serranillo ore deposit is directly related to the Logrosán granite, which extends towards this area in depth, as revealed by gravity survey (Chicharro et al., 2015; Chapter 6, this volume). Moreover, there are strong similarities on the paragenetic, textural, and geochemical features of endogranitic and exogranitic occurrences. The inference is that the exo- and endogranite mineralization resulted from the same hydrothermal activity. The slight difference of timing between endogranitic and exogranitic mineralization suggests that there were at least two hydrothermal pulses (308-306 Ma and ~303 Ma).

The narrow range of ages 306-308 Ma is considered to be the timing of the main Sn-(W) mineralization. These ages are quite consistent and overlap the emplacement timing of the genetically related granite (308 ± 0.8 Ma), assuming that the longevity of the associated hydrothermal system is expected to be at around 2 Ma (e.g., Kent and McDougall, 1995; Sillitoe, 1994). Similar timing has been recognized for the Variscan Sn-W ore deposit related to the Carris granite (Portugal) by Moura et al. (2014). Sn-W ores contemporaneous or penecontemporaneous to the granite-related emplacement has been also recorded, for instance, for the tin mineralization in the Dadoushan deposit of the Gejiu district (China) (Cheng et al., 2012), or the Xuebaoding Sn-W-Be deposit (China) (Zhang et al. 2014).

4.8.2. Nature and origin of mineralizing fluids

The isotopic composition of fluids at equilibrium with the magmatic (granite and pegmatite), metasomatic (quartz-tourmaline veins), and hydrothermal (altered host-rocks and quartz-cassiterite veins) minerals are represented in Figure 4.22. The $\delta^{18}O_{fluid}$ values decrease from the magmatic to the hydrothermal minerals (Fig. 4.22a and 4.22b). A raising trend for the δD_{fluid} is observed from the magmatic phases to the hydrothermal phases (Fig. 4.22c and 4.22d). A rise of δO_{fluid} and a drop of δD_{fluid} values while decreasing temperature may be expected if the system

remained closed, according to the mineral isotopic equilibration equations. The inverse evolution reflects the equilibration with successively ^{18}O-depleted and D-enriched fluids with time in an open system.

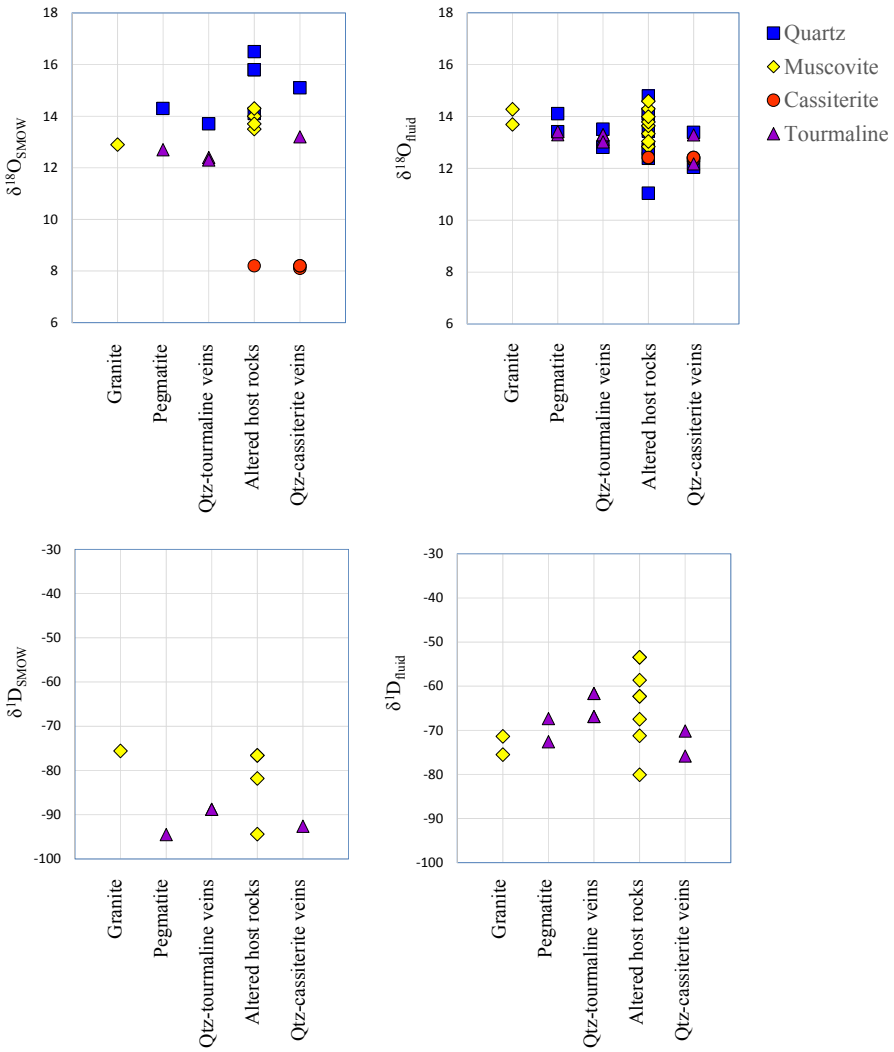

Fig. 4.22: Plot of mineral isotopic signature vs. time represented by granite, pegmatite, quart-tourmaline veins, host-rock alteration and quartz cassiterite vein for: **a)** $\delta^{18}O_{mineral}$; **b)** $\delta^{18}O_{fluid}$; **c)** $\delta D_{mineral}$; **d)** δD_{fluid}.

In the conventional δO-δD diagram (Fig. 4.23) the standard fields for different types of water (Sheppard, 1986; Ohmoto, 1986) have been represented and compared to the calculated fluid signatures determined for tourmaline and muscovite from granite and pegmatite (magmatic), quartz-tourmaline veins (metasomatic), and altered host-rocks and quartz-cassiterite veins (hydrothermal). The fields of isotopic composition of the Logrosán granite, and of the SGC metasediments have been also outlined in Figure 4.23. The granite whole-rock samples show a trend through the supergene/hypogene line, probably related to a hydrothermal kaolinitation process (Sheppard et al., 1969), ever since the Logrosán granite shows kaolinization in sectors. The Logrosán granite whole rock isotopic analyses do not fit with the primary magmatic field,

nor with the peraluminous magmatic field and shows higher $\delta^{18}O$ values than the field of the peraluminous Cornubian granites outlined by Sheppard (1977). $\delta^{18}O$ values higher than 10‰ have been frequently found in Variscan granites from Western Europe (Tartèse and Boulvais, 2010; Hoefs and Emmermann, 1983) and the southern CIZ (e.g., Castelo Branco Batholith: 12.2-13.7‰, Antunes et al., 2008). These elevated $\delta^{18}O$ values are typical of high-SiO_2 peraluminous granites, especially those derived from a sedimentary or metasedimentary protolith (Taylor, 1978), which is the case for the Logrosán granite (Chicharro et al. 2014; Chapter 3, this volume). The SGC metasedimentary isotopic field overlaps with the metamorphic field defined by Taylor (1974).

The minerals vary isotopically in a vertical path, toward higher δD values (Fig. 4.23). The δD signature of minerals and rocks are very sensitive to the δD composition of interacting fluids because hydrogen is a minor component of most minerals and rocks (Rollinson, 1993). There is a general trend from granitic to hydrothermal minerals. They tend to go out of equilibrium for the Logrosán magmatic field, toward the equilibrium with the SGC metasediment field. Mixing with a metamorphic fluid, of higher δD and lower δO composition, may explain this evolution. Moreover, the presence of N_2 and CH_4 in fluid inclusions suggests the participation of a significant organic-rich metamorphic fluid in the system (e.g., Linnen, 1991; Huff and Nabelek, 2007; Cepedal et al., 2013).

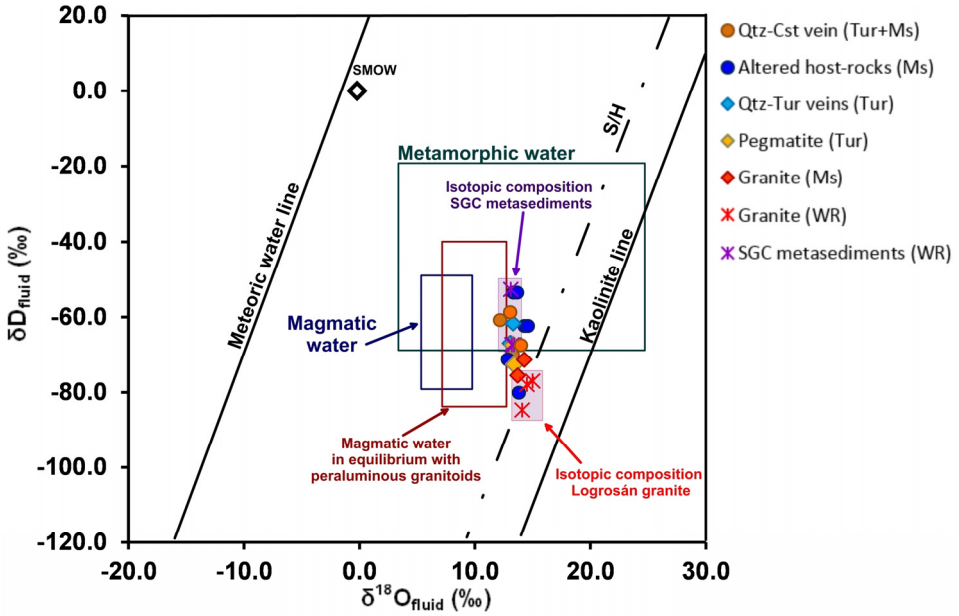

Fig. 4.23: δO-δD plot of the isotopic compositions of fluids from Logrosán. SMOW: Standard Mean Ocean Water. Reference data: Sheppard (1986), Ohmoto (1986) and Craig (1961).

The Logrosán ores show negative $\delta^{34}S$ values corresponding to a light source of sulfur (Table 4.12). Data of $\delta^{34}S$ vary between -5.5 and -2.4 ‰. There is very little variation in the $\delta^{34}S$ values of arsenopyrite and chalcopyrite, although arsenopyrite reaches the highest values. This is

consistent with the fact that chalcopyrite forms generally at lower temperatures, while arsenopyrite forms during the whole Sulfide Stage and, consequently, in a wider temperature range. However, the sulfide ores, either from intra- or extragranitic ores, show a relatively uniform and narrow $\delta^{34}S$ composition. This suggests a homogeneous source and H_2S dominant fluids (Ohmoto and Rye, 1979), which is the dominant sulfur species in solution in S-type granitoids (Burnham and Ohmoto, 1980). The $\delta^{34}S$ composition of the Logrosán sulfide ores is lighter in comparison with other granite-related Sn-W ore deposits (e.g., Kontak, 1990). The measured values are concordant with the ilmenite-serie granitoids formed by partial melting of predominantly sedimentary protoliths, which have $\delta^{34}S$ values less than 0‰ (Ishihara and Sazaki, 1989). Sulfides from magmatic sources have $\delta^{34}S$ signatures between -5 and 5 ‰ after Ohmoto and Rye (1979). Traces of H_2S have been recognized in the Logrosán fluid inclusions by Raman spectroscopy. The H_2S fractionation between sulfides and granitic melts is minor, and therefore, the $\delta^{34}S$ signature of S-type granites is expected to be the same as the $\delta^{34}S$ signature of the sulfide minerals (Ohmoto, 1986). Therefore, little variation in the $\delta^{34}S$ signature of individual arsenopyrite crystals, showing values below -5 ‰, are supposed to respond to a decrease of $\delta^{34}S$ at the beginning of the Sulfide Stage. This would explain the precipitation of sulfide minerals by an increase of the fO_2 as a consequence of a new fluid input (Ohmoto, 1972). More oxidizing conditions may be the combination of this oxidized fluid input and a phase-separation process (Dubessy et al., 1987), which is also inferred from the fluid inclusion data.

4.8.3. Evolution of mineralization

The earliest Nb-Ta phases are restricted to small pockets within metasedimentary SGC rocks from the El Serranillo sector. These host rocks were affected by metasomatism and alteration (silicification, muscovitization and tourmalinization), owing to multiple veining episodes. Discrete columbite crystals show oscillatory zoning, which has been interpreted as a magmatic feature (e.g., Černý et al., 1992; Lahti, 1987). Oscillatory zoning, as a result of non-equilibrium fractional crystallization from the magmatic source, may be in agreement with complex fractional crystallization paths described for the latest evolved Logrosán granite units (Chicharro et al., 2014; Chapter 3, this volume). The textural features of the columbite and Nb-Ta rutile intergrowths suggest a simultaneous crystallization of both phases. These magmatic features, the setting of these ores and the lack of association with pegmatitic bodies suggest that Nb-Ta phases were dispersed directly from the Logrosán granite along multiple fractures. The channels defined stockworks and halos of alteration within the metasedimentary host rocks surrounding the Logrosán granite. Nb and Ta are highly incompatible elements in a magmatic system, and are enriched in highly fractioned granites. Although they show very low partitioning toward an aqueous fluid or a granitic melt (e.g., Chevychelov et al., 2010), Nb and Ta can be concentrated

and transported in F-rich solutions (Keppler, 1993; Linnen, 1998; Linnen and Keppler, 1997; Zaraisky et al., 2010). Moreover, the solubility of Nb-Ta phases is strongly temperature dependent (Linnen and Keppler, 1997; Van Lichtervelde et al., 2010). In addition, Ti mobility at high temperatures is also higher in F-rich solutions and acid environments, because Ti forms complexes with F^-, Cl^- and OH^- (Ryzhenko et al., 2006). Hence, the first generation of columbite and Nb-Ta rutile found exclusively in the El Serranillo sector can be explained with Nb, Ta and Ti transport by hydrothermal fluids of probable late-magmatic origin from the granitic source, and their precipitation in contact with metasedimentary country rocks. Owing to the younger age of the extragranite mineralization (El Serranillo), it may also be associated with a more evolved granitic unit richer in incompatible elements and probably younger in age (~303 Ma). The precipitation of the early cassiterite, postdating the first Nb-Ta phases, indicates that the fluid became saturated with Sn after Nb, Ta and Ti. Also, the existence of patchy zoning in early Nb-Ta phases is interpreted as a re-equilibration of primary minerals with later fluids (e.g., Tindle and Breaks, 2000). These fluids, responsible for the alteration of the Nb-Ta phases, have been mostly regarded as late-magmatic in origin (e.g., Abella et al., 1995; London, 1990). However, Černý et al., (1992) suggest that metamorphic fluids may also be involved. Modification of the primary Nb-Ta phases (e.g., patchy zoning) may indicate that the hydrothermal fluid derives from a mixing of magmatic and metamorphic fluids, probably induced by variations in pressure and temperature (Müller and Halls, 2005). However, Nb-Ta rutile and columbite (Nb-Ta rutile II and columbite II) inclusions within cassiterite are characterized by a drop of Ta and an increase in Nb contents, with respect to the early Nb-Ta phases (Table 4.2). Hence, the Ta/(Ta+Nb) ratio decreases from the earlier to the later Nb-Ta phases, which is opposed to the typical evolutionary trend defined by a Ta enrichment of Nb-Ta oxides during melt fractionation (Beurlen et al., 2008; Tindle et al., 1998). Therefore, primary textural features of the early Nb-Ta phases were probably modified by the subsequent hydrothermal pulses responsible for cassiterite precipitation, most likely in combination with metamorphic fluids. As discussed below, fluid inclusion studies in the Logrosán ore deposits, showing N_2-CH_4-CO_2-H_2O gaseous phases support the participation of metamorphic fluids, and in this respect, complex volatile-rich fluid inclusions have been found in similar ore deposits from western Spain (e.g., Mangas and Arribas, 1987). The lack of geochemical discrepancies between Cst II and III from the San Cristóbal and El Serranillo sectors suggests a homogenous ore-forming scenario for the main cassiterite precipitation during most of the Stage I - Oxide Stage.

4.8.4. Fluid evolution

The fluid inclusions of the Logrosán ore deposits show complex volatile compositions (N_2-CO_2-CH_4-H_2O) (Fig. 4.24). Volatile phases have been recognized in other granite-related ore deposits

(e.g., Dolníček et al., 2012; Fu et al., 2014; Giuliani, 1984; Liao et al., 2014; Moura et al., 2014; Noronha et al., 1999; Vindel et al., 1996; Ortega et al., 1992; Pohl and Günther, 1991; Wilkinson, 1990). The bulk and gas composition evolution is presented in Figure 4.24, and the estimated isochores for the different fluid inclusion types are presented in Figure 4.25.

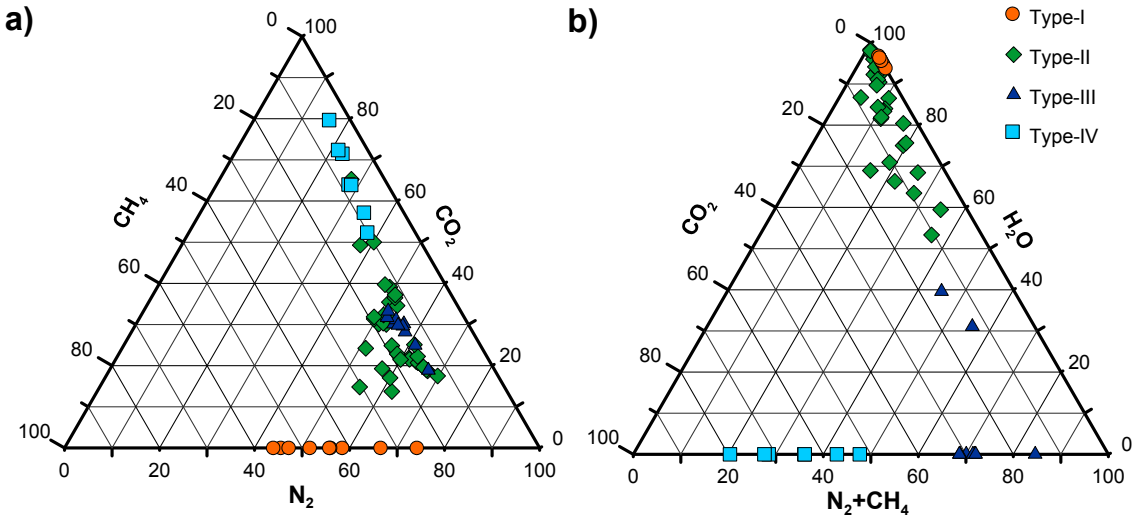

Fig. 4.24: a) XN_2-XCO_2-XCH_4 and **b)** $X(N_2+CH_4)$-XH_2O-XCO_2 ternary diagrams showing the volatile and bulk composition of the Logrosán ore deposit fluid inclusions.

The low-salinity N_2-CH_4-H_2O type-I fluid inclusions correspond to the Oxide Stage, they are found exclusively as primary fluid inclusions within the cassiterite crystals. The gas composition (N_2-CH_4) (Fig. 4.24) points to a metamorphic fluid influence, as suggested also by the stable isotope studies and mineralogical evidence. The N_2 more likely derives from the hydrolysis of phyllosilicates during the regional metamorphism, while the CH_4 may derive from organic matter sources (e.g., Roedder, 1984; Dubessy et al., 1989; Shepherd et al., 1991; Cepedal et al., 2013). Therefore, the SGC metasediments are thought to be the primary source of nitrogen and methane. However, nitrogen and methane might also derive from the altered granite. This is explained by the fact that the ammonium (NH_4^+) enrichment and the degree of alteration is dependent (Hall et al., 1991). Moreover, the enrichment of ammonium in granites seems to be related to organic-rich pelitic protoliths (e.g., the Spanish Central System granites, Hall et al. 1996), being the SGC metasediments the protolith of the Logrosán granite (Chicharro et al., 2014; Chapter 3, this volume). The lack of carbonic material in inclusions suggests that CH_4 was assimilated during fluid migration by the reaction between poorly organized carbonic material and hydrothermal fluids (Xu, 2000). Assimilation and recycling of CH_4-N_2 from metamorphic host-rocks by granites related to Sn-W mineralization has been pointed out previously by Wilkinson (1990) and Pohl and Günther (1991). The cassiterite probably precipitated due to the interaction of organogenic fluids from the SGC metasedimentary rocks with late-magmatic fluids. This is in agreement with the presence of altered host-rocks and quartz-cassiterite vein oxygen and

hydrogen isotopic compositions. The magmatic fluids are inferred by the introduction of CO_2 in type-II fluid inclusions, and by the stable isotope constraints. The lack of CO_2 in the oldest fluid inclusions (type-I) might be attributed to the carbon devolatilization and/or leaching during contact metamorphism and the low solubility of CO_2 in granitic melts at upper crustal pressure (Fogel and Rutherford, 1990; Linnen and William-Jones, 1995). Another possibility is that CO_2 was not introduced in the system, but derived from the oxidation of CH_4 (Fuertes-Fuente, et al., 2000). However, the wide range of compositional volatile-phase proportions in successive fluids (type-II, type III and type-IV fluid inclusions) rather suggest that CO_2 was mainly introduced by the magmatic derived-fluid. The mixing process between two fluids of different origin, magmatic and metamorphic produced this immiscibility. Fluid-mixing processes for ore precipitation have been described for similar Sn-W ore deposits (e.g., Giuliani, 1984; Giuliani et al., 1988; Pohl and Günther, 1991; Noronha et al., 1999; Wilkinson, 1990; Martínez-Abad et al., 2015). Fluids related to type-II fluid inclusions of the Sulfide Stage are characterized by the presence of CO_2 in the system (Fig. 4.24), which indicates a higher O_2 fugacity (Eugster and Wilston, 1985). This is also in agreement with $\delta^{34}S$ isotopes. Type-II fluid inclusions are very heterogeneous, coexisting different vapor-liquid ratios, compositions and homogenization styles (Table 4.9, Fig. 4.24). The high- and low-density type-II fluid inclusion isochores intersect at approximately 400ºC and 100 MPa (Fig. 4.25). Intersecting isochores are commonly pointed to as evidence for immiscibility conditions (Brown, 1998). This intersection may indicate the P-T trapping conditions at which the H_2O-N_2-CO_2-CH_4 heterogeneous mixture was trapped (Roedder and Bodnar, 1980). The heterogeneity of type-II fluid inclusions preserved in quartz (Table 4.9) accompanying the sulfides suggests that their formation is related to a process of effervescence (phase separation), resulting in fluid inclusions with variable aqueous/vapor ratios. This process was due to a decrease in pressure and temperature as a result of hydraulic fracture. Type-III and type-IV fluid inclusions (both recognized as secondary in early quartz) most likely are the consequence of the same process of immiscibility. The volatile heterogeneous phases represented by the low-density type-III and type-IV fluid inclusions suggest that the effervescence might have been incomplete. This intermittent effervescence process may be recognized in the separation of N_2-CH_4 from CO_2 within type-III and type-IV fluid inclusions; a compositional separation that starts appearing in type-II fluid inclusions (Fig. 4.24a). This would explain also subsequent lower water contents in fluid inclusions with time (Fig. 4.24b). The rapid sealing and reopening of the fractures at low pressure conditions (<100 MPa) (Fig. 4.25) may explain an intermittent effervescence event. The last episodes recognized in the system correspond to the influx of cool meteoric fluids and are represented by aqueous type-V fluid inclusions.

4.8.5. Controls of Sn-(W) mineralization

The cassiterite mineralization is almost contemporaneous with the Logrosán granite emplacement. An early Nb-Ta oxide precipitation hosted by altered host-rocks from the exogranitic ore deposits (Fig. 4.7) shows late-magmatic features (e.g., oscillatory zoning). Moreover, the quartz accompanying the Nb-Ta mineralization shows a $\delta^{18}O_{quartz}$ value close to the quartz from pegmatites, and to the whole rock values of the granite Main Unit (Table 4.10). Hence, the early Nb-Ta disseminated mineralization is more likely related to a late-magmatic phase rather than to the main hydrothermal mineralization event, as discussed above and by Chicharro et al. (2015). This is in good agreement with the relationship between the granite timing (ID-TIMS age of 307.88 ± 0.86 Ma; and weighted $^{206}Pb/^{238}U$ average age of 303.0 ± 2.3 Ma) and the Ar-Ar ages obtained for the muscovite associated with the subsequent cassiterite mineralization (from 311 ± 3 Ma to 303 ± 3 Ma). The mineralization postdates barren quartz-tourmaline veins and tourmaline miarolitic cavities, which is an evidence for volatile phase saturation in magmas and fluid saturation at near *solidus* conditions (Candela, 1997). The presence of volatiles in the melt contributes to low *solidus* temperatures, allowing the granite emplacement to take place at shallower depths (Chapter 7, this volume).

The source of tin is assumed to be magmatic as Sn is being enriched during the fractionation of the Logrosán granite (Table 4.7). The relatively high fluorine contents in the Logrosán granite, especially in the altered units (Table 4.7, Fig. 4.13), suggest that tin may have been transported as a Sn(II)-fluoride complex (Yushan and Shuqing, 1986). Nevertheless, there are no F-minerals in the Logrosán ore deposits, such as fluorite or topaz. Instead, tourmaline is present widely as a metasomatic and hydrothermal mineral, as occurs in most Sn-W deposits. It is known that boron and fluoride can form stable complexes such as $B(OH)_{3-n}F_n$, HBF_4, $NaBF_4$ and others in H_2O-rich solutions (Thomas, 2002).Whether Sn^{2+}-B-F and Sn^{2+}-B-F-Cl-hydroxyl complexes exist also under the required conditions remains unknown (Thomas et al., 2003). In any case, Sn is transported under reduced conditions (Burnham and Ohmoto, 1980; Ishihara, 1977). Some authors have attributed greisenization as the major and probably sole control for cassiterite precipitation in greisen-hosted tin deposits (Halter et al., 1996). The host-rock greisen-like alteration in the Logrosán ore deposits consists mainly of narrow vein muscovite-rich selvages. Neutralizing reactions (hydrolysis of feldspars) by increasing the surface contact area between the hydrothermal fluids and the aluminosilicate rocks are more effective in structural weakness zones (e.g., the stockworks from the El Serranillo sector). The alteration found in the Logrosán ore deposits may have contributed to the ore precipitation, but it is unlikely to have caused just by itself the destabilization of tin-bearing complexes in solution. The isotopic and fluid inclusion

evidence suggests that a mixing of metamorphic and magmatic fluids caused the cassiterite precipitation. Variable mixing of magmatic and metamorphic fluids characterize the initial steps of some other ore-forming Variscan systems (Mateus and Noronha, 2001), especially in geochemical systems associated with post-tectonic granitoids emplaced at relatively shallow depths (4-5 km).

The emplacement of plutonic intrusions in shallow metasedimentary rocks generates convective systems (e.g., Jackson et al., 1982; Sheppard, 1977; Taylor, 1978). During the Logrosán granite emplacement, convective cells were produced in the adjacent SGC metasedimentary rocks, not only in those affected by contact metamorphism. This process allowed the circulation of N_2-CH_4-rich organogenic fluids from the nearby metasedimentary host-rocks. The convective cells may have affected the granite itself, allowing a moderately recycling and assimilation of these fluids, as proposed for the Cornubian batholith by Wilkinson (1990). This would explain the prevalence of N_2-(CH_4) fluids over CO_2 during most of the fluid evolution of the Logrosán ore deposits. The magmatic fluids, enriched in F and B, concentrated toward the roof of the granite stock. This process could have released large amounts of aqueous fluid that, together with the excess of volatiles, would have resulted in muscovitization and neutralizing reactions of feldspars. At the same time, the overpressure caused an intense hydrofracturing in these specific areas, corresponding to the higher granitic body curvatures, as recognized by gravity (Chicharro et al. 2015; Chapter 7, this volume). The organogenic fluids derived from the metasedimentary host-rocks (N_2-CH_4-bearing) and the magmatic fluids from the granite (Sn and CO_2-bearing) were mixed in an open space system. The subsequent increase in the oxygen fugacity and the release of pressure caused the cassiterite precipitation.

The P-T evolution of the ore deposition is based on estimated temperatures by isotope thermometry and arsenopyrite chemistry combined with those calculated from fluid inclusion isochores. In the case of the Oxide Stage, the highest temperature estimate has been calculated by the geothermometer of Polyakov et al. (2005) using the isotopic signature of the quartz-cassiterite pair, which gives a temperature of 536 ºC (Table 4.11). The lowest temperature estimate corresponds to the homogenization temperature frequency maximum of type-I fluid inclusions (Th ~ 380 ºC) (Fig. 4.20; Table 4.9). Regarding the Sulfide Stage, the upper temperature limit corresponds to the arsenopyrite geothermometer, which yields a maximum temperature of 456 ºC (Fig. 4.21; Table 4.13). The lowest limit is attributed to the minimum homogenization temperature for type-II fluid inclusions (Fig. 4.20; Table 4.9); a unique critical homogenization temperature found in type-II fluid inclusions is also taken into account. The pressure limits have been estimated from the calculated isochores for each type of fluid inclusion, using the temperature limits to estimate the corresponding pressures. According to these temperature ranges, the

maximum depth for the Logrosán granite ore deposit formation varies between 7 and 10 km (Fig. 4.25). This depth should be overestimated because an overpressure due the high volatile contents of the granite is expected. The Oxide Stage is characterized by the participation of N_2-CH_4-rich fluids derived from the metasedimentary SGC sequence, and by a noteworthy release of pressure and increase of the oxygen fugacity caused by fracturing. The mixing of fluids is clearly inferred at the end of the Oxide Stage and the beginning of the Sulfide Stage by the intersection of the isochores, the compositional heterogeneity (N_2-CO_2-CH_4), and the separation of high- and low-density fluid inclusions which evidence immiscibility. Type-III and type-IV isochores are interpreted as the result of late openings and closures of the veins at very low pressures and depths at the end of the Sulfide Stage. To sum up, the P-T conditions of the Logrosán ore deposits are located approximately at 460-540 ºC and 120-270 MPa for the Oxide Stage; and at 320-460 ºC and 30-160 MPa for the Sulfide Stage (Fig. 4.25).

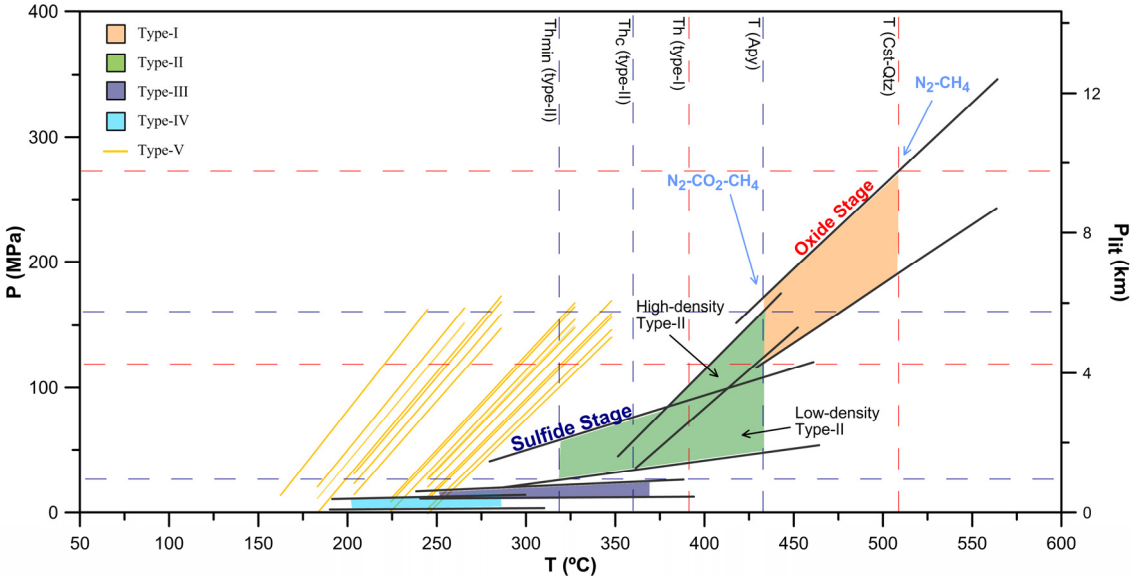

Fig. 4.25: Pressure–temperature reconstruction of conditions prevailing in the Logrosán ore deposits; data from geothermometry and probable trapping conditions of the different fluid inclusions. Red dotted lines represent the Oxide Stage; blue dotted lines represent the Sulfide Stage.

Chapter 5: PHOSPHATE MINERALIZATION

SUMMARY:

La Costanaza, the most important phosphate vein ore deposit in Europe is located nearby the Logrosán granite. The description of this remarkable mineralization, focused on the chemical composition of the hydrothermal apatite, is developed in this chapter. Hydrothermal quartz-apatite ores spatially related to granitic plutons occur exclusively in the South Central Iberian Zone. Based on geochemical features, a comparative study between the hydrothermal phosphate ores and the apatite from phosphate-rich beds in the country-rocks (the Schist Greywacke Complex) and from the adjacent phosphorous-rich granitic plutons is undertaken from Logrosán and similar occurrences. Thus, a genetic interpretation for this ore deposits is discussed.

PHOSPHATE MINERALIZATION

5.1. General features

The Logrosán phosphate mineralization consists of quartz-apatite veins hosted by the Schist Greywacke Complex (SGC). They are found nearby the Logrosán granite and its metamorphic aureole. There are several quartz-apatite veins within the Logrosán area, although they outcrop rarely on surface: La Costanaza, Ginjal, Cañuelo, Mingote, Casillón, and Barrero (Locutora et al., 2006). La Costanaza mine is the most relevant vein, either economically and historically; it is also the best represented, mined and easily accessible, and the one studied in this work. The quartz-apatite veins are almost parallel between them, with variable directions (N20-N70), following broadly the foliation of the SGC metasedimentary sequence (Fig. 5.1). The La Costanaza mine has an entrance, and is also connected by several mining wells (Pozo Calle, Pozo María, and Pozo Magdalena). The La Costanaza vein consists of braided veins and veinlets of variable dimensions. On the whole, it reaches almost 5 km long, and up to 8 meter width. It used to have 15 levels (more than 210 meters depth; Fernández-Amo et al., 2010), of which only two levels are currently accessible. A contemporary cartography of the two first levels of the mine which are nowadays accessible can be found in Rivas Dorado (2013). The cartography of the mine in the times of the active mining labors (first decades of s. XX) are described in Gutzwiller (1919).

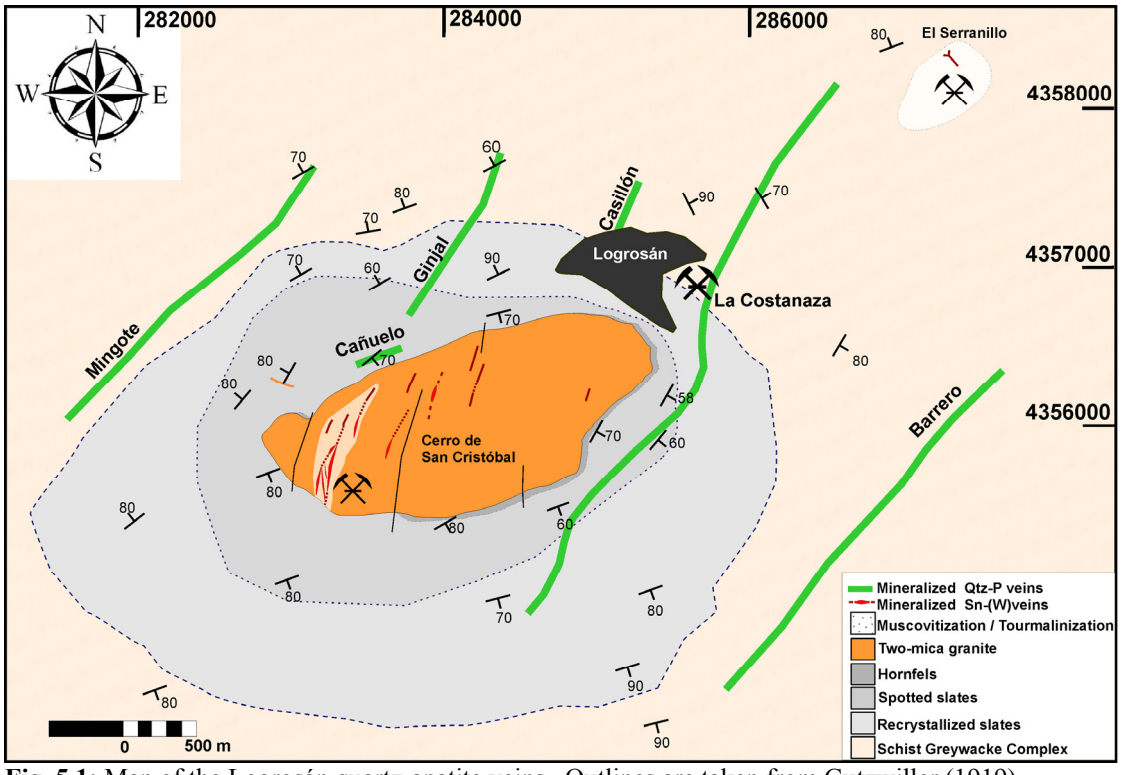

Fig. 5.1: Map of the Logrosán quartz-apatite veins. Outlines are taken from Gutzwiller (1919).

5.1.1. Macroscopic observations

The La Costanaza deposit is hosted by Neoproterozoic metasediments (SGC) close to the Logrosán granite contact. The SGC metasediments nearby the La Costanaza mine entrance show no evidence of thermal metamorphism. The phosphate ore is structurally controlled, occurring as individual veins and veinlets from a few centimeters to up to 3 meters wide. They display N20-75º E direction and vertical to subvertical dip. Most veins show sinuous outlines (Fig. 5.2a), stockworks and brecciated structures (Fig. 5.2b). Hydrothermal alteration (silicification and dolomitization) has been observed in the enclosing rocks. The La Costanaza veins are characterized by successive bands alternating colloform (Fig. 5.2c) and crustiform apatite, and fine drusy quartz which indicates successive reopening. There are two texturally different types of apatite: (1) white fibrous radial crystal aggregates (dahllite), which is the dominant type in the ore, and (2) prismatic apatite, which is present as fine white crystals in the edge, and sometimes also in the center of the veins. Sulfides are minor components occurring as interstitial crystals within the quartz-apatite bands, and the 'saddle' dolomite crust (Fig. 5.2d).

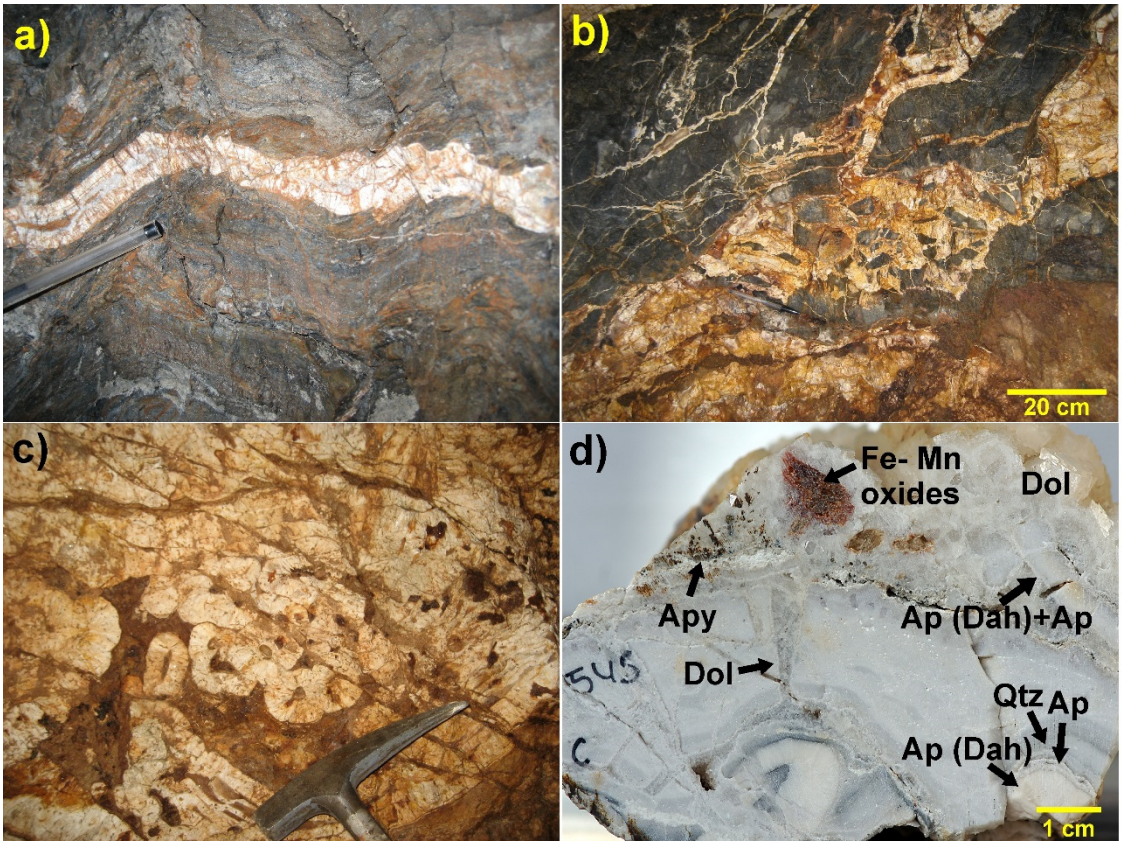

Fig. 5.2: a) Sinuous quartz–apatite vein hosted in the SGC. **b)** Quartz-apatite stockwork and brecciated textures. **c)** Colloform textures. **d)** At the bottom on the far right, detailed of the white fibrous apatite (Ap (Dah)) prismatic apatite (Ap), and quartz (Qtz) alternating bands. On top, dolomite (Dol) crust, hosting arsenopyrite (Apy) and Fe-oxides. Note the dolomite cutting the quartz-apatite bands and the apatite remnant band within the crust.

5.1.2. Microscopic characteristics

The mineralogy of the La Costanaza ore deposit is relatively simple. In the La Costanaza vein, quartz and apatite are the two dominant minerals. FRX images have been used to better understand the textures and chronological relationships of the minerals. Apatite and quartz may occur alternating in concentric bands (Fig. 5.3a). Moreover, when the apatite is massive, microcrystalline quartz veins cut the apatite (Fig. 5.3b). Besides quartz and apatite, the veins also comprise minor sulfides, dolomite, minor calcite, Fe-Mg carbonates, and Fe-Mn-oxides.

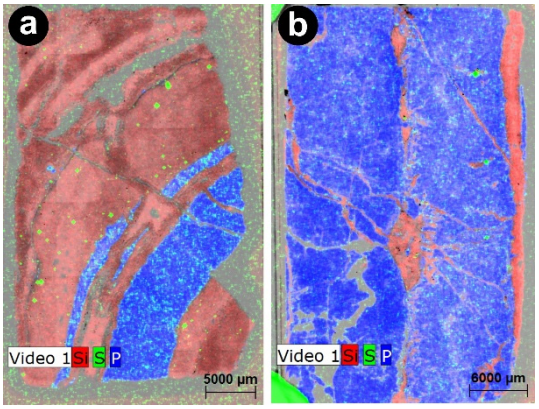

Fig. 5.3: FRX images of quartz-apatite veins **a)** Concentric bands of apatite (P) and quartz (Q) cutting the SGC. **b)** Massive apatite hosted by the SGC and cut by microcrystalline quartz veins. Minor sulfides (S) in bright green are recognized.

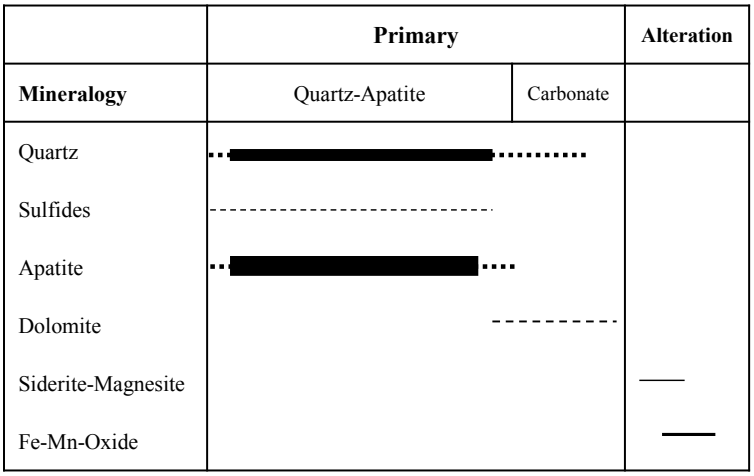

Fig. 5.4: Paragenetic sequence scheme from the La Costanaza quartz-apatite vein ore deposit.

The paragenetic sequence is summarized in Fig. 5.4. The main mineral phases in the first paragenetic stage correspond to quartz and apatite, occurring in alternating bands. Apatite occur mostly as fibrous-radial aggregates (the so-called dahllite) (Fig. 5.5a), but also as needle-like (Fig. 5.5b), tabular, prismatic, or pseudohexagonal crystals (Fig. 5.5a, 5.5c). Idiomorphic apatite sometimes occurs at the end of the fibrous-radial aggregates filling open-spaces (Fig. 5.5a). However, concentric and repetitive bands of different apatite types and quartz make it difficult to establish an accurate chronology among the different apatite types in this ore deposit. In any case, the fibrous-radial aggregates (dhallite) are very abundant and form the large milky-white masses characteristic of the veins (Fig. 5.2d and Fig. 5.5a). Dahllite and idiomorphic apatite contain minor quantities of interstitial sulfides, which textures suggest an early to coeval deposition (Fig. 5.5.d).

Besides, crystalline quartz accompanying the apatite ore, cryptocrystalline quartz veinlets and amorphous silica (Fig. 5.5c) occur as later phases.

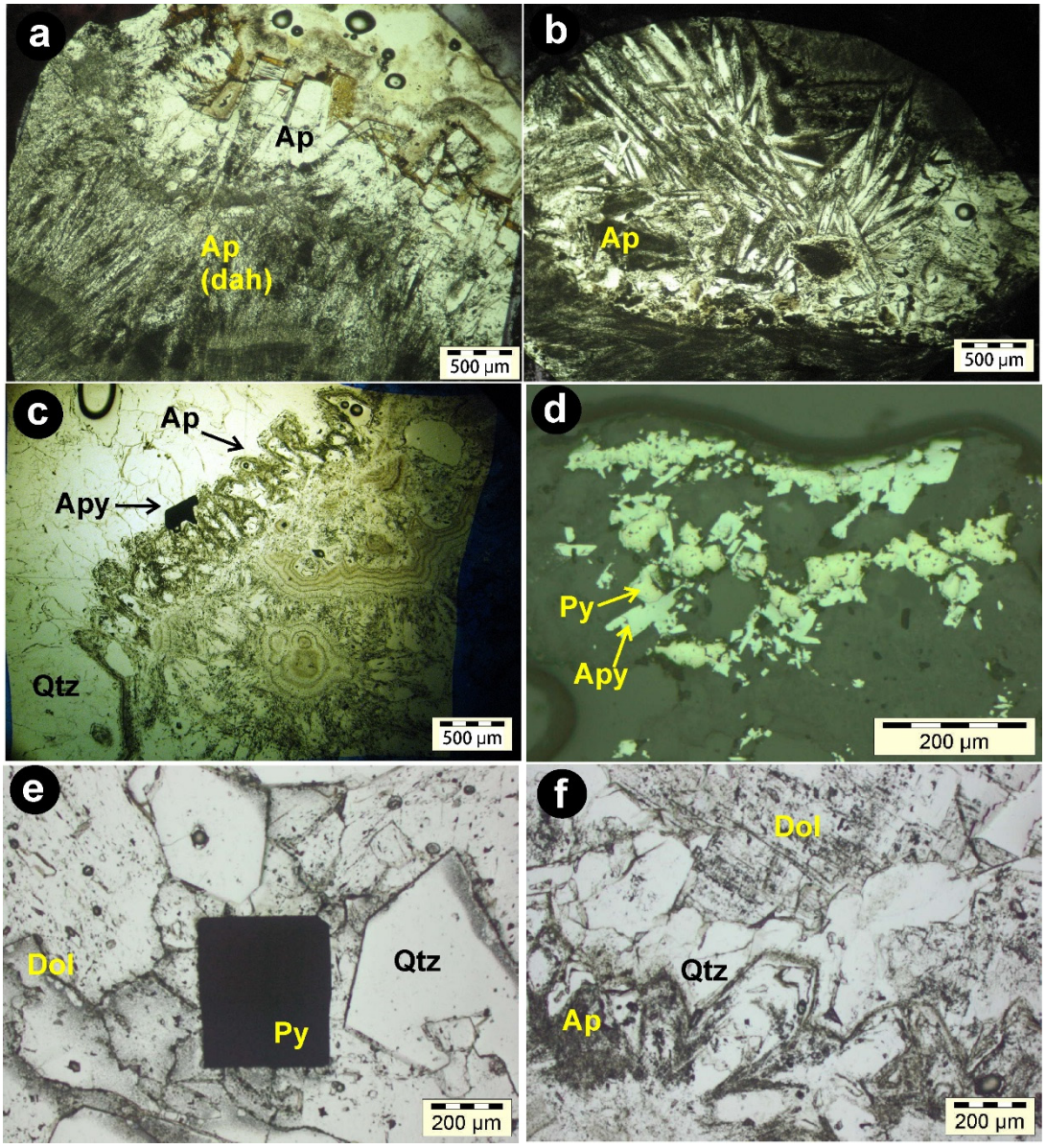

Fig. 5.5: a) Fibrous-radial apatite (Dah) and prismatic apatite (Ap). Transmitted light. **b)** Needle-like apatite filling a small cavity. Transmitted light. **c)** Apatite (Ap) in contact with Arsenopyrite (Apy). Crystalline primary quartz (Qtz) to the left, and amorphous silica to the right. Transmitted light. **d)** Arsenopyrite (Apy) and pyrite (Py) aggregate within carbonate. Reflected light. **e)** Early pyrite cube and quartz in a dolomite crust. Transmitted light. **f)** Remnants of apatite in quartz and dolomite crust. Transmitted light.

A carbonate druse is locally found at the outer part of the veins, hosting fragments of quartz-apatite bands (Fig. 5.5f). Carbonates consist of saddle dolomite, which replaces the previous apatite mineralization (Fig. 5.5e). Some apatite remnants may be also recognized within the dolomite crust. Among the carbonate cement, quartz and pyrite with well-developed crystal faces may be found, indicating primary features (Fig. 5.5e). Nevertheless, sulfides appear mostly as early small interstitial aggregates (Fig. 5.5d). Since sulfides occur mostly in apparent relation with

the carbonates, but also with dahllite and idiomorphic apatite, it is suggested that the sulfide phases were present all over the hydrothermal process. Among the sulfides, arsenopyrite is the dominant. Arsenopyrite occurs as small (<5mm), idiomorphic crystals in intergrowth textures with cubes or truncated cubes of pyrite (Fig. 5.5d). Other sulfides include chalcopyrite, minor marcasite and Ni-Co-Fe sulfarsenides. Later phases, such as siderite, and Fe-Mn oxides, correspond to the alteration stage.

5.2. Mineral chemistry

The whole dataset of major and trace-element composition of selected mineral phases from the Logrosán phosphate ore deposits are shown in the electronic supplementary material (Supplementary Table 8 and Supplementary Table 9).

5.2.1. Apatite

Composition data of hydrothermal apatite from the La Costanaza ore deposit are summarized in Table 5.1. Apatite from the La Costanaza ore deposit is compositionally a fluorapatite (3.01−4.12 wt.% F), CaO ranges from 49.04 to 56.78 wt.%, and P_2O_5 varies from 39.84 to 42.71 wt.%. Apatite has variable contents of strontium, reaching high values (0.04−5.75 wt.% SrO). Other major elements are negligible. Trace elements are not abundant. Volatiles are relatively high, as lithium (1.65−67.83 ppm), and boron (3.17−8.56 ppm). Beryllium content varies from 0.10 to 21.57 ppm. Total REE contents of La Costanaza apatite are low, ranging from 0.36 to 164 ppm, and being generally slightly LREE-enriched. It displays mostly positive Eu anomalies (Eu/Eu*= 0.53−4.26). Uranium (< 1 ppm), thorium (< 8 ppm) and lead (< 5 ppm) are quite low.

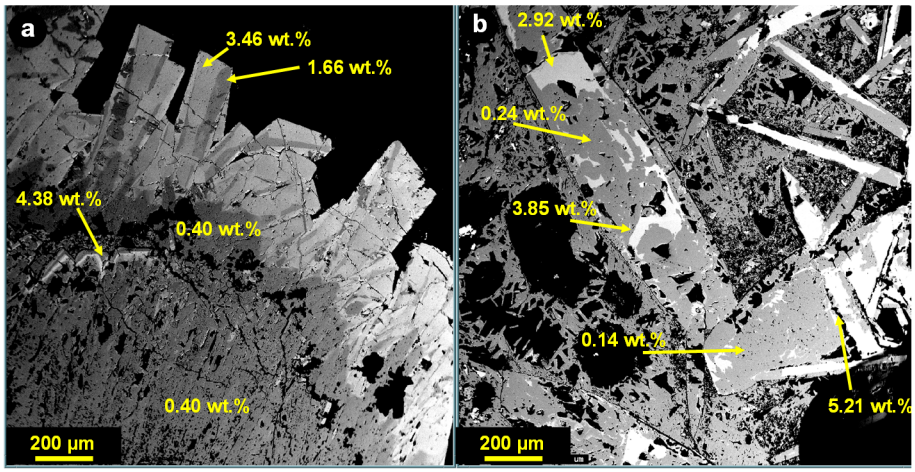

Fig. 5.6: Back scattered images. **a)** Dahllite (Ap I) with low SrO content (in wt.%). Prismatic zoned apatite, showing SrO (in wt.%) chemical heterogeneities. **b)** Patchy-zoned apatite II within apatite I and host-rock fragment matrix.

Table 5.1: Major (wt.%; EMPA) and trace (ppm; LA-ICP-MS) composition of representative apatite from the La Costanaza ore deposit.

	112192			**112191**				**112190**				
	I	**I**	**I**	**I**	**I**	**II**	**II**	**I**	**I**	**II**	**II**	**II**
Element	**9**	**11**	**12**	**22**	**33**	**14**	**16**	**75**	**67**	**66**	**71**	**79**
P_2O_5	41.42	41.54	41.95	42.33	41.28	41.56	41.50	41.87	41.50	41.72	40.46	41.17
SiO_2	0.00	0.00	0.00	0.00	0.00	0.00	0.00	0.00	0.00	0.00	0.00	0.00
FeO	0.00	0.03	0.00	0.00	0.00	0.00	0.10	0.01	0.00	0.19	0.09	0.22
MnO	0.01	0.05	0.04	0.02	0.00	0.03	0.78	0.00	0.06	0.54	0.18	0.28
MgO	0.00	0.00	0.00	0.00	0.00	0.00	0.00	0.00	0.00	0.00	0.00	0.00
CaO	55.69	55.92	55.94	55.91	55.52	55.76	52.05	55.84	56.43	50.24	52.84	52.68
Na_2O	0.00	0.00	0.00	0.00	0.00	0.00	0.01	0.00	0.00	0.01	0.07	0.00
SrO	0.30	0.29	0.20	0.29	0.21	0.20	3.14	0.37	0.11	5.53	4.17	3.85
F	3.36	3.94	3.69	3.69	3.84	3.76	3.39	3.88	3.62	3.33	3.60	3.65
Cl	0.00	0.00	0.00	0.00	0.00	0.00	0.01	0.01	0.02	0.00	0.00	0.00
Sum	100.8	101.8	101.8	102.2	100.8	101.3	101.0	102.0	101.7	101.6	101.4	101.8
H_2O*	0.17	0.00	0.04	0.05	0.00	0.00	0.14	0.00	0.06	0.17	0.03	0.02
O=F,Cl	1.42	1.66	1.55	1.55	1.62	1.58	1.43	1.63	1.53	1.40	1.52	1.54
Total	99.54	100.1	100.3	100.7	99.23	99.73	99.69	100.3	100.3	100.3	99.92	100.3
Nº ions on the basis of 25 oxygens												
P	5.943	5.938	5.964	5.985	5.944	5.949	6.009	5.961	5.919	6.050	5.907	5.959
Si	0.000	0.000	0.000	0.000	0.000	0.000	0.000	0.000	0.000	0.000	0.000	0.000
Fe	0.000	0.004	0.000	0.000	0.000	0.000	0.014	0.001	0.000	0.027	0.013	0.031
Mn	0.002	0.006	0.005	0.003	0.000	0.004	0.114	0.000	0.009	0.078	0.026	0.041
Mg	0.000	0.000	0.000	0.000	0.000	0.000	0.000	0.000	0.000	0.000	0.000	0.000
Ca	10.11	10.12	10.07	10.01	10.12	10.10	9.54	10.06	10.18	9.22	9.76	9.65
Na	0.000	0.000	0.000	0.000	0.000	0.000	0.004	0.000	0.000	0.004	0.023	0.000
Sr	0.029	0.028	0.019	0.028	0.021	0.020	0.311	0.036	0.010	0.549	0.417	0.381
OH*	0.198	0.000	0.040	0.052	0.000	0.000	0.163	0.000	0.068	0.197	0.035	0.028
F	1.802	2.101	1.960	1.948	2.064	2.011	1.835	2.061	1.926	1.803	1.965	1.972
Cl	0.000	0.001	0.000	0.000	0.001	0.000	0.003	0.001	0.006	0.000	0.000	0.000
Li	b.d.l.	b.d.l.	11.62	26.36	16.9	b.d.l.	13.27	9.68	b.d.l.	1.65	40.6	b.d.l.
Be	0.91	0.22	0.53	0.26	0.99	4.05	0.61	0.72	2.69	2.91	9.92	10.45
B	6.65	6.97	8.00	6.69	7.16	6.98	8.25	4.00	3.67	3.17	3.89	5.55
Sc	3.33	b.d.l.	b.d.l.	b.d.l.	1.18	b.d.l.	b.d.l.	1.42	3.71	2.95	1.74	0.87
Sr	2951	1672	1346	1440	2374	28218	1647	2740	1828	1445	33823	29455
Y	9.93	96.0	25.0	12.3	3.61	1.55	16.9	1.63	10.2	7.85	2.31	0.29
Zr	0.03	0.11	0.34	0.23	0.13	b.d.l.	3.90	0.04	0.22	0.05	0.16	0.11
Nb	b.d.l.	0.03	0.00	b.d.l.	0.10	0.11	0.13	0.01	0.01	0.00	b.d.l.	0.01
La	0.25	4.24	0.87	0.05	0.07	0.01	0.25	0.07	0.21	0.15	1.25	0.02
Ce	1.18	8.70	3.16	0.19	0.36	0.03	1.04	0.18	1.23	1.10	4.93	0.02
Pr	0.27	1.43	0.82	0.05	0.08	0.01	0.32	0.04	0.31	0.26	0.83	0.00
Nd	2.32	8.11	7.47	0.50	0.68	0.09	3.40	0.24	1.91	1.72	3.27	0.03
Sm	1.67	4.71	5.51	0.39	0.59	0.06	2.92	0.12	0.80	0.82	0.72	0.03
Eu	2.12	3.82	3.09	0.51	1.16	0.09	1.79	0.19	0.34	0.30	0.12	0.03
Gd	2.53	8.04	8.27	1.52	1.13	0.28	5.63	0.44	1.42	1.32	0.58	0.09
Tb	0.32	1.52	1.07	0.23	0.15	0.05	0.80	0.06	0.24	0.20	0.09	0.01
Dy	1.79	10.72	5.03	1.77	0.78	0.23	4.43	0.27	1.48	1.33	0.43	0.05
Ho	0.29	2.23	0.81	0.35	0.12	0.04	0.61	0.07	0.31	0.24	0.07	0.01
Er	0.73	6.36	1.77	0.95	0.29	0.11	1.43	0.13	0.81	0.63	0.18	0.03
Tm	0.08	0.97	0.20	0.12	0.04	0.02	0.15	0.02	0.08	0.07	0.01	0.00
Yb	0.63	6.69	1.30	0.74	0.09	0.06	0.72	0.08	0.52	0.36	0.08	0.02
Lu	0.07	0.85	0.15	0.08	0.01	0.01	0.08	0.01	0.07	0.06	0.02	0.00
Hf	0.00	b.d.l.	0.00	b.d.l.	0.00	0.00	0.03	b.d.l.	0.01	b.d.l.	b.d.l.	0.00
Ta	0.00	b.d.l.	b.d.l.	b.d.l.	b.d.l.	0.00	0.00	b.d.l.	0.00	b.d.l.	b.d.l.	0.00
Pb	0.22	0.05	0.15	0.09	0.30	5.13	0.52	0.06	0.04	0.01	0.49	0.59
Th	0.00	b.d.l.	0.01	2.37	1.65	b.d.l.	5.19	0.00	0.01	0.01	7.61	b.d.l.
U	0.37	0.36	0.50	0.01	0.02	0.00	0.10	0.01	0.03	0.01	0.02	0.02
ΣREE	14.25	68.39	39.52	7.45	5.55	1.08	23.57	1.91	9.72	8.55	12.59	0.36

Apatite I and non-zoned apatite II are compositionally very similar. However, apatite II is often compositionally zoned. The zonation pattern is usually of patchy-zoned type. Apatite II crystals display the highest REE and Sr contents in brighter zones when observed it in back-scattered images (Fig. 5.6). Strontium contents in apatite I is always below 1 wt.%. Nevertheless, patchy-zoned apatite variations in the same crystal may reach above 3 wt.%. Moreover, later crystals seem to be enriched in strontium (Fig. 5.6b).

5.2.2. Sulfides

Chemical composition of representative arsenopyrite, pyrite and chalcopyrite from the La Costanaza ore deposit are given in Table 5.2. Arsenopyrite and pyrite occasionally coexist in the margin of the La Costanaza veins (Fig. 5.7a). Most of the arsenopyrite crystals are homogeneous or slightly zoned (Fig. 5.7b). The As content ranges between 42.33 and 47.14 wt.% and the Fe content is almost constant, around 35 wt.%. Total concentration of Bi, Ag, Mn, Ni, Cd, Pb, Cu, Sn, Zn and Sb is small and does not exceed 0.4 wt.%. Pyrite has Fe varying from 45.58 to 47.44 wt.%, and S ranging from 50.42 to 54.90 wt%. Pyrite may have minor quantities of As (up to 2.40 wt.%) and Pb (average of 0.27 wt.%). Chalcopyrite occur isolated as small crystals (< 500 µm) or in the edges of arsenopyrite crystals. Chalcopyrite composition is quite homogeneous (Fe: 29.79-31.14 wt.%; Cu: 32.19-35.43 wt%; and S: 34.17-35.40 wt.%). Very minor stannite has also been recognized. Besides, minor Ni-Co-Fe sulfarsenides replacing arsenopyrite and pyrite have been found (Fig. 5.7b). They correspond to the gersdorffite-cobaltite solid-solution. The compositional variety in the few specimens found is $Co_{0.29\text{-}0.44}(Ni_{0.46\text{-}0.48}Fe_{0.21\text{-}0.32})As_{1.14\text{-}1.17}S$.

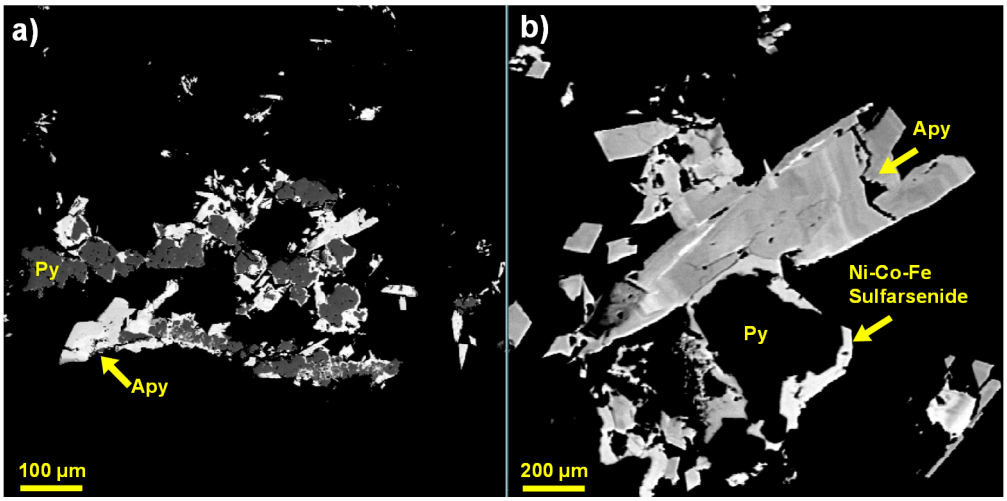

Fig. 5.7: Back scattered images. **a)** Arsenopyrite and pyrite aggregate. **b)** Detail of (a) Arsenopyrite overgrown by Ni-Co-Fe sulfarsenide, which also enclose pyrite.

Table 5.2: Major (wt.%; EMPA) composition of representative sulfides from the La Costanaza ore deposit.

	Arsenopyrite				Pyrite				Chalcopyrite		Ni-Co-Fe sulfarsenides
	113545				113545				113545		113545
wt.%	**15**	**2**	**8**	**20**	**18**	**28**	**36**	**45**	**7**	**10**	**5**
Zn	0.00	b.d.l.	b.d.l.	0.00	0.03	b.d.l.	0.02	0.00	0.00	0.00	b.d.l.
Ag	0.00	0.01	b.d.l.	0.00	0.00	0.01	0.01	0.00	0.00	0.00	0.02
Co	0.03	0.22	0.51	0.10	0.14	0.04	0.06	0.05	0.02	0.02	9.52
Bi	0.05	0.10	0.61	0.05	0.20	0.05	0.12	0.09	0.08	0.10	0.14
Ni	0.00	0.15	0.42	0.06	0.20	b.d.l.	b.d.l.	b.d.l.	0.00	0.00	15.57
Fe	35.57	35.89	35.02	35.46	46.80	45.60	46.26	46.03	30.46	31.06	9.73
Mn	0.00	0.04	0.04	0.04	0.00	b.d.l.	b.d.l.	b.d.l.	0.00	0.00	0.04
Cu	0.15	b.d.l.	b.d.l.	0.02	0.00	b.d.l.	b.d.l.	b.d.l.	34.53	34.07	b.d.l.
Cd	0.00	b.d.l.	b.d.l.	b.d.l.	0.00	b.d.l.	b.d.l.	b.d.l.	0.00	0.00	b.d.l.
Sn	0.00	b.d.l.	0.06	b.d.l.	0.01	b.d.l.	b.d.l.	0.01	0.33	0.01	0.02
Sb	0.08	0.02	b.d.l.	0.15	0.06	0.08	0.01	0.03	0.01	0.02	b.d.l.
Pb	0.11	0.16	0.33	0.15	0.28	0.28	0.27	0.27	0.23	0.21	0.13
As	46.51	44.01	44.12	46.84	0.78	2.40	b.d.l.	0.33	0.00	0.03	46.81
S	16.95	18.88	18.80	17.07	51.83	50.92	53.44	53.58	34.44	34.22	17.60
Total	99.5	99.5	99.9	99.9	100.3	99.4	100.2	100.4	100.1	99.7	99.6
apfu											
Zn	0.000	0.000	0.000	0.000	0.000	0.000	0.000	0.000	0.000	0.000	0.000
Ag	0.000	0.000	0.000	0.000	0.000	0.000	0.000	0.000	0.000	0.000	0.000
Co	0.001	0.006	0.015	0.003	0.003	0.001	0.001	0.001	0.001	0.001	0.294
Bi	0.000	0.001	0.005	0.000	0.001	0.000	0.001	0.001	0.001	0.001	0.001
Ni	0.000	0.004	0.012	0.002	0.004	0.000	0.000	0.000	0.000	0.000	0.483
Fe	1.205	1.091	1.069	1.193	1.037	1.028	0.994	0.986	1.015	1.042	0.318
Mn	0.000	0.001	0.001	0.001	0.000	0.000	0.000	0.000	0.000	0.000	0.001
Cu	0.005	0.000	0.000	0.001	0.000	0.000	0.000	0.000	1.012	1.004	0.000
Cd	0.000	0.000	0.000	0.000	0.000	0.000	0.000	0.000	0.000	0.000	0.000
Sn	0.000	0.000	0.001	0.000	0.000	0.000	0.000	0.000	0.005	0.000	0.000
Sb	0.001	0.000	0.000	0.002	0.001	0.001	0.000	0.000	0.000	0.000	0.000
Pb	0.001	0.001	0.003	0.001	0.002	0.002	0.002	0.002	0.002	0.002	0.001
As	1.174	0.998	1.004	1.174	0.013	0.040	0.000	0.005	0.000	0.001	1.138
S	1	1	1	1	2	2	2	2	2	2	1

5.2.3. Carbonates

Chemical composition of carbonates from the La Costanaza ore deposit is summarized in Table 5.3. The main carbonate found in the mineralization stage is the saddle dolomite. Dolomite occurs as a coarse-crystalline cement-breccia-like crust in the outer margin of the quartz-apatite veins. Dolomite from the La Costanaza is a Fe-rich dolomite. Although $CaCO_3$ is quite constant (48.08-49.61 mol.%), $FeCO_3$ and $MgCO_3$ show a range from 2.43-15.89 mol.%$FeCO_3$, and 35.25-47.93mol.% $MgCO_3$; Fe and Mg correlates perfectly. Manganese and strontium are minor elements in saddle dolomite composition (0.03-0.95 mol.% $MnCO_3$, and 0.01-0.12 mol.% $SrCO_3$). Dolomite displays concentric growth zoning, with outer zones enriched in Fe and impoverished in Mg (Fig. 5.8). Ankerite and siderite occur as alteration phases, replacing both, the saddle dolomite and the quartz-apatite bands.

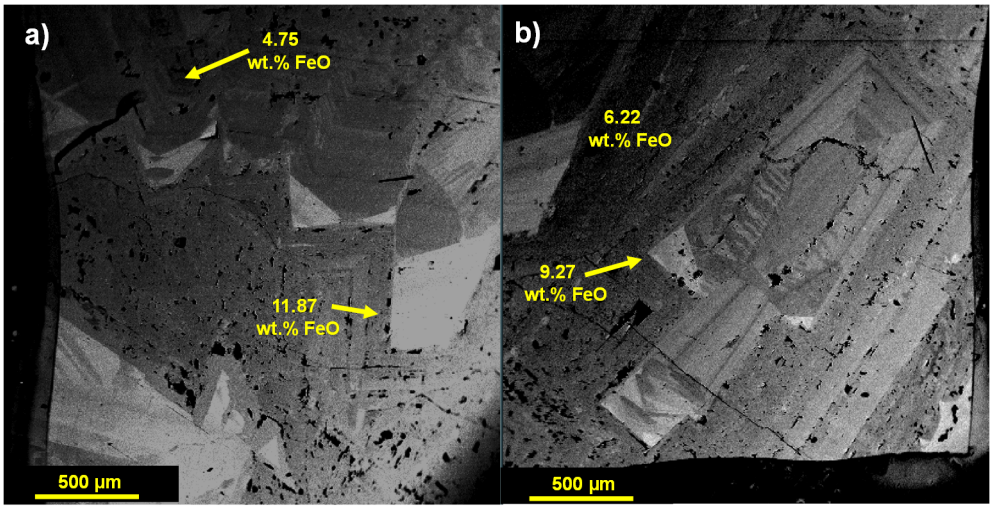

Fig. 5.8: a) Growth pattern zonation of dolomite, with outer zones richer in Fe and impoverished in Mg (bright gray). **b)** Zoned dolomite rhomb with a general concentric pattern.

Table 5.3: Major (wt.%; LA-ICP-MS) composition of representative carbonates from La Costanaza.

	Dolomite							Ankerite-Siderite			
	113545	113545	113545	113545	113545	113545	113545	111940	111940	111941	111940
Element	**21**	**23**	**24**	**26**	**27**	**28**	**29**	**55**	**56**	**77**	**71**
CaO	29.44	29.05	29.30	28.03	29.01	28.73	29.07	0.86	0.48	0.09	b.d.l.
MgO	17.91	20.17	17.56	14.77	18.96	15.48	18.05	20.87	27.34	24.26	0.01
MnO	0.50	0.02	0.72	0.53	0.19	0.66	0.36	2.09	0.74	1.10	b.d.l.
FeO	6.50	1.82	7.22	11.87	4.75	9.27	6.32	33.98	26.27	30.37	59.43
SrO	0.03	0.01	0.09	0.06	0.05	0.08	0.13	b.d.l.	0.04	0.01	0.03
Wt% element											
Ca	21.04	20.76	20.94	20.03	20.73	20.53	20.78	0.61	0.34	0.06	0.00
Mg	10.80	12.17	10.59	8.91	11.44	9.33	10.89	12.59	16.49	14.63	0.01
Mn	0.38	0.02	0.56	0.41	0.14	0.51	0.28	1.62	0.57	0.85	0.00
Fe	5.05	1.41	5.61	9.23	3.69	7.21	4.91	26.41	20.42	23.61	46.19
Sr	0.03	0.01	0.08	0.05	0.04	0.06	0.11	0.00	0.03	0.01	0.03
C backcalc	12.82	12.54	12.85	12.48	12.69	12.43	12.74	12.44	12.77	12.51	9.94
O backcalc	51.21	50.11	51.34	49.89	50.72	49.68	50.90	49.70	51.02	49.99	39.73
Total	101.3	97.02	102.0	101.0	99.45	99.76	100.6	103.4	101.6	101.7	95.90
Ca	0.52	0.52	0.52	0.50	0.52	0.51	0.52	0.02	0.01	0.00	0.00
Mg	0.44	0.50	0.44	0.37	0.47	0.38	0.45	0.52	0.68	0.60	0.00
Mn	0.01	0.00	0.01	0.01	0.00	0.01	0.01	0.03	0.01	0.02	0.00
Fe	0.09	0.03	0.10	0.17	0.07	0.13	0.09	0.47	0.37	0.42	0.83
Sr	0.00	0.00	0.00	0.00	0.00	0.00	0.00	0.00	0.00	0.00	0.00
C	1.1	1.0	1.1	1.0	1.1	1.0	1.1	1.0	1.1	1.0	0.8
O	3.20	3.13	3.21	3.12	3.17	3.11	3.18	3.11	3.19	3.12	2.48
Ca	0.98	0.99	0.98	0.96	0.98	0.99	0.98	0.03	0.02	0.00	0.00
Mg	0.83	0.96	0.81	0.70	0.89	0.74	0.84	1.00	1.28	1.16	0.00
Mn	0.01	0.00	0.02	0.01	0.00	0.02	0.01	0.06	0.02	0.03	0.00
Fe	0.17	0.05	0.19	0.32	0.13	0.25	0.17	0.91	0.69	0.81	2.00
Sr	0.00	0.00	0.00	0.00	0.00	0.00	0.00	0.00	0.00	0.00	0.00
C	2	2	2	2	2	2	2	2	2	2	2
O	6	6	6	6	6	6	6	6	6	6	6
$CaCO_3$	49.19	49.61	48.85	48.08	48.95	49.49	48.88	1.48	0.80	0.15	0.00
$MgCO_3$	41.64	47.93	40.72	35.25	44.51	37.08	42.22	50.00	63.79	57.77	0.04
$MnCO_3$	0.66	0.03	0.95	0.72	0.25	0.89	0.48	2.85	0.98	1.49	0.00
$FeCO_3$	8.48	2.43	9.40	15.89	6.25	12.46	8.29	45.67	34.40	40.58	99.93
$SrCO_3$	0.03	0.01	0.08	0.06	0.04	0.07	0.12	0.00	0.03	0.01	0.03
Total	100	100	100	100	100	100	100	100	100	100	100

5.3. Fluid inclusion study

Fluid inclusions in quartz-apatite veins from the La Costanaza ore deposit have not been detected in dahllite, owing to its lack of clarity; and they are found only rarely in prismatic apatite. Moreover, most of fluid inclusions hosted by apatite crystals are too small (<3μm) for accurate measurements. Thus, fluid inclusion measurements have been performed on quartz coexisting with apatite. Primary and secondary fluid inclusion types have been identified in quartz from the quart-apatite veins. Primary fluid inclusions have been identified isolated, which is a criteria for primary fluid inclusion recognition after Roedder (1984), or parallel to quartz apatite boundaries (Fig. 5.9a). Secondary fluid inclusion trails have been identified cutting the quartz and the apatite. All fluid inclusions are small in size, being frequently below 5 μm and up to 15 μm. They are biphasic at room temperature, with vapor bubbles ranging from 5 to 40% in primary fluid inclusions, and from 5 to 10% in secondary fluid inclusions. Fluid inclusions display the first melting temperature (T_e) at about -21 ºC, suggesting a H_2O-NaCl system free of other dissolved salts. The temperature of final ice melting (Tm_{ice}) in primary fluid inclusions ranges from -0.3 to -0.8 ºC, which corresponds to salinities between 0.5 and 1.4 wt.% NaCl equiv. Secondary fluid inclusions ice melting temperatures (Tm_{ice}) are very close to pure water (-0.1 and -0.2 ºC), corresponding to very low salinities (0.2–0.4 wt.% NaCl equiv.). Primary fluid inclusions homogenize into liquid phase (T_h) from 225 to 360 ºC, while secondary fluid inclusions show T_h ranging between 140 and 190 ºC (Fig. 5.9b). Microthermometric data are summarized in Table 5.3.

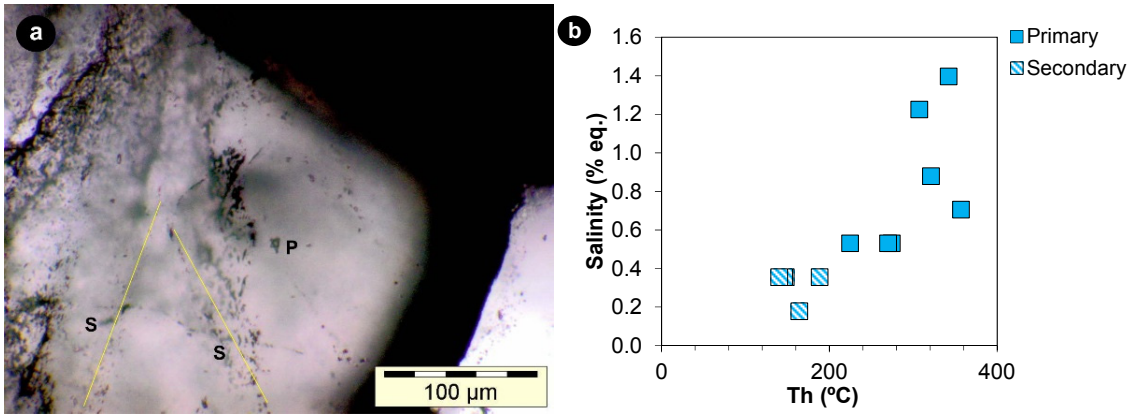

Fig. 5.9: a) Primary fluid inclusion (P) and trails of secondary fluid inclusions (S) in quartz from the La Costanaza ore deposit. **b)** Th (ºC) versus salinity (wt.% NaCl equiv.) plot.

5.4. Stable isotope data

The $\delta^{18}O_{SMOW}$ values of hydrothermal quartz in La Costanaza vary from +13.8 to +16.7‰, while the dolomite has a $\delta^{18}O_{SMOW}$ value of 20.8‰ (and a $\delta^{13}C_{PDB}$ of −8.5‰) (Table 5.4). Hydrothermal quartz from quartz-apatite veins has isotopic signatures similar to the $\delta^{18}O_{SMOW}$ of the nearby Logrosán granite (+14.1 to +15.0‰). These signatures are heavier than the $\delta^{18}O_{SMOW}$ range measured in metasedimentary rocks of this study in the central sector of the SGC (13.1 - 13.4‰), but are similar to other $\delta^{18}O$ values given by other authors for metasedimentary rocks of the SGC in the same area (ranging from +11.6 to +15.7‰, after Ugidos et al., 1997) (Fig. 5.10).

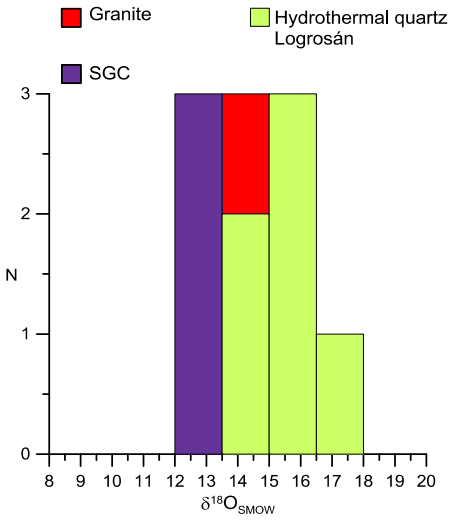

Fig. 5.10: Histogram of $\delta^{18}O_{SMOW}$ values for quartz from the Logrosán quartz-apatite veins, granites and metasediments from the SGC.

Table 5.4: Stable isotopic data of the Logrosán apatite, granite, and SGC metasediments.

Sample	Rock	Mineral	$\delta^{18}O_{SMOW}$	$\delta^{13}C_{PDB}$	$\delta^{18}O_{PDB}$
MC 3A	Qtz-apatite vein	Dol	20.8	-8.52	-9.8
MC	Qtz-apatite vein	Qtz	15.9	-	-
MC	Qtz-apatite vein	Qtz	15.5	-	-
MC3C	Qtz-apatite vein	Qtz	16.7	-	-
MC4	Qtz-apatite vein	Qtz	15.1	-	-
COS13	Qtz-apatite vein	Qtz	13.8	-	-
COS13	Qtz-apatite vein	Qtz	14.2	-	-
177	Granite	WR	15.0	-	-
111912	Granite	WR	14.1	-	-
111979	Granite	WR	14.5	-	-
CEG1	SGC	WR	13.1	-	-
CEG2	SGC	WR	13.2	-	-
CEG2	SGC	WR	13.4	-	-

5.5. Discussion

5.5.1. Nature of the hydrothermal fluids

The source of the ore-forming hydrothermal fluids is a main subject of debate for Iberian-type phosphate ore deposits, so-called after Aizpurúa et al. (1982). Whether they are related to magmatic system, or fluids of unknown origin equilibrated with granites or with Neoproterozoic metasedimentary sequences is still under discussion.

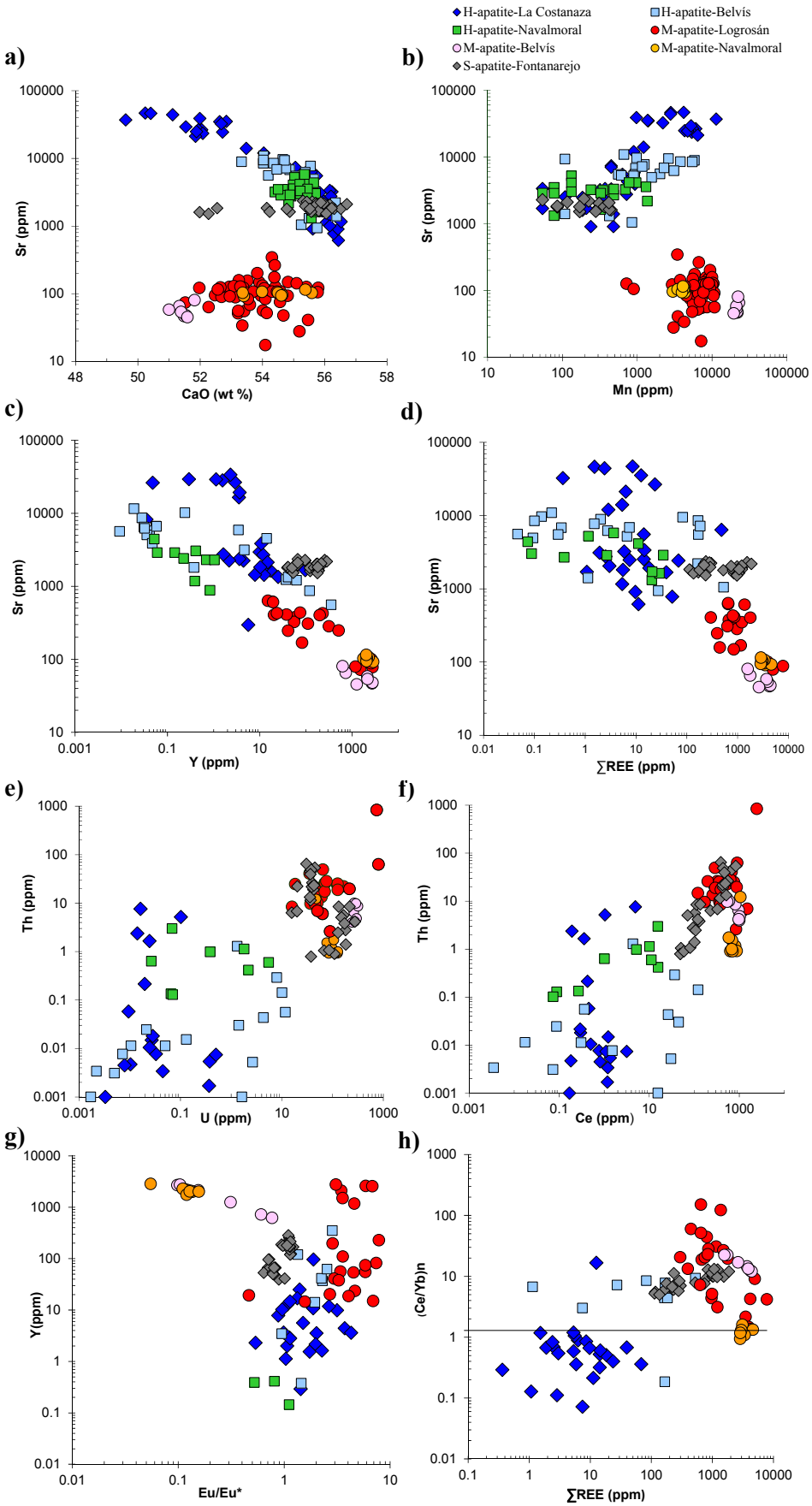

Fig. 5.11: Trace element composition of hydrothermal (H), magmatic (M) and sedimentary (S) apatites : **a)** Sr vs. CaO; **b)** Sr vs. Mn; **c)** Sr vs. Y; **d)** Sr vs. total REE; **e)** Th vs. U; **f)** Th vs. Ce; **g)** Y vs. Eu/Eu*; **h)** (Ce/Yb)n vs. total REE. Data from Belvís and Navalmoral after Vindel et al. (2014).

A comparison of hydrothermal apatite from the ore deposits (H-apatites), magmatic apatite from the granite (M-apatites) and apatite from metasedimentary phosphorous-rich (phosphorite) levels or nodules of the Schist Greywacke Complex (S-apatite) has been accomplished. The hydrothermal apatite from the La Costanaza ore deposit, and the magmatic apatite from the Logrosán granite data have been compared with some other similar localities (Belvís de Monroy and Navalmoral de la Mata). These localities also have extra- and/or intragranitic hydrothermal Iberian-type phosphate ores (Vindel et al., 2014).

H-apatite is rich in Sr in comparison to M-apatite, whereas S-apatite plot in the low Sr pole of the H-apatite compositional field (Fig. 5.11). A plot of Sr-CaO shows a negative slope in H-apatite suggesting Sr-Ca substitution (Fig. 5.11a). Plots of Sr versus Mn and Y show a negative correlation in H-apatite (Fig. 5.11b and 5.11c). Total REE contents of H-apatite are generally low compared to those of M-apatite and S-apatite, whose values reach up to 7800 ppm and up to 1500 ppm, respectively (Fig. 5.11d). Th and U contents in H-apatite are low in contrast to M- and S-apatites, that show variable amounts of Th (1-800 ppm) and U (16 to 800) (Fig. 5.11e). High Th contents could be recognized in the Logrosán magmatic apatite (Fig. 5.11e). A positive slope for Th-U and for Th-Ce is observed for M-, H- and S-apatites (Fig. 5.11e and 5.11f).

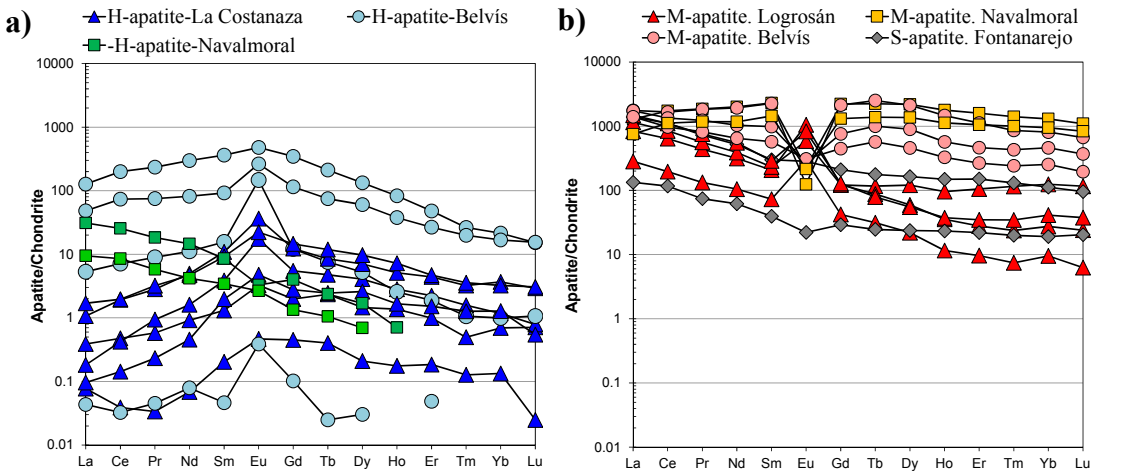

Fig. 5.12: Chondrite-normalized REE patterns of apatite. Normalizing values from Sun and McDonough (1989). **a)** Hydrothermal apatite; **b)** Magmatic apatite. Data from Belvís y Navalmoral after Vindel et al. (2014).

Chondrite-normalized REE patterns of representative H-, M- and S-apatites are shown in Fig. 5.12a and 5.12b. The Navalmoral H-apatite presents a REE pattern different from that of La Costanaza and Belvís hydrothermal apatites. It shows a LREE-enriched trend with a slightly negative Eu anomaly and HREE below detection limits. The other hydrothermal apatites (La Costanaza and Belvís) mainly show concave downwards REE patterns with variable positive Eu anomalies (most Eu/Eu*= 1-4 and Eu/Eu*= 1-9, respectively) (Fig. 5.12a). Magmatic apatite

shows flatter REE patterns than H-types and tend to have prominent negative Eu anomalies with Eu/Eu* values between 0.05-0.6 (Figs. 5.11g and 5.12b); excepting the Logrosán granite apatite, which shows a marked positive Eu/Eu* anomaly and certain degree of REE fractionation with $(Ce/Yb)_n$ values above 1 (Figs. 5.11h and 5.12b). Metasedimentary S-apatite shows flat patterns with slight negative Eu anomalies (Fig. 5.12b).

The high Sr content and the Mn-Y-REE-Th-U-Pb depletion of H-apatite (Logrosán, Belvís-Navalmoral) suggest different sources for H-and M-apatite formation (Fig. 5.10). Strontium (<500 ppm), Mn (10^3 - 10^4) and Y (10 - 10^3) contents in magmatic apatite are very similar to those of other granitoids, indicating the partitioning of Sr into plagioclase (Belousova et al., 2002). H-apatite from Logrosán, Belvís and Navalmoral show SrO ranging between 0.3 and 1.4 wt.% SrO. This high Sr content could have been incorporated during the circulation of the ore-forming fluids through phosphate occurrences in Neoproterozoic sediments (S-apatite: 0.16-0.22 wt.% SrO) or through certain carbonate beds. The Ediacaran carbonate unit (Íbor Group), close to the Belvís and Navalmoral quartz-apatite veins, includes dolomite with Sr up to 0.5 wt.% (Herrero et. al., 2011). In addition, chondrite-normalized REE patterns show convex-up shape for most of the H-apatites, in contrast with the almost flat REE patterns of the granitic M-apatites. Positive Eu anomalies (Eu^{2+}) in H-apatites indicates reducing conditions, while negative Eu anomalies (Eu^{3+}) in the M-apatites from the Belvís and Navalmoral granites points at oxidizing conditions and marked feldspar fractionation. The origin of positive Eu anomalies in the M-apatite from the Logrosán granite could be related to variable redox conditions, to compositional heterogeneities in the felsic magma or to the influence of co-crystallization of other magmatic phases (Chu et al., 2009).

An attempt was made to determine the ore-forming conditions of the different apatite-rich hydrothermal veins of the area (Vindel et al., 2014), combining arsenopyrite geothermometry with fluid inclusion data. The ore-forming fluids show a simple cooling (T_h from 360 to 110ºC) of low salinity fluids (0.2 and 1.4 wt.% NaCl equiv.) in the La Costanaza and Navalmoral veins (Fig. 5.13). On the other hand, aqueous fluids trapped in the Belvís apatite have low to moderate salinities (0.2 and 6.7 wt.% NaCl equiv.) at lower temperature (T_h: 125 to 165ºC), showing a dilution process. Because of its refractory nature, arsenopyrite composition reflects formation temperatures (Kretschmar and Scott, 1976). Although the arsenopyrite geothermometer should be used with caution (Kerestedjian, 1997; Sharp et al., 1985), it could provide an estimate of formation temperatures in conjunction with fluid inclusion and geological data. The arsenopyrite geothermometer for ore deposits formed at temperatures higher than 300 °C was proposed by Kretschmar and Scott (1976) and re-examined by Sharp et al. (1985). Arsenopyrite grains showing > 1 at.% As variation from core to rim were rejected for geothermometry. The average

composition of suitable arsenopyrite from the La Costanaza veins clusters at 32.07-32.50 at.% As. This values correspond to temperatures of 440±10°C, close to the maximum T values estimated with fluid inclusion data. The estimated medium-to-low temperature of ore formation suggests that the hydrothermal fluids could not be directly related neither to granite intrusion, nor even to the fast cooling event of these small and shallow felsic plutons.

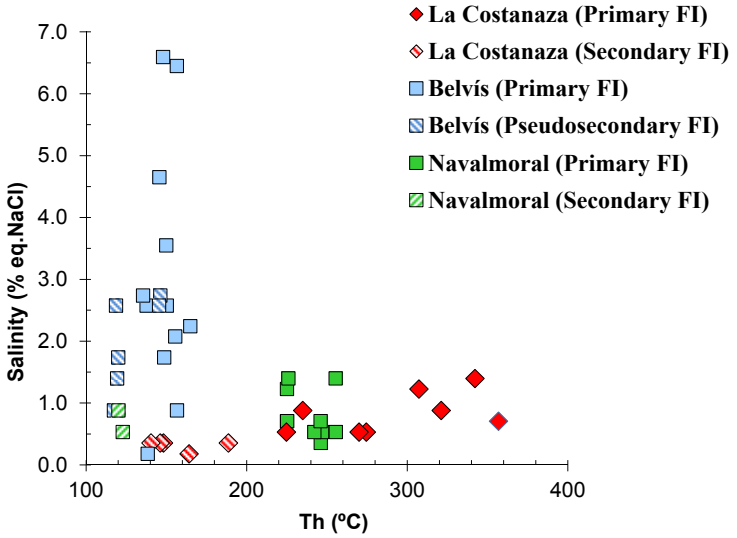

Fig. 5.13. Plot showing homogenization temperature (Th) versus salinity (wt.% NaCl equiv.). Data from Belvís and Navalmoral after Vindel et al. (2014).

In summary, the source of the phosphorous hydrothermal ore-forming fluids is problematic. Nonetheless, the most similar apatite chemical composition between hydrothermal and sedimentary types suggests a more genetic proximity between them. Moreover, dolomite found in the La Costanaza quartz–apatite veins has a $\delta^{18}O_{SMOW}$ value of 20.8‰ (and a $\delta^{13}C_{PDB}$ of −8.5‰), which correspond to high temperature hydrothermal dolomite (Allan and Wiggins, 1993). These data are in the same range of hydrothermal dolomite phases (D3 and D4) affecting hydrothermally altered carbonate beds from the Ediacaran rocks of the Ibor Group of the SGC (Herrero et al., 2011). The precipitation of the Co-Ni-Fe sulfarsenide suite, found in the first stages of the La Costanaza ore deposit, unravel some clues about the nature and genesis of the mineralizing fluids. After Jochum (2000), Co-Ni-Fe sulfarsenides precipitate owing to thermochemical processes of sulfate reduction during interaction of hydrothermal fluids with organic matter in the wallrock, which is suitable for the SGC metasediments. Hence, geochemistry and isotopic data allow us to suggest a model involving the circulation of ore fluids probably permeating through the proximate granite and metasediments, but with a major contribution of surrounding metasedimentary country rocks.

5.5.2. The question of the age of the P-rich veins

The extremely low U and Th contents shown by the hydrothermal apatite (mostly below 1 ppm, Table 5.1) made it impossible to date these phosphates by conventional U-Pb methods, including fission tracks. Moreover, the absence of associated phyllosilicates, or other accessory minerals (e.g., zircon, monazite), contributed to the failure in geochronological dating.

Hydrothermal activity in central Spain has been related to three main stages yet not well geochronologically constrained (Tornos et al., 2000; Martín Crespo et al., 2002; Galindo et al., 2010): (i) mineralization related to the end of the Variscan magmatic activity and the initiation of proto-rifting with scarce alkaline intrusions (293-255 Ma); (ii) hydrothermal activity starting from the Early Jurassic tholeiitic rifting, related to the Atlantic opening, and giving rise to F-Ba-Pb-Zn ore veins in many places of the CIZ (210-120 Ma), including the nearby Toledo shear zone (Villaseca et al., 2005); (iii) minor hydrothermal activity and alteration related to the Cretaceous-Tertiary boundary (75-50 Ma), also identified by apatite fission-track analyses in granitic and metamorphic rocks of the Montes de Toledo area, but related to low-T fluids (≤ 80ºC after Barbero et al., 2005). A scarce mantle-derived alkaline magmatic activity from 103 to 69 Ma has been recorded dispersedly within the Iberian microplate: Portugal (Grange et al., 2010), Galicia (Ancochea et al., 1992), Basque country and Catalonian coastal Range (Ubide, 2013).

Although more work needs to be made, the moderate-T hydrothermal activity described in the studied P-rich veins (up to 350-440 ºC), in agreement with dolomitization processes in carbonate rocks of the SGC (up to 500 ºC, Herrero et al., 2010), suggest that the studied ores cannot be related to the Cretaceous-Tertiary low-T activity of the area. The great isotopic similarity and T conditions between carbonates of the studied veins and the dolomitization events in carbonate metasediments of the SGC, make it more probable a Mesozoic age for their formation. We propose the disconnection of this hydrothermal activity from the Logrosán granite intrusions timing. This hypothesis is based on the lack of clear petrogenetic relationship of the studied P-rich veins with the associated granitoids, as suggested by the contrasted chemical composition between M- and H-apatite types, and on the absence of spatial relationship of granitoids with the hydrothermal dolomitization processes of carbonate rocks of the SGC. Small granite intrusions (e.g., Logrosán and Belvís) necessarily lose heat quickly in such epizonal environments (the SGC), and hence they lack of effective time to generate significant hydrothermal events. A clue may be found in the $^{40}Ar/^{39}Ar$ step-heating age spectrum and isochron diagrams of muscovite analyzed to constraint the age of the Sn-(W) Logrosán ore deposits (Fig. 4.16, Chapter 4, this volume). Most samples show a resetting between 200 and 260 Ma, approximately, which could

be related to the hydrothermal event responsible for the phosphate mineralization. This important issue needs to be confirmed by future accurate geochronological data.

5.5.3. The southern CIZ as a phosphorous-rich domain

The presence of disperse phosphate rocks and even of phosphorite deposits within the lithostratigraphic units of the SGC is largely known (e.g., Perconig et al., 1986; Gabaldón et al., 1986), but even more remarkable is the contrasted geochemical features between metasedimentary rocks from this southern part of the CIZ in comparison with those of the northern CIZ. The metasedimentary rocks of the southern CIZ are on average richer in P than those from the northern part (Villaseca et al., 2014), thus defining a P-rich Neoproterozoic sedimentary realm.

It is noteworthy that most of the phosphorous-rich Variscan granites described in the Iberian belt are restricted to this southern domain of the CIZ (Villaseca, 2011; Villaseca et al., 2008). These P-rich plutons suggest granite derivation from pelitic and greywackeous sources isotopically similar to those of the SGC (e.g., Ramírez and Menéndez, 1999; Menéndez and Bea, 2004; Antunes et al., 2008; Villaseca et al., 2008), attesting to a major crustal recycling of those P-rich metasediments during the Variscan orogeny.

The studied phosphorous rich veins would represent a second event of recycling of metasediments (in principle from the SGC) within the southern CIZ during post-Variscan hydrothermal fluid circulation, which would give rise to the only known quartz-apatite veins in western Europe. The intense geochemical reworking of original P-rich metasediments during partial melting or hydrothermal events could originate these rare P-rich ores suitably called as “Iberian-type”.

Chapter 6: GRAVITY SURVEY

SUMMARY:

In this chapter a modeling of the Logrosán granite system after a gravity profile is described. The gravity survey was carried out in the Logrosán area, covering the granite and the surrounding country rocks. The scope was to investigate the shape and extent of the pluton at depth.

GRAVITY MODELING

6.1. The metamorphic aureole

The metamorphic aureole developed as a result of the Logrosán granite intrusion is concentrically zoned around the granite. It is asymmetric, extending mostly to the SSE and the WSW (Fig. 6.1a). It shows from the inner to the outer part progressively less affected contact metamorphic rocks (Fig. 6.1). An inner narrow zone near the granite , mainly restricted to the southern border, consists of hornfel rocks composed of Qtz + Bt + Mus + Tur. Quartz-tourmaline veins and tourmaline-rich alteration sectors clearly bound the granite. Although andalusite was reported earlier by Sos Baynat (1967) and Rossi (1975), we found no evidence of this mineral during this study. A large intermediate zone of "spotted slates" (the so-called 'pizarras mosqueadas') is also recognized; the mineral association in this zone consists of a matrix with Bt + Qtz ± Mus ± Chl, and millimetric nodules of Chl + Tu ± Mus ± Qtz ± Hem, probably fully retrograded cordierite. This second zone extends preferentially to the NW. The outer zone is characterized by highly recrystallized slates with some metaquartzite levels.

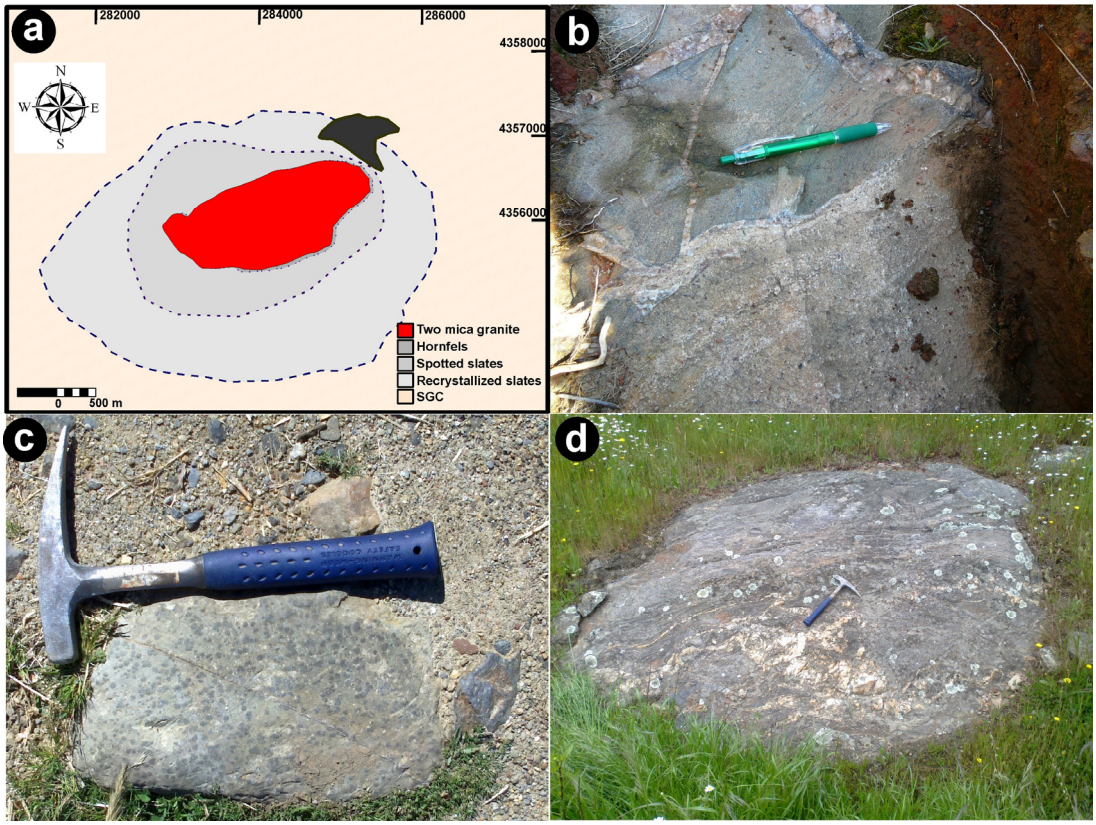

Fig. 6.1: a) Geological sketch of the Logrosán granite and its metamorphic aureole. **b)** Hornfel cut by quartz-tourmaline veins in the granite-SGC metasediments contact. **c)** Spotted slates. **d)** Recrystallized slates of the outer metamorphic contact aureole with quartz veins.

6.2. Gravity data handling

Thirty six gravity measurements were obtained along the two main axes of the Logrosán granite, with a total length of about 10 km per axis. The data were corrected for Earth-tide effects; free-air and Bouguer reductions were also applied (Table 6.1). Terrain corrections were calculated in the field up to 150 m from each station using the Hammer chart corrections, and from 150 m to a distance of 22 km, using the Kane (1962) algorithm, with a density of 2.67 g cm^{-3}. The curvature correction (Bullard B zone) up to 166.7 km was also computed. The normal gravity at sea level was determined using the World Geodetic System (WGS84) formula. The density reduction used was 2.67 g cm^{-3}. The gravity stations measured on the Logrosán granite and surrounded country rocks were tied to the base station located at Trujillo town that belongs to the Spanish gravimetric network (Instituto Geográfico Nacional), with a value of 979977.95 mGal. A comparison of 4 duplicate gravity measurements for the two profiles revealed a root mean square (RMS) error of ± 0.32 mGal. In order to minimize edge effects, 5 gravity stations from the Bouguer anomaly map of the Iberian Peninsula (Mezcúa *et al.*, 1996) were used to extend the profiles length by ~10 km in each direction (Fig. 6.2a). Kriging was used to interpolate the gravity data to a regular grid of 250 m x 250 m to produce a detailed Bouguer anomaly map and showed a distinct east–west regional trend, which is transverse to the gravity low associated with the pluton and also to the pluton boundaries (Fig. 6.2b). This regional trend, assumed to be due to deep sources, was removed with a second-degree polynomial surface. Figure 6.2c shows the residual gravity anomaly map.

6.3. Rock densities

As the aim is to recognize minor variations in the gravity field, a representative density study of the rocks from the Logrosán area has been accomplished. For this purpose, density determinations were made on 16 fresh samples from the granite, and on 16 samples from the SGC metasedimentary rocks (Table 6.2). The density of the granite samples do not barely vary (2.63-2.68 g/cc), while the SGC rock densities range from 2.68 to 3.01 g/cc. Average densities of 2.65 g/cc, and 2.79 g/cc have been used from the granite and SGC rocks, respectively, for the gravity profile.

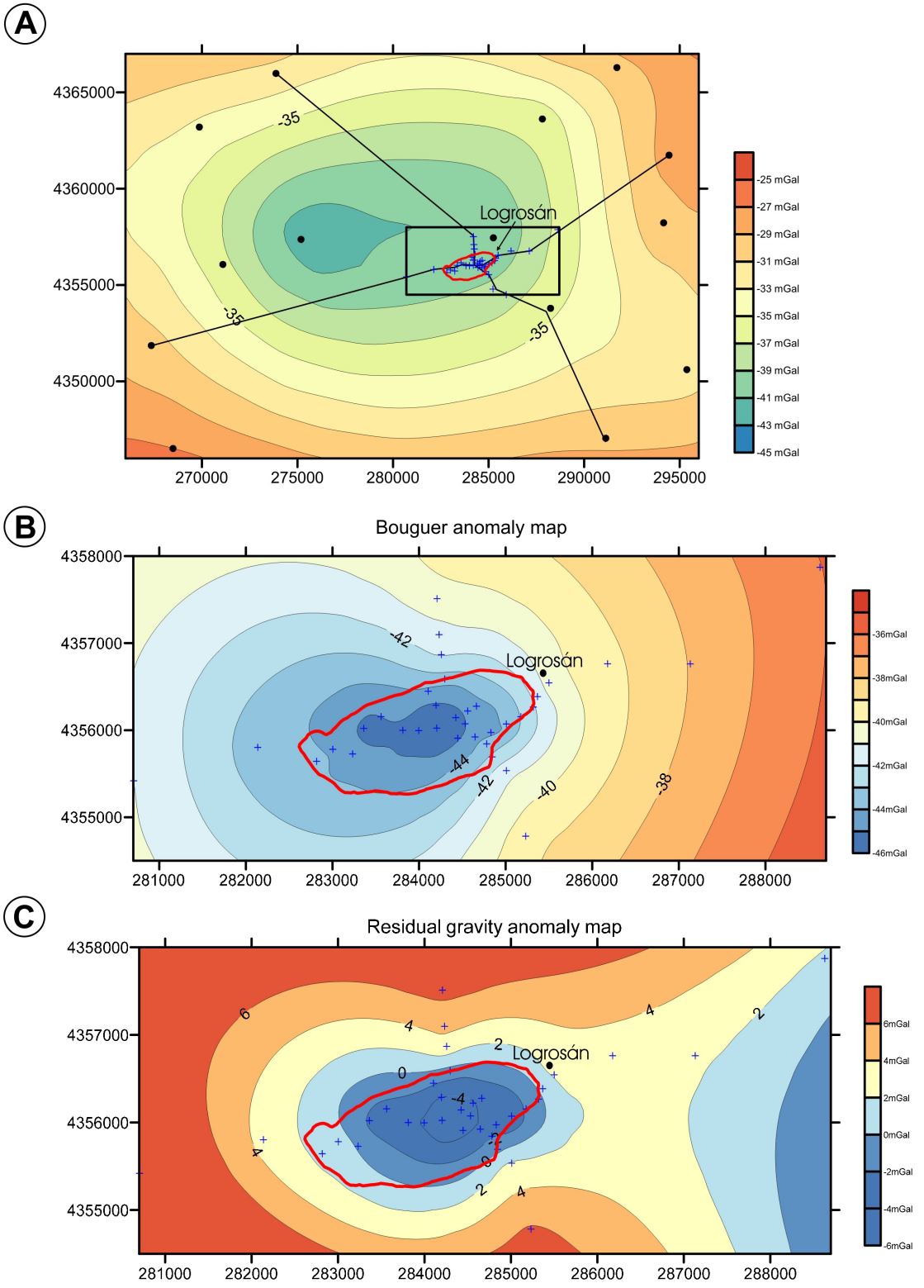

Fig. 6.2: a) Bouguer anomaly map from the gravity stations (black circles) of the Instituto Geográfico Nacional (IGN). Black lines - location of the two gravity profiles; red line - Logrosán pluton boundary. **b)** Detailed Bouguer anomaly map incorporating gravity stations (blue crosses). **c)** Residual Bouguer anomaly map.

Table 6.1: Gravity stations and data reduction of the Logrosán granite gravity survey.

		Longitude	Latitude	X	Y	Elevation (m)	Terrain	_Gscale	Gravity	TideCorr	Closure	Gravity Avg.	RepDiff	FreeAir	Bouguer	Bouguer Corr. (mGal)
705-1	3237.90	-5.880759	39.453253	252129	4371038	512	-	3326.3272	979977.95	0.0972480	0	979977.95	0	14.732345	-42.55866	
705-1	3237.79	-5.880759	39.453253	252129	4371038	512	-	3326.0663	979977.95	-0.0506160	-0.260865		0			
732-1	3207.43	-5.500651	39.325746	284447	4355908	596	0.1042974	3294.897	979946.73	-0.0316420		979947.19	0.4626538	21.208688	-45.48162	-45.37733
732-1	3208.38	-5.500651	39.325746	284447	4355908	596	0.1042974	3295.965	979947.66	0.0603857			0.4626538			
732-2	3203.28	-5.499707	39.327253	284533	4356073	624	0.0688229	3290.7115	979942.42	0.0459903		979942.42		24.946263	-44.87715	-44.80833
732-3	3198.89	-5.498265	39.329104	284663	4356275	645	0.0281634	3286.1857	979937.92	0.0299926		979937.92		26.7598	-45.41344	-45.38528
732-4	3198.47	-5.499418	39.328583	284562	4356220	646	0.0494041	3285.7383	979937.50	0.0140247		979937.5		26.689984	-45.59515	-45.54575
732-5	3200.11	-5.500993	39.327856	284424	4356143	638	0.0256354	3287.4132	979939.19	0.0041950		979939.19		25.975127	-45.41484	-45.3892
732-6	3197.72	-5.503505	39.326721	284204	4356023	648	0.0365718	3284.9481	979936.74	-0.0057340		979936.74		26.711861	-45.79707	-45.7605
732-7	3195.95	-5.505895	39.326417	283997	4355995	657	0.1959707	3283.1222	979934.92	-0.0132730		979934.92		27.702533	-45.81346	-45.61749
732-8	3197.94	-5.508029	39.326398	283813	4355998	652	0.1918532	3285.1599	979936.97	-0.0199520		979936.97		28.210283	-44.74623	-44.55438
705-1	3237.76	-5.880759	39.453253	252129	4371038	512	-	3326.0554	979977.95	-0.0306630	-0.047245	979977.95	0	14.732345	-42.55866	
705-1	3237.82	-5.880759	39.453253	252129	4371038	512	-	3326.1027	979977.95	-0.0450550	0		0			
707-1	3241.59	-5.503525	39.336396	284232	4357097	444	0.0823537	3330.0778	979981.96	0.0572560		979981.96		8.1234436	-41.5586	-41.47625
707-2	3247.19	-5.503936	39.340108	284208	4357510	423	0.0253761	3335.7609	979987.65	-0.0124510		979987.67	0.0168139	7.0236195	-40.3086	-40.28322
707-2	3247.17	-5.503936	39.340108	284208	4357510	423	0.0253761	3335.8034	979987.69	0.0506202			0.0168139			
707-3	3244.52	-5.452784	39.344450	288630	4357871	460	0.0921759	3333.0540	979984.94	0.0235196		979984.94		15.327935	-36.14445	-36.05228
732-10	3221.92	-5.49014	39.330269	285367	4356385	542	0.1389382	3309.7961	979961.65	-0.0179010		979961.65		18.598069	-42.04983	-41.91089
732-11	3219.41	-5.490646	39.329177	285320	4356265	554	0.1888433	3307.2246	979959.08	-0.0108640		979959.08		19.82767	-42.16299	-41.97415
732-12	3214.81	-5.492280	39.328142	285176	4356154	572	0.2197446	3302.5043	979954.36	-0.0056930		979954.36		20.754603	-43.25019	-43.03045
732-13	3211.38	-5.494201	39.327353	285008	4356071	583	0.3694597	3298.9865	979950.84	6.064E-05		979950.84		20.702108	-44.53355	-44.16409
732-14	3212.23	-5.496233	39.326426	284830	4355973	578	0.3422469	3299.8656	979951.72	0.0059363		979951.72		20.121152	-44.55502	-44.21278
732-15	3211.18	-5.498349	39.325922	284646	4355922	584	0.1114014	3298.7947	979950.65	0.0137364		979950.65		20.947717	-44.39984	-44.28844
732-16	3219.73	-5.496759	39.325235	284781	4355842	541	0.1906335	3307.5872	979959.45	0.0229716		979959.45		16.532697	-44.00331	-43.81267
732-17	3229.20	-5.495969	39.323901	284845	4355692	497	0.0962631	3317.3247	979969.18	0.0321118		979969.18		12.811523	-42.80104	-42.70477
732-18	3234.39	-5.494018	39.322528	285009	4355535	477	0.0392517	3322.6652	979974.53	0.0410031		979974.53		12.103029	-41.2716	-41.23235
732-19	3228.79	-5.502608	39.331830	284297	4356588	497	0.0889601	3316.9318	979968.80	0.0603653		979968.75	0.0452552	11.674516	-43.93804	-43.84908
732-19	3228.68	-5.502608	39.331830	284297	4356588	497	0.0889601	3316.8248	979968.70	0.0664389			0.0452552			
732-20	3220.93	-5.504788	39.330513	284105	4356447	534	0.5736347	3308.8700	979960.74	0.0730693		979960.74		15.195345	-44.55738	-43.98375
732-21	3210.68	-5.503682	39.329086	284196	4356286	582	0.3077061	3298.3463	979950.21	0.0789027		979950.21		19.612104	-45.51166	-45.20395
732-22	3237.89	-5.519458	39.322944	282817	4355642	444	0.0588444	3326.3063	979978.18	0.0866984		979978.18		5.5337585	-44.14829	-44.08944
732-23	3228.53	-5.517335	39.324233	283004	4355780	494	0.0633213	3316.6911	979968.57	0.0868384		979968.57		11.237247	-44.03962	-43.9763
732-24	3221.47	-5.514664	39.323813	283233	4355727	528	0.1176243	3309.4356	979961.31	0.0839438		979961.31		14.512862	-44.56849	-44.45086
732-25	3214.94	-5.513251	39.326483	283363	4356020	558	0.1889755	3302.7240	979954.60	0.0804095		979954.6		16.823572	-45.61467	-45.4257
732-26	3217.17	-5.510988	39.327749	283562	4356155	548	0.3104845	3305.0117	979956.89	0.0772979		979956.89		15.914041	-45.40524	-45.09475
732-27	3237.67	-5.503162	39.334341	284257	4356868	464	0.0797941	3326.0549	979977.94	0.0612953		979977.94		10.454019	-41.46596	-41.38616
732-28	3234.36	-5.480871	39.333863	286177	4356762	492	0.0107851	3322.6326	979974.52	0.0392566		979974.52		15.718152	-39.33492	-39.32414
732-29	3239.93	-5.469800	39.33409	287132	4356761	470	0.0108344	3328.3434	979980.23	0.0281177		979980.23		14.621327	-37.97003	-37.95919
732-30	3237.51	-5.483058	39.313402	285926	4354496	471	0.001559	3325.8460	979977.73	0.0167413		979977.73		14.268367	-38.43488	-38.43332
732-31	3241.01	-5.491192	39.315805	285232	4354782	449	0.0246792	3329.4369	979981.33	0.0121558		979981.33		10.857755	-39.38377	-39.35909
732-32	3241.01	-5.543863	39.320395	280705	4355418	443	0.0049198	3329.4279	979981.32	0.0031094		979981.32		8.5914344	-40.97871	-40.97379
732-33	3243.26	-5.527391	39.324213	282137	4355802	420	0.0052912	3331.7320	979983.62	-0.0041100		979983.62		3.4603299	-43.5362	-43.53091
732-9	3228.73	-5.488649	39.331733	285500	4356544	515	0.0382365	3316.7848	979968.64	-0.0249050		979968.62	0.0154165	17.108363	-40.51833	-40.4801
732-9	3228.62	-5.488649	39.331733	285500	4356544	515	0.0382365	3316.7437	979968.61	0.0469865			0.0154165			

Table 6.2: Density calculations for the granite and SGC samples from the Logrosán area.

Sample	Rock type	Dry weight (md) (gr)	Weight 24 h (mh) (gr)	Weight 24 h (ms) (gr)	d real (gr/cm^3)	d ap (gr/cm^3)	Firmness index	Open porosity (%)	Saturation (%)	d real (Kg/m^3)	d ap (kg/m^3)	Volume (cm^3)
111970	Granite	34.27	21.49	34.67	2.682	2.600	0.970	3.035	1.167	2681.53	2600.15	12.78
111976	Granite	27.94	17.44	28.43	2.661	2.542	0.955	4.459	1.754	2660.95	2542.31	10.50
111978	Granite	29.45	18.35	29.85	2.653	2.561	0.965	3.478	1.358	2653.15	2560.87	11.10
111979	Granite	29.44	18.29	30.13	2.640	2.486	0.942	5.828	2.344	2640.36	2486.49	11.15
111911	Granite	36.65	22.76	37.02	2.639	2.570	0.974	2.595	1.010	2638.59	2570.13	13.89
111912	Granite	34.16	21.29	34.56	2.654	2.574	0.970	3.014	1.171	2654.23	2574.23	12.87
112688	Granite	31.01	19.27	31.82	2.641	2.471	0.935	6.454	2.612	2641.40	2470.92	11.74
112690	Granite	38.60	23.96	39.70	2.637	2.452	0.930	6.989	2.850	2636.61	2452.35	14.64
112696	Granite	35.27	21.90	36.02	2.638	2.498	0.947	5.312	2.126	2638.00	2497.88	13.37
112698	Granite	32.71	20.37	33.81	2.651	2.434	0.918	8.185	3.363	2650.73	2433.78	12.34
732.1	Granite	25.40	15.93	25.70	2.682	2.600	0.969	3.071	1.181	2682.15	2599.80	9.47
732.3	Granite	32.88	20.37	33.26	2.628	2.551	0.971	2.948	1.156	2628.30	2550.81	12.51
732.4	Granite	34.62	21.53	35.35	2.645	2.505	0.947	5.282	2.109	2644.77	2505.07	13.09
732.7	Granite	33.66	20.92	34.11	2.642	2.552	0.966	3.412	1.337	2642.07	2551.93	12.74
732.14	Granite	33.63	20.96	34.14	2.654	2.552	0.961	3.869	1.517	2654.30	2551.59	12.67
732.23	Granite	31.63	19.66	32.18	2.642	2.526	0.956	4.393	1.739	2642.44	2526.36	11.97
111966	SGC	30.34	19.31	30.95	2.751	2.607	0.948	5.241	2.011	2750.68	2606.53	11.03
111967	SGC	38.03	24.11	38.29	2.732	2.682	0.982	1.834	0.684	2732.04	2681.95	13.92
111981	SGC	23.35	14.88	23.98	2.757	2.566	0.931	6.923	2.698	2756.79	2565.93	8.47
111971	SGC	39.99	25.74	40.95	2.806	2.629	0.937	6.312	2.401	2806.32	2629.19	14.25
112691	SGC	37.91	24.31	38.93	2.788	2.593	0.930	6.977	2.691	2787.50	2593.02	13.60
112692	SGC	21.32	13.36	22.14	2.678	2.428	0.907	9.339	3.846	2678.39	2428.25	7.96
112693	SGC	11.95	7.50	12.40	2.685	2.439	0.908	9.184	3.766	2685.39	2438.78	4.45
112694	SGC	28.24	18.79	28.57	2.988	2.888	0.966	3.374	1.169	2988.36	2887.53	9.45
112695A	SGC	26.69	17.82	27.41	3.009	2.783	0.925	7.508	2.698	3009.02	2783.11	8.87
112695B	SGC	32.81	20.98	34.21	2.773	2.480	0.894	10.582	4.267	2773.46	2479.97	11.83
112697	SGC	41.83	26.59	42.46	2.745	2.636	0.960	3.970	1.506	2744.75	2635.79	15.24
112699	SGC	29.12	18.63	29.67	2.776	2.638	0.950	4.982	1.889	2775.98	2637.68	10.49
112700	SGC	39.67	25.26	40.21	2.753	2.654	0.964	3.612	1.361	2752.95	2653.51	14.41
112689	SGC	30.83	19.64	31.02	2.755	2.709	0.983	1.670	0.616	2755.14	2709.14	11.19
112703	SGC	10.56	6.76	11.06	2.779	2.456	0.884	11.628	4.735	2778.95	2455.81	3.80
112705	SGC	36.56	23.52	37.22	2.804	2.669	0.952	4.818	1.805	2803.68	2668.61	13.04

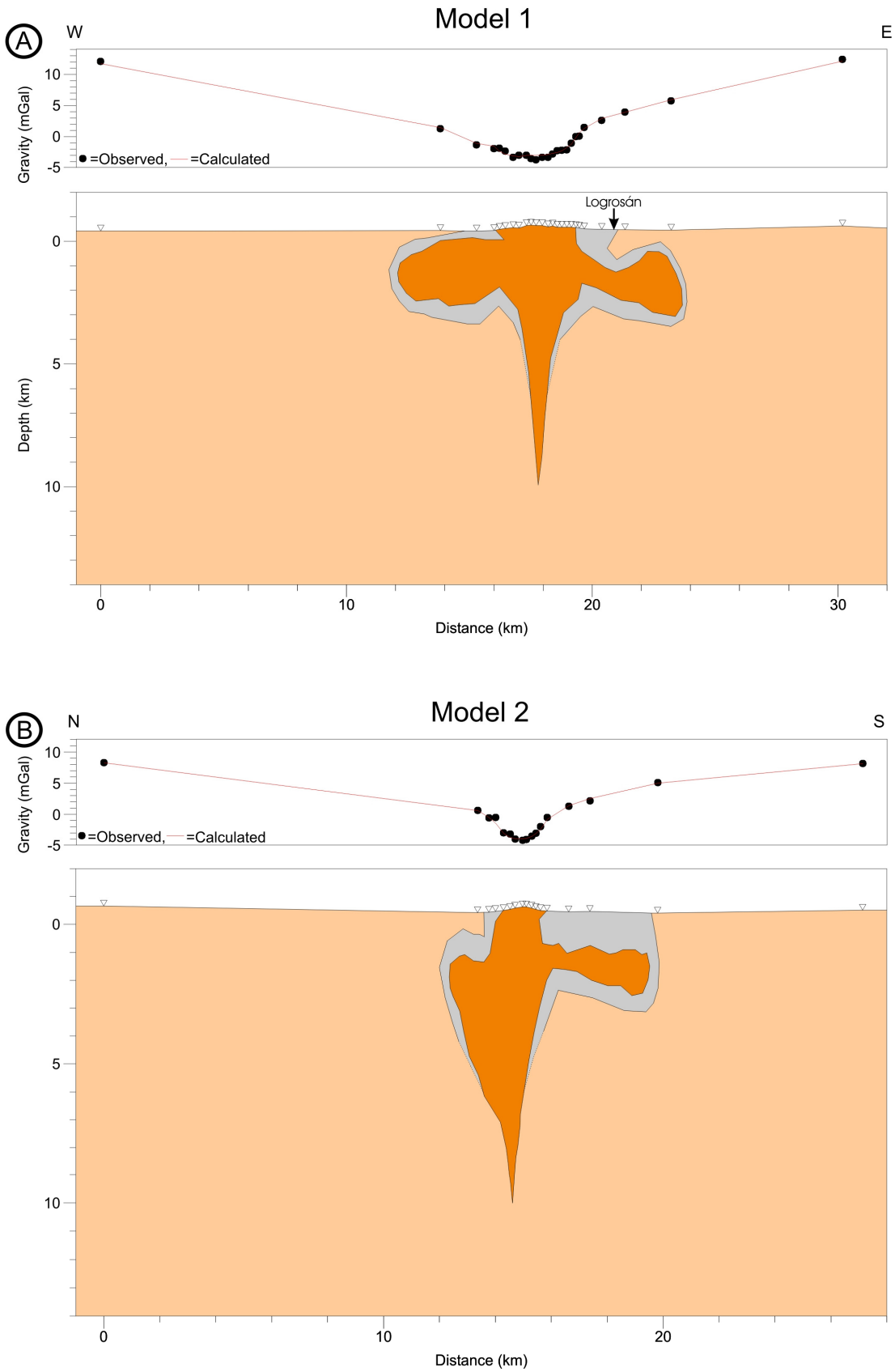

Fig. 6.3: 2+3/4D forward gravity modeling of the residual gravity anomaly map. **a)** Model 1. **b)** Model 2. Open triangles - location of the gravity stations.

6.4. Gravity modeling

The gravity profile interpretation unravel valuable insights and a better understanding of the form of the Logrosán granite (see also Chicharro et al., 2015). The Logrosán pluton produces an overall residual anomaly with maximum amplitude of about -5 mGal, and an ENE–WSW trend. The absolute gravity low is located near to the center of the pluton. The 0 mGal contour agrees well with the granitic body, indicating that the residual anomaly, obtained after subtracting the deep effects, corresponds to the gravity signature of the pluton (Fig. 6.3). Owing to the lower density of the granitic rocks compared to the metamorphic host rocks, the gravity signature of the plutons is typically a gravity low. This gravity anomaly depends on the dimensions, density contrast, and depth of the granitic pluton. The pluton dimensions and geometry were modeled using the obtained residual anomaly. Using the gravity stations along the profiles, two density models crossing the minimum anomaly values were constructed. One model, E–W. is subparallel to the pluton main axis, whereas the N–S model is transverse to this axis (Fig. 6.3a and 6.3b). Each model consists of three different density bodies: the Logrosán pluton, the host rock affected by contact metamorphism, and the regional metamorphic host rock. In order to take into account the finite length of the granitic body in the direction orthogonal to the profiles, the modeling process was undertaken in 2+3/4D using GM-SYS Profile Modeling (2009) software.

- Model 1 corresponds to the E–W profile, with a total length of 30 km (Fig. 6.3a). The residual gravity low reaches a minimum value of -4 mGal at the central part of the pluton (from km 17 to km18), which has been interpreted as the location of the root. In order to achieve a good model fit, a typical mushroom-shaped body was considered. The total lateral extension of the body is ~12 km, and the maximum depth is ~10 km. The overall geometry is slightly asymmetric: the western end of the pluton is thicker (~2.5 km) and shallower (at a depth of ~0.3 km) than the eastern one (~2 km thick and ~0.8 km deep). Nevertheless, a separate smaller granite body located in the eastern part instead of an asymmetric mushroom-shaped is not discarded. According to the field data, a ~0.5 km-thick contact metamorphic aureole has been included, surrounding the granitic pluton. As revealed by the gravity model, the pluton has a large extension compared to its current outcrop (~3.5 km). The final RMS misfit of the model is ±0.342 mGal, which has a similar magnitude than the RMS error of the gravity field survey.

- Model 2 corresponds to the N–S profile, with a total length of 27 km (Fig. 6.3b). As in model 1, the residual gravity low reaches -4.5 mGal at the central part (km 15), corresponding to the location of the root. Owing the lower dimensions (~1.8 km) of the

outcropping pluton in the N–S orientation, the gravity low of the N–S profile is narrower than the gravity low of the E–W profile. A good model fit is obtained with a very asymmetric geometry, different from model 1. Although the maximum depth reached by the root is similar in both profiles (~10 km), the total lateral extension of the body in the N–S direction is just ~7 km. Moreover, the northern end of the pluton has a much more reduced extent (~1.5 km), and is deeper (~1.5 km depth) than the southern one (~3.8 km lateral extent and ~1.1 km depth). This would explain why the contact metamorphic aureole is larger in the south. The final RMS misfit of the model is ±0.288 mGal. Similarly to the model 1, a separate small granite body to the north is not discarded, although the extension of the metamorphic aureole through this point makes it less plausible.

In the following chapter (Chapter 7) these gravity data are envisaged together with the available information of the Logrosán granite and ores to interpret the metallogenic model of the Logrosán ore deposits.

Chapter 7: GEOLOGIC AND METALLOGENIC MODELING

SUMMARY:

The main conclusions discussed in the previous chapters have been integrated in this summarizing chapter in order to envisage a complete model for explaining the geological processes involved in the origin of the Sn-(W) Logrosán ore deposits. An outline of the potential exploration targets in the Logrosán ore deposits has been considered by evaluating the interrelationships of geophysical, mineralogical, geochemical and petrological aspects in an overall scenario. The outlook developed here can be used as general statements for the understanding of other worldwide Sn-W granite-related ore deposits.

GEOLOGIC AND METALLOGENIC MODELING

7.1. P-T conditions of granite emplacement

The Logrosán granite was emplaced in the upper crust during late Variscan time (at ca. 308 Ma). The lack of deformation structures in the Logrosán granite agrees with its post-tectonic character. Layering in the Logrosán granite can be rarely recognized in the proximity to the SGC host-rocks (Fig. 7.1a). This fabric is formed while the granite is still molten, i.e., it is syn-magmatic. Compositional layering in granites may be the result of changes in volume on cooling due to fluctuations of pressure caused by the granite emplacement, or simply by magmatic flow processes (e.g., Barbey, 2008). The granite emplacement triggered thermal metamorphism and induced local deformation on the regional S_1 foliation in the vicinity of the granitic cupola (Fig. 7.1b).

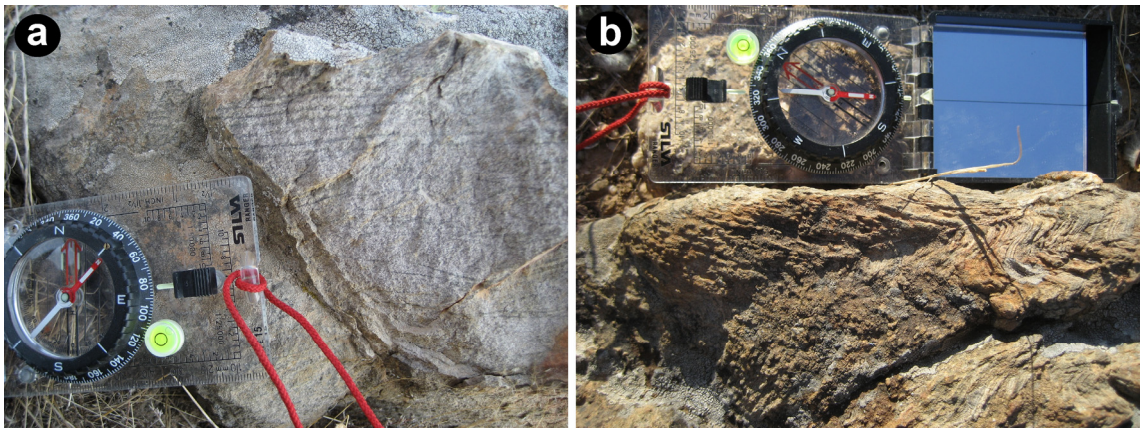

Fig. 7.1: a) Compositional layering developed in the Logrosán granite near the SGC contact; **b)** Folding in a micaschist. Cleavage and crenulation of regional S1 foliation.

The contact metamorphic aureole is zoned, from hornfels in the inner zone, to spotted slates, and recrystallized slates in the outer zone. The mineralogy of the metamorphic contact aureole is composed essentially of quartz, muscovite, biotite, chlorite and tourmaline. Although Sos Baynat (1967) mentions the presence of andalusite and cordierite in the hornfels of the thermal aureole around the Logrosán granite, in this research no evidence of their neoformation during the granite emplacement has been found. The lack of any aluminium silicate polymorph complicates the evaluation of the emplacement depth level of the Logrosán granite, which might have been emplaced at epizonal P-T conditions below the Al_2SiO_5 triple point (i.e., less than c. 10 km). Nonetheless, the presence of boron and fluorine in a granite system depresses its *solidus* temperature and allows reaching shallower levels of emplacement (Manning and Pichavant, 1984). In the Logrosán granite, fluorine is mainly found in the structure of muscovite and magmatic apatite, reaching considerable contents in whole-rock geochemistry. Boron is found in

tourmaline, which is a ubiquitous mineral during the late magmatic and the metasomatic processes. Being the Logrosán granite phosphorous-rich, it is noteworthy to point that phosphorus also lowers *solidus* temperature and increases the solubility of Al and high field strength elements (HFSE) in the melt (London and Manning, 1995). The occurrence of pegmatite pods in the granite suggests that it was fluxed element-rich (B-F-Li); which increases the solubility of water in these residual magmas (Pichavant, 1981). According to the high F content of the Logrosán granite, the initial emplacement conditions could be close to the intersection of the wet granite *solidus* and to the F-rich muscovite breakdown reaction (Fig. 7.2). Since a release of boron is expected according to the common presence of early quartz-tourmaline veins and tourmaline-bearing pegmatite pods; the peraluminous melt stability field co-existing with F-rich muscovite should be enlarged until reaching the 2% B_2O_3 line proposed by Manning and Pichavant (1983). Therefore, the P-T emplacement conditions estimated for the Logrosán granite are in the range of 1 to 2 kbar and 650 to 700 ºC (Fig. 7.2). Ti-in-zircon temperatures (average of 840 ºC) and Zr melt saturation temperatures (700-780 ºC) (see Chapter 3) are higher than the temperatures obtained here. These higher temperatures are comprehensible, because zircon is one of the earliest minerals to be formed (close to *liquidus* conditions), and the highly fractionated character of the Logrosán granite would have been obtained after taken place during a relatively large time (toward *solidus* conditions). In fact, a lowering of the *solidus* would not only have caused shallower pressures of emplacement, but additional time for differentiation should be also expected. This would have favored the concentration of incompatible elements in the residual melt, such us tin (Sn). Besides, the lower temperature obtained by zircon saturation thermometry overlaps with the emplacement temperature proposed. Temperatures around 700 ºC have been obtained by stable isotopes in pegmatitic quartz-tourmaline pairs (see Chapter 4). The range of P-T estimated for the Logrosán granite emplacement (P: 1-2 kbar; T: 650-700 ºC) agrees perfectly with the conditions proposed for the almost coeval cassiterite precipitation (P: 1.2-2.7 kbar; T: ~540 ºC) during the late stages of granite cooling in a granite-hydrothermal open system (see Chapter 4). The estimated P-T crystallization conditions for the Logrosán granite are very similar to those deduced for most of the fractionated plutons of the Montes de Toledo Batholith: 670-700 ºC and 1-2 kbar (Villaseca et al., 2008; Merino et al., 2013; 2014), and for the Nisa-Alburquerque batholith: 700-750 ºC and around 2.5 kbar (González Menéndez et al., 2011).

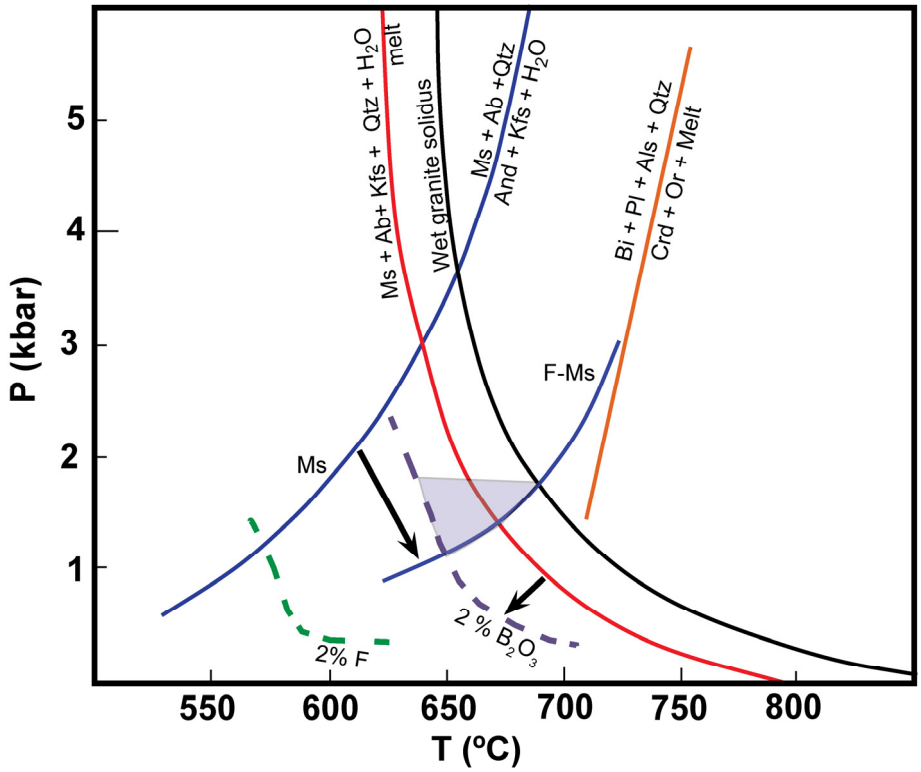

Fig. 7.2: P–T diagram showing the estimated crystallization conditions for the Logrosán granite (colored area). Melting curves and reaction involving muscovite are taken from Johannes and Holtz (1996). F-Ms curve after Pichavant et al. (1988). *Solidus* curves for water-saturated haplogranitic systems with F and B, after Manning and Pichavant (1983).

7.2. Key features for cassiterite precipitation

Tin (Sn^{2+}) has an incompatible and litophile character (Taylor, 1979; Eugster, 1985) and becomes enriched in highly fractionated reduced magmas. These granites are usually post-orogenic peraluminous S-type granites formed in collisional orogenic settings (e.g., European Variscides, Mesoproterozoic Kibera Belt in Africa, Mesozoic orogen from the south Chinese Platform) or near plate boundaries (e.g., Southeast Asian Tin Province, Bolivia and Peru) (Pohl, 2011). The Nd and Sr isotope data of the tin-bearing granites indicate a continental crustal source (e.g., Cornwall, Malaysia), as occurs in the Logrosán granite (see Chapter 3). However, some of them have very spread Nd values, which suggest the involvement of mantle material (e.g., Bolvia, Erzgebirge) (see Lehmann, 1990 for a review). The orogenic setting becomes the first key feature for the formation of Sn-W ore deposits, because the generation of magmas by crustal melting in a thick crust provides more time for fractionation. Moreover, the shallower the emplacement, the more the chances of the concentration of incompatible elements in the residual melts.

The host rocks of the Logrosán ore deposits, either the granite (San Cristóbal sector) or the metasediments (El Serranillo sector), show a metasomatic alteration characterized by

muscovitization and tourmalinization. Similarities in alteration patterns also indicate akin processes for the generation of both mineralized sectors. Pervasive alteration is supposed to start at high temperatures, when magmatic and post-magmatic processes are hardly undistinguishable (Burnham and Ohmoto, 1980). After Taylor (1979), the magmatism related to Sn-W ore deposits may be either fluorine-rich, or boron-rich. Lehman et al. (2000) observe that greisen and disseminated ores are associated with fluorine-rich magmas, while boron dominated magma provinces consist of hydrothermal quartz-vein deposits. Sheeted veins are more usual than disseminated cassiterite ore deposits in Logrosán, similarly to Cornwall (UK), Pilok (Thailand), the Kibara belt (Africa), or Panasqueira (Portugal); while, for instance, in Erzgebirge and Nigeria the disseminated-mineralization and ore pockets are more common. This may respond to the degree of fracturing of the host rocks. In this respect, since high boron contents in the system imply fracturing of the confining rocks, vein mineralization could be favored in Sn-W ore deposits related to boron-rich magmas in contrast to fluorine-rich magmas. As a matter of fact, tourmalinization is a frequent metasomatic process in the metasediments of the SGC surrounding the Logrosán granite, and represents a distinctive feature in the exogranitic El Serranillo ore deposit. Tourmaline also occurs in the numerous barren quartz-tourmaline veins, in quartz-cassiterite veins, and in miarolitic cavities within the Logrosán granite. The San Rafael ore deposit (Perú; Mlynarczyk et al. 2003), the tin-bearing granites of the Cornubian batholith (UK; Charoy, 1982, London and Manning, 1995; Williamson et al., 2000), the plutonic complex of Cévennes (French Massif Central; Chauvet et al., 2012), the Pilok area (Thailand; Linnen and Williams-Jones, 1995), among others, also present pervasive tourmalinization, to a greater or a lesser degree. The source of boron in the Logrosán granite is supposed to be derived from the partial melting of the SGC metasediments, which are boron-rich (Pereira and Shaw, 1997; Bea et al., 2009), and enriched by fractionation processes. Tourmalinization indicates a subsolidus metasomatic alteration and, evidently, the presence of B-rich fluids. In addition, as H_2O has a high solubility in B-rich magmas, boron extraction producing an aqueous fluid is achieved at shallow levels. The vapor separation was delayed owing to the ascent of the magma to shallower levels, and the consequently lower confining pressures. Therefore, the subsequent degassing of the residual melts involved more volume expansion and higher fluid overpressures, causing intense fracturing and/or brecciation of the confining rocks (e.g., Halls, 1994). Other alteration processes in the Logrosán Sn-(W) ore deposits include feldspar hydrolysis, which is consistent with the complete replacement of feldspars by muscovite in selvages at high temperature (sericitization), and kaolinization at lower temperature. These mineral conversions provide necessary neutralizing reactions (H^+ consumption via hydrolysis) for cassiterite precipitation. After Heinrich (1990) the grade of this alteration is dependent on the initial feldspar content and the neutralization capacity of the host rocks, which control the acidity of the system. Neutralizing reactions by increasing the surface contact area between the hydrothermal fluids and the

aluminosilicate rocks are more effective in structural weakness zones (e.g., the stockworks from the El Serranillo sector). However, greisenization in the Logrosán ore deposits is mostly restricted to the vein selvages, in contrast to other strongly greisenized granites (e.g., East Kemptville; Halter et al., 1996). Logrosán would belong to a mixed situation B>F in the classification between F-rich and B-rich greisen systems of Pollard et al. (1987). This same authors distinguish between closed and open systems, the former being generally not or weak mineralized. The multiple stockworks and veins suggest that the Logrosán ore deposit was developed in an open system.

The ore fluids involved in the Logrosán cassiterite precipitation have some peculiar features: they are N_2-(CH_4-CO_2)-rich aqueous fluids with low salinity. However, most numerical models suggest that in plutons crystallizing at shallow levels the salinity of the exsolving fluid increases as the degree of magma crystallization is higher (Cline and Bodnar, 1991). As a matter of fact, hypersaline fluids are commonly found in sub-volcanic Sn-W ore deposits, while low to moderately saline and aqueous carbonic (CO_2) fluids are typical of plutonic Sn-W ore deposits (Linnen, 1998). Aqueous-carbonic and moderately saline fluids are found in Sn-W ore deposits from the Central Iberian Zone (e.g., Moura et al., 2014; Noronha et al., 1999), the Kibaran Belt (e.g., Pohl and Günther, 1991); Cornwall (e.g., Wilkinson, 1990) or Thailand (Linnen and William-Jones, 1995). The aqueous-carbonic fluids of the previous examples may contain N_2-CH_4 components but CO_2 is the dominant volatile phase, contrary to Logrosán, where CO_2 is not even present in the earliest fluid inclusions. Moreover, the salinity in Logrosán fluid inclusions is very low comparing to these analogous ore deposits. The low salinity of early and late fluids in the Logrosán ore deposits may be explained by the low pressure at which vapor saturation occurs, which implicates that the late magmatic fluids would have decreasingly lower salinity (e.g., Linnen, 1991).

The emplacement into shallow levels and the metasomatism deduced by the host-rock alteration suggest that a long-term interaction of the granite with the host-rocks occurred during the contact metamorphism. This implies that large hydrothermal convective systems would have involved fluid circulation through the nearby SGC metasediments, which is also described in Cornwall (Wilkinson, 1990) and Pilok (Linnen and William-Jones, 1995). In the Pilok and Cornwall ore deposits a magmatic-metamorphic mixing is suggested for the cassiterite precipitation, although remobilization of metals by metamorphic-derived fluids or a purely magmatic-derived fluids are not discarded. A clear magmatic fluid component is not present in Logrosán, at least not in the first stages of the mineralization, where only N_2-CH_4 aqueous fluid inclusions appear. Nonetheless, the source of the metals is inferred to be the highly fractionated Logrosán granite. Therefore, the N_2-CH_4 fluids were probably originated from the SGC metasediments during the

contact metamorphism and the metasomatic process. These volatile-rich metamorphic-derived fluids circulated through convective cells through the metasedimentary host rocks and the granite.

Tin is only mobile under reduced conditions in the form of Sn^{2+}, mostly as fluoride or chloride complexes. The N_2-CH_4 metamorphic-derived fluids provide these reduced conditions, as well as the low oxygen fugacities of ilmenite-series granites and nearby pelitic metasediments. The intense brecciation and the boron metasomatism decreased due to the release of the overpressure after the granite emplacement. The tourmaline occurring in pegmatites and early quartz-tourmaline veins is Fe-rich (schorl), which implies somehow oxidizing conditions in these late-magmatic stages. Nevertheless, the highly reduced metamorphic-derived metal-bearing fluids kept circulating. Subsequently, the extensional N30 system, together with the greisenized process, began. There was a release of pressure, the temperature decreased and the neutralization of feldspars favored the increase of the oxygen fugacity. The metal-bearing complexes were then destabilized and the Sn-(W) ores precipitated. The precipitation is fully controlled by the veins and veinlets, being richer where they branch or interconnect. The open system allowed the metamorphic-derived fluids and the magmatic-fluid mixing. The CO_2 was introduced in the system as the result of the fluid mixing and its increase was partly due to the oxidation of CH_4. These new fluids are represented by the fluid inclusions in quartz coeval to the cassiterite and by the post-dating N-S sulfide veins. Sulfide veins have late volatile-rich fluid inclusions which possibly indicate a non-stabilized system with continuous openings of the veins. In conclusion, P-T conditions, volatile enrichment in the melt, the mixing of the metamorphic and magmatic fluids, and the redox state have being the key features for the Logrosán Sn-(W) granite-related ore deposit formation. The understanding of these observations could contribute as an important clue to the origin of similar Sn-W ore deposits.

7.3. Integration of the metallogenic and the gravity modeling

The wide extension of the metamorphic contact aureole is consistent with a flat-shaped ("mushroom" type) granitic cupola emplaced at shallow levels. The Logrosán granite defines a 12 km wide, thin (2–2.5 km) mushroom shaped body, along a E–W axis, and a smaller (7 km) asymmetric body along a N–S axis; a rather typical geometry displayed by many Variscan granites in Europe (Vignerese et al., 1999). According to Vignerese et al. (1999), flat-floored granites are found in the uppermost crust, forming under prevailing subhorizontal extensional conditions. As indicated by the gravity profile, the Logrosán granite has a ~ 10 km deep magma feeder zone (Fig. 7.3). In this respect, the presence of a single feeder is consistent with the emplacement conditions suggested for small flat-floored granites elsewhere (e.g., Ameglio et al,

1997; Benn et al. 1998; Roman-Berdiel et al. 1995; Vignerese et al., 1999). Taking into account that the density of the root pluton probably increases with depth, this 10 km depth of the granitic root may be overestimated. Unfortunately, the proximity in rheological conditions at these depths, where thermal contrast is not high enough, and the progressively minor magma volume of the roof zone, makes it impossible to refine this root depth approach. In this regard, there is neither local nor regional evidence indicating a structural control of the granite emplacement by deep large faults. The gravity profile could have been interpreted as a separated body in the eastern sector (Fig. 7.3), but the vertical profile of the main granite (the east edge, in Fig. 7.3) must be explained by a major structure, and no faults have been recognized. Therefore, a more evolved granitic unit reaching higher fractionation was proposed as the most plausible cause for this slightly later and more evolved mineralization. Thus, the best model to explain the Logrosán magmatic system is that proposed in the Chapter above (Fig. 6.3a and Fig. 7.4).

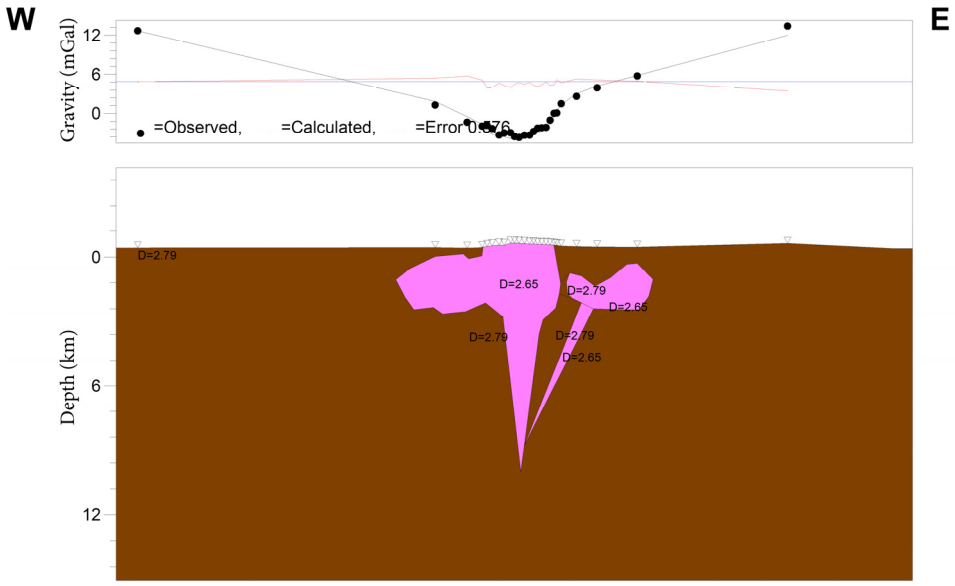

Fig. 7.3: W-E gravity alternative interpretation. Note that the author prefers the model of figure 6.3a and 7.4 (see text).

The El Serranillo is the only exogranitic Sn-(W) ore deposit in the vicinity of the Logrosán cupola, thus the main discussion will be focused on the E–W gravity profile (Fig. 6.3a and Fig. 7.4). The intrusion of the Logrosán granite generated an overpressure system, resulting in hydraulic fracturing of the granitic cupola roof and country rocks (e.g., Burnham, 1979). The volatile-rich gas-liquid phase was carried through these channels, to areas affected by lesser pressure and temperature. The Sn-(W) mineralization in the studied sectors occurs as disseminations and veins, always emplaced within felsic host rocks. The gravity modeling allows an understanding of the San Cristóbal and El Serranillo ore deposits as the result of the single prolonged metallogenic event, related to the emplacement of the Logrosán granite, which is also supported by

mineralogical similarities and paragenetic features. In the El Serranillo sector, slightly younger ages (~ 303 Ma), although overlapping within analytical error, are related to the presence of disseminated Nb-Ta mineralization not found in the endogranitic ore deposit (see Chapter 4).

7.4. Implications for the Sn-W ore exploration within a brownfield type scenario

Gravity data of exposed plutons have been widely used to determine granite emplacement mechanisms (e.g., Taylor, 2007; Vignerese, 1995) or granite petrogenesis (Tartèse et al., 2001). Regional gravity surveys are useful to predict hidden granitic bodies, which may be related to the location of buried deposits (e.g., Liu and Peng, 2004). In this respect, the location of alteration zones is also essential to select areas of potential ore deposits. In the study area, muscovitized or tourmalinized host rocks may lead to the identification of mineralized veins. Although the identification of alteration areas is an important field exploration tool, this should be carefully considered. According to this, feldspar hydrolysis may provide insufficient criteria for ore discovery (Heinrich, 1990). Indeed, acidity neutralizing reactions with muscovitization in structural weakness areas may result in a wide halo of subeconomic veinlets (e.g., cassiterite in Panasqueira mine, Portugal: Kelly and Rye, 1979). The extensive or partially (spots or patches) tourmalinite generation are ubiquitous in Sn-W metallogenic areas (e.g., Cornwall, UK: Charoy, 1982; San Rafael, Peru: Mlynarczyk and Williams-Jones, 2006). Tourmalinization areas are related to intense brecciation and fracturing, and can be used as a powerful tool in the search for potential economic-grade ores.

The application of detailed gravity modeling in matured exploration environments is not a common practice in Sn-W exploration. However, there are some important examples of the use of this technique in mineral exploration for other type of ores. For instance, gravity is a common exploration tool for massive sulfides, given the high density of these mineralized bodies. Additionally, Romeo et al., (2008) conducted detailed gravity modeling focused on the mechanism of emplacement of the Aguablanca Ni-Cu-PGE stock, which is related to a mafic pluton in the Central Iberian Zone. Dufréchou et al., (2011) presented a mapping of subsurface intrusions in an IOCG ore deposit in high grade areas (Grenville Province, Québec). In the Greenville Province, the occurrence of a positive anomaly underneath mineralization is explained by the presence of mafic to intermediate intrusive rocks beneath the hydrothermal system, or by a higher concentration of magnetite and sulfides (Dufréchou et al., 2011). The distribution of the deposits in relation to the gravity field has been applied in a regional scale for Variscan Sn–W–Mo in the Krušné hory/Erzgebirge granite batholith (Štemprok and Blecha, 2015); these authors

consider contrarily that there is no distinct relationship between the masses of Late Variscan granites and the distribution and the sizes of associated W ± Mo and Sn–W deposits. As a matter of fact, major anomalies defining a profile might indicate a concentration of ores, but it may not be possible to draw an exhaustive picturing; however, second-order variations in a gravity profile may be envisaged as possible targets in a detailed gravity survey. Consequently, minor highs (within an overall low gravity scenario) at Logrosán coincide with the presence of Sn deposits. In addition, if we take into account that gravity modeling allows the identification of areas that have undergone a greater tectonic stress and are more susceptible to fracture, we may have a key for target definition. On the other hand, the shape at depth of granite plutons provides important information for ore exploration. Irregularities in the roof of concealed granites and steep gravity gradients on granite cupola walls in Cornwall were identified as targeting areas (Beer et al., 1975). Therefore, the granite geometry at depth could be used to recognize suitable areas where fluid transport and ore deposition may have occurred. In summary, based on the granite gravity profile and the presence of alteration, two main sectors susceptible of being explored in the Logrosán ore field have been defined. Two of these targets are located on the southern and western sectors of the granite, where higher curvatures have been identified by gravity. Another area with suitable characteristics on the northern side of the granite corresponds to a Cu mineralization which matches well the (district-scale) metal zoning pattern described in Cornwall and elsewhere for Sn-W and Cu deposits (e.g., Guilbert and Park, 1986). In Figure 7.4 the synopsis of the Logrosán ore deposits model and suitable targets is presented.

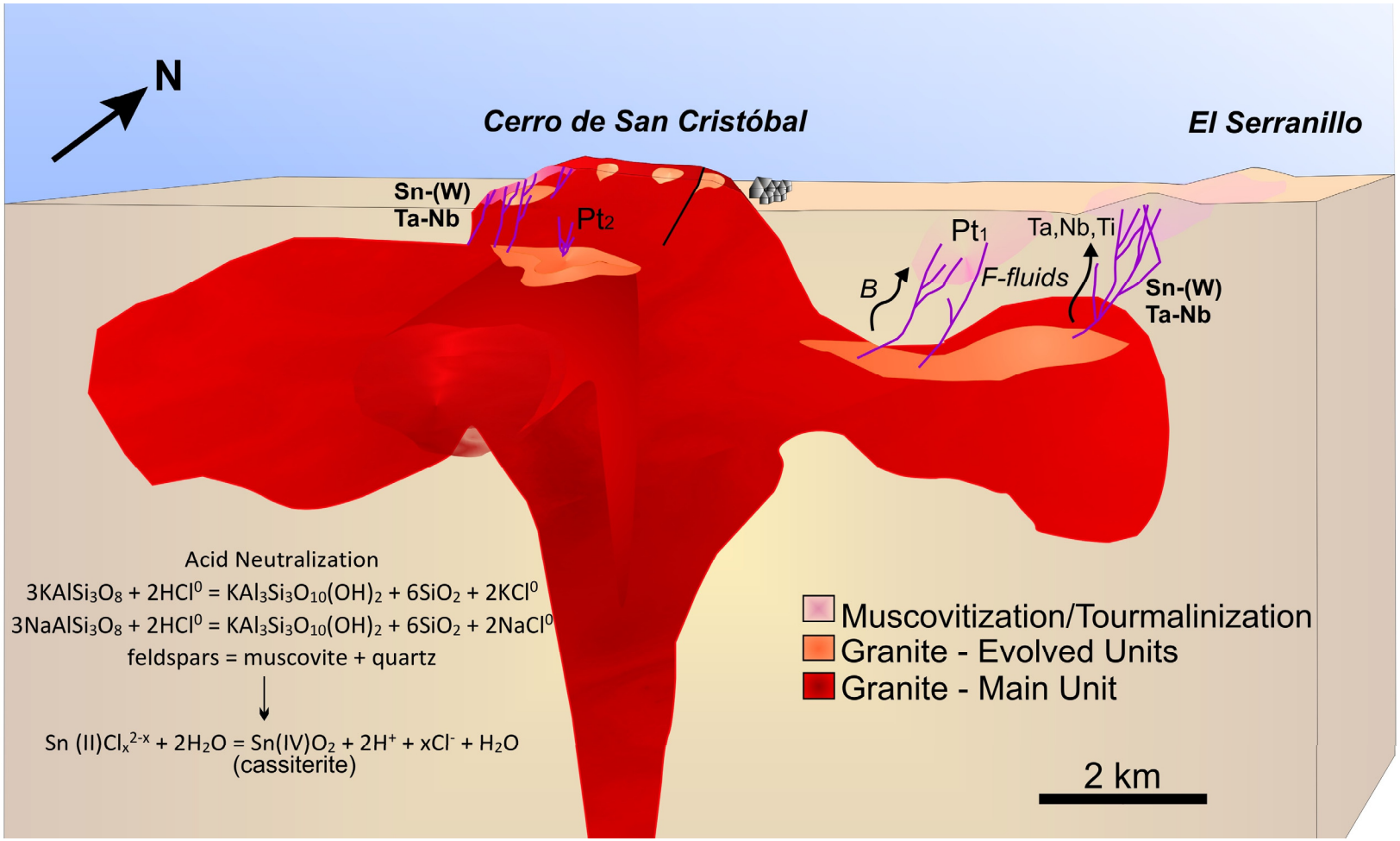

Fig. 7.4: Geology, mineralization and potential targets (Pt_1 and Pt_2) of the Logrosán Sn-(W) ore deposits. After the shallow emplacement of the Logrosán granite, B-rich magmatic fluids caused intense fracturing and/or brecciation owing to overpressure. Convective hydrothermal cells causing the mobilization of metamorphic-derived fluids which carried the Nb-Ta-Ti-Sn-(W) phases under reduced conditions within the granite and the metamorphic aureole. These phases migrated through the host SGC metasediments, and precipitated when the temperature decreased and the oxygen fugacity increased. Late-magmatic and hydrothermal fluids (F-rich) exsolved from the magma caused extensive alteration (feldspar hydrolysis) around the granite cupola and the host metasedimentary rocks, favoring the cassiterite precipitation.

FINAL CONCLUSIONS

Conclusions

The Logrosán cupola is a felsic, highly fractionated, phosphorous-rich and strongly peraluminous (ASI = 1.2 - 2) tin-granite (Sn = 11 – 67 ppm). Two distinct units can be distinguished using field, petrographic and geochemical evidences: (i) a medium- to coarse-grained monzogranite (Main Unit) occupying the main granite outcrop; and (ii) more fractionated leucogranite bodies (Evolved Units) mostly concentrated on the summits of the pluton. The whole-rock geochemistry does not indicate that a simple fractional crystallization process may produce both the Main and the Evolved granite suites. Instead, complex Sr, Ba, Rb, Eu and CaO trends rather suggest inputs of different felsic magma batches from a deep magma reservoir. The spread in the $^{87}Sr/^{86}Sr$ initial ratios and Hf-isotope composition also suggests that isotopically heterogeneous magmas intruded almost coevally in different episodes.

The integration of whole-rock geochemistry with O, Sr, Nd and Hf isotopic signatures suggests that the Logrosán granite is the result of partial melting of heterogeneous metasedimentary material. The lack of mafic enclaves and the variabilities of $^{87}Sr/^{86}Sr$ data in an almost constant low εNd values dismiss the participation of mantle-derived magmas. Zircon inheritance (mostly Neoproterozoic zircons) combined with the metasedimentary nature of the proposed protolith, as well as the Sr-Nd signature correlations between the metagreywackes of the Neoproterozoic metasediments and the granite allow suggesting that the Schist Greywacke Complex is the most plausible source of the Logrosán granitic magma.

The tin-rich Logrosán granite was formed in the collisional orogenic scenario which characterizes the Variscan orogeny, and intruded at post-orogenic time. U–Pb zircon analyses yield a concordia age of 307.88 ± 0.86 Ma which is considered the age of the emplacement of the Logrosán granite, coeval with other post-Variscan granites of the Central Iberian Zone. The Logrosán granite was emplaced at epizonal P-T conditions (P: 1-2 kbar; T: 650-700 ºC). The Ti-in-zircon thermometry (836 ºC) and Zr melt saturation temperatures (700-780 ºC) provide an estimated temperature for the parental magma at liquidus to solidus conditions. The phosphorous-rich and fluxed element-rich (B-F-Li) magma increases the solubility of H_2O in the melt, and decreases the solidus magma temperature, thus allowing to reach shallower depths and increasing the fractionation degree in a relatively extended time toward solidus conditions. This process also favors the concentration of incompatible elements (e.g., Sn, Nb, Ta, W) in the residual melt.

The Logrosán Sn-(W) ore deposits are hosted in two different sectors, the Cerro de San Cristóbal and El Serranillo, within granitic and metasedimentary rocks, respectively. Gravity modeling has

revealed the extension of the Logrosán granite at shallow depth throughout the area of the El Serranillo, allowing subsurface interpretation of both ore deposits and unraveling that both mineralization processes could be caused by a single granite body. Tin mineralization in the Logrosán deposits occurs as disseminated and vein-type ores in endo- and exogranitic locations. The host-rocks are tourmalinized, muscovitized, greisenized, and lately silificied and kaolinized. The ore assemblage of the Sn-(W) Logrosán ores comprises mainly cassiterite and, in a lesser degree, Nb-Ta phases (columbite and Nb-Ta rutile); the occurrence of W-bearing minerals is of minor importance. Textural and compositional features (e.g., compositional zonation of Nb-Ta phases) suggest the participation of late-magmatic residual fluid-rich melts, interacting with different hydrothermal fluids through the mineralization. The paragenetic sequence suggests that the fluid saturated first with Nb-Ta, and later with Sn.

The granite massif operated as a thermal focus during the emplacement and crystallization at very shallow depths, affecting the surrounding rocks, the Schist Greywacke Complex metasediments. This thermal perturbation might have generated a geothermal and fluid gradients in the inner aureole around the pluton during cooling. Then, it is considered that convective cells mobilized fluids from the metasedimentary host-rocks, which eventually penetrate into the granite body, being enriched in metals. A first boron metasomatic stage is represented by pervasive tourmalinization of the granite and the nearby SGC metasediments, especially in the contact zones between them; and multiple barren quartz-tourmaline veins and veinlets without dominant strikes. This is typical of B-rich magmas and B-rich greisen-like ore deposits, where the fracturing processes are abundant due to the high volatile content of magmas. The degassing of the residual melts produced higher fluid overpressures, therefore, the gradual increase of pressure combined with cooling and contraction of the roof rock and crystallization of the magma resulted in focusing of the ore fluids and more effective fracturing. The Sn^{2+} (complexed with Cl^- or, more likely, F^-) were carried by the highly reduced metamorphic-derived fluids, with N_2-CH_4 aqueous composition. Stable isotopes and fluid inclusion studies provide constraints of the metamorphic fluid origin. The drop of pressure owing to the N30 fracturing, the mixing between metamorphic and magmatic fluids, and an increase of the oxygen fugacity disturbed these complexes and the cassiterite precipitated. The mixing of metamorphic-derived and magmatic fluids is suggested by the introduction of CO_2 in the system and the wide variability of H_2O-N_2-CH_4-CO_2 proportions. The following sulfide deposition was due to an effervescence process (phase-separation). The P-T conditions of the Logrosán ore deposits are set approximately at 460-540 ºC and 120-270 MPa for the Oxide Stage; and at 320-460 ºC and 30-160 MPa for the Sulfide Stage.

The Logrosán granite emplacement timing (at ca. 308 Ma) and the Ar-Ar dating of muscovite coexisting with cassiterite indicate that the mineralization started almost contemporaneously to

the granite emplacement. The precipitation of cassiterite in the Logrosán ore deposits was probably caused by late-magmatic and metamorphic fluid mixing in an open system, in at least, two different mineralization pulses (~308-306 Ma endogranitic, and ~303 Ma for the exogranitic stage).

Gravity data modeling of the Logrosán granite suggests a mushroom shaped body elongated by ~12 km in the W-E direction and ~7 km along the N-S axis. The thickness of the uppermost part of the granite ranges from 2 to 2.5 km. The integration of gravity data with extrapolated geological information and alteration patterns allows a much better definition of potential targets for hidden Sn-(W) ore deposits in the Logrosán ore field, and for equivalent scenarios throughout the Variscan belt. In this regard: (i) whenever a consistent metamorphic contact aureole extends far beyond what should be expected by the size of the granite outcrop, search for a flat-shaped granite at shallow depth; and (ii) if the right alteration patterns are present on the surface (at least some evidence of these mineralogical units, e.g., tourmalinization, greisenization, etc.), then Sn-(W) deposits may be present in the hidden contacts between the granite sill-like intrusions and the host-rock.

Hydrothermal quartz-apatite veins of La Costanaza (Logrosán) are the main example of a distinctive type of phosphate ore deposits occurring exclusively in the southern Central Iberian Zone within the European Variscan Belt. Hydrothermal (of the quartz-apatite veins, H-apatite) and magmatic apatites (of the granite, M-apatite) show markedly different chemical compositions. The Sr-rich character of H-apatite is expected to be inherited from the protolith: phosphate and carbonate levels within the Neoproterozoic metasediments. A post-Variscan long lasting hydrothermal activity (probably during Mesozoic times) is in agreement with the fluid inclusion, isotopic results and the chemical evolution of the REE of the hydrothermal apatite. Extensive fluid circulation would have taken place along extension faults, breccias and stockworks, mostly interacting with phosphate and carbonate beds of the Neoproterozoic Schist-Greywacke Complex. Mineral precipitation was then controlled by cooling and dilution of aqueous low-salinity fluids allowing the formation of the quartz-apatite ores.

Contributions to original knowledge

Granite

During the last two decades, U-Pb zircon geochronology has been applied to different granite plutons of the Iberian Belt (e.g., Dias et al., 1998; Fernández-Suárez et al., 2000). Much more

recently, combined micro-analytical U-Pb and Lu-Hf isotope systematics on zircon grains have been used to identify source components and to constrain the age of heterogeneous inheritances incorporated in the granite genesis. This integrated isotope information contributed significantly to the discussions about the origin of the Central Iberian granites (e.g., Teixera et al., 2011; Villaseca et al., 2012). Other batholiths of this southern part of the CIZ have been dated by U-Pb zircon or monazite geochronology (Castelo Branco: Antunes et al., 2008; Cabeza de Araya: Gutiérrez-Alonso et al., 2011; Nisa-Alburquerque: Solá et al., 2009; Montes de Toledo: Orejana et al., 2012). However, none of them were studied by the combined U-Pb and Hf-isotope approach as in the work of Logrosán by Chicharro et al. (2014), developed in this PhD dissertation (Chapter 3), although the same approach was also applied by Merino (2014) and Merino et al. (2014) in the Montes de Toledo batholith. Moreover, the combination of zircon U–Pb CA-ID-TIMS and LA-ICP-MS geochronology in the Logrosán granite is used to better constrain the age of the granite emplacement and of the inherited zircons. These data together with the Hf-isotope study allow a better understanding of the nature of the parental material involved in the granitic magmas.

Sn-W ore deposits

There are multiple studies about the granite-related Sn-W ore deposits, of which the reviews of Lehman (1990) are probably the best known ones. Nevertheless, there are some aspects which remain unclear, such as the concentration of ore metals via magmatic or hydrothermal processes, the source of metal-bearing fluids, and the mechanisms for ore deposition. The present PhD dissertation provide new geochemical, geochronological, fluid inclusion and isotopic data to better constrain the relationship and timing of the late-magmatic and hydrothermal systems from the Logrosán granite Sn-(W) ore deposits. Among the main achievements and important contributions, the following should be considered:

- The Logrosán Sn-(W) ore deposits have a very complex fluid inclusion system (H_2O-N_2-CH_4-CO_2-NaCl) with low salinity and vapor-dominated later phases, apparently not described in any other Sn-W ore deposit (or other kind of ore deposit) before.
- The combination of the granite U-Pb geochronology and the Ar-Ar dating of muscovite allows determining the timing of the ore precipitation with respect to the granite emplacement. Since there are endo- and exogranitic ores, the evolution of the hydrothermal event may be further evaluated and understood.
- The comparison of geochemistry of fresh and altered (e.g., greisenized, muscovitized, sericitized) granites, and the study of the alteration (mainly muscovitization and

tourmalinization) provide further constraints on the magmatic-metasomatic-hydrothermal transition processes and its relationship with the ore deposition.

- This is one of the very few Sn-(W) granite-related ore deposits where the nature and sources of metal-rich-fluids is strongly constrained by the composition of fluid inclusions and isotope studies.
- A gravity survey has been accomplished to understand the shape of the granite in depth. This gravity profile combined with geological and field observations allows interpreting a global metallogenic modeling, including the identification of targets and unexposed bodies. This simple method may be extrapolated as an exploration tool to other granite-related ore deposits.

Hydrothermal phosphate ore deposits

The knowledge about hydrothermal phosphate ore deposits is almost inexistent, in part because this kind of mineralization is unique of the Central Iberian Zone. The La Costanaza mine in Logrosán constitutes the most important hydrothermal phosphate ore in Europe. For this reason, a research focused on this topic was undertook in the work of Vindel et al. (2014) and is expanded in this PhD dissertation. Besides the Logrosán P ores, other Iberian-type hydrothermal quartz-apatite veins have been considered for discussion, such as Belvís de Monroy and Navalmoral de la Mata, as well as the phosphorite occurrences of sedimentary origin in the upper part of the regional Schist-Greywacke Complex. The aims and achieving results in this field are:

- A new description of the main features of hydrothermal quartz-apatite vein deposits.
- The first major and trace chemical data of these hydrothermal ores, which are especially useful to gather information about the source of these elements.
- A comparative study of the apatite chemistry from the veins (hydrothermal) with the possible sources: apatite from related granites (magmatic) and apatite from the Neoproterozoic metasediments (sedimentary).
- The first temperature condition approach of apatite hydrothermal formation based on arsenopyrite geothermometry.
- The first hydrothermal system evaluation through fluid inclusion measurements.
- A compilation of information on possible sources of the mineralizing fluids and protoliths involved through stable isotope analysis.
- After the obtained results, new ideas about the origin of the hydrothermal phosphate mineralization are proposed and opened to discussion.

Suggestions for future works

The lines of investigation calling for further research in the Logrosán ore deposits that are applicable to the general knowledge of Sn-W ore deposits, or to phosphate hydrothermal ores are:

- A trace and rare-element study of cassiterite and Nb-Ta phases might help to better understand the ore-forming fluid origin of the Logrosán Sn-(W) ore deposits.
- U-Pb cassiterite geochronology could be undertaken in order to have a most effective approach for the determination of the timing of Sn-W mineralization events.
- The revision of other Sn-W ore deposits, especially the study of fluid inclusions in the Central Iberian Zone Sn-W ore deposits, would be desirable. The metamorphic origin of fluids found in the Logrosán granite might be corroborated by other similar tin-fertile granites, such as Trujillo or Montánchez.
- The study of Cu-Pb-Zn targets nearby the Logrosán granite, to better define and characterize a possible metal zoning pattern around granite bodies, described in Cornwall and elsewhere for Sn–W and Cu deposits.
- The importance of the "Iberian-type" phosphate hydrothermal veins merits future detailed research, by studying other locations in the Central Iberian Zone. Moreover, an accurate geochronological work (Lu-Hf in apatite separates?) would be highly required to prove or deny the possible relationship of this mineralization and the nearby granites.

CONCLUSIONES FINALES

Conclusiones

La cúpula de Logrosán consiste en un granito félsico, muy fraccionado, perfosfórico, fuertemente peralumínico (ASI = 1.2 - 2) y muy rico en estaño (Sn = 11 - 67 ppm). A partir de los datos cartográficos, petrográficos y geoquímicos se distinguen dos unidades plutónicas: (i) un monzogranito de grano medio-grueso (Unidad Principal – Main Unit) que ocupa la mayor extensión del granito aflorante; y (ii) varios cuerpos leucograníticos más fraccionados (Unidades Evolucionadas – Evolved Units), principalmente concentrados en las partes topográficamente más altas del plutón. La geoquímica de roca total indica que un proceso simple de cristalización fraccionada no dio origen a la diversidad granítica encontrada en el plutón de Logrosán. En su lugar, las complejas líneas de variabilidad química que exhiben componentes como el Sr, Ba, Rb, Eu y CaO se ajustan más a la posibilidad de que los responsables de la formación de las distintas Unidades plutónicas fueran inyecciones pene-contemporáneas de distintos magmas félsicos procedentes de una cámara magmática profunda. En este sentido, las grandes divergencias en las relaciones iniciales de $^{87}Sr/^{86}Sr$ y la composición de los isótopos de Hf en circones separados refuerzan la idea de que varios magmas de distinta composición isotópica fueran inyectados en distintos pulsos muy próximos en el tiempo.

La integración de la geoquímica de roca total y de las signaturas isotópicas de O, Sr, Nd y Hf permite interpretar que el granito de Logrosán es el resultado de la fusión parcial de materiales metasedimentarios heterogéneos. La ausencia de enclaves máficos, y las variaciones de los datos de $^{87}Sr/^{86}Sr$ y unos valores casi constantes de εNd (en un rango muy poco negativo: -4.0 a -4.3) excluyen la participación de magmas de derivación mantélica en el origen de estos magmas graníticos. Las herencias en circones (en su mayoría de edad neoproterozoica) combinadas con la naturaleza metasedimentaria del supuesto protolito, así como la similitud en relaciones isotópicas iniciales de los sistemas de Sr y Nd entre las metagrauvacas de los metasedimentos neoproterozoicos y del granito, permiten concluir que el Complejo Esquisto Grauváquico es la fuente metasedimentaria más viable para la formación de los magmas que originaron el plutón de Logrosán.

El granito estannífero de Logrosán se formó en un contexto orogénico de tipo colisión continente-continente (orogenia Varisca) y se emplazó en tiempos post-orogénicos. La geocronología U-Pb en circón da una edad de concordia de 307.88 ± 0.86 Ma, que es considerada como la edad del emplazamiento del granito. Esta edad es contemporánea a la de otros granitos post-variscos de la Zona Centro Ibérica. El granito de Logrosán se emplazó en condiciones epizonales (P: 1-2 kbar; T: 650-700 ºC). La termometría en base al Ti en circones (836 ºC) y las temperaturas de saturación

en Zr del granito (700-780 ºC) son consideradas como temperaturas del magma parental en condiciones de *líquidus* a *sólidus*. Los elementos fluyentes tipo B, F o Li, y la presencia de fósforo en el magma hacen que la solubilidad del H_2O se incremente en el fundido residual. También hacen disminuir la temperatura del *sólidus* granítico, de esta manera, el magma puede alcanzar profundidades más someras y el grado de fraccionamiento se intensifica al disponer de un periodo de tiempo relativamente más prolongado para terminar de cristalizar. Además, este proceso favorece la concentración de elementos incompatibles (e.g., Sn, Nb, Ta, W) en el fundido residual.

Los yacimientos de Sn-(W) de Logrosán se localizan en dos sectores diferentes, el Cerro de San Cristóbal y El Serranillo, en el granito y en el encajante de rocas metasedimentarias, respectivamente. El modelado gravimétrico revela que el granito de Logrosán se extiende a poca profundidad hacia el sector de El Serranillo (al NE), indicando que ambos procesos de mineralización están ligados a un mismo cuerpo granítico. La mineralización de Sn de Logrosán se presenta como diseminaciones y filones de tipo stockwork en emplazamientos intra- y extragraníticos. Las rocas encajantes han sido afectadas por varios tipos de alteraciones, entre ellas, turmalinización, moscovitización y greisenización, y posteriormente por silicificación y caolinización. La asociación mineral de los yacimientos de Sn-(W) de Logrosán comprende principalmente casiterita y, en menor grado, fases minerales de Nb-Ta (columbita y rutilo rico en Nb-Ta, o ilmenorutilo); mientras que la presencia de minerales de W es casi irrelevante. Existen evidencias de la posible implicación de procesos tardi-magmáticos en las características texturales y composicionales observadas en las fases de Nb-Ta (e.g., zonados composicionales); éstas habrían sido posteriormente modificadas por sucesivos fluidos hidrotermales. La secuencia paragenética además sugiere que el fluido portador de los metales se saturó en primer lugar en Nb-Ta y, posteriormente, en Sn.

El granito de Logrosán actuó como una fuente térmica durante su emplazamiento y consolidación a profundidades muy someras, provocando la generación de células convectivas en las rocas circundantes, los metasedimentos del Complejo Esquisto Grauváquico. De esta manera, se propone que los fluidos procedentes del metamórfico fueron movilizados y penetraron en el granito enriqueciéndose en metales. Un estadio temprano de metasomatismo de boro se representa por la intensa turmalinización del granito y de los metasedimentos, principalmente en el contacto entre ambos; y por múltiples filones y filoncillos de cuarzo-turmalina sin direcciones preferentes. Esto es típico de un magma rico en B y de depósitos tipo greisen dominantes en boro, donde los procesos de fracturación son abundantes debido al alto contenido en volátiles del magma. La liberación de los gases de los fundidos residuales produjo mayores presiones confinantes, por lo tanto, un incremento gradual de la presión combinado con un enfriamiento y contracción del techo

de la cúpula granítica permitieron la focalización de los fluidos mineralizantes y una fracturación más efectiva. El Sn^{2+} (en complejos con Cl^- o, más probablemente, con F^-) pudo ser movilizado por los fluidos de condiciones muy reductoras y con composiciones acuoso-volátiles de tipo N_2-CH_4. Los estudios de isótopos estables y de inclusiones fluidas sugieren un origen metamórfico para estos fluidos mineralizantes. Al formarse las fracturas N30 se produjo una caída de presión, los fluidos de origen metamórfico y magmático se mezclaron y hubo un incremento en la fugacidad del oxígeno. En consecuencia, los complejos estanníferos se desestabilizaron y la casiterita precipitó. La participación de un fluido de origen magmático se asume por la introducción de CO_2 en el sistema y por la amplia variabilidad en las proporciones de H_2O-N_2-CH_4-CO_2. La precipitación del próximo estadio de la mineralización, es decir, la de los sulfuros se debió a procesos de efervescencia (separación de fases). Las condiciones P-T de los yacimientos de Logrosán están establecidas aproximadamente a 460-540 ºC y 120-270 MPa para el Estadio Oxidado; y a 320-460 ºC y 30-160 MPa para el Estadio Sulfurado.

La edad de emplazamiento del granito (hace ca. 308 Ma) y la datación Ar-Ar de moscovitas coexistentes con casiterita indican que la mineralización se inició casi contemporáneamente al emplazamiento del granito. La precipitación de la casiterita en los yacimientos de Logrosán fue probablemente causada por la mezcla de fluidos tardi-magmáticos y metamórficos en, al menos, dos pulsos mineralizantes distintos (~308-306 Ma de carácter intragranítico y ~303 Ma para el estadio extragranítico).

El modelado gravimétrico del granito de Logrosán sugiere que se trata de un cuerpo setiforme achatado, de unos 12 km en la dirección W-E y unos 7 km a lo largo del eje N-S. El espesor de la parte superior del granito está estimado entre 2 y 2.5 km. La integración de los datos gravimétricos con la información geológica y las pautas de alteración permiten la definición de indicios mineros potenciales tanto en las inmediaciones de Logrosán, como por extrapolación en otros escenarios del cinturón Varisco. En este sentido: (i) cuando una aureola de metamorfismo de contacto se extiende considerablemente con respecto a las dimensiones del granito aflorante, probablemente el granito sea de mucha mayor envergadura y presente una forma achatada en profundidad; y (ii) si las pautas de alteración adecuadas se observan en superficie (o al menos algunas evidencias de las mismas: turmalinizaciones, greisen, etc.), entonces es esperable encontrar concentraciones de Sn-(W) a profundidades muy someras, o incluso en superficie, localizadas entre la intrusión del granito no aflorante y las rocas encajantes.

Los filones hidrotermales de cuarzo-apatito de La Costanaza (Logrosán) constituyen el ejemplo principal de un tipo distintivo de yacimientos de fosfato localizados exclusivamente en el sur de la Zona Centro Ibérica dentro del cinturón varisco europeo. Los apatitos hidrotermales (de los

filones de cuarzo-apatito, H-apatito) y magmáticos (M-apatito) muestran diferencias composicionales marcadas, lo cual induce a desligar el origen de los fosfatos hidrotermales del magmatismo varisco. Las altas concentraciones de Sr del H-apatito son probablemente un reflejo de la herencia de los niveles fosfatados y carbonatados de los metasedimentos neoproterozoicos. Una actividad hidrotermal de larga duración (tal vez durante el Mesozoico) es consistente con los resultados isotópicos, de inclusiones fluidas y con la evolución química de elementos de tierras raras del apatito filoniano. Esta actividad hidrotermal post-varisca habría tenido lugar a lo largo de fallas, brechas y stockworks, principalmente interaccionando con los niveles fosfatados y carbonatados presentes en las rocas metasedimentarias del Complejo Esquisto Grauváquico. El control de la precipitación mineral se relaciona con procesos de enfriamiento y dilución de fluidos acuosos de baja salinidad que dieron lugar a la formación de los yacimientos de cuarzo-apatito.

Nuevas contribuciones al conocimiento

Granito

Durante las últimas dos décadas, la geocronología de U-Pb se ha aplicado en diferentes plutones graníticos del Cinturón Ibérico (e.g., Dias et al., 1998; Fernández-Suárez et al., 2000). Recientemente, se ha aplicado también la sistemática isotópica de U-Pb y Lu-Hf en granos de circón para identificar los componentes fuente y precisar la edad de los circones xenolíticos incorporados en la génesis de los granitos. Esta información integrada ha contribuido de manera significativa a la discusión sobre el origen de los granitos de la Zona Centro Ibérica (e.g., Teixera et al., 2011; Villaseca et al., 2012). Otros batolitos del sur de la Zona Centro Ibérica también han sido datados por geocronología U-Pb en circón o monacita (Castelo Branco: Antunes et al., 2008; Cabeza de Araya: Gutiérrez-Alonso et al., 2011; Nisa-Alburquerque: Solá et al., 2009; Montes de Toledo: Orejana et al. 2012). Sin embargo, ninguno de ellos había sido estudiado mediante el enfoque combinado de U-Pb e isótopos de Hf en circones, como se lleva a cabo en el trabajo de Logrosán de Chicharro et al. (2014), desarrollado en esta Tesis Doctoral. Este enfoque ha sido aplicado paralelamente en el batolito de los Montes de Toledo por Merino et al. (2014) y Merino (2014). Además, la combinación de geocronología U-Pb CA-ID-TIMS y LA-ICP-MS en circón ha sido usada en el granito de Logrosán para precisar mejor la edad de emplazamiento del granito y la edad de los circones heredados. Estos datos junto con los isótopos de Hf en circón permiten comprender mejor la naturaleza del material parental involucrado en el origen de los magmas graníticos.

Yacimientos de Sn-W

Existen múltiples estudios sobre los granitos asociados a mineralizaciones de Sn-W, de los cuales quizá el más conocido sea la síntesis de Lehman (1990). Sin embargo, hay algunos aspectos que aún no se conocen con exactitud, tales como la concentración de los metales vía procesos magmáticos o hidrotermales, la fuente de los fluidos portadores de metales y los mecanismos de precipitación mineral. La presente Tesis Doctoral aporta nuevos datos geoquímicos, geocronológicos, de inclusiones fluidas e isotópicos para definir y ajustar mejor las relaciones genéticas y temporales de los sistemas tardi-magmáticos e hidrotermales en los yacimientos de Sn-(W), como es el de Logrosán. Entre los principales resultados, los siguientes debieran ser considerados:

- Los yacimientos de Sn-(W) de Logrosán presentan un sistema muy complejo de inclusiones fluidas (H_2O-N_2-CH_4-CO_2-NaCl) de baja salinidad con fases tardías vapor-dominantes, que aparentemente no ha sido descrito en ningún otro yacimiento de Sn-W (o de otro tipo) con anterioridad.
- La combinación de la geocronología de U-Pb en el granito y de Ar-Ar en moscovita permite determinar con precisión la relación temporal entre la precipitación mineral y el emplazamiento del granito. Puesto que además el yacimento tiene manifestaciones tanto endo- como exograníticas, la evolución hidrotermal puede ser evaluada y comprendida en detalle.
- La comparación de la geoquímica entre granitos frescos y alterados (e.g., greisenizados, moscovitizados, sericitizados...) y el estudio de la alteración (moscovitización y turmalinización, principalmente) supone un mayor entendimiento de los procesos de transición magmáticos, metasomáticos e hidrotermales y de su relación con la precipitación mineral.
- Este es uno de los pocos yacimientos de Sn-(W) asociados a granitos donde la naturaleza y las fuentes de los fluidos portadores de los metales pueden deducirse con bastante claridad a partir de los estudios isotópicos y de inclusiones fluidas.
- Esta Tesis Doctoral incluye un estudio gravimétrico para definir la forma y extensión del granito en profundidad. El perfil gravimétrico combinado con las observaciones geológicas permite interpretar un modelo global metalogénico, que incluye la identificación de indicios y de granitos no aflorantes. Este sencillo método puede ser extrapolado como herramienta de exploración a cualquier otro escenario en el cual existan yacimientos asociados a granitos.

Yacimientos hidrotermales de fosfato

El conocimiento sobre los yacimientos hidrotermales de fosfato es casi inexistente, en parte porque este tipo de mineralización es exclusiva de la Zona Centro Ibérica. La mina de La Costanaza constituye el yacimiento de fosfato mineral más importante en Europa. Por esta razón, se realizó una investigación centrada en este tema en el trabajo de Vindel et al. (2014) que es desarrollada en esta Tesis Doctoral. Además de los yacimientos de fósforo de Logrosán, otros filones de cuarzo-apatito han sido considerados en la discusión, tales como los de Belvís de Monroy y Navalmoral de la Mata. Y también se han considerado las concentraciones fosfatadas de origen sedimentario (fosforita) presentes en el Complejo Esquisto Grauváquico. Los objetivos y resultados que se aportan en este campo son:

- Una nueva descripción de las principales características de los depósitos hidrotermales de cuarzo-apatito.
- Las primeros datos de elementos mayores y trazas de estas mineralizaciones, lo que es especialmente útil para deducir la posible fuente de estos elementos.
- Un estudio comparativo de la química del apatito de los filones (hidrotermal) con los apatitos de las posibles fuentes: apatito de los granitos asociados (magmático) y apatito de los metasedimentos neoproterozoicos (sedimentario).
- La primera aproximación a las condiciones de temperatura de la formación del apatito hidrotermal basado en el geotermómetro de la arsenopirita.
- Una compilación de información sobre las posibles fuentes de los fluidos mineralizantes y los protolitos a través de un estudio isotópico.
- A partir de los resultados obtenidos se plantea una nueva visión sobre el origen de esta mineralización que queda abierta a discusión.

Sugerencias para trabajos futuros

Las líneas de investigación que precisan más atención en cuanto a los yacimientos de Logrosán y que pueden ser aplicables al conocimiento general de otros yacimientos de Sn-W o de P son:

- Un estudio de la química mineral de elementos traza (incluyendo elementos del grupo de las tierras raras) en la casiterita y en las fases minerales de Nb-Ta podría ayudar a entender mejor el origen de los fluidos mineralizadores en los yacimientos de Sn-(W) de Logrosán.

- La geocronología de U-Pb en casiterita podría ser aplicada para obtener edades aún más precisas y determinar con mayor exactitud la evolución de los eventos de mineralización del Sn-W
- La revisión de otros yacimientos de Sn-W, especialmente el estudio de inclusiones fluidas en depósitos de Sn-W de la Zona Centro Ibérica, sería conveniente. El origen metamórfico de los fluidos estudiados en Logrosán podría ser corroborado en otros granitos estanníferos similares, como el de Trujillo o el de Montánchez.
- El estudio de los indicios de Cu-Pb-Zn en las proximidades del granito de Logrosán podría ser útil para caracterizar la muy probable zonación previamente descrita en Cornwall, y en otros lugares, en relación a los yacimientos perigraníticos de Sn-W-Cu.
- La importancia de los filones hidrotermales de cuarzo-apatito de "tipo Ibérico" merece una investigación futura detallada, en primer lugar con el estudio de otras localizaciones en la Zona Centro Ibérica. Además, un trabajo geocronológico (tal vez Lu-Hf en apatitos separados) sería altamente requerido para confirmar o negar la relación de este tipo de mineralización con los granitos adyacentes.

REFERENCES

Ábalos, A., Carreras, J., Druguet, E., Escuder, J., Gómez Pugnaire, M.T., Lorenzo, S., 2002. Variscan and Pre-Variscan Tectonics. In: Gibbons, W. and Moreno, M.T. (Eds.), The Geology of Spain. Geological Society of London, London, pp. 155–183.

Ábalos, B., Gil Ibarguchi, J.I., Sánchez-Lorda, M.E., Paquette, J.L., 2012. African/Amazonian Proterozoic correlations of Iberia: A detrital zircon U-Pb study of early Cambrian conglomerates from the Sierra de la Demanda (northern Spain). Tectonics 31, TC3003. doi:10.1029/2011TC003041.

Abdel-Rahman, A.F.M., 1994. Nature of biotites from alkaline, calc-alkaline, and peraluminous magmas. Journal of petrology 35, 525-541. doi:10.1093/petrology/35.2.525

Abella, P.A., Corbella, M., Melgarejo, J.C., 1995. Nb-Ta- minerals from the Cap de Creus pegmatite field, eastern Pyrenees: distribution and geochemical trends. Mineralogy and Petrology 55, 53-69. doi:10.1007/BF01162579

Adams, W., 2015. Overview of the Tin Market in 2015. http://www.fastmarkets.com/

Aizpurúa, J., Gumiel, P., Pineda, A., 1982. Introducción al estudio de los yacimientos de fosfatos del Macizo Ibérico meridional. Boletín Geológico y Minero 93: 390-414.

Alderton, D.H.M., Harmon, R.S., 1991. Fluid inclusion and stable isotope evidence for the origin of mineralizing fluids in south-west England. Mineralogical Magazine 55, 605-611. doi:10.1180/minmag.1991.055.381.13

Allan, J. R., Wiggins, W.D., 1993. Dolomite reservoirs: Geochemical techniques for evaluating origin and distribution. Amerrican Association of Petroleum Geologists 36, 129 pp.

Alonso Olazábal, A., 2001. El Plutón de Campanario - La Haba: Caracterización petrológica y fábrica magnética, PhD Thesis. Universidad del País Vasco, 322 pp.

Améglio, L., Vigneresse, J.L., Bouchez, J.L., 1997. Granite pluton geometry and emplacement mode inferred from combined fabric and gravity data. In: Bouchez, J.L. Hutton, D.H.W. Stephens, W.E. (Eds.), Granite: From Segregation of Melt to Emplacement Fabrics. Kluwer, Dordrecht, pp. 199–214.

Ancochea, E., Huertas, M.J., Ibarrola, E., Snelling, N., 1992. Diques basálticos en las proximidades de Orense. Evidencia de actividad magmática Cretácica en el noroeste de la península Ibérica. Revista de la Sociedad Geológica de España 5, 65-71.

Andersen, T., Griffin, W., Pearson, N., 2002. Crustal evolution in the SW part of the Baltic Shield: the Hf isotope evidence. Journal of Petrology 43, 1725-1747. doi:10.1093/petrology/43.9.1725

Andrews, P., 2014. Craig Meredith and the San Cristóbal Hill. XV Congreso Internacional sobre Patrimonio Geológico y Minero – XIX Sesión Científica de la SEDPGYM, Resúmenes.

Antunes, I., Neiva, A., Silva, M., Corfu, F., 2008. Geochemistry of S-type granitic rocks from the reversely zoned Castelo Branco pluton (central Portugal). Lithos 103, 445-465. doi:10.1016/j.lithos.2007.10.003

Antunes, I.M.H.R., Neiva, A.M.R., Silva, M.M.V.G., 2010. Isotopic geochronology of granitic rocks from the Central Iberian Zone: comparison of methodologies. Estudios Geológicos 66, 45-50. doi:10.3989/egeol.40143.097

Azor, A., Rubatto, D., Simancas, J.F., González Lodeiro, F., Martínez Poyatos, D., Martín Parra, L.M., Matas, J., 2008 Rheic Ocean ophiolitic remnants in southern Iberia questioned by SHRIMP U-Pb zircon ages on the Beja-Acebuches amphibolites. Tectonics 27, TC5006. doi: 10.1029/2008TC002306

Bakker, R.J., 2003. Package FLUIDS 1. Computer programs for analysis of fluid inclusion data and for modelling bulk fluid properties. Chemical Geology 194, 3-23. doi:10.1016/S0009-2541(02)00268-1

Ballèvre, M., Paris, F., Robardet, M., 1992. Corrélations ibéro-armoricaines au Paléozoïque: une confrontation des données paléobiogéographiques et tectonométamorphiques. Comptes rendus de l'Académie des sciences. Série 2, Mécanique, Physique, Chimie, Sciences de l'univers, Sciences de la Terre 315, 1783-1789.

Ballèvre, M., Bosse, V., Ducassou, C., Pitra, P., 2009. Palaeozoic history of the Armorican Massif: models for the tectonic evolution of the suture zones. Comptes Rendus Geoscience 341, 174-201. doi:10.1016/j.crte.2008.11.009

Barbero, L., Villaseca, C., 2000. Eclogite facies relics in metabasites Sierra de Guadarrama (Spanish Central System): PT estimations and implications for from the the Hercynian evolution. Mineralogical Magazine 64, 815-836. doi:10.1180/002646100549814

Barbero, L., Glasmacher, U.A., Villaseca, C., López-García, J.A., Martín-Romera, C. 2005. Long-term thermo-tectonic evolution of the Montes de Toledo area (Central Hercynian Belt, Spain): constraints from apatite fission-track analysis. International Journal of Earth Sciences 94, 193-203. doi:10.1007/s00531-004-0455-y

Barbey, P., Gasquet, D., Pin, C., Bourgeix, A.L., 2008. Igneous banding, schlieren and mafic enclaves in calc-alkaline granites: the Budduso pluton (Sardinia). Lithos 104, 147-163. doi:10.1016/j.lithos.2007.12.004

Bea, F., Pereira, M.D., Corretgé, L.G., Fershtater, G.B., 1994. Differentiation of strongly peraluminous, perphosphorus granites: the Pedrobernardo pluton, central Spain. Geochimica et Cosmochimica Acta 58, 2609-2627. doi:10.1016/0016-7037(94)90132-5

Bea, F., Montero, P., Molina, J.F., 1999. Mafic precursors, peraluminous granitoids, and late lamprophyres in the Avila batholith: a model for the generation of Variscan batholiths in Iberia. The Journal of geology 107, 399-419. doi:10.1086/314356

Bea, F., Montero, P., Zinger, T., 2003. The nature, origin, and thermal influence of the granite source layer of Central Iberia. The Journal of Geology 111, 579-595. doi:10.1086/376767

Bea, F., Montero, P., González-Lodeiro, F., Talavera, C., 2007. Zircon inheritance reveals exceptionally fast crustal magma generation processes in Central Iberia during the Cambro-Ordovician. Journal of Petrology 48, 2327-2339. doi:10.1093/petrology/egm061

Bea, F., Pesquera, A., González, P., Torres-Ruiz, J., Gil-Crespo, P.P., 2009. Tourmaline $^{40}Ar/^{39}Ar$ chronology of tourmaline-rich rocks from Central Iberia dates the main Variscan deformation phases. Geologica Acta 7, 399-412 doi:10.1344/104.000001446

Bea, F., Montero, P., Talavera, C., Abu Anbar, M., Scarrow, J. H., Molina, J. F., Moreno, J. A., 2010. The palaeogeographic position of Central Iberia in Gondwana during the Ordovician: evidence from zircon chronology and Nd isotopes. Terra Nova 22, 341-346. doi:10.1111/j.1365-3121.2010.00957.x

Beer, K.E., Burley, A.J., Tombs, J.M., 1975. The concealed granite roof in south-west Cornwall. Mineral Reconnaisance Programme Report. Institute Geological Sciences, London. 16 pp. (Unpubl).

Beetsma, J.J., 1995. The late Proterozoic/Paleozoic and Hercynian crustal evolution of the Iberian Massif, N Portugal, as traced by geochemistry and Sr-Nd-Pb isotope systematics of pre-Hercynian terrigenous sediments and Hercynian granitoids. PhD Thesis, Vrije Universiteit, Amsterdam, 223 pp.

Belousova, E., Griffin, W.L., O'Reilly, S.Y., Fisher, N., 2002. Igneous zircon: trace element composition as an indicator of source rock type. Contributions to Mineralogy and Petrology 143, 602-622. doi:10.1007/s00410-002-0364-7

Benn, K., Ham, N.M., Pignotta, G. S., Bleeker, W. 1998. Emplacement and deformation of granites during transpression–Magnetic fabrics of the Archean Sparow pluton, Slave Province, Canada. Journal of Structural Geology 20, 1247–1259. doi:10.1016/S0191-8141(98)00065-0

Beurlen, H., Da Silva, M.R., Thomas, R., Soares, D.R., Olivier, P., 2008. Nb–Ta–(Ti–Sn) oxide mineral chemistry as tracer of rare-element granitic pegmatite fractionation in the Borborema Province, Northeastern Brazil. Mineralium Deposita 43, 207-228. doi:10.1007/s00126-007-0152-4

Billinton Española S.A., 1982. Estudio geológico del Cerro San Cristóbal (Logrosán). Internal report.

Black, L., Gulson, B., 1978. The age of the mud tank carbonatite, strangways range, northern territory. BMR Journal of Australian Geology and Geophysics 3, 227-232.

Bodnar, T.S., 1993. Revised equation and table for determining the freezing point depression of H_2O–NaCl solutions. Geochimica et Cosmochimica Acta 57, 683-684. doi: 10.1016/0016-7037(93)90378-A

Boixereu, E., 2003. Historia y patrimonio minero de Logrosán (Cáceres). La mina de fosforita de La Costanaza. Cuadernos del Museo Geominero 2, 169-176.

Boixereu E., 2004. Mina de fosfato de Logrosán, Cáceres. Tierra y Tecnología 26, 26-34.

Borthwick, J., Harmon, R.S., 1982. A note regarding CIF_3 as an alternative to BrF_5 for oxygen isotope analysis. Geochimica et Cosmochimica Acta 46, 1665-1668. doi:10.1016/0016-7037(82)90321-0

Bottinga, Y., Javoy, M., 1975. Oxygen isotope partitioning among the minerals in igneous and metamorphic rocks. Reviews of Geophysics 13, 401-418. doi:10.1029/RG013i002p00401

Bouvier, A., Vervoort, J.D., Patchett, P.J., 2008. The Lu–Hf and Sm–Nd isotopic composition of CHUR: constraints from unequilibrated chondrites and implications for the bulk composition of terrestrial planets. Earth and Planetary Science Letters 273, 48-57. doi:10.1016/j.epsl.2008.06.010

Bowles, G., 1789. lntroducción a la Historia Natural y a la Geografía Física de España. Imprenta Real. Madrid. 534 pp.

Breaks, F.W., Moore, J.M., 1992. The Ghost Lake Batholith, Superior Province of northwestern Ontario; a fertile, S-type, peraluminous granite-rare-element pegmatite system. The Canadian Mineralogist 30, 835-875.

Breiter, K., Förster, H. J., Seltmann, R., 1999. Variscan silicic magmatism and related tin-tungsten mineralization in the Erzgebirge-Slavkovský les metallogenic province. Mineralium Deposita 34, 505-521. doi:10.1007/s001260050217

Broska, I., Petrík, I., 2008. Genesis and stability of accessory phosphates in silicic magmatic rocks: a Western Carpathian case study. Mineralogia 39: 53-66. doi:10.2478/v10002-008-0004-6

Brown P.E., 1998. Fluid inclusion modeling for hydrothermal system. Reviews in Economic Geology 10, 151–171

Burnham, C.W., 1979. Magmas and hydrothermal fluids. In: Barnes, H.L. (Eds.), Geochemistry of hydrothermal ore deposits, John Wiley, pp. 71-136.

Burnham, C.W., and Ohmoto, H., 1980, Late-stage processes of felsic magmatism. In: Ishihara, S., and Takenouchi, S. (Eds.), Granitic magmatism and related mineralization: Tokyo, Japan, Mining Geology Special Issue 8, pp. 1–11.

Burnham, C.W., 1997. Magmas and hydrothermal fluids. In: Barnes H.L. (Ed.), Geochemistry of Hydrothermal Ore Deposits, vol. 3. John Wiley and Sons, Inc. New York, pp. 63–123.

Burt, D.M., 1989. Vector representation of tourmaline compositions. American mineralogist 74, 826-839.

Calles, A.P., Pena, A.M., Jiménez, S.G., 1994. Logrosán: Naturaleza y Arte Público. Excelentísimo Ayuntamiento de Logrosán.

Candela, P.A., 1997. A review of shallow, ore-related granites: textures, volatiles, and ore metals. Journal of petrology 38, 1619-1633. doi:10.1093/petroj/38.12.1619

Capdevila, R., Corretge, G., Floor, P., 1973. Les granitoides varisques de la Meseta Ibérique. Bulletin de la Société géologique de France 3-4, 209-228.

Carracedo, M., Paquette, J.L., Alonso Olazábal, A., Santos Zalduegui, J.F., García de Madinabeitia, S., Tiepolo, M., Gil Ibarguchi, J.I., 2009. U-Pb dating of granodiorite and granite units of the Los Pedroches batholith. Implications for geodynamic models of the southern Central Iberian Zone (Iberian Massif). International Journal of Earth Sciences 98, 1609-1624. doi:10.1007/s00531-008-0317-0

Carruzzo, S., 2003. Granite-hosted mineral deposits of the New Ross area, South Mountain Batholith, Nova Scotia, Canada. PhD Thesis. Dalhousie University, 571 pp.

Castro, A., 1985. The Central Extremadure Batholith - Geotectonic implications (European Hercynian Belt) - An outlet. Tectonophysics 120, 57-68. doi: 10.1016/0040-1951(85)90086-1

Castro, A., Patiño, E., Corretgé, L.G., De La Rosa, J., El-Biad, M., El-Hmidi, H., 1999. Origin of peraluminous granites and granodiorites, Iberian massif, Spain: an experimental test of granite petrogenesis. Contributions to Mineralogy and Petrology 135, 255-276. doi:10.1007/s004100050511

Castro, A., Corretgé, L.G., El-Biad, M., El-Hmidi, H., Fernández, C., Douce, A.E.P., 2000. Experimental constraints on Hercynian anatexis in the Iberian Massif, Spain. Journal of Petrology 41, 1471-1488. doi: 10.1093/petrology/41.10.1471

Cawood, P. A., Buchan, C., 2007. Linking accretionary orogenesis with supercontinent assembly. Earth-Science Reviews 82, 217-256. doi:10.1016/j.earscirev.2007.03.003

Cepedal, A., Fuertes-Fuente, M., Martín-Izard A., García-Nieto, J., Boiron, M.C., 2013. An intrusion-related gold deposit (IRGD) in the NW of Spain, the Linares deposit: igneous rocks, veins and related alterations, ore features and fluids involved. Journal of Geochemical Exploration 124, 101-126. doi:10.1016/j.gexplo.2012.08.010

Černý, P., Ercit, T.S., Wise, M.A., 1992. The tantalite–tapiolite gap: natural assemblages versus experimental data. The Canadian Mineralogist 30, 587–596.

Chacko, T., Hu, X., Mayeda, T.K., Clayton, R. N., Goldsmith, J.R., 1996. Oxygen isotope fractionations in muscovite, phlogopite, and rutile. Geochimica et Cosmochimica Acta 60, 2595-2608. doi: 10.1016/0016-7037(96)00112-3

Chappell, B., White, A., Wyborn, D., 1987. The importance of residual source material (restite) in granite petrogenesis. Journal of Petrology 28, 1111-1138. doi:10.1093/petrology/28.6.1111

Chappell, B., White, A., Williams, I., 1991. A transverse section through granites of the Lachlan Fold Belt. Second Hutton Symposium on Granites and Related Rocks, Canberra, pp. 1-125.

Charoy, B., 1982. Tourmalinization in Cornwall, England. In: Evans, A.M. (Eds.), Metallization associated with acid magmatism. Wiley, London, pp. 63-70.

Chauvet, A., Volland-Tuduri, N., Lerouge, C., Bouchot, V., Monié, P., Charonnat, X., Faure, M., 2012. Geochronological and geochemical characterization of magmatic-hydrothermal events within the Southern Variscan external domain (Cévennes area, France). International Journal of Earth Sciences 101, 69-86. doi: 10.1007/s00531-011-0639-1

Cheilletz A., Pelleter E., Martin-Izard A., Tornos F., 2005. World skarn deposits: skarns of Western Europe. Economic Geology 100th Anniversary Volume, 1 -10.

Chen, X.C., Hu, R.Z., Bi, X.W., Li, H.M., Lan, J.B., Zhao, C.H., Zhu, J.J., 2014. Cassiterite LA-MC-ICP-MS U/Pb and muscovite $^{40}Ar/^{39}Ar$ dating of tin deposits in the Tengchong-Lianghe tin district, NW Yunnan, China. Mineralium Deposita 49, 843-860. doi:10.1007/s00126-014-0513-8

Cheng, Y., Mao, J., Yang, Z., 2012. Geology and vein tin mineralization in the Dadoushan deposit, Gejiu district, SW China. Mineralium Deposita 47, 701-712. doi:10.1007/s00126-012-0409-4

Cheng, Y., Mao, J., Chang, Z., Pirajno, F., 2013. The origin of the world class tin-polymetallic deposits in the Gejiu district, SW China: Constraints from metal zoning characteristics and $^{40}Ar–^{39}Ar$ geochronology. Ore Geology Reviews 53, 50-62. doi:10.1016/j.oregeorev.2012.12.008

Chesley, J.T., Halliday, A.N., Snee, L.W., Mezger, K., Sheperd, T.J., Scrivener, R.C., 1993. Thermochronology of the Cornubian Batholith in southwest England: implications for pluton emplacement and protracted hydrothermal mineralisation. Geochimica et Cosmochimica Acta 57, 1817-1835. doi:10.1016/0016-7037(93)90115-D

Chevychelov, V.Y., Borodulin, G.P., Zaraisky, G.P., 2010. Solubility of columbite, $(Mn, Fe)(Nb, Ta)_2O_6$, in granitoid and alkaline melts at 650–850° C and 30–400 MPa: An experimental investigation. Geochemistry International 48, 456-464. doi:10.1134/S0016702910050034

Chicharro E., 2009. Caracterización de las mineralizaciones de Sn-(W) asociadas al stock granítico de Logrosán (Cáceres). Unpublished Master Thesis, Universidad Complutense de Madrid.

Chicharro, E., Boixereu, E., Villaseca, C., López-García, J.Á., 2011. Contribución a la puesta en valor del patrimonio geológico y minero del geoparque de las Villuercas: el cerro de San Cristóbal (Logrosán, Cáceres). De Re Metallica 17, 47-54.

Chicharro, E., Villaseca, C., Valverde-Vaquero, P., Belousova, E., López-García, J.Á., 2013. U-Pb Geochronology and Source Constraints for Late S-Type Variscan Magmatism Related to Sn-W Metallogeny: The Logrosán Granite Pluton (Central Iberian Zone). Mineralogical Magazine. 77, 874.

Chicharro E., Villaseca C., Valverde-Vaquero P., Belousova E., López-García J.Á., 2014. Zircon U-Pb and Hf isotopic constraints on the genesis of a post-kinematic S-type Variscan tin granite: the Logrosán cupola (Central Iberian Zone). Journal of Iberian Geology 40, 451-470. doi:10.5209/rev_JIGE.2014.v40.n3.43928

Chicharro, E., Martín-Crespo, T., Gómez-Ortiz, D., López-García, J.Á., Oyarzun, R., Villaseca, C., 2015. Geology and gravity modeling of the Logrosán Sn–(W) ore deposits (Central Iberian Zone, Spain). Ore Geology Reviews 65, 294-307. doi:10.1016/j.oregeorev.2014.10.005

Choffat, P., 1909. Note sur les filons de phosphorite de Logrosán. Bulletin de la Société belge de géologie de paléontologie et d'hydrologie 23, 98-113.

Chu, M.F., Wang, K.L., Griffin, W.L., Chung, S.L., O´Reilly, S.Y., Pearson, N.J., Iizuka, Y., 2009. Apatite composition: tracing petrogenetic processes in transhimalayan granitoids. Journal of Petrology 50, 1829-1855. doi:10.1093/petrology/egp054doi:10.1093/petrology/egp054

Clayton R. N., Mayeda T. K., 1963. The use of bromine pentafluoride in the extraction of oxygen from oxides and silicates for isotopic analysis. Geochimica et Cosmochimica Acta 27, 43-52. doi:10.1016/0016-7037(63)90071-1

Clayton, R.N., O'Neil, J.R., Mayeda, T.K., 1972. Oxygen isotope exchange between quartz and water. Journal of Geophysical Research 77, 3057-3067. doi:10.1016/0016-7037(79)90099-1

Cline, J. S., Bodnar, R.J., 1991. Can economic porphyry copper mineralization be generated by a typical calc-alkaline melt? Journal of Geophysical Research 96, 8113-8126. doi: 10.1029/91JB00053

Cocks, L.R.M., Torsvik, T.H., 2002. Earth geography from 500 to 400 million years ago: a faunal and palaeomagnetic review. Journal of the Geological Society 159, 631-644. doi: 10.1144/0016-764901-118

Conrad, W.K., Nicholls, I.A., Wall, V.J., 1988. Water-saturated and-undersaturated melting of metaluminous and peraluminous crustal compositions at 10 kb: evidence for the origin of silicic magmas in the Taupo Volcanic Zone, New Zealand, and other occurrences. Journal of Petrology, 29: 765-803.

Corretgé L.G., Ugidos J.M., Martínez F.J., 1977. Les séries granitiques varisques du secteur Centre-Occidental Espagonol. En: La Chaîne Varisque d'Europe Moyenne et Occidentale. Coll Internat C.N.R.S. Rennes 243, 453–461

Craig, H., 1961. Isotopic variations in meteoric waters. Science 133, 1702-1703.

Crowe, D.E., Valley, J.W., Baker, K.L., 1990. Micro-analysis of sulfur-isotope ratios and zonation by laser microprobe. Geochimica et Cosmochimica Acta 54, 2075-2092. doi:10.1016/0016-7037(90)90272-M

Dallmeyer, R.D., Martínez-Catalán, J.R., Arenas, R., Gil-Ibarguchi, J.I., Gutiérrez-Alonso, G., Farias, P., Bastida, F. y Aller, J., 1997. Diachronous Variscan tectonothermal activity in the NW Iberian Massif: Evidence from $^{40}Ar/^{39}Ar$ dating of regional fabrics. Tectonophysics 277, 307-377. doi:10.1016/S0040-1951(97)00035-8

Darbyshire, D.P.F. and Shepherd, T.J., 1985. Chronology of granite magmatism and associated mineralization, SW England. Journal of the Geological Society of London 142, 1159-1177. doi:10.1144/gsjgs.142.6.1159

De la Roche, H., 1964. Sur l'expression graphique des relations entre la composition chimique et la composition minéralogique quantitative des roches cristallines. Sciences de la Terre 9, 293-337.

Debon, F., Le Fort, P., 1983. A chemical–mineralogical classification of common plutonic rocks and associations. Transactions of the Royal Society of Edinburgh: Earth Sciences 73, 135-149.

Derré, C., 1982. Caractéristiques de la distribution des gisements à étain et tungstène dans l'ouest de l'Europe. Mineralium Deposita 17, 55-77.

Dias, G., Leterrier, J., 1994. The genesis of felsic-mafic plutonic associations: a Sr and Nd isotopic study of the Hercynian Braga granitoid massif (northern Portugal). Lithos 32, 207-223. doi:10.1016/0024-4937(94)90040-X

Dias, G., Leterrier, J., Mendes, A., Simoes, P., Bertrand, J., 1998. U–Pb zircon and monazite geochronology of post-collisional Hercynian granitoids from the Central Iberian Zone (Northern Portugal). Lithos 45, 349-369. doi:10.1016/S0024-4937(98)00039-5

Dias, G., Simões, P., Ferreira, N., Leterrier, J., 2002. Mantle and crustal sources in the genesis of late-Hercynian granitoids (NW Portugal. geochemical and Sr-Nd isotopic constraints. Gondwana Research 5, 287-305. doi:10.1016/S1342-937X(05)70724-3

Díaz-Alvarado, J., Castro, A., Fernández, C., Moreno-Ventas, I., 2011. Assessing bulk assimilation in cordierite-bearing granitoids from the Central System Batholith, Spain; experimental, geochemical and geochronological constraints. Journal of Petrology 52, 223-256. doi:10.1093/petrology/egq078

Díez Balda, M.A., Martínez Catalán, J.R., Ayarza, P., 1995. Syn-collisional extensional collapse parallel to the orogenic trend in a domain of steep tectonics: the Salamanca detachment zone (Central Iberian Zone, Spain). Journal of Structural Geology 17, 163–182. doi:10.1016/0191-8141(94)E0042-W

Díez-Fernández, R., Castiñeiras, P., Barreiro, J.G., 2012. Age constraints on Lower Paleozoic convection system: magmatic events in the NW Iberian Gondwana margin. Gondwana Research 21, 1066-1079. doi:10.1016/j.gr.2011.07.028

Díez-Fernández, R., Pereira, M.F., Foster, D.A., 2015. Peralkaline and alkaline magmatism of the Ossa-Morena zone (SW Iberia): Age, source, and implications for the Paleozoic evolution of Gondwanan lithosphere. Lithosphere 7, 73-90. doi:10.1130/L379.1

Dolníček, Z., René, M., Prochaska, W., Kovář, M., 2012. Fluid evolution of the Hub Stock, Horní Slavkov–Krásno Sn–W ore district, Bohemian Massif, Czech Republic. Mineralium Deposita 47, 821-833. doi:10.1007/s00126-012-0400-0

Duan, Z., Møller, N., Weare, J.H., 1992. An equation of state for the CH_4–CO_2–H_2O system: I. Pure systems from 0 to 1000 °C and 0 to 8000 bar. Geochimica et Cosmochimica Acta 56, 2605-2617. doi:10.1016/0016-7037(92)90347-L

Duan, Z., Møller, N., Weare, J.H., 1996. A general equation of state for supercritical fluid mixtures and molecular dynamics simulation of mixture PVTX properties. Geochimica et Cosmochimica Acta, 60, 1209-1216. doi:10.1016/0016-7037(96)00004-X

Dubessy, J., Nguyen-Trung, C., Cathelineau, M., Cuney, M., Leroy, J., Poty, B., Ramboz, C.; Charoy, B., Weisbrod, A., Weisbrod, A., 1987. Physical and chemical controls (fO_2, T, pH) of the opposite behaviour of U and Sn-W as examplified by hydrothermal deposits in France and Great-Britain, and solubility data. Bulletin de Mineralogie 110, 261-281

Dubessy, J., Poty, B., Ramboz, C., 1989. Advances in COHNS fluid geochemistry based on micro-Raman spectrometric analysis of fluid inclusions. European Journal of Mineralogy 1, 517-534. doi:10.1127/ejm/1/4/0517

Dufréchou, G., Harris, L.B., Corriveau, L., Antonoff, V., 2011. Gravity evidence for a mafic intrusion beneath a mineralized zone in the Bondy gneiss complex, Grenville Province, Quebec—Exploration implications. Journal of Applied Geophysics 75, 62-76. doi:10.1016/j.jappgeo.2011.06.029

Egozcué, J., Mallada, L., 1876. Memoria geológico-minera de la provincial de Cáceres. Memorias de la Comisión del Mapa Geológico de España, 4.

ENADMISA, 1982. Investigación del área de Logrosán (Cáceres). Internal report.

Eugster, H.P., 1985. Granites and hydrothermal ore deposits: a geochemical framework. Mineralogical Magazine, 49: 7-23.

Eugster, H.P., Wilson, G.A., 1985. Transport and deposition of ore-forming elements in hydrothermal systems associated with granites. In: Darnley A.G. (Ed.), High heat production (HHP) granites, hydrothermal circulation and ore genesis. Institute of Mining and Metallurgy, London. pp. 87-98

Fallick, A., McConville, P., Boyce, A., Burgess, R., 1992. Laser microprobe stable isotope measurements on geological materials: Some experimental considerations (with special reference to ^{34}S in sulphides). Chemical Geology 101, 53-61.

Farias, P., Gallastegui, G., González Lodeiro, F., Marquínez, J., Martín Parra, L.M., Martínez Catalán, J.R., Pablo de Maciá, J.G., Rodríguez Fernández, L.R., 1987. In: Aportaciones al conocimiento de la litoestratigrafía y estructura de Galicia Central. Memorias del Museo y Laboratorio Mineralógico y Geológico, de la Facultad de Ciencias, Universidad de Oporto 1, 411-431.

Fernández-Amo, F.J., Rebollada Casado, E., Carvajal Gómez, D.J., 2010. Mina Costanaza (Logrosán, Cáceres): Patrimonio Minero y Lugar de Interés Geoturísitico. In: Florido, P., and Rábano, I., (Eds.), Una Vision Multidisciplinar del Patrimonio Gelogico y Minero. Cuadernos del Museo Minero 12, IGME, pp. 269-276.

Fernández-Suárez, J., Dunning, G., Jenner, G., Gutiérrez-Alonso, G., 2000. Variscan collisional magmatism and deformation in NW Iberia: constraints from U–Pb geochronology of granitoids. Journal of the Geological Society 157, 565-576. doi:10.1144/jgs.157.3.565

Ferreira, N., Macedo, C.A.R., Sousa, M.B., 1987. Cronostratigrafia dos granitos da região de Moimenta da Beira-Tabuaço-Penedono. In: Aportaciones al conocimiento de la litoestratigrafía y estructura de Galicia Central. Memorias del Museo y Laboratorio Mineralógico y Geológico, de la Facultad de Ciencias, Universidad de Oporto 1, 287-301.

Ferry, J., Watson, E., 2007. New thermodynamic models and revised calibrations for the Ti-in-zircon and Zr-in-rutile thermometers. Contributions to Mineralogy and Petrology 154, 429-437. doi:10.1007/s00410-007-0201-0

Flinter, B., 1971. Tin in acid granitoids: a search for a geochemical scheme of mineral exploration. Proceedings of the 3rd International Geochemical Exploration Symposium, Toronto, pp. 323-330.

Flowers, G.C., 1979. Correction of Holloway's (1977) adaptation of the modified Redlich-Kwong equation of state for calculation of the fugacities of molecular species in supercritical fluids of geologic interest. Contributions to Mineralogy and Petrology 69, 315-318. doi:10.1007/BF00372333

Fogel, R.A., Rutherford, M.J., 1990. The solubility of carbon dioxide in rhyolitic melts; a quantitative FTIR study. American Mineralogist 75, 1311-1326.

Förster, H.J., 1998a. The chemical composition of REE-Y-Th-U-rich accessory minerals in peraluminous granites of the Erzgebirge-Fichtelgebirge region, Germany; Part I, The monazite-(Ce)-brabantite solid solution series. American Mineralogist 83, 259-272.

Förster, H.J., 1998b. The chemical composition of REE-Y-Th-U-rich accessory minerals in peraluminous granites of the Erzgebirge-Fichtelgebirge region, Germany. Part II: Xenotime. American Mineralogist 83, 1302-1315.

Foster, M. D., 1960. Interpretation of the composition of trioctahedral micas. Professional Papers of the U.S. Geological Survey 354-B, 11-49.

Franke, W., Żelaźniewicz, A., 2000. The eastern termination of the Variscides: terrane correlation and kinematic evolution. Geological Society, London, Special Publications 179, 63-86. doi:10.1144/GSL.SP.2000.179.01.06

Fu, B., Mernagh, T.P., Fairmaid, A. M., Phillips, D., Kendrick, M.A., 2014. CH_4-N_2 in the Maldon gold deposit, central Victoria, Australia. Ore Geology Reviews, 58, 225-237. doi:10.1016/j.oregeorev.2013.11.006

Fuertes-Fuente, M., Martin-Izard, A., Boiron, M.C., Viñuela, J.M., 2000. P-T path and fluid evolution in the Franqueira granitic pegmatite, central Galicia, northwestern Spain. The Canadian Mineralogist 38, 1163-1175. doi: 10.2113/gscanmin.38.5.1163

Gabaldón López, V., Hernández Urroz, S., Lorenzo Álvarez, S., Picart Boira, J., Santamaría Casavovas, J., Solé Pont, F.J., 1986. Sedimentary facies and stratigraphy of Precambrian-Cambrian phosphorite on the Valdecasa Anticline, Central Iberian Zone, Spain. In: Notholt, A.J.G., Sheldon, R.P., Davidson, D.F. (Eds.), Phosphate deposits of the world 2. Cambridge University Press, Cambridge, pp. 422-428.

Galindo, C., Casquet, C., Tornos, F., 2010. Actividad paleo-hidrotermal episódica en la Sierra de Guadarrama (Sistema Central Español): nuevas edades K-Ar y correlación tectónica con la Cordillera Ibérica. Geogaceta. 48, 159-162.

Gallagher, V., 1988. Coupled substitutions in schorl-dravite tourmaline - new evidence from southeast Ireland. Mineralogical Magazine 52: 637-650.

García de Madinabeitia, S., Roda-Robles, E., Pesquera, A., Sánchez, M.E,. Gil Ibarguchi, J.I., 2013. Characterization of complex Fe-Mn phosphates by LA-ICP-MS methods. Mineralogical Magazine. 77, 1142.

García-Moreno, O., Corretgé, L.G., Castro, A., 2007. Processes of assimilation in the genesis of cordierite leucomonzogranites from the Iberian Massif: a short review. The Canadian Mineralogist 45, 71-85. doi:10.2113/gscanmin.45.1.71

Giuliani, G., 1984. Les concentrations filoniennes à tungstène-étain du massif granitique des Zaër (Maroc Central): Minéralisations et phases fluides associées. Mineralium Deposita, 19, 193-201. doi: 10.1007/BF00199785

Giuliani, G., Li, Y.D., Sheng, T.F., 1988. Fluid inclusion study of Xihuashan tungsten deposit in the southern Jiangxi province, China. Mineralium Deposita 23, 24-33. doi:10.1007/BF00204224

GM-SYS Profile Modeling, 2009. Extension to Oasis Montaj. Geosoft, Inc. Queens Quay Terminal, PO Box 131, Toronto, Canada.

Godfrey, J.D., 1962. The deuterium content of hydrous minerals from the east-central Sierra Nevada and Yosemite National Park. Geochimica et Cosmochimica Acta 26, 1215-1245. doi:10.1016/0016-7037(62)90053-4

Gomes, M.E.P., Neiva. A.M.R., 2002. Petrogenesis of tin-bearing granites from Ervedosa, northern Portugal: the importance of magmatic processes. Chemie der Erde, 62: 47–72. doi:10.1078/0009-2819-00002

González Menéndez, L., Bea, F., 2004. Magmatismo de la zona Centroibérica: El batolito de Nisa-Alburquerque. In: Vera, J.A. (Ed.), Geología de España. SGE-IGME, Madrid, pp. 120-122.

Grange, M., Scharer, U., Merle, R., Girardeau, J., Cornen, G., 2010. Plume-lithospheric interaction during migration of Cretaceous alkaline magmatism in SW Portugal: evidence from U-Pb ages and Pb-Sr-Hf isotopes. Journal of Petrology 51, 1143-1170. doi: 10.1093/petrology/egq018

Griffin, W.L., Pearson, N. J., Belousova, E.A., Jackson, S.R., van Achterbergh, E., O'Reilly, S. Y., Shee, S. R., 2000. The Hf isotope composition of cratonic mantle: LAM-MC-ICPMS analysis of zircon megacrysts in kimberlites. Geochimica et Cosmochimica Acta 64, 133-147. doi:10.1016/S0016-7037(99)00343-9

Griffin, W. L., Pearson, N. J., Belousova, E. A., Jackson, S. R., van Achterbergh, E., O'Reilly, S. Y., Shee, S. R., 2002. Zircon chemistry and magma mixing, SE China: in-situ analysis of Hf isotopes, Tonglu and Pingtan igneous complexes. Lithos 61, 237-269. doi:10.1016/S0024-4937(02)00082-8

Griffin, W., Belousova, E., Shee, S., Pearson, N., O'reilly, S., 2004. Archean crustal evolution in the northern Yilgarn Craton: U–Pb and Hf-isotope evidence from detrital zircons. Precambrian Research 131, 231-282. doi:10.1016/j.precamres.2003.12.011

Guijarro, J., 1982a. Las mineralizaciones de W-Sn ligadas a los plutones graníticos de Trujillo y Logrosán (Cáceres, España). Ph.D Thesis, Universidad Autónoma de Madrid. Madrid. 510 pp.

Guijarro, J., Casas, J., Hoyos, M.A., 1982b. Estudio de la alteración de minerales de estaño en el yacimiento de Cerro de San Cristóbal, Cáceres. Anales de Edafología y Agrobiología 41, 1921-1931.

Guijarro, J., Hoyos, M.A., Casas, J., Martín de Vidales, J.L., 1983. Estudio de las inclusions fluidas en los filones del stockwerk estannífero del Cerro de San Cristóbal, Logrosán, España. Boletín Geológico y Minero 94, 521-529.

Guijarro, J., Astudillo, J., Moreno, A., Gutiérrez, A., 1985a. Distribución de uranio y torio en el plutón de Trujillo, Cáceres, España. Boletín Geológico y Minero 96, 186-196.

Guijarro, J., Monserur, J., Gutiérrez-Maroto, A., 1985b. Estudio del stockwork asociado a la apófisis adamellítica de Logrosán (Cáceres, España). Boletín de la Sociedad Española de Mineralogía 8, 197-205.

Guijarro, J., Moreno-Gutiérrez, A., Gutiérrez-Maroto, A., 1986. Petrología y geoquímica de la apófosis adamellítica de Logrosán. Boletín Geológico y Minero 97, 757-771.

Guilbert, J.M., Park, C.F., Jr., 1986. The geology of ore deposits. W.H. Freeman and Co., New York, pp. 985.

Guo, J. B., Qian, Y. Q., .1997 Hydrogen isotopic fractionation and hydrogen diffusion in the tourmaline-water system. Geochimica et Cosmochimica Acta 16, 4679-4688. doi:10.1016/S0016-7037(97)00252-4

Gutiérrez-Alonso, G., Fernandez-Suarez J., Jeffries T.E., Jenner G.A., Tubrett M.N., Cox R., Jackson S.E., 2003. Terrane accretion and dispersal in the northern Gondwana margin. An Early Paleozoic analogue of a long-lived active margin. Tectonophysics 365, 221-232. doi: 10.1016/S0040-1951(03)00023-4

Gutiérrez-Alonso, G., Fernández-Suárez, J., Weil, A.B., Murphy, J.B., Nance, R.D., Corfú, F., Johnston, S. T., 2008. Self-subduction of the Pangaean global plate. Nature Geoscience 1, 549-553. doi:10.1038/ngeo250

Gutiérrez-Alonso, G., Fernández-Suárez, J., Jeffries, T.E., Johnston, S.T., Pastor-Galán, D., Murphy, J.B., Franco, M.P., Gonzalo, J.C., 2011. Diachronous post-orogenic magmatism within a developing orocline in Iberia, European Variscides. Tectonics 30, TC5008. doi:10.1029/2010TC002845

Gutzwiller, 1919. Informe sobre los yacimientos de fosforita de Logrosán, prov. de Cáceres. 24 pp.

Hall, A., Bencini, A., Poli, G., 1991. Magmatic and hydrothermal ammonium in granites of the Tuscan magmatic province, Italy. Geochimica et Cosmochimica Acta 55, 3657-3664. doi:10.1016/0016-7037(91)90063-B

Halls, C., 1994. Energy and mechanism in the magmatic-hydrothermal evolution of the Cornubian batholiths: a review. In: Seltmann, R., Kampf, H., Moller P. (Eds.), Metallogeny of Collisional Orogens. Czech Geological Survey, Prague, pp. 274–294.

Hall, A., Pereira, M.D., Bea, F., 1996. The abundance of ammonium in the granites of central Spain, and the behaviour of the ammonium ion during anatexis and fractional crystallization. Mineralogy and Petrology 56, 105-123. doi:10.1007/BF01162659

Halter, W.E., Williams-Jones, A.E., Kontak, D.J., 1996. The role of greisenization in cassiterite precipitation at the East Kemptville tin deposit, Nova Scotia. Economic Geology 91, 368-385. doi: 10.2113/gsecongeo.91.2.368

Hanchar, J.M., Watson, E.B., 2003. Zircon saturation thermometry. Reviews in Mineralogy and Geochemistry 53, 89-112. doi:10.2113/0530089

Hawthorne, F.C., Henry, D.J., 1999. Classification of the minerals of the tourmaline group. European Journal of Mineralogy 11, 201-216.

Hedenquist, J.W., Henley, R.W. 1985. The importance of CO_2 on freezing point measurements of fluid inclusions; evidence from active geothermal systems and implications for epithermal ore deposition. Economic geology 80, 1379-1406. doi:10.2113/gsecongeo.80.5.137

Heinrich, C.A., 1990. The chemistry of hydrothermal tin (-tungsten) ore deposition. Economic Geology 85, 457-481. doi:10.2113/gsecongeo.85.3.457

Henry, D.J., Guidotti, C.V., 1985. Tourmaline as a petrogenetic indicator mineral - An example from the staurolite-grade metapelites of NW Maine. American Mineralogist, 70: 1-15.

Henry, D. J., Dutrow, B. L., Selverstone, J., 2003. Compositional asymmetry in replacement tourmaline--An example from the Tauern Window, Eastern Alps. American Mineralogist 88: 1399-1399.

Henry, B., Liegeois, J.P., Nouar, O., Derder, M.E.M., Bayou, B., Bruguier, O., Ouabadi, A., Belhai, D., Amenna, M., Hemmi, A., Ayache, M., 2009. Repeated granitoid intrusions during the Neoproterozoic along the western boundary of the Saharan metacraton, Eastern Hoggar, Tuareg shield, Algeria: an AMS and U-Pb zircon age study. Tectonophysics 474, 417–434. doi:10.1016/j.tecto.2009.04.022

Herrero, M.J., Martín-Pérez, A., Alonso-Zarza, A.M., Gil-Peña, I., Meléndez, A., Martín-García, R., 2011. Petrography and geochemistry of the magnesites and dolostones of the Ediacaran Ibor Group (635 to 542 Ma), Western Spain: Evidences of their hydrothermal origin. Sedimentary Geology 240, 71-84. doi:10.1016/j.sedgeo.2011.08.007

Herrger, C. 1800. Descripción orictognóstica del apatito térreo de Logrosán. Anales de Historia Natural 2, 168-171.

Hoefs, J., Emmermann, R., 1983. The oxygen isotope composition of Hercynian granites and pre-Hercynian gneisses from the Schwarzwald, SW Germany. Contributions to Mineralogy and Petrology 83, 320-329. doi: 10.1007/BF00371200

Hoefs, J., 2009. Stable isotope geochemistry. Springer-Verlag, Berlin. 285 pp.

Holloway, J.R., 1977. Fugacity and activity of molecular species in supercritical fluids. Thermodynamics in Geology, NATO Advanced Study Institutes Series 30, 161-181.

Hoshino, M., Kimata, M., Nishida, N., Shimizu, M., Akasaka, T., 2010. Crystal chemistry of zircon from granitic rocks, Japan: genetic implications of HREE, U and Th enrichment. Neues Jahrbuch für Mineralogie Abhandlungen 187, 167-188. doi:10.1127/0077-7757/2010/0177

Hoskin, P.W., Schaltegger, U., 2003. The composition of zircon and igneous and metamorphic petrogenesis. Reviews in Mineralogy and Geochemistry 53, 27-62. doi:10.2113/0530027

Huff, T. A., Nabelek, P. I., 2007. Production of carbonic fluids during metamorphism of graphitic pelites in a collisional orogen—an assessment from fluid inclusions. Geochimica et Cosmochimica Acta 71, 4997-5015. doi: 10.1016/j.gca.2007.08.001

IGME, 1950. Estadística Minera y Metalúrgica de España, Cáceres: 203-205.

IGME, 1981a. Mapa geológico de España a escala 1:50.000, hoja nº 707, Logrosán, Servicio de Publicaciones IGME, Madrid.

IGME, 1981b. Mapa geológico de España a escala 1:50.000, hoja nº 706, Madroñera, Servicio de Publicaciones IGME, Madrid.

IGME, 1990. Mapa geológico de España a escala 1:50.000, hoja nº 731, Zorita, Servicio de Publicaciones IGME, Madrid.

IGME, 1995. Mapa geológico de España a escala 1:50.000, hoja nº 732, Valdecaballeros, Servicio de Publicaciones IGME, Madrid.

Isachsen, C.E., Coleman, D.S. and Schmitz, M., 2007. PbMacDat program. Available at http://www.earthtime.org.

Ishihara, S., 1977. The magnetite-serie and ilmenite-series granitic rocks: Mining Geology 27, 293-305.

Ishihara, S., Sasaki, A., 1989. Sulfur isotopic ratios of the magnetite-series and ilmenite-series granitoids of the Sierra Nevada batholith—A reconnaissance study. Geology 17, 788-791. doi:10.1130/0091-7613(1989)017<0788:SIROTM>2.3.CO;2

Jackson N. J., Halliday, A .N., Sheppard, S.M.F., Mitchell, J.G., 1982. Hydrothermal activity in the St. Just mining district, Cornwall, England. In: Evans, M. (Ed.), Metallization Associated with acid magmatism Chichester, Wiley, pp. 137-179.

Jackson, N.J., Willis-Richards, J., Manning, D.A.C., Sams, M.S., 1989. Evolution of the Cornubian ore field, southwest England: Part II. Mineral deposits and ore-forming processes. Economic Geology 84, 1101-l 133. doi: 10.2113/gsecongeo.84.5.1101

Jackson, S.E., Pearson, N.J., Griffin, W.L., Belousova, E.A., 2004. The application of laser ablation-inductively coupled plasma-mass spectrometry to in situ U-Pb zircon geochronology. Chemical Geology 211, 47–69. doi: 10.1016/j.chemgeo.2004.06.017

Jaffey, A., Flynn, K., Glendenin, L., Bentley, W., Essling, A., 1971. Precision measurement of the half-lives and specific activities of U^{235} and U^{238}. Physical Review C - Nuclear Physics 4, 1889-1906. doi:10.1103/PhysRevC.4.1889

Jeffries, T.E., 2001. Elemental analysis by laser ablation ICP-MS. In: Alfassi, Z., (Ed.), Non-destructive Elemental Analysis. Blackwell Science, Oxford, pp. 115–150.

Jenkin, G.R.T., 1988. Stable isotope studies in the Caledonides of SW Connemara, Ireland, PhD Thesis, University of Glasgow.

Jiang, S.Y., 1998. Stable and radiogenic isotope studies of tourmaline: an overview. Journal of Geosciences 43, 75-90.

Jochum, J., 2000. Variscan and post-Variscan lead–zinc mineralization, Rhenish Massif, Germany: evidence for sulfide precipitation via thermochemical sulfate reduction. Mineralium Deposita 35, 451-464. doi:10.1007/s001260050255

Jochum, K.P., Weis, U., Stoll, B., Kuzmin, D., Yang, Q., Raczek, I., Jabob, D.E., Stracke, A., Birbaum, K., Frick, D.A., Günther, D., Enzweiler, J., 2011. Determination of Reference Values for NIST SRM 610–617 Glasses Following ISO Guidelines. Geostandards and Geoanalytical Research 35, 397-429. doi:10.1111/j.1751-908X.2011.00120.

Johannes W., Holtz F., 1996. Petrogenesis and Experimental Petrology of Granitic Rocks. Springer-Verlag, Berlin, 335 pp.

Julivert, M., Fontboté, J., Ribeiro, A., Conde, L., 1972. Mapa Tectónico de la Península Ibérica Y Baleares, E. 1:1.000.000. IGME, Madrid.

Junta de Extremadura, 1993a. La Minería de Extremadura. Consejería de Industria y Turismo, Mérida. 516 pp.

Junta De Extremadura, 1993b. Minerales Gemológicos De Extremadura. Consejeria de Industria y Turismo, Mérida. 149 pp.

Junta de Extremadura, 2007. Memoria del Mapa Metalogenético de Extremadura a escala 1:250000. Dirección General de Ordenación Industrial, Energía y Minas. Consejería de Economía y Trabajo, Madrid. 359 pp.

Junta de Extremadura, 2010. Patrimonio Geológico de Extremadura. Geodiversidad y Lugares de Interés Geológico. Consejería de Industria, Energía y Medio Ambiente, Mérida. 478 pp.

Kane, M.F., 1962. A comprehensive system of terrain corrections using a digital computer. Geophysics 27, 445–462.

Karayeva, Z., 1968. Geochemistry of mineralized granitoids. Doklady Akademii Nauk SSRR, 179, 164-166.

Kelley, S., Fallick, A., 1990. High precision spatially resolved analysis of ^{34}S in sulphides using a laser extraction technique. Geochimica et Cosmochimica Acta 54, 883-888. doi:10.1016/0016-7037(90)90381-T

Kelly, W.C., Rye, R.O., 1979. Geologic, fluid inclusions and stable isotope studies of the tin-tungsten deposits of Panasqueira, Portugal. Economic Geology 74, 1721-1822. doi:10.2113/gsecongeo.74.8.1721

Kent, A.J.R., McDougall, I., 1995. ^{40}Ar-^{39}Ar and U-Pb age constraints on the timing of gold mineralization in the Kalgoorlie gold field, Western Australia. Economic Geology, 90, 845-859. doi:10.2113/gsecongeo.90.4.845

Keppler, H., 1993. Influence of fluorine on the enrichment of high field strength trace elements in granitic rocks. Contributions to Mineralogy and Petrology 114: 479–488. doi:10.1007/BF00321752

Kerestedjian, T., 1997. Chemical and morphological features of arsenopyrite, concerning its use a geothermometer. Mineralogy and Petrology 60, 231-243. doi: 10.1007/BF01173710

Knight C.L., Bodnar R.J., 1989. Synthetic fluid inclusions. IX. Critical PVTX properties of NaCl-H_2O solutions. Geochimica et Cosmochimica Acta 53, 3-8. doi:10.1016/0016-7037(89)90267-6

Kontak, D.J., 1990. A sulfur isotope study of main-stage tin and base metal mineralization at the East Kemptville tin deposit, Yarmouth County, Nova Scotia, Canada; evidence for magmatic origin of metals and sulfur. Economic Geology 85, 399-407. doi: 10.2113/gsecongeo.85.2.399

Kotzer, T.G., Kyser, T.K., King, R.W., Kerrich, R., 1993. An empirical oxygen-and hydrogen-isotope geothermometer for quartz-tourmaline and tourmaline-water. Geochimica et Cosmochimica Acta 57, 3421-3426. doi:10.1016/0016-7037(93)90548-B

Kretschmar, U., Scott, S.D., 1976. Phase relations involving arsenopyrite in the system Fe-As-S and their application. The Canadian Mineralogist 14, 364-386.

Krogh, T.E., 1973. A low-contamination method for hydrothermal decomposition of zircon and extraction of U and Pb for isotopic age determinations. Geochimica et Cosmochimica Acta 37, 485-494. doi:10.1016/0016-7037(73)90213-5

Krogh, T.E., 1982. Improved accuracy of U-Pb zircon ages by the creation of more concordant systems using an air abrasion technique. Geochimica et Cosmochimica Acta 46, 637-649. doi:10.1016/0016-7037(82)90165-X

Kroner, U., Hahn, T., Romer, R.L., Linnemann, U., 2007. The Variscan orogeny in the Saxo-Thuringian Zone—heterogenous overprint of Cadomian/Palaeozoic Peri-Gondwana crust. In: Linnemann, U., Nance, R.D., Kraft, P., Zulauf, G. (Eds.), The Evolution Of The Rheic Ocean: From Avalonian–Cadomian Active Margin To Alleghenian–Variscan Collision: Geological Society Of America Special Paper 423, pp. 153–172.

Kroner, U., Romer, R.L., 2013. Two plates - Many subduction zones: The Variscan orogeny reconsidered. Gondwana Research 24, 298-329. doi:10.1016/j.gr.2013.03.001

Lahti, S.I., 1987. Zoning in columbite–tantalite crystals from the granitic pegmatites of the Erajarvi area, southern Finland. Geochimica et Cosmochimica Acta 51, 509–517. doi:10.1016/0016-7037(87)90065-2

Lee, B.I., Kesler, M.G., 1975. A generalized thermodynamic correlation based on three-parameter corresponding states. AIChE Journal, 21, 510-527. doi:10.1002/aic.690210313

Lehman, B., 1990. Metallogeny of tin. Lecture notes in earth sciences. Springer-Verlag, 32. Berlin. 211pp.

Lehmann, B., Dietrich, A., Heinhorst, J., Métrich, N., Mosbah, M., Palacios, C., Schneider H.J., Wallianos A., Webster, J, Winkelmann, L. 2000. Boron in the Bolivian tin belt. Mineralium Deposita 35: 223-232. doi:10.1007/s001260050017

Liao, S., Chen, S., Deng, X., Li, P., Zhao, J., Liao, R., 2014. Fluid inclusion characteristics and geological significance of the Xi'ao copper–tin polymetallic deposit in Gejiu, Yunnan Province. Journal of Asian Earth Sciences, 79, 455-467. doi:10.1016/j.jseaes.2013.10.023

Liew, T., Hofmann, A., 1988. Precambrian crustal components, plutonic associations, plate environment of the Hercynian Fold Belt of central Europe: indications from a Nd and Sr isotopic study. Contributions to Mineralogy and Petrology 98, 129-138. doi:10.1007/BF00402106

Linnemann, U., McNaughton, N.J., Romer, R.L., Gehmlich, M., Drost, K., Tonk, C., 2004. West African provenance for Saxo-Thuringia (Bohemian Massif): did Armorica ever leave pre-Pangean Gondwana?–U/Pb-SHRIMP zircon evidence and the Nd-isotopic record. International Journal of Earth Sciences 93, 683-705. doi:10.1007/s00531-004-0413-8

Linnemann, U., Gerdes, A., Drost, K., Buschmann, B, 2007. The continuum between Cadomian orogenesis and opening of the Rheic Ocean: Constraints from LA-ICP-MS U-Pb zircon dating and analysis of plate-tectonic setting (Saxo-Thuringian zone, northeastern Bohemian Massif, Germany). Geological Society of America Special Papers 423, 61-96. doi:10.1130/2007.2423(03)

Linnen, R.L., 1991. Contrasting origins of Sn-W mineralization in western Thailand. Phd Thesis, McGill University, Montreal. 415 pp.

Linnen, R. L., Williams-Jones, A.E. 1995. Genesis of a magmatic metamorphic hydrothermal system; the Sn-W polymetallic deposits at Pilok, Thailand. Economic Geology, 90: 1148-1166. doi:10.2113/gsecongeo.90.5.1148

Linnen, R.L., Keppler, H., 1997. Columbite solubility in granitic melts: consequences for the enrichment and fractionation of Nb and Ta in the Earth's crust. Contributions to Mineralogy and Petrology 128, 213–227. doi:10.1007/s004100050304

Linnen, R.L., 1998. Depth of emplacement, fluid provenance and metallogeny in granitic terranes: a comparison of western Thailand with other tin belts. Mineralium Deposita 33, 461-476. doi:10.1007/s001260050163

Linnen, R.L., Keppler, H., 2002. Melt composition control of Zr/Hf fractionation in magmatic processes. Geochimica et Cosmochimica Acta 66, 3293-3301. doi:10.1016/S0016-7037(02)00924-9

Liu, L.M., Peng, S.L., 2004. Prediction of hidden ore bodies by synthesis of geological, geophysical and geochemical information based on dynamic model in Fenghuangshan ore field, Tongling district, China. Journal of Geochemical Exploration 81, 81-98.doi:10.1016/j.gexplo.2003.08.004

Llorens, T., 2011. La mineralizaciones magmático-hidrotermales de Sn-W-(Nb-Ta) del distrito de Navasfrías (SO de Salamanca). PhD Thesis. Universidad de Salamanca, 355 pp.

Llorens, T., Moro, M.C., 2012a. Oxide minerals in the granitic cupola of the Jálama Batholith, Salamanca, Spain. Part I: accessory Sn, Nb, Ta and Ti minerals in leucogranites, aplites and pegmatites. Journal of Geosciences 57, 25-43. doi:10.3190/jgeosci.113

Llorens, T., Moro, M.C., 2012b. Oxide minerals in the granitic cupola of the Jálama Batholith, Salamanca, Spain. Part II: Sn, W and Ti minerals in intra-granitic quartz veins. Journal of Geosciences 57, 155–171. doi:10.3190/jgeosci.119

Locutura, J., Alcalde C. (Eds.), 2007. Mapa Metalogenético de Extremadura a escala 1:250.000. IGME-Junta de Extremadura.

London, D., 1990. Internal differentiation of rare-element pegmatites; a synthesis of recent research. Geological Society of America, Special Papers 246, 35-50.

London, D., Manning, D.A. 1995. Chemical variation and significance of tourmaline from Southwest England. Economic geology, 90: 495-519. doi: 10.2113/gsecongeo.90.3.495

López Plaza, M., Martínez Catalán, J.M., 1987. Síntesis estructural de los granitoides del Macizo Hespérico. In: Bea, F. Carnicero, A. Gonzalo, J.C. López Plaza, M. Rodríguez Alonso M.D. (Eds.), Geología de los granitoides y rocas asociadas del Macizo Hespérico. Rueda, Madrid, pp. 195-220.

López-Guijarro, R., Armendáriz, M., Fernández-Suárez, J., Quesada, C., Murphy, J.B., Pin, Ch., Bellido F., 2008. Ediacaran–Palaeozoic tectonic evolution of the Ossa Morena and Central Iberian zones (SW Iberia) as revealed by Sm–Nd isotope systematics. Tectonophysics 461, 202-214. doi:10.1016/j.tecto.2008.06.006

López-Moro, F.J., López-Plaza, M., Romer, R.L., 2012. Generation and emplacement of shear-related highly mobile crustal melts: the synkinematic leucogranites from the Variscan Tormes Dome, Western Spain. International Journal of Earth Sciences 101, 1273-1298. doi:10.1007/s00531-011-0728-1

Lotze, F., 1945. Zur gliederung des Varisciden der Iberischen Meseta. GeotektonischeForschungen 6, 78–92.

Ludwig, K.R., 2003. User's manual for Isoplot 3.00: A geochronological toolkit for Microsoft Excel. Kenneth R. Ludwig.

Mangas J., Arribas, A., 1987. Fluid inclusion study in different types of tin deposits associated with the Hercynian granites of western Spain. Chemical Geology 61, 1–4, 193–208. doi:10.1016/0009-2541(87)90039-8

Mangas, J., Arribas, A., 1988. Hydrothermal fluid evolution of the Sn-W mineralization in the Parrilla ore deposit (Caceres, Spain). Journal of the Geological Society 145, 147-155. doi: 10.1144/gsjgs.145.1.0147

Manning, D., Pichavant, M., 1984. Experimental studies of the role of fluorine and boron in the formation of late-stage granitic rocks and associated mineralisation. Mezhdunarodnyj geologicheskij kongress 27, pp. 386-387

Manning, D.A.C., Pichavant, M. 1983. The role of fluorine and boron in the generation of granitic melts. Migmatites, melting and metamorphism 94, 1153-1154.

Marignac, C., Cuney, M., 1999. Ore deposits of the French Massif Central: insight into the metallogenesis of the Variscan collision belt. Mineralium Deposita 34, 472-504. doi: 10.1007/s001260050216

Mark D.M., Barfod D.N., Stuart F.M., Imlach J., 2009. The ARGUS multi-collector noble gas mass spectrometer: Performance for $^{40}Ar/^{39}Ar$ geochronology. Geochemistry Geophysics Geosystems 10, 1-13. doi:10.1029/2009GC002643

Martín Crespo, T., Delgado, A., Vindel, E., López-García, J.A., Fabre, C., 2002. The latest Post-Variscan fluids in the Spanish Central System: evidence from fluid inclusion and stable isotope data. Marine and Petroleum Geology 19, 323-337. doi: 10.1016/S0264-8172(02)00020-X

Martínez Catalán, J.R., Arenas, R., García, F.D., Cuadra, P.G., Gómez-Barreiro, J., González Cuadra, P., Abati, J., Castiñeiras, P., Fernández-Suárez, J., Sánchez Martínez, S., Andonaegui, P., González Clavijo, E., Díez Montes, A., Rubio Pascual, F.J., Aguado, B.V., 2007. Space and time in the tectonic evolution of the northwestern Iberian Massif. Implications for the comprehension of the Variscan belt. In: Hatcher, R.D. Jr. Carlson, M.P. McBride, J.H. and Martínez Catalán, J.R. (Eds.), 4-D Framework of Continental Crust.Geological Society of America Memoir, v. 200, p. 403-423. Boulder, Colorado. doi: 10.1130/2007.1200(21)

Martínez Catalán, J.R., 2011, Are the oroclines of the Variscan belt related to late Variscan strike-slip tectonics?: Terra Nova 23, 241–247. doi:10.1111/j.1365-3121.2011.01005.x

Martínez Catalán, J.R., 2012. The Central Iberian arc, an orocline centered in the Iberian Massif and some implications for the Variscan belt. International Journal of Earth Sciences 101, 1299-1314. doi:10.1007/s00531-011-0715-6

Martínez-Abad, I, Cepedal, A., Arias, D., Martín-Izard, A., 2015. The Vilalba gold district, a new discovery in the Variscan terranes of the NW of Spain: A geologic, fluid inclusion and stable isotope study. Ore Geology Reviews 66, 344-365. doi:10.1016/j.oregeorev.2014.10.021

Martins, H.C.B., Sant'Ovaia, H., Noronha, F., 2009. Genesis and emplacement of felsic Variscan plutons within a deep crustal lineation, the Penacova-Régua-Verín fault: an integrated geophysics and geochemical study (NW Iberian Peninsula). Lithos 111, 142-155. doi:10.1016/j.lithos.2008.10.018

Martins, T., Lima, A., Simmons, W.B., Falster, A.U., Noronha, F., 2011. Geochemical fractionation of Nb-Ta oxides in Li-bearing pegmatites from the Barroso-Alvao pegmatite field, Northern Portugal. Canadian Mineralogist 49, 777-791. doi:10.3749/canmin.49.3.777

Mateus, A., Noronha, F., 2001. Late-Variscan uplift of the Iberian Terrane as a response to isostatic rebound; implications for the brittle-ductile transition, fluid circulation and metallogenesis. Memorias del Museo y Laboratorio Mineralógico y Geológico, de la Facultad de Ciencias, Universidad de Oporto 7, 295-298.

Mateus, A., Noronha, F., 2010. Sistemas mineralizantes epigenéticos na Zona Centro-Ibérica; expressão da estruturação orogénica meso- a tardivarisca. In: Cotelo Neiva, J.M., Ribeiro, A., Mendes Victor, L., Noronha, F., Magalhães Ramalho, M. (Eds). Ciências Geológicas: Ensino, Investigação e sua História Vol. II, Geologia Aplicada, pp. 47-61.

Matte, P., 1986. Tectonics and plate tectonics model for the Variscan belt of Europe. Tectonophysics 126, 329–374. doi: 10.1016/0040-1951(86)90237-4

Matte, P., 1991. Accretionary history and crustal evolution of the Variscan Belt in western Europe. Tectonophysics 196, 309–339. doi: 10.1016/0040-1951(91)90328-P

Matte, P., 2001. The Variscan collage and orogeny (480–290 Ma) and the tectonic definition of the Armorica microplate: a review. Terra nova 13, 122-128. doi:10.1046/j.1365-3121.2001.00327.x

Mattinson, J.M., 2005. Zircon U–Pb chemical abrasion ("CA-TIMS") method: combined annealing and multi-step partial dissolution analysis for improved precision and accuracy of zircon ages. Chemical Geology 220, 47-66. doi:10.1016/j.chemgeo.2005.03.011

McCrea, J.M., 1950. On the isotopic chemistry of carbonates and a paleotemperature scale. The Journal of Chemical Physics 18, 849-857. doi: 10.1063/1.1747785

McDonough, W.F., Sun, S., 1995. The composition of the Earth. Chemical Geology 120, 223-253. doi: 10.1016/0009-2541(94)00140-4

Mendes, A.C., Dias, G., 2004. Mantle-like Sr–Nd isotope composition of Fe–K subalkaline granites: the Peneda–Gerês Variscan massif (NW Iberian Peninsula). Terra Nova 16, 109-115. doi:10.1111/j.1365-3121.2004.00537.x

Menéndez, L.G., Bea, F., 2004. El batolito Nisa-Alburquerque. In: Vera, J.A. (Ed.), Geología de España. IGME-SGE, Madrid, pp.120-122.

Meredith, C., 1998. La Mina El Cerro de San Cristobal: a Bronze Age tin mine (Extremadura, Spain). Papers from the Institute of Archaeology, 9, 57-69.

Merino, 2014. Geochemistry, U–Pb geochronology and Hf-isotope zircon composition of Variscan granitoids from the Montes de Toledo batholith. PhD Thesis. Universidad Complutense de Madrid, 299 pp.

Merino, E., Villaseca, C., Orejana, D., Jeffries, T., 2013. Gahnite, chrysoberyl and beryl co-occurrences as accessory minerals in a highly evolved peraluminous pluton: The Belvís de Monroy leucogranite (Cáceres, Spain). Lithos 179, 137-156. doi:10.1016/j.lithos.2013.08.004

Merino, E., Villaseca, C., Orejana, D., Pérez-Soba, C., Belousova, E., Andersen, T., 2014. Tracing magmasources of three different S-type peraluminous granitoid series by in situ U-PB geochronology and Hf-isotope zircon composition: the Variscan Montes de Toledo batholith (central Spain) Lithos. doi:10.1016/j.lithos.2014.04.013

Mezcúa J., Gil A., Benarroch, R., 1996. Estudio gravimétrico de la Península Ibérica y Baleares. Instituto Geográfico Nacional, Madrid, 19 pp.

Miller, C.F., Stoddard, E.F., Bradfish, L.J., Dollase, W.A., 1981. Composition of plutonic muscovite: genetic implications. The Canadian Mineralogist 19: 25-34.

Miller, C.F., McDowell, S.M., Mapes, R.W., 2003. Hot and cold granites? Implications of zircon saturation temperatures and preservation of inheritance. Geology 31, 529-532. doi:10.1130/0091-76132003)031<0529:HACGIO>2.0.CO;2

Mlynarczyk, M.S., Sherlock, R.L., Williams-Jones, A.E., 2003. San Rafael, Peru: geology and structure of the worlds richest tin lode. Mineralium Deposita 38, 555-567. doi:10.1007/s00126-002-0334-z

Mlynarczyk, M. S., Williams-Jones, A. E., 2006. Zoned tourmaline associated with cassiterite: implications for fluid evolution and tin mineralization in the San Rafael Sn–Cu deposit, southeastern Peru. The Canadian Mineralogist 44, 347-365.doi:10.2113/gscanmin.44.2.347

Monier, G., Robert, J. L., 1986. Muscovite solid solutions in the system K_2O-MgO-FeO-Al_2O_3-SiO_2-H_2O: an experimental study at 2 kbar PH_2O and comparison with natural Li-free white micas. Mineralogical Magazine 50: 257-266.

Montero, P., Talavera, C., Bea, F., Lodeiro, F.G., Whitehouse, M. J., 2009. Zircon geochronology of the Ollo de Sapo Formation and the age of the Cambro-Ordovician rifting in Iberia. The Journal of Geology 117, 174-191. doi:10.1086/595017

Moreno Ventas, I., Rogers, G., Castro, A., 1995. The role of hybridization in the genesis of Hercynian granitodis in the gredos massif, Spain: inferences from Sr-Nd isotopes. Contributions to Mineralogy and Petrology 120, 137-149. doi:10.1007/BF00287111

Moreno, F., Matas J., Leyva, F., Díez, A., Fuente, J.V., Carrasco, A., Gutiérrez J.C., 2004. Memoria explicativa Hoja 732 (Valdecaballeros). In: V. Monteserín (Eds.) Mapa geológico de España. E: 1:50.000. IGME, Madrid.

Moura, A., Dória, A., Neiva, A. M. R., Leal Gomes, C., Creaser, R. A., 2014. Metallogenesis at the Carris W–Mo–Sn deposit (Gerês, Portugal): constraints from fluid inclusions, mineral geochemistry, Re–Os and He–Ar isotopes. Ore Geology Reviews 56, 73-93. doi:10.1016/j.oregeorev.2013.08.001

Müller, A., Halls, C., 2005. Rutile – the tin–tungsten host in the intrusive tourmaline breccia at Wheal Remfry, SW England. In: Mao, J., Bierle F.P. (Eds.), Mineral Deposit Research: Meeting the Global Challenge. Proceedings of the Eighth Biennial SGA Meeting. Springer Berlin Heidelberg, pp 441–444.

Murciego, A., García Sánchez, A., Dusausoy, Y., Martín Pozas, J.M., Ruck, R., 1997. Geochemistry and EPR of cassiterites from the Iberian Hercynian Massif. Mineralogical Magazine, 61: 357-365.

Murphy, J.B., Gutierrez-Alonso, G., Nance, R.D., Fernandez-Suarez, J., Keppie, J.D., Quesada, C., Strachan, R.A., Dostal, J., 2006. Origin of the Rheic Ocean: rifting along a Neoproterozoic suture? Geology 34, 325–328. doi:10.1130/G22068.1

Murphy, J.B., Nance, R.D., 2008. The Pangea conundrum. Geology 36, 703-706. doi: 10.1130/G24966A.1

Murphy, J. B., Keppie, J. D., Nance, R. D., Dostal, J., 2010. Comparative evolution of the Iapetus and Rheic Oceans: a North America perspective. Gondwana Research 17, 482-499. doi:10.1016/j.gr.2009.08.009.

Nachit, H., Razafimahefa, N., Stussi, J.M., Carron, J.P., 1985. Composition chimique des biotites et typologie magmatique des granitoides. Comptes rendus de l'Académie des sciences. Série 2, Mécanique, Physique, Chimie, Sciences de l'univers, Sciences de la Terre 301: 813-818.

Nance, R.D., Linnemann, U., 2008. The Rheic Ocean: origin, evolution and significance. GSA Today 18, 4–12. doi: 10.1130/GSATG24A.1

Nance, R.D., Murphy, J.B., Strachan, R.A., Keppie, J.D., Gutiérrez-Alonso, G., Fernández-Suárez, J., Quesada, C., Linnemann, U., D'Lemos, R.S. and Pisarevsky, S.A., 2008. Neoproterozoic-early Paleozoic paleogeography of the peri-Gondwanan terranes: Amazonian versus West African connections. In: Ennih,

N. and Liégeois, J.P. (Eds.), The Boundaries of the West African Craton. Geological Society of London, Special Publication 297, pp. 345-383.

Nance, R.D., Keppie, J.D., Miller, B.V., Murphy, J.B., Dostal, J., 2009. 1Palaeozoic palaeogeography of Mexico: constraints from detrital zircon age data. Geological Society of London Special Publication 327, 239–269 doi: 10.1144/SP327.12.

Nance, R.D., Gutiérrez-Alonso, G., Keppie, J.D., Linnemann, U., Murphy, J.B., Quesada, C., Strachan, R.A., Woodcock, N.H., 2010. Evolution of the Rheic Ocean. Gondwana Research 17, 194-222. doi: 10.1016/j.gr.2009.08.001

Naranjo F., Peñuelas, L., 1860. Extracto de una memoria sobre la fosforita de Logrosán. Madrid.

Neiva, A.M.R., 1996. Geochemistry of cassiterite and its inclusions and exsolution products from tin and tungsten deposits in Portugal. Canadian Mineral 34, 745–768.

Neiva, A.M.R., 2008. Geochemistry of cassiterite and wolframite from tin and tungsten quartz veins in Portugal. Ore Geology Reviews 33, 221-238. doi:10.1016/j.oregeorev.2006.05.013

Neiva, A.M.R., Williams, I.S., Ramos, J.M.F., Gomes, M.E.P., Silva, M.M.V.G., Antunes, I.M.H.R., 2009. Geochemical and isotopic constraints on the petrogenesis of Early Ordovician granodiorite and Variscan two-mica granites from the Gouveia area, central Portugal. Lithos 111, 186–202. doi:10.1016/j.lithos.2009.01.005

Neiva, A. M. R., Silva, P.B., Corfu, F., Ramos, J.M.F., 2011. Sequential melting and fractional crystallization: Granites from Guarda-Sabugal area, central Portugal. Chemie der Erde-Geochemistry 71, 227-245. doi:10.1016/j.chemer.2011.06.002

Neiva, A., Teixeira, R., Lima, S., Silva, P., 2013. Idade, origem e protólitos de granitos Variscos de três áreas portuguesas. Memorias da Academia das Ciências de Lisboa, Classe Ciências, Lisboa, 13 pp.

Nekrasov, I.J., Sorokin, V.I., Osadchii, E.G., 1979. Fe and Zn partitioning between stannite and sphalerite and its application in geothermometry. Physics and Chemistry of the Earth 11, 739-742.

Noronha, F., Doria, A., Dubessy, J., Charoy, B., 1992. Characterization and timing of the different types of fluids present in the barren and ore-veins of the W-Sn deposit of Panasqueira, Central Portugal. Mineralium Deposita 27, 72-79. doi:10.1007/BF00196084

Noronha, F., Vindel Catena, E., López García, J.Á., Dória, A., García García, E., Boiron, M.C., Cathelineau, M., 1999. Fluids related to tungsten ore deposits in Northern Portugal and Spanish Central System: a comparative study. Revista de la Sociedad Geológica de España 12, 397-403.

O'Neil J. R., 1986. Theoretical and experimental aspects of isotopic fractionation. In: Valley, J.W., Taylor, H.P. and O'Neil, J.R. (Eds.), Stable Isotopes in High Temperature Geological Processes. Reviews in Mineralogy 16, pp. 1–16.

O'Neil, J.R., Taylor, H.P., 1967. The oxygen isotope and cation exchange chemistry of feldspars. American Mineralogist 52, 1414-1437.

Ohmoto, H., 1972. Systematics of sulfur and carbon isotopes in hydrothermal ore deposits. Economic Geology 67, 551-578.

Ohmoto, H., 1986. Stable isotope geochemistry of ore deposits. Reviews in Mineralogy and Geochemistry 16, 491-559.

Ohmoto, H.Y, Rye, R.O., 1979: Isotopes of sulfur and carbon. In: Wiley, J. and Sons (Eds.), Geochemistry of hydrothermal ore deposits. New York, pp. 509-567.

Orejana, D., Merino, E., Villaseca, C., Pérez-Soba, C., Cuesta, A., 2011. Electron microprobe monazite geochronology of granitic intrusions from the Montes de Toledo batholith (central Spain). The Journal of Geology 47, 41-58. doi:10.1002/gj.1331

Orejana, D., Villaseca, C., Valverde-Vaquero, P., Belousova, E.A., Armstrong, R.A., 2012. U–Pb geochronology and zircon composition of late Variscan S-and I-type granitoids from the Spanish Central System batholith. International Journal of Earth Sciences 101, 1789-1815. doi: 10.1007/s00531-012-0750-y

Orejana, D., Merino Martínez, E., Villaseca, C. y Andersen, T., 2015. Ediacaran-Cambrian paleogeography and geodynamic setting of the Central Iberian one: constraints from coupled U-Pb-Hf isotopes of detrital zircons. Precambrian Research 261: 234-251. doi:10.1016/j.precamres.2015.02.009

Ortega, L., Oyarzun, R., Gallego, M., 1996. The Mari Rosa late Hercynian Sb-Au deposit, western Spain. Mineralium Deposita 31, 172-187. doi:10.1007/BF00204025

Pavón Soldevila, I., Rodríguez Díaz, A., Navascués, J.J.E., 1998. El poblamiento protohistórico en el Tajo Medio: Excavaciones de urgencia en El Risco y Aliseda (Cáceres). In: Extremadura Protohistórica: paleoambiente, economía y poblamiento. Servicio de Publicaciones de la Universidad de Extremadura, Cáceres, pp. 121-156.

Pavón Soldevila, I., Rodríguez Díaz, A., Duque Espino, D.M., 2010. El estaño de Logrosán, Extremadura y Tartessos. II Jornadas Internacionales de Historia y Literatura en la comarca de Las Villuercas. Investigación y didáctica, 35-64.

Perconig, E., Vázquez, F., Velando, F., Leyva, F., 1986. Proterozoic and Cambrian phosphorites-deposits: Fontanarejo, Spain. In: Cook, P.J., Shergold, J.H. (Eds.), Phosphate deposits of the world 1. Cambridge University Press, Cambridge, pp. 220-234.

Pereira, E., Ribeiro, A., Meireles, C., 1993. Cisalhamentos hercínicos e controlo das mineralizações de Sn–W, Au e U na Zona Centro-Ibérica, em Portugal. Cadernos do Laboratorio Xeolóxico de Laxe 18, 89–119.

Pereira, M.D., Shaw, D.M., 1997. Behaviour of boron in the generation of an anatectic complex: The Pen˜ a Negra complex, central Spain. Lithos 40, 179-188. doi:10.1016/S0024-4937(97)00009-1

Pereira, M.F., Linnemann, U., Hofmann, M., Chichorro, M., Solá. A. R., Medina, J., Silva, J. B., 2012. The provenance of Late Ediacaran and Early Ordovician siliciclastic rocks in the Southwest Central Iberian Zone: Constraints from detrital zircon data on northern Gondwana margin evolution during the late Neoproterozoic. Precambrian Research 192, 166-189. doi:10.1016/j.precamres.2011.10.019

Pérez-Soba, C., Villaseca, C., Del Tánago, J.G., Nasdala, L., 2007. The composition of zircon in the peraluminous Hercynian granites of the Spanish Central System batholith. The Canadian Mineralogist 45, 509-527. doi:10.2113/gscanmin.45.3.509

Pérez-Soba, C., Villaseca, C., Orejana, D., Jeffries, T., 2014. Uranium-rich accessory minerals in the peraluminous and perphosphorous Belvís de Monroy pluton (Iberian Variscan belt). Contributions to Mineralogy and Petrology 167, 1-25. doi: 10.1007/s00410-014-1008-4

Pichavant, M., 1981. An experimental study of the effect of boron on a water-saturated haplogranite at 1 Kbar vapour pressure. Contributions to Mineralogy and Petrology 76, 430-439.

Pichavant, M., Kontak, D.J., Herrera, J.V. Clark, A.H., 1988. The Miocene–Pliocene Masucani volcanics, SE Peru I. Mineralogy and magmatic evolution of a two-mica aluminosilicate-bearing ignimbrite suite. Contributions to Mineralogy and Petrology 100, 300–324. doi:10.1007/BF00379741

Pirajno, F., 1992. Hydrothermal Mineral Deposits. Principles and Fundamental Concepts for the Exploration Geologist. Springer-Verlag, Berlin. 709 pp.

Pirajno, F., Smithies, R. H., 1992. The FeO/(FeO+ MgO) ratio of tourmaline: a useful indicator of spatial variations in granite-related hydrothermal mineral deposits. Journal of Geochemical Exploration 42, 371-381.

Pohl, W., Günther, M. A., 1991. The origin of Kibaran (late Mid-Proterozoic) tin, tungsten and gold quartz vein deposits in Central Africa: a fluid inclusions study. Mineralium Deposita 26, 51-59. doi: 10.1007/BF00202365

Pohl, W.L., 2011. Economic Geology. Principles and Practice. John Wiley & Sons. 663 pp.

Pollard, P. J., Pichavant, M., Charoy, B., 1987. Contrasting evolution of fluorine-and boron-rich tin systems. Mineralium Deposita 22: 315-321. doi:10.1007/BF00204525

Polyakov, V.B., Mineev, S.D., Clayton, R.N., Hu, G., Gurevich, V.M., Khramov, D.A., Gavrichev, K.S., Gorbunov, V.E., Golushina L.N., 2005. Oxygen isotope fractionation factors involving cassiterite (SnO2): I. Calculation of reduced partition function ratios from heat capacity and X-ray resonant studies. Geochimica et Cosmochimica Acta 69: 1287–1300. doi: 10.1016/j.gca.2004.08.034

Proust, L., 1799. Sobre la piedra fosfórica de Extremadura. Anales del Real Laboratorio de Química de Segovia, 1, 439-450, and 453-456.

Pupin, J.P., 2000. Granite genesis related to geodynamics from Hf-Y in zircon. Transactions-Royal Society of Edinburgh 91, 245-256. doi:10.1130/0-8137-2350-7.245

Quesada, C., 1991. Geological constraints on the Paleozoic tectonic evolution of tectonostratigraphic terranes in the Iberian Massif. Tectonophysics 185, 225-245. doi:10.1016/0040-1951(91)90446-Y

Quesada, C., Dallmeyer, R. D., 1994. Tectonothermal evolution of the Badajoz-Córdoba shear zone (SW Iberia): characteristics and $^{40}Ar/^{39}Ar$ mineral age constraints. Tectonophysics 231, 195-213. doi:10.1016/0040-1951(94)90130-9

Quesada, C., Linnemann, U., D'Lemos, R., and Pisarevsky, S.A., 2008. Neoproterozoic-early Paleozoic tectonostratigraphy and palaeogeography of the peri-Gondwanan terranes: Amazonian versus West African connections. In: Ennih, N., and Liégeois, J.P. (Eds.), The boundaries of the West African Craton. Geological Society of London, Special Publication 297, pp. 345–383

Rambaud, F., Caraballo, J.M., Barrera, J.L., 1983. Los yacimientos de cuarzo-apatito (fosforita) en el Macizo Hespérico Español: el caso de Aldea Moret-Zarza la Mayor (Cáceres). Cuadernos do Laboratorio Xeolóxico de Laxe 6, 387-408.

Ramboz, C., Schnapper, D., Dubessy, J., 1985. The evolution of H_2O-CO_2-CH_4-bearing fluid in a wolframite vein: Reconstruction from fluid inclusion studies. Geochimica et Cosmochimica Acta 49, 205-219. doi:10.1016/0016-7037(85)90205-4

Ramírez, J., Menéndez, L., 1999. A geochemical study of two peraluminous granites from south-central Iberia; the Nisa-Albuquerque and Jalama batholiths. Mineralogical Magazine 63, 85-104. doi:10.1180/002646199548330

Recio, C., Fallick, A., Ugidos, J., 1992. A stable isotopic (δ18O, δD) study of late Hercynian granites and their host-rocks in the Central Iberian Massif (Spain). Transactions-Royal Society of Edinburgh 83, 247-257. doi:10.1017/S0263593300007938

Renne, P.R., Balco, G., Ludwig, K.R., Mundil, R., Min, K., 2011. Response to the comment by W.H. Schwarz et al. on Joint determination of K-40 decay constants and Ar-40*/K-40 for the Fish Canyon sanidine standard, and improved accuracy for Ar-40/Ar-39 geochronology by PR Renne, et al. (2010). Geochimica et Cosmochimica Acta 75, 5097–5100. doi:10.1016/j.gca.2011.06.021.

Ribeiro, A., 1990. Central-Iberian Zone: Introduction. In: R.D. Dallmeyer, E. Martínez García, (Eds.), Pre-Mesozoic Geology of Iberia. Springer Verlag, Berlín, pp. 143-144.

Ricken, W., Schrader, S., Oncken, O., Plesch, A., 2000. Turbidite basin and mass dynamics related to orogenic wedge growth; the Rheno-Hercynian case. Geological Society of London, Special Publications 179, 257-280. doi:10.1144/GSL.SP.2000.179.01.16

Rieder, M., Cavazzini, G., D'yakonov, Y. S., Frank-Kamenetskii, V. A., Gottardi, G., Guggenheim, S., Koval, P.V., Müller, G., Neiva, A. M. R., Radoslovich, E., Robert, J.L., Sassi, F.P., Takeda, H., Weiss, Z., Wones, D. R., 1999. Nomenclature of the micas. Mineralogical Magazine 63, 267-279.

Rivas Dorado, S., 2013. Cartografía y caracterización mineral de la mina de fosfato "La Costanaza", Logrosán (Cáceres). Unpublished Master Thesis, Universidad Complutense de Madrid.

Roda-Robles, E., Pesquera, A., Gil, P.P., Torres-Ruiz, J., Fontan, F., 2004. Tourmaline from the rare-element Pinilla pegmatite (Central Iberian Zone, Zamora, Spain): chemical variation and implications for pegmatitic evolution. Mineralogy and Petrology 81, 249-263. doi: 10.1007/s00710-004-0042-8

Roda-Robles, E., Vieeira, R., Pesquera, A., Lima, A., 2010. Chemical variations and significance of phosphates from the Fregeneda-Almendra pegmatite field, Central Iberian Zone (Spain and Portugal). Mineralogy and Petrology 100, 23-34. doi:10.1007/s00710-010-0117-7

Roda-Robles, E., Pesquera, A., Gil-Crespo, P. P., & Torres-Ruiz, J., 2011. Occurrence, paragenesis and compositional evolution of tourmaline from the Tormes Dome area, Central Iberian Zone, Spain. The Canadian Mineralogist 49, 207-224. doi: 10.3749/canmin.49.1.207

Roda-Robles, E., Pesquera, A., Gil-Crespo, P., Torres-Ruiz, J., 2012. From granite to highly evolved pegmatite: A case study of the Pinilla de Fermoselle granite-pegmatite system (Zamora, Spain). Lithos 153, 192-207. doi:10.1016/j.lithos.2012.04.027

Rodríguez Alonso, M.D., Díez Balda, M.A., Perejón, A., Pieren, A., Liñán, E., López Díaz, F., Moreno, F., Gámez Vintaned, J.A., González Lodeiro, F., Martínez Poyatos, D., Vegas, R., 2004. La secuencia litoestratigráfica del Neoproterozoico-Cámbrico Inferior. In: Vera, J.A. (Ed.). Geología de España. SGE-IGME, Madrid, pp.78-81.

Rodríguez Díaz, A., Pavón Soldevila, I., Duque Espino, D.M., Ponce de León Iglesias, M., Hunt Ortiz, M.A., Merideth, C., 2013. La explotación tartésica de la casiterita entre los ríos Tajo y Guadiana: San Cristóbal de Logrosán (Cáceres). Trabajos de Prehistoria 70, 95-113.

Rodríguez, L.R., López, F., Martín, J., Rubio, F., 2008. Mapa Geológico de la Península Ibérica, Baleares y Canarias, E: 1: 1.000.000. IGME, Madrid.

Roedder, E., Bodnar, R.J., 1980. Geologic pressure determinations from fluid inclusion studies. Annual Review of Earth and Planetary Sciences 8, 263.

Roedder, E., 1984. Fluid inclusions. Reviews in Mineralogy 12. Mineralogical Society of America, Michigan. 646 pp.

Rollinson, H.R., 1993. Using geochemical data: evaluation, presentation, interpretation. Longman, Harlow. 352 pp.

Roman-Berdiel, T., Gapais, D., Brun, J.P., 1995. Analogue model of laccolith formation. Journal of Structural Geology 17, 1337–1346. doi:10.1016/0191-8141(95)00012-3

Romeo, I., Tejero, R., Capote, R., Lunar, R., 2008. 3D gravity modelling of the Aguablanca Stock, tectonic control and emplacement of a Variscan gabbronorite bearing a Ni–Cu–PGE ore, SW Iberia. Geological Magazine 145, 345-359. doi:10.1017/S0016756808004470

Romer, R. L., Thomas, R., Stein, H. J., Rhede, D. 2007. Dating multiply overprinted Sn-mineralized granites-examples from the Erzgebirge, Germany. Mineralium Deposita 42, 337-359. doi:10.1007/s00126-006-0114-2

Rønsbo, J.G., 2008. Apatite in the Ilímaussaq alkaline complex: Occurrence, zonation and compositional variation. Lithos 106, 71-82. doi:10.1016/j.lithos.2008.06.006

Roskill Market Outlook Reports, 2015. Tin 2015 9th edition. 8 pp.

Roso de Luna, M., 1898. Logrosán (Legajo histórico). 385 pp.

Rossi, P., 1975. Géologie et gitologie du Cerro San Cristóbal, Logrosán, Cáceres, Espagne. Thèse Laboratoire de géologie structurale et appliquée d'Orsay, Université de Paris Sud. Orsay. 86 pp.

Routhier, P., Aye, F., Boyer, C., Lecolle, M., Molière, P., Picot P., Roger, G., 1978. La Ceinture sud-ibérique à amas sulfurés dans sa partie espagnole médiane: tableau géologique et métallogénique: synthèse sur le type amas sulfurés volcano-sédimentaires. Mémoire du BRGM 94, 265 pp.

Rubio Ordóñez, A., Valverde-Vaquero, P., Corretgé, L.G., Cuesta-Fernández, A., Gallastegui, G., Fernández-González, M., Gerdes, A., 2012. An Early Ordovician tonalitic–granodioritic belt along the Schistose-Greywacke domain of the Central Iberian zone (Iberian Massif, Variscan belt). Geological Magazine 149, 927. doi:10.1017/S0016756811001129

Ruiz, C., Fernández-Leyva, C., Locutura, J., 2008. Geochemistry, geochronology and mineralisation potential of the granites in the Central Iberian Zone: the Jálama Batholith. Chemie der Erde-Geochemistry 68, 413-429. doi:10.1016/j.chemer.2006.11.001

Ryzhenko, B., Kovalenko, N., Prisyagina, N., 2006. Titanium complexation in hydrothermal systems. Geochemistry International 44, 879–895. doi:10.1134/S0016702906090047

Saavedra Alonso, J., Pellitero Pascual, E., García-Sánchez, A., Madruga, F., 1977. Estudio del granito mineralizado del Jálama, Salamanca-Cáceres, España. Boletin Geológico y Minero 88, 333-344.

Sánchez Martínez, S., Arenas, R., Fernández-Suárez, J., Jeffries, T.E., 2009. From Rodinia to Pangaea: ophiolites from NW Iberia as witness for a long-lived continental margin. Geological Society of London, Special Publications 327, 317-341. doi: 10.1144/SP327.14

Sánchez-García, T., Bellido, F., Pereira, M. F., Chichorro, M., Quesada, C., Pin, C., Silva, J.B., 2010). Rift-related volcanism predating the birth of the Rheic Ocean (Ossa-Morena zone, SW Iberia). Gondwana Research 17, 392-407. doi:10.1016/j.gr.2009.10.005

Scherer, E., Münker, C., Mezger, K., 2001. Calibration of the lutetium-hafnium clock. Science 293, 683-687. doi:10.1126/science.1061372

Scotese, C.R., 1997. Continental Drift, 7th ed. PALEOMAP Project, Arlington, Texas. 79 pp.

Sha, L-K., Chappell, B.W., 1999. Apatite chemical composition, determined by electron microprobe and laser-ablation inductively coupled plasma mass spectrometry, as a probe into granite petrogenesis. Geochimica et Cosmochimica Acta 63, 3861-3881. doi: 10.1016/S0016-7037(99)00210-0

Sharp, Z. D., Essene, E. J., Kelly, W. C., 1985. A re-examination of the arsenopyrite geothermometer: pressure considerations and applications to natural assemblages. Journal of the Mineralogical Association of Canada 23, 517-534.

Shepherd, T. J., Bottrell, S. H., Miller, M. F., 1991. Fluid inclusion volatiles as an exploration guide to black shale-hosted gold deposits, Dolgellau gold belt, North Wales, UK. Journal of Geochemical Exploration 42, 5-24. doi:10.1016/0375-6742(91)90058-3

Sheppard, S.M., 1986. Characterization and isotopic variations in natural waters. Reviews in Mineralogy and Geochemistry 16, 165-183.

Sheppard, S.M., Nielsen, R.L., Taylor, H.P., 1969. Oxygen and hydrogen isotope ratios of clay minerals from porphyry copper deposits. Economic Geology 64, 755-777. doi:10.2113/gsecongeo.64.7.755

Sheppard, S.M.F., 1977. The Cornubian batholith, SW England: D/H and $^{18}O/^{16}O$ studies of kaolinite and other alteration minerals. Journal of the Geological Society 133, 573-591. doi: 10.1144/gsjgs.133.6.0573

Sillitoe, R.H., 1994. Erosion and collapse of volcanoes: Causes of telescoping in intrusion-centered ore deposits. Geology 22, 945-948. doi:10.1130/0091-7613(1994)022<0945:EACOVC>2.3.CO;2

Snee, L.W., Sutter, J.F., Kelly, W.C., 1988. Thermochronology of economic mineral deposits; dating the stages of mineralization at Panasqueira, Portugal, by high-precision $^{40}/^{39}Ar$ age spectrum techniques on muscovite. Economic Geology 83, 335-354. doi:10.2113/gsecongeo.83.2.335

Soave, G., 1972. Equilibrium constants from a modified Redlich-Kwong equation of state. Chemical Engineering Science 27, 1197-1203. doi:10.1016/0009-2509(72)80096-4

Söderlund, U., Johansson, L., 2002. A simple way to extract baddeleyite (ZrO_2). Geochemisty Geophysics Geosystems 3, 1–7. doi:10.1029/2001GC000212

Solá, A.R., Pereira, M.F., Williams, I.S., Ribeiro, M.L., Neiva, A.M.R. Bea, F., Zinger, T., 2008. New insights from U-Pb zircon dating of Early Ordovician magmatism on the northern Gondwana margin: The Urra Formation (SW Iberian Massif, Portugal). Tectonophysics 461, 114–129. doi:10.1016/j.tecto.2008.01.011

Solá, A.R., Williams, I.S., Neiva, A.M., Ribeiro, M.L., 2009. U–Th–Pb SHRIMP ages and oxygen isotope composition of zircon from two contrasting late Variscan granitoids, Nisa-Albuquerque batholith, SW Iberian Massif: Petrologic and regional implications. Lithos 111, 156-167. doi:10.1016/j.lithos.2009.03.045

Sos Baynat, V., 1967. Geología, Mineralogía y Mineralogenia de la Sierra de San Cristóbal, Logrosán (Cáceres). Memorias de la Real Academia de Ciencias. Serie Ciencias Naturales, 22, pp. 141.

Sos Baynat, V., 1977. Los hallazgos prehistóricos de Logrosán (Cáceres). Institución Provincial de Badajoz. Intervención de Servicios Culturales, Badajoz, pp. 47.

Sos Baynat, V., 1981. Sobre la edad geológica de las casiteritas de Logrosán. Boletim de la Sociedad Geológica de Portugal, XXII: 89-92

Sparks, R.S.J, Folkes, C,B., Humphreys, M.C.S., Barfod, D.N., Clavero, J., Sunagua, M.C., McNutt, S.R., Pritchard, M.E., 2008. Uturuncu volcano, Bolivia: Volcanic unrest due to mid-crustal magma intrusion. American Journal of Science 308, 727-769.

Speer, J.A., 1982. Zircon. In: P.H. Ribbe (Ed.), Orthosilicates. Reviews in Mineralogy and Geochemistry 5. Mineralogical Society of America, Virginia, pp. 67–112.

Stacey, J.T., Kramers, J., 1975. Approximation of terrestrial lead isotope evolution by a two-stage model. Earth and Planetary Science Letters 26, 207-221. doi:10.1016/0012-821X(75)90088-6

Stampfli, G.M., Borel, G.D., 2002. A plate tectonic model for the Paleozoic and Mesozoic constrained by dynamic plate boundaries and restored synthetic oceanic isochrones. Earth and Planetary Science Letters 196, 17-33.

Štemprok, M., Blecha, V., 2015. Variscan Sn–W–Mo metallogeny in the gravity picture of the Krušné hory/Erzgebirge granite batholith (Central Europe). Ore Geology Reviews 69, 285-300. doi:10.1016/j.oregeorev.2015.02.014

Stemprok, M., 1980. Tin and tungsten deposits of the West-Central European Variscides. In: Ridge, J.D. (Ed.) Proceedings, Fifth Quadrennial IAGOD Symposium. Stuttgart, pp. 495-500.

Štemprok, M., Seltmann, R., 1994. The metallogeny of the Erzgebirge (Krušné hory). Metallogeny of collisional orogens, 61-69. In: Seltmann, R., Kämpf, H., Möller P., (Eds.): Metallogeny of Collisional Orogens, Czech Geol. Survey, Prague, pp. 61–69.

Stepanov, A. S., Hermann, J., 2013. Fractionation of Nb and Ta by biotite and phengite: Implications for the "missing Nb paradox". Geology 41, 303-306. doi: 10.1130/G33781.1

Stone, M., Klomínský, J., Rajpoot, G.S., 1997. Composition of trioctahedral micas in the Karlovy Vary pluton, Czech Republic and a comparison with those in the Cornubian batholith, SW England. Mineralogical Magazine 61, 791-807.

Streckeisen, A., 1976. To each plutonic rock its proper name. Earth-science reviews 12, 1-33.

Sun, S. S., McDonough, W.F., 1989. Chemical and isotopic systematics of oceanic basalts: implications for mantle composition and processes. Geological Society, London, Special Publications 42, 313-345. doi:10.1144/GSL.SP.1989.042.01.19

Suzuoki, T., Epstein, S. 1976. Hydrogen isotope fractionation between OH-bearing minerals and water. Geochimica et Cosmochimica Acta 40, 1229-1240. doi:10.1016/0016-7037(76)90158-7

Sylvester, P.J., 1998. Post-collisional strongly peraluminous granites, Lithos 45, 29–44. doi:10.1016/S0024-4937(98)00024-3

Tait, J. A., Bachtadse, V., Franke, W., Soffel, H.C., 1997. Geodynamic evolution of the European Variscan fold belt: palaeomagnetic and geological constraints. Geologische Rundschau 86, 585-598. doi:10.1007/s005310050165

Talavera, C., Montero, P., Martínez Poyatos, D., Williams, I., 2012. Ediacaran to Lower Ordovician age for rocks ascribed to the Schist–Graywacke Complex (Iberian Massif, Spain. Evidence from detrital zircon SHRIMP U–Pb geochronology. Gondwana Research 22, 928-942. doi:10.1016/j.gr.2012.03.008

Tartèse, R., Boulvais, P., Poujol, M., Vigneresse, J.L., 2001. Granite petrogenesis revealed by combined gravimetric and radiometric imaging. Tectonophysics 501, 98–103. doi: 10.1016/j.tecto.2011.02.003

Tartèse, R., Boulvais, P., 2010. Differentiation of peraluminous leucogranites "en route" to the surface. Lithos 114, 353-368. doi:10.1016/j.lithos.2009.09.011

Taylor, H.P., 1974. The application of oxygen and hydrogen isotope studies to problems of hydrothermal alteration and ore deposition. Economic geology 69, 843-883. doi:10.2113/gsecongeo.69.6.843

Taylor, H.P., 1978. Oxygen and hydrogen isotope studies of plutonic granitic rocks. Earth and Planetary Science Letters 38, 177-210. doi: 10.1016/0012-821X(78)90131-0

Taylor, R.G., 1979. Geology of Tin Deposits. Elsevier, Amsterdam, The Netherlands. 543 pp.

Taylor, G.K., 2007. Pluton shapes in the Cornubian Batholith: new perspectives from gravity modelling. Journal of the Geological Society 164, 525–528. doi: 10.1144/0016-76492006-104

Teixeira, R.J.S., Neiva, A.M.R., Silva, P.B., Gomes, M.E.P, Andersen, Ramos, .J.M.F., 2011. Combined U–Pb geochronology and Lu–Hf isotope systematics by LAM–ICPMS of zircons from granites and metasedimentary rocks of Carrazeda de Ansiães and Sabugal areas, Portugal, to constrain granite sources. Lithos 125, 321-334. doi:10.1016/j.lithos.2011.02.015

Teixeira, R.J.S., Neiva, A.M.R., Gomes, M.E.P., Corfu, F., Cuesta, A., Croudace, I.W., 2012. The role of fractional crystallization in the genesis of early syn-D 3, tin-mineralized Variscan two-mica granites from the Carrazeda de Ansiães area, northern Portugal. Lithos 153, 177-191. doi:10.1016/j.lithos.2012.04.024

Thiéry, R., van den Kerkhof, A.M., Dubessy, J., 1994. vX properties of CH_4-CO_2 and CO_2-N_2 fluid inclusions; modelling for T< 31 ºC and P< 400 bars. European Journal of Mineralogy 6, 753-771. doi:10.1127/ejm/6/6/0753

Thomas, R., 2002. Determination of the H_3BO_3 concentration in fluid and melt inclusions in granite pegmatites by laser Raman microprobe spectroscopy. American Mineralogist, 87, 56-68. doi:10.2138/am-2002-0107

Thomas, R., Förster, H. J., Heinrich, W., 2003. The behaviour of boron in a peraluminous granite-pegmatite system and associated hydrothermal solutions: a melt and fluid-inclusion study. Contributions to Mineralogy and Petrology 144, 457-472. doi:10.1007/s00410-002-0410-5

Timón, S. M., 2008. El skarn de scheelita de Los Santos (Salamanca). Química mineral, inclusiones fluidas e isótopos estables. PhD Thesis, Universidad de Salamanca. 396 pp.

Tindle, A.G., Breaks, F.W., Webb, P.C., 1998. Wodginite-group minerals from the Separation Rapids rare-element granitic pegmatite group, northwestern Ontario. The Canadian Mineralogist 36, 637-658.

Tindle, A. G., Webb, P. C., 1990. Estimation of lithium contents in trioctahedral micas using microprobe data: application to micas from granitic rocks. European Journal of Mineralogy, 595-610. doi:10.1127/ejm/2/5/0595

Tindle, A.G., Breaks, F.W., 2000. Columbite-tantalite mineral chemistry from rare-element granitic pegmatites: Separation Lake area, N.W. Ontario, Mineralogy and Petrology 70, 165-198. doi:10.1007/s007100070002

Tornos, F., Gumiel, P., 1992: El wolframio y estaño: aspectos económicos y metalogénicos. In: García Guinéa, J., Martínez Frías, J. (Eds.). Recursos Minerales de España, CSIC, pp. 379-394

Tornos, F., Delgado, A., Casquet, C., Galindo, C., 2000. 300 Million years of episodic hydrothermal activity: stable isotope evidence from hydrothermal rocks of the Eastern Iberian Central System. Mineralium Deposita 35, 551-569. doi: 10.1007/s001260050261

Trotter, J.A., Eggins, S.A., 2006. Chemical systematics of conodont apatite determined by laser ablation ICPMS. Chemical Geology 233, 196–216. doi: 10.1016/j.chemgeo.2006.03.004

Ubide, T., 2013. The Cretaceous alkaline magmatism in norhteast Iberia. Igneous processes and geodynamic implications. Doctoral Thesis, Universidad de Zaragoza, 223 pp.

Ugidos, J., Valladares, M.I., Recio, C., Rogers, G., Fallick, A.E., Stephens, W.E., 1997. Provenance of Upper Precambrian-Lower Cambrian shales in the Central Iberian Zone, Spain: evidence from a chemical and isotopic study. Chemical Geology 136, 55-70. doi:10.1016/S0009-2541(96)00138-6

Unrug, R., Harańczyk, C., Chocyk-Jamińska, M., 1999. Easternmost Avalonian and Armorican–Cadomian terranes of central Europe and Caledonian–Variscan evolution of the polydeformed Kraków mobile belt: geological constraints. Tectonophysics 302, 133-157. doi:10.1016/S0040-1951(98)00278-9

USGS, 2013. Historical Statistics for Mineral and Material Commodities in the United States. Department the Interior, US Survey.

USGS, 2015. Mineral Commodities Summaries: Tin. Department the Interior, US Survey. pp. 168-166.

Vallance, J., Cathelineau, M., Marignac, C., Boiron, M.C., Fourcade, S., Martineau, F., Fabre, C., 2001. Microfracturing and fluid mixing in granites: W–(Sn) ore deposition at Vaulry (NW French Massif Central). Tectonophysics 336, 43-61. doi: 10.1016/S0040-1951(01)00093-2

Valle Aguado, B., Azevedo, M.R., Schaltegger, U., Martínez Catalán, J.R., Nolan, J., 2005. U-Pb zircon and monazite geochronology of Variscan magmatism related to ynconvergence extension in Central Northern Portugal. Lithos 82, 169-184. doi: 10.1016/j.lithos.2004.12.012

Van Achterbergh, E., Ryan, C.G., Griffin, W.L., 2001. GLITTER version 4. Macquarie Research Ltd., Sidney.

Van den Kerkhof, A., 1988. Phase transitions and molar volumes of CO_2-CH_4-N_2 inclusions. Bulletin de minéralogie, 111(3-4): 257-266.

Van den Kerkhof, A. M., 1990. Isochoric phase diagrams in the systems CO2-CH4 and CO2-N2: Application to fluid inclusions Application to fluid inclusions. Geochimica et Cosmochimica Acta, 54, 621-629. doi:10.1016/0016-7037(90)90358-R

Van den Kerkhof, A., Thiéry, R., 2001. Carbonic inclusions. Lithos, 55, 49-68. doi:10.1016/S0024-4937(00)00038-4

Van Lichtervelde, M., Holtz, F., Hanchar, J.M., 2010. Solubility of manganotantalite, zircon and hafnon in highly fluxed peralkaline to peraluminous pegmatitic melts. Contributions to Mineralogy and Petrology 160, 17–32. doi:10.1007/s00410-009-0462-x

Van Staal, C.R., Dewey, J.F., Mac Niocaill, C., McKerrow, W.S., 1998. The Cambrian-Silurian tectonic evolution of the Northern Appalachians and British Caledonides; history of a complex, west and southwest Pacific-type segment of Iapetus. In: Blundell, D., Scott, A.C. (Eds.), Lyell: The Past is the Key to the Present, 143. Geological Society of London Special Publication, pp. 199-242.

Vigneresse, J.L., 1995. Control of granite emplacement by regional deformation. Tectonophysics 249, 173–186. doi:10.1016/0040-1951(95)00004-7

Vigneresse, J.L., Tikoff, B., Améglio, L., 1999. Modification of the regional stress field by magma intrusion and formation of tabular granitic plutons. Tectonophysics 302, 203-224. doi:10.1016/S0040-1951(98)00285-6

Vilanova y Piera, J. 1890. Geología y Protohistoria Ibéricas. Historia General de España, I. El Progreso. Madrid.

Villaseca, C., 2011. On the origin of granite types in the Central Iberian Zone: Contribution from integrated U-Pb and Hf isotope studies of zircon. Libro actas VIII Congreso Ibérico de Geoquímica, pp. 29-34.

Villaseca, C., Barbero, L., 1994. Chemical variability of AI-Ti-Fe-Mg minerals in peraluminous granitoid rocks from Central Spain. European Journal of Mineralogy 691, 710.

Villaseca, C., Barbero, L., Herreros, V., 1998a. A re-examination of the typology of peraluminous granite types in intracontinental orogenic belts. Transactions of the Royal Society of Edinburgh, Earth Sciences 89, 113–119. doi:10.1017/S0263593300007045

Villaseca, C., Barbero, L, Rogers, G., 1998b. Crustal origin of Hercynian peraluminous granitic batholiths of Central Spain: petrological, geochemical and isotopic (Sr, Nd) constraints. Lithos 43, 55-79. doi:10.1016/S0024-4937(98)00002-4

Villaseca, C., Downes, H., Pin, C., Barbero, L., 1999. Nature and composition of the lower continental crust in central Spain and the granulite-granite linkage: inferences from granulite xenoliths. Journal of Petrology 40, 1465–1496. doi:10.1093/petroj/40.10.1465

Villaseca, C., Herreros, V., 2000. A sustained felsic magmatic system: the Hercynian granitic batholith of the Spanish Central System. Transactions of the Royal Society of Edinburgh 91, 207-219. doi:10.1017/S0263593300007380

Villaseca, C., López-García, J.A., Barbero, L., 2005. Estudio de la composición isotópica (Pb-S-O) de las mineralizaciones de Pb-Zn de Mazarambroz (Banda Milonítica de Toledo). Geogaceta 38, 271-3.

Villaseca C., Pérez-Soba C., Merino E., Orejana D., López-García J.A., Billstrom K., 2008. Contrasted crustal sources for peraluminous granites of the segmented Montes de Toledo Batholith (Iberian Variscan Belt). Journal of Geosciences 53, 263-280. doi:10.3190/jgeosci.035

Villaseca, C., Bellido, F., Pérez-Soba, C., Billström, K., 2009. Multiple crustal sources for post-tectonic I-type granites in the Hercynian Iberian Belt. Mineralogy and Petrology 96, 197-211. doi:10.1007/s00710-009-0057-2

Villaseca, C., Belousova, E., Orejana, D., Castiñeiras, P., Pérez-Soba, C., 2011. Presence of Palaeoproterozoic and Archean components in the granulite-facies rocks of central Iberia: The Hf isotopic evidence. Precambrian Research 187, 143-154. doi:10.1016/j.precamres.2011.03.001

Villaseca, C., Orejana, D., Belousova, E.A., 2012. Recycled metaigneous crustal sources for S-and I-type Variscan granitoids from the Spanish Central System batholith: Constraints from Hf isotope zircon composition. Lithos 153, 84-93. doi:10.1016/j.lithos.2012.03.024

Villaseca, C., Merino, E.; Oyarzun R.; Orejana, D.; Pérez-Soba, C.; Chicharro E., 2014. Contrasting chemical and isotopic signatures from Neoproterozoic metasedimentary rocks in the Central Iberian Zone (Spain) of pre-Variscan Europe: Implications for terrane analysis and Early Ordovician magmatic belts. Precambrian Research 245, 131-145. doi:10.1016/j.precamres.2014.02.006

Villaseca, C., Castiñeiras, P., Orejana, D., 2015. Early Ordovician metabasites from the Spanish Central System: A remnant of intraplate HP rocks in the Central Iberian Zone. Gondwana Research 27, 392-409. doi:10.1016/j.gr.2013.10.007

Vindel, E., López-García, J.Á., García, E., Boiron, M.C., Cathelineau, M., 1996. Estudio de inclusiones fluidas en granitos microfisurados. Mineralizaciones de W-Sn del Sistema Central Español. Geogaceta 20, 1558-1560.

Vindel, E., Chicharro, E., Villaseca, C., López-García, J. Á., Sánchez, V. 2014. Hydrothermal phosphate vein-type ores from the southern Central Iberian Zone, Spain: Evidence for their relationship to granites and Neoproterozoic metasedimentary rocks. Ore Geology Reviews 62, 143-155. doi:10.1016/j.oregeorev.2014.03.011

Wagner, T., Boyce, A.J., Jonsson, E., Fallick, A.E., 2004. Laser microprobe sulphur isotope analysis of arsenopyrite: experimental calibration and application to the Boliden Au–Cu–As massive sulphide deposit. Ore Geology Reviews 25, 311-325. doi:10.1016/j.oregeorev.2004.05.002

Wang, X., Griffin, W., Chen, J., 2010. Hf contents and Zr/Hf ratios in granitic zircons. Geochemical Journal 44, 65-72. doi:10.2343/geochemj.1.0043

Watson, E.B., Harrison, T.M., 1983. Zircon saturation revisited: temperature and composition effects in a variety of crustal magma types. Earth and Planetary Science Letters 64: 295-304. doi:10.1016/0012-821X(83)90211-X

Watson, E.B., Harrison, T.M., 2005. Zircon Thermometer Reveals Minimum Melting Conditions on Earliest Earth. Science 308, 841-844. doi:10.1126/science.1110873

Wiedenbeck, M., Allé, P., Corfu, F., Griffin, W.L., Meier, M., Oberli, F., von Quadt, A., Roddick, J.C., Spiegel, W., 1995. Three natural zircon standards for U-Th-Pb, Lu-Hf, trace element and REE analyses. Geostandards Newsletter 19, 1-23. doi:10.1111/j.1751-908X.1995.tb00147.x

Wilkinson, J.J., 1990. The role of metamorphic fluids in the development of the Cornubian orefield: fluid inclusion evidence from south Cornwall. Mineralogical Magazine 54, 219-230. doi:10.1180/minmag.1990.054.375.08

Williamson, B. J., Spratt, J., Adams, J. T., Tindle, A. G., Stanley, C. J., 2000. Geochemical constraints from zoned hydrothermal tourmalines on fluid evolution and Sn mineralization: an example from fault breccias at Roche, SW England. Journal of Petrology 41: 1439-1453. doi:10.1093/petrology/41.9.1439

Woodhead, J.D., Hergt, J.M., 2005. A preliminary appraisal of seven natural zircon reference materials for in situ Hf isotope determination. Geostandards and Geoanalytical Research 29, 183-195. doi:10.1111/j.1751-908X.2005.tb00891.x

Xu, G., 2000. Methane-rich fluid inclusions in the Proterozoic Zn–Pb–Ag deposit at Dugald River, NW Queensland: potential as an exploration guide. Applied Geochemistry 15, 1-12. doi:10.1016/S0883-2927(99)00019-0

Yuan, S., Peng, J., Hao, S., Li, H., Geng, J., Zhang, D., 2011. *In situ* LA-MC-ICP-MS and ID-TIMS U–Pb geochronology of cassiterite in the giant Furong tin deposit, Hunan Province, South China: New constraints on the timing of tin–polymetallic mineralization. Ore Geology Reviews 43, 235-242. doi:10.1016/j.oregeorev.2011.08.002

Yushan, L., Shuqing, C., 1986. An experimental study on cassiterite solubility and tin transport during mineralization. Acta Geologica Sinica 1, 78-88.

Zaraisky G.P., Korzhinskaya V, Kotova N., 2010. Experimental studies of Ta2O5 and columbite–tantalite solubility in fluoride solutions from 300 to 550 °C and 50 to 100 MPa. Mineralogy and Petrology 99, 287–300. doi:10.1007/s00710-010-0112-z

Zeck, H., Wingate, M., Pooley, G., 2007. Ion microprobe U–Pb zircon geochronology of a late tectonic granitic–gabbroic rock complex within the Hercynian Iberian belt. Geological Magazine 144, 157-177. doi:10.1017/S0016756806002652

Zhang, D., Peng, J., Coulson, I. M., Hou, L., Li, S., 2014. Cassiterite U–Pb and muscovite ^{40}Ar–^{39}Ar age constraints on the timing of mineralization in the Xuebaoding Sn–W–Be deposit, western China. Ore Geology Reviews 62, 315-322. doi:10.1016/j.oregeorev.2014.04.011

Zheng, Y.F., 1991. Calculation of oxygen isotope fractionation in metal oxides. Geochimica et Cosmochimica Acta 55, 2299-2307. doi:10.1016/0016-7037(91)90105-E

Zheng, Y. F., 1993. Calculation of oxygen isotope fractionation in hydroxyl-bearing silicates. Earth and Planetary Science Letters 120, 247-263. doi:10.1016/0012-821X(93)90243-3

Ziegler, P., 1989. Evolution of Laurussia. Kluwer, Dordrecht. 102 pp.

ELECRONIC SUPPLEMENTARY MATERIAL

Supplementary files of mineral chemistry analyses for this PhD Thesis can be obtained on request to the author (evachicharro@ucm.es).

- Supplementary Table 1 (EMPA_Granite)
- Supplementary Table 2 (LA-ICP-MS_Granite)
- Supplementary Table 3 (EMPA_Qtz-Cst veins)
- Supplementary Table 4 (LA-ICP-MS_Qtz-Cst veins)
- Supplementary Table 5 (EMPA_Qtz-Sulf veins)
- Supplementary Table 6 (EMPA_Qtz-Tur veins)
- Supplementary Table 7 (LA-ICP-MS_Qtz-Tur veins)
- Supplementary Table 8 (EMPA_Qtz-Ap veins)
- Supplementary Table 9 (LA-ICP-MS_Qtz-Ap veins)

For, after all, how do we know that two and two make four? Or that the force of gravity works? Or that the past is unchangeable? If both the past and the external world exist only in the mind, and if the mind itself is controllable – what then?

(George Orwell – 1984)

This PhD Thesis has been performed at the Crystallography and Mineralogy and at the Petrology and Geochemistry Departments of the Geological Science Faculty of the Complutense University of Madrid

Esta Tesis Doctoral se ha realizado en los Departamentos de Cristalografía y Mineralogía y de Petrología y Geoquímica de la Facultad de Ciencias Geológicas de la Universidad Complutense de Madrid

Eva Chicharro Álvarez

Madrid, 2015

Front Cover: Logrosán granite view from the north

Back Cover: Old Logrosán railway line and train station